Chemomechanics at the cell-material interface :
Measurements and implications of forced molecular unbinding

by

SUNYOUNG LEE

Bachelor of Science, Chemical Engineering, Seoul National University
Seoul, Korea, 2002
Master of Science, Materials Science and Engineering
Massachusetts Institute of Technology, Cambridge, Massachusetts, 2005

Submitted to the Department of Materials Science and Engineering
In partial fulfillment of the requirements for the degree of
DOCTOR OF PHILOSOPHY IN MATERIALS SCIENCE AND ENGINEERING
At the
MASSACHUSETTS INSTITUTE OF TECHNOLOGY

June 2009
Presented: 23 February 2009

Signature of Author:_____
Department of Materials Science and Engineering
23 February 2009

Certified by:_____
Krystyn J. Van Vliet
Thomas Lord Assistant Professor of Materials Science and Engineering
Thesis Advisor

Accepted by:_____
Christine Ortiz
Associate Professor of Materials Science and Engineering
Chair, Departmental Committee on Graduate Students

Chemomechanics at the cell-material interface :
Measurements and implications of forced molecular unbinding

by
SUNYOUNG LEE

ABSTRACT

The main goal of this thesis is to study the coupled interactions between chemically and mechanically characterized materials and cells that are relevant to microvascular physiology and pathology. In particular, the mechanical characterization of cell surface structure and force generation are realized via various atomic force microscopy (AFM) imaging techniques including AFM cell force spectroscopy and functionalized force imaging. In these approaches, the recognition of mechanical responses of cells or mapping of cell surface receptors is mediated by chemomechanically characterized AFM cantilevers. The high spatial and force resolution of AFM imaging techniques and force spectroscopy enabled investigation of mechanical interaction at the cell-cell or cell-material interfaces. This interaction was studied via the mapping of specific receptors on endothelial cell surfaces and the detection of pN-scale force transmission through ligand-receptor pairs on the plasma membrane with biophysical interpretation of cellular force generation. This thesis consists of four major chapters: the recognition of vascular endothelial growth factor receptors and of anti-angiogenic oligopeptide receptors on endothelial cell surfaces, mechanical interaction between endothelial cells and pericytes that encompass capillary blood vessels; cell-matrix contact via focal complexes; and leukemia cells rolling on endothelial cell surfaces and P-selectin-conjugated glass substrata. This thesis also includes appendices that detail the effect of force transducer stiffness on the measurement of unbinding force, nerve cell imaging to

observe the connection between axons and dendrites, and chemomechanical characterization of polyelectrolyte multilayers, biodegradable hydrogels, and biological glues.

In Chapter 2, transmembrane receptors on endothelial cell surfaces are mapped and associated binding kinetics/thermodynamics of ligand-receptor pairs are quantified via AFM functionalized force imaging or single-molecule recognition imaging. Functionalized force imaging is then used to identify unknown receptors, receptors for an oligopeptide isolated from tissue inhibitor of metalloproteinase-2, called Loop 6. In Chapter 3, mechanical stress by pericytes that envelop capillary blood vessels is quantified, demonstrating that pericytes exert significant mechanical strain on the extracellular environment. In Chapter 4, picoNewton-scale force dynamics at fibroblasts' focal complexes, measured in real-time through cell force spectroscopy, demonstrates that cells exert mechanical force that can speed the rupture of ligand-receptor pairs in focal complexes during migration and adhesion to underlying substrata. The last part of this thesis, Chapter 5, discusses the role of actin-mediated force in leukemia cell rolling on endothelial cell surfaces. The measurement of picoNewton-scale force dynamics using cell force spectroscopy suggests that, in addition to drag force exerted by blood flow, cytoskeletal force dynamics contribute to the cell rolling process. Together, these studies from the single-molecule to whole-cell level detail the strong coupling between mechanical force and ligand-receptor reaction kinetics.

Thesis supervisor : Krystyn J. Van Vliet, Thomas Lord Assistant Professor

Department of Materials Science and Engineering

Department of Biological Engineering

ACKNOWLEDGMENTS

Now I recall my days spent at MIT for five and half years, full of great joy and frustration, all mixed together. Sometimes, I just wanted to quit because I thought that research was not what I wanted to do. Sometimes I wanted to further pursue research careers because I could not forget the great joy of finding and developing what others have not. Having lived these innumerable moments in a place where I used to not know anyone, I now want to thank numerous individuals without whom I wouldn't have been able to finish my thesis defense presentation. First and foremost, I want to thank my thesis advisor, Professor Krystyn J. Van Vliet. All I can say is that I have been extremely fortunate to work with her. She truly enjoys and wants to enjoy the work that she does. I know how patient she has been with a student who was not able to understand English very well and whose initial research potential was minimal. She was a true mentor and counselor who guided me throughout my most difficult times. If I would be able to go back to my first year and start my graduate study again, I would not hesitate to be her student (of course, if she wants to work with me again).

I want to thank my thesis committee members, Professor Angela Belcher and Professor Darrell Irvine for their eagerness to give their time for my thesis committee meetings during the busiest times of each semester. I truly benefited from all their advice on my thesis presentation and research projects.

I want to acknowledge Professor Young-sup Yoon at Emory University School of Medicine. His previous and current life stories as a cardiologist and physician-scientist have encouraged me the most in my entire life, especially when I was drifting aimlessly. He has been my role model and helped influence my decision toward the everyday lives of people around me as well as underserved people in poor countries.

Interactions with my labmates have been very helpful and I learned so much from them. I'd like to thank Emily Walton, Adam Zeiger, Dessy Nikova, Ranjani Krishnan, John Maloney, Catherine Tweedie, Todd Thompson, Emilio Silva, Georgios Constantinides, Timothy Lau, Jack Milwid, Binu Oommen, Meng Qu, Karen Stewart, Mukul Kabir, Joan Mao, Ilke Kalcioglu, Sezen Curgul, and Hansohl Cho. Particularly, I want to thank the "bio" people who have infused me with great insights into how cells interact with materials at the cell-material interface.

Professor Seungpyo Hong at the University of Illinois at Chicago went beyond the

normal role of a collaborator. His research insight and warm fellowship with his family enriched my life at MIT. My friends from Korea, shared with me a lot of common experiences and feelings, and did not let me forget the fact that I was not alone. Thank you to Daeyeon Lee, Junsang Doh, Ju Jin An, Yoon Sung Nam, Taeho Shin, Sung Gap Im, Dae Kun Hwang, Tek Hyung Lee, Ki Wan Bong, Jinyoung Baek, Chang Hoon Lim, Seung Woo Lee, Dongwan Ahn, Jaebum Joo, Hyungho Shin, Jeeyoung Choi, Juhyun Park, Jongseung Yoon, Heejae Kim, Ki Tae Nam, Yeon Sik Jung, Byungwoo Kang, Dong Soo Yoon, Tae Seok Moon, Woo Keun Chung, Seok Joon Kwon, Yang Hyo Kim, YongKeun Park, Taeminn Song, Jin Young Kim, Jongnam Park, Kwonmoo Lee, Kisuk Kang, Jihun Oh, Jae Hyung Yi, Jin-Seok Ko, Joonil Seog, WooChul Jung, Jinho Jang, Byung Soo Kim, Inseok Choi, Choongyeon Cho, and their families.

I want to express my gratitude to my collaborators from Harvard University, MIT and Tufts University: Professor Marsha Moses and Dr. Cecilia Fernandez at Harvard Medical School, Professor Ira M. Herman and Dr. Maciej Kotecki at Tufts University School of Medicine, and Professor Robert Langer, Professor Jeffrey Karp, Ms. Vanessa Lundin, Mr. Huanan Zhang, Professor Paula Hammond, Professor Sebastian Seung, Mr. Neville Sanjana, Professor Sangeeta Bhatia, Dr. Salman Khetani, Ms. Alice A. Chen, Professor Elazor Edelman, Dr. Natalie Artzi, Professor Doyle, and Dr. Aubin-Tam, all of which are from MIT.

The most important thing on the earth is love. I could not find a word to describe how thankful I am for my wife Shinyoung's love that has been the sweetest and most beautiful. I could not have been survived a single moment without her sacrifice, love, and patience. She has been a friend to which I can talk about anything; about people, research, and life at MIT. It's just great to have someone with whom I can walk along the Charles River and any places. I am simply indebted. Although I do not have kids now, when I think about raising children, I imagine how my parents have lived during the toughest time of their lives, growing their two sons and a daughter. My parents, Eun Sung Lee and Jung Sim Song, whose being is much more important than what they do and where they are. I hope that I can give my future children the love that my parents have lavished me with. I won't be able to forget their dedication, sacrifice, and prayers until the very last moment of my life. I thank my father, mother, and grandmothers-in-law, for their prayers, love, support, and above all letting me be with Shinyoung.

Table of Contents

List of Figures

images of (B – D) indicate that there is no degradation of the surface topography over this timescale. Scan rate = 1 μm/sec; scalebars = 500 nm. (E) demonstrates cytoskeletal bundles represented in a fluorescence image of FITC-phalloidin-stained F-actin and an AFM contact mode image (inset); scalebars = 10 μm. Four cytoskeletal bundles are manifest as lighter (high) regions in (F – I); for visual clarity, the position and apparent width of these bundles is shown only in (H), where blue bands are reconstructed from height traces as shown in (I). (I) Indicated line trace of the height image in (F) shows the apparent position and width of three cytoskeletal bundles that deflect the cantilever due to their comparatively higher stiffness; this width agrees reasonably well with that measured in fluorescence optical images such as (E).

Figure 2.2 Confirmation of anti-VEGFR2 binding specificity on cell surfaces. After imaging fixed HUVECs with anti-VEGFR2-functionalized probe ((A) phase image; (B, C) magnetic AC mode recognition image in indicated region of interest). Thirty minutes after the addition of 5 μg/mL soluble mouse monoclonal anti-human anti-CD31 IgG1 (C), no competitive blocking of recognition events was observed. This indicates these recognition events represent specific binding between probe-bound anti-VEGFR2 and VEGFR2 on the HUVEC surface. The height image corresponding to this region (inset) indicates the position of cytoskeletal bundles beneath the cell membrane; the white lines marking the bundle edges were constructed from height traces of the region, as shown in (E). (D) Output voltage scale for (B) and (C) demonstrates recognition signal compared to background in a line scan over a region including three binding events. Black discs just below the line trace minima indicate the position of strong recognition events. (E) This height trace of the line indicated in (C) enables comparison of the position of the underlying cytoskeletal bundles with respective to recognition events attributed to VEGFR2 locations. (B – E) demonstrate that VEGFR2 is non-uniformly distributed near cytoskeletal bundles beneath the plasma membrane. Scan rate = 10 μm/sec in (A); 1 μm/sec in (B, C). White scale bars = 10 μm; black scale bars = 500 nm.

Figure 2.3. Confirmation of probe functionalization. FITC-labeled anti-IgG1 binds to Si_3N_4 probes functionalized with primary antibody, anti-VEGFR2 (A), but does not bind to Si_3N_4 probes functionalized with only the distensible poly(ethylene glycol)-based linker (B). In the absence of this linker, the primary antibody can bind nonspecifically and aggregate on the Si_3N_4 surface, as visualized in (C) via subsequent binding of the FITC-labeled anti-IgG1. Scale bars = 50 μm.

Figure 2.4 Confirmation of anti-VEGFR2 binding specificity on HUVECs. (A) Functionalized force imaging of human 3T3 fibroblast cells (phase image) with anti-VEGFR2-functionalized probe does not indicate binding in either the topography image (B) or recognition image (C) of these cells, which do not to endogenously express VEGFR2 as shown in Fig. 8. Scan rate = 10 μm/sec in A and 1 μm/sec in (B, C). White scalebar = 10 μm; black scalebars = 500 nm.

Figure 2.5 Identification of VEGFR 2 on HUVECs and human 3T3 fibroblasts. (A) Flow cytometry confirms significant presentation of VEGFR2 on HUVECs (blue), but not on 3T3 fibroblasts (green), using the same antibodies as in functionalized force imaging. IgG isotype control on HUVECs also demonstrates anti-VEGFR2 specificity (red). (B - C) Immunocytochemistry using the same antibodies as in functionalized force imaging confirms gross spatial distribution of VEGFR2 on HUVECs in B, but the absence of VEGFR2 on 3T3 fibroblasts in (C). Scalebars = 10 μm.

Figure 2.6 Force spectroscopy analysis of binding events on fixed HUVECs. (A - B) Representative specific ligand-receptor unbinding trajectory (force-displacement response) at recognition sites included in the probability density function of >600 rupture forces indicating two maxima of 33 pN and 64 pN. (C - D) Representative nonspecific unbinding trajectories (force-displacement curve) at >400 non-recognition sites on the cell surface indicate a nonspecific rupture force level of ~13 pN. Effective loading rate = 11.7 nN/sec. Bond lifetime τ in (A) is proportional to the binding displacement and is used to calculate binding constants (see Materials and Methods).

Figure 2.7 Time course of competitive binding to HUVEC surface. Recognition sites from images such as Fig. 1B decrease with time post-blocking via addition of 5 μg/mL soluble anti-VEGFR2 during sustained functionalized force imaging of the cell surface with an antibody-functionalized probe at 27°C. As the number of observable binding sites decreases during blocking, the number of receptors bound by the soluble antibodies correspondingly increases (•). Kinetic constants can be determined by application of a binding kinetic model for which k_{off} is assumed from independent force spectroscopy experiments (—), or by a least-squares best fit to the experimental data (—). See Materials and Methods for detailed calculation of binding kinetic constants.

Figure 2.8 Single receptor imaging on living HUVEC surface. (A) Portion of living cell imaged with anti-VEGFR2-functionalized probe in magnetic AC mode at 27°C, phase

image. Scan rate = 10 μm/sec; scalebar = 10 μm. Ligand-receptor binding results in punctate image contrast (circled regions indicate a subset of the observed receptors) in phase lag images (B, C) that is competitively inhibited by addition of soluble anti-VEGFR2 antibody (data not shown). Scan rate = 1 μm/sec; scalebars = 500 nm. The time lapse between (B) and (C) is 30 min. Note the mechanical contrast and displacement of the underlying cytoskeletal actin (normal to arrow) over this timescale. These images indicate $1.32 \pm 0.44 \times 10^5$ receptors/cell (n = 6).

Figure 2.9 Loop 6 functionalization on the silicon nitride probe and its verification. (a) Bare silicon nitride cantilever treated with streptavidin-fluorescein - no specific bindings. (b) BSA-biotin-adsorbed silicon nitride cantilever treated with Texas red-streptavidin - specific bindings, which confirmed BSA-biotin molecules were active. (c) BSA-biotin-adsorbed silicon nitride cantilever, followed by streptavidin immobilization, treated with biotin-fluorescein - specific bindings, which confirmed streptavidin attached to BSA-biotin molecules was active. (d) BSA-biotin-adsorbed silicon nitride cantilever, followed by streptavidin immobilization treated with Texas red-streptavidin – no specific binding. (e) BSA-biotin-adsorbed silicon nitride cantilever, followed by streptavidin immobilization, and biotinylated Loop6 treated with biotin-fluorescein. No specific binding is observed because biotinylated Loop 6 occupied the binding position to biotin-fluorescein. Scale bars = 50 μm.

Figure 2.10 Recognition of binding events between Loop 6 tethered to the AFM probes and cell receptors. (a) Fixed hdMVEC surface – phase image. Scale bar = 10 μm. (b) Area of interest from (a) is shown – phase image. Scale bar = 1000 nm. (c) Recognition image shows strong binding events. Individual binding spots that represent strong binding between Loop 6 and receptors are shown before the addition of blocking Loop 6. (d) The same area as (c) at 10 minutes after the addition of soluble Loop 6. Height cross-section (black line) shows height trace and cytoskeletal fiber beneath the plasma membrane. (d) The same area as (c) and (d) is shown at post blocking time of 30 minutes. (c), (d), and (e) are all recognition images. Scale bars = 200 nm.

Figure 2.11 Force spectroscopy analysis of binding events. (a) Measurement of rupture force from 337 force curves on the binding spots. Histogram and Gaussian curve reveals that rupture force between Loop 6 and its receptor is 30.92 ± 8.41 pN. (b) Rupture force vs. displacement curve shows the specificity of binding events. (c) Measurement of binding force from 145 force curves was made on the areas that didn't show binding

spots. Histogram and Gaussian curve shows that noise force was 15.38 ± 3.28 pN. (d) Compared to (b), strong binding is not shown in the rupture force vs. displacement curve. All the curves were obtained with a loading rate of 4,400 pN/sec.

Figure 2.12 Analysis of the number of binding sites. Change in the number of binding sites, which is visualized in Fig. 1 on hdMVEC surface, is shown in real time. The number of binding sites is decreasing after the addition of soluble Loop 6, which verify the specificity of Loop 6 binding to receptors. Purple dots represent experimental data, and a solid line comes from fitting as shown in supporting information.

Figure 2.12 Analysis of the number of binding sites. Change in the number of binding sites, which is visualized in Fig. 1 on hdMVEC surface, is shown in real time. The number of binding sites is decreasing after the addition of soluble Loop 6, which verify the specificity of Loop 6 binding to receptors. Purple dots represent experimental data, and a solid line comes from fitting as shown in supporting information.

Figure 2.14 Fixed cell surface with bare probe. (a) hdMVEC surface was imaged with a bare probe. Scale bare = 5 μm. (b) The topography image of the area marked in (a) was shown. (c) is the recognition image of the same area as (b). No binding events were recognized when the cell surface was imaged with the bare probe.

Figure 2.15 Identification of Loop 6 receptors. (a) Phase image of fixed cell with a Loop 6 functionalized probe in MAC mode is shown. Scale bar = 10 μm. (b) demonstrates specific receptors for Loop 6 that are represented as dark spots. (c) shows the same area as (b) at 12 min after the addition of antibody against insulin-like growth factor receptor 1 (IGFR1). Anti-IGFR-1 bound to receptors occludes binding sites. (d) is the cell image at 42 minutes after the addition of anti-IGFR-1. Scale bars of b, c, and d = 500 nm. (e) is an image of another fixed cell with the same probe used to get images of a – d after one set of experiment (a – d) was conducted to verify the activity of the probe through which specificity of ligand-receptor binding was confirmed. Scale bar = 10 μm. (f) demonstrates another binding event on a cell surface of different cell sample. Scale bar = 500 nm.

Figure 2.16. (A – C) Time-lapsed functionalized force imaging of streptavidin conjugated mica with biotin-conjugated probe at 4°C (277 K). (A) Recognition image of streptavidin molecules with biotin-conjugated probe (t_{pb} = 0 min) before the addition of

blocking biotin shows dark spots that represent specific binding between biotin and streptavidin. One example of specific binding events is represented in the circle. Scale bar = 300 μm. (B) Same region as (A) at t_{pb} = 7 min after the addition of biotin and (C) at t_{pb} = 38 min. Scan rate of (A), (B), and (C) = 1,5 μm/sec. (D) Time course of competitive binding of biotin to streptavidin mica. The number of biotin-streptavidin complexes increases with the function modeled above with respect to time post-blocking at 4°C (277 K). Square (■) indicates observed data, and line (–) represents best fit. Kinetic constants/energy were calculated from the best fit, as described in the text.

Figure 2.17 Calculation of (A) binding and (B) activation energy in biotin-streptavidin system. (A) Entropy (■), enthalpy (♦), and free energy (▲) show different time-dependence. Magnitude of both entropy and enthalpy increases as temperature increases, whereas free energy, which is the combination of entropy and enthalpy, increases slowly. (B) Plot of the Eyring equation of biotin-streptavidin binding system. From the slope and intercept are activation entropy, enthalpy, and associated free energy calculated as discussed above. (C) The slope of enthalpy vs. temperature graph represents heat capacity. Heat capacity of biotin-streptavidin system is barely dependent on temperature within the temperature range of 277- 310 K. This independence of temperature implies that biotin-streptavidin binding is not coupled with local folding.

Figure 2.18 (A – C) Time-lapsed functionalized force imaging of VEGFR2 and anti-VEGFR2 on fixed HUVECs at 37°C (310 K). (A) Recognition image of cell surface with anti-VEGFR2-conjugated probe (t_{pb} = 0 min) before the addition of blocking antibody shows dark spots that represent specific binding between receptor and antibody. One example of specific binding events is represented in the circle. Scale bar = 200 nm. (B) Same region as (A) at t_{pb} = 3.5 min after the addition of anti-VEGFR2 and (C) at t_{pb} = 25 min. Scan rate of (A), (B), and (C) = 1,000 nm/sec. Line-trace from height image (image not shown here) in (C) demonstrates that receptors are concentrated near/above cytoskeleton underneath the plasma membrane. The area between two dotted lines represents cytoskeletal bundle. (D) Time course of competitive binding on the cell surface. The number of antibody-receptor complexes increases with the modeled function with respect to time post-blocking at 37°C (310 K). Circle (●) indicates observed data, and line (–) represents best fit. Kinetic constants/energy were calculated from the best fit, which was discussed in Materials and Methods.

Figure 2.19 Calculation of binding (A) and activation energy (B) in the VEGFR2-anti-

VEGFR2 system. (A) Entropy (■), enthalpy (♦), and free energy (▲) each show different dependence on time. The magnitude of both entropy and enthalpy increases as temperature increases, whereas free energy, which is the combination of entropy and enthalpy, increases slowly. (B) Plot of the Eyring equation for the antibody-receptor system. Activation entropy, enthalpy, and associated free energy are calculated from the slope and intercept, as discussed above. (C) The slope of the enthalpy vs. temperature graph represents heat capacity. The heat capacity of VEGFR2 and anti-VEGFRs is barely dependent on temperature within the temperature range of 277- 310 K. This temperature independence implies that antibody-receptor binding is not coupled with local folding like in the biotin-streptavidin system discussed above.

Figure 3.1 Schematic of AFM-enabled imaging and cellular mechanical analyses. Pericytes are grown on silicone rubber (see Materials and Methods for substrata preparation). (A) Cellular mechanics are detected as a quantifiable deflection of the cantilevered probe, while mechanical contacts within AFM imaging mode and mechanical analyses are aided by optical microscopy-incorporated AFM. Using the closed loop scanner, the cantilevered probe is placed at specific positions of interest as shown in (B) and (C). (B) and (C) optical microscopy images show mechanical tests at pericyte membranes on and off the substrata wrinkles, respectively. Inset images in (B) and (C) are AFM deflection images, and blue asterisks (*) represent specific points at which mechanical tests are conducted at current positions of AFM cantilevered probes in optical images. (D) summarizes the cell elastic moduli on (16.3 kPa) and off (7.4 kPa) these wrinkles, measured as schematized in (A). Scale bar = 20 μm.

Figure 3.2 Actin-dependent alterations in pericyte shape, contractile phenotype and elastic moduli. In (A), (B), and (C), AFM deflection images demonstrate changes in pericyte shape. Concomitantly, cell shape and PDMS deformation, either before or 65 min after the addition of pharmacological inhibitors specifically impact actin (de)polymerization and/or actomyosin contraction: (A), latrunculin A (1 μM); (B), blebbistatin (25 μM); (C), ML-7 (300 nM), respectively (see Table 3.1). (D) demonstrates the elastic moduli of pericyte membranes, as schematized in Fig. 1 (see Materials and Methods for elastic moduli measurement), before and after inhibitors, at pericyte membranes on and off deformed (wrinkled) PDMS substrate domains. Table 3.2 summarizes elastic moduli with inhibitors. Scale bars = 20 μm. All the mechanical tests were conducted with more than five cells (n = 5) and 30 mechanical tests at each point.

Figure 3.3 Change in elastic moduli and cell shape with addition of cytoskeletal-specific agents. The same set of experiments as shown in Fig. 2 was conducted with pharmacological reagents that increase the activity of the actin cyskeleton: nodozale (670 nM) (A) and jasplakinolide (670 nM) (B): see Table 1. (C) Mechanical tests were conducted before and after addition of these reagents at cell membranes on and off PDMS wrinkles. See Table for summary of elastic moduli with nocodazole and jasplakinolide. All the mechanical tests were conducted with more than five cells (N = 5) and 30 mechanical tests (n = 30) on and off wrinkles. Scale bars = 20 μm.

Figure 3.4 Fluorescent images of actin-stained pericytes with pharmacological inhibitors. Fixed pericytes were stained with Alexa 488 phalloidin at 37°C: (A), untreated pericytes; (B), those treated with latrunculin A (1 μM); (C), blebbistatin (25 μM); (D), ML-7 (300 nM); (E), nocodazole (670 nM); and (F), jasplakinolide (670 nM). Scale bars = 20 μm.

Figure 3.5 Calculation of strain exerted by pericyte and PDMS elastic moduli. (A) is a topographic AFM image, and an inset image is a deflection image associated with the topography image obtained in AFM contact mode. From height information provided by topography images, PDMS strain exerted by pericytes can be calculated as shown in (B). (B) is a height trace of a white line in (A). For the calculation of strain ε, a purple line in (B) was considered a final length (l_f) of substrata, and the original length (l_o) of a green trace was measured, from which nominal engineering strain was measured (see Materials and Methods). (C) Over 30 wrinkles (n = 30) were considered for the strain calculation, and the range of PDMS strain that pericytes exerted ranged from 1.3 – 38 % (average 16 ± 12 %). PDMS stress-strain response adapted from (*3*). Slopes in graph (C) represent elastic moduli of PDMS. As shown in the graph, within the range of pericyte-exerted strain, elastic moduli of PDMS substrata are not constant. Scale bars = 20 μm.

Figure 3.6 Schematic of pericyte force exertion to the basement membrane and endothelial cell. This figure represents a cross section of a capillary blood vessel. The cell surrounding the vessel is pericyte, and endothelial cell makes a lining of the capillary blood vessel. The basement membrane plays a role as a substratum between pericyte and endothelial cell. Pericyte applies actin-mediated force (blue arrows) to the basement membrane and may modify the mechanical properties of the underlying basement membrane or substratum (e.g., silicone rubber in this paper), which affects the

microenvironment of endothelial cells.

Figure 4.1 Schematic of AFM measurement of intracellular force dynamics. (a) Optical microscope-aided AFM enables the localization of spherical probes on specific regions of cell surfaces. FN is conjugated on AFM cantilevered probes. Dynamic force transmitted via physical connection between integrin, FN, and cytoskeleton is detected in real time in form of deflection of cantilevered probes. Mechanical contact is controlled via feedback between a piezoelectric position controller and a photodetector that receives signals of a cantilevered probe. Free deflection is recorded as in (b), with feedback loop turned off as soon as intended normal stress is applied to cell surfaces. Dotted arrow shows cell migration direction. It has been demonstrated by other researchers that focal complexes are created at dorsal cell surfaces as demonstrated in (a), as well as on the ventral surfaces when activated with the mechanical contact of extracellular matrix molecules, here FN(*4*). As shown in (b), real-time deflection created by cell-generated force is converted to units of force. Dynamic force was characterized in terms of time and force displacement intervals, τ_i and ΔF_i, respectively.

Figure 4.2 3T3 fibroblast (fixed) under fluorescence microscopy and optical microscopy with a fibronectin-conjugated bead. (a) fibronectin-conjugated bead (2.5 μm in diameter) placed on the fibroblast membrane. The black arrow indicate the fibronectin-conjugated bead. (b) vinculin-stained fluorescent image for same region as the optical image of (a), using anti-vinculin antibody. Vinculin was used as a marker of focal adhesion. (b) demonstrates the creation of vinculin around the fibronectin-conjugated bead and further the formation of focal adhesion. The white arrow shows vinculin near the bead. Scale bars = 10 μm.

Figure 4.3 Changes in live 3T3 fibroblast morphology with addition of blebbistatin and fresh medium. (a–f) demonstrate changes in live 3T3 fibroblast morphology under optical microscopy during measurement of cytoskeletal dynamics with cantilevered spherical probes, where blue asterisks indicate location of dynamic force spectra collection and dark triangle at right is AFM cantilever withdrawn from contact after data acquisition. (a–c) correspond to experiments for which spectra were acquired at the cell front, whereas (d–f) correspond to spectra acquired at trailing edge. Probes were intentionally not placed on lamellipodial regions because it was reported that force generated in lamellipodial regions was minimal(*3*). Instead, probes were placed on ectoplasmic/lamella regions as shown in (a–c). Scale bars = 20 μm. Fluorescence

images (g–i) demonstrate changes in morphology of 3T3 fibroblast under fluorescence microscopy through F-actin staining (See Materials and Methods). (a) Fixed cells stained with phalloidin-FITC, before the addition of blebbistatin; (b), at 1 h after the addition of 25 μM of blebbistatin; (c) 3T3 fibroblast after 25 μM of blebbistatin, followed by wash-out of blebbistatin-containing medium and addition of fresh medium. Scale bars = 20 μm.

Figure 4.4 Fluorescence images of phalloidin-stained F-actin in 3T3 fibroblasts. (a–c) demonstrate changes in morphology of 3T3 fibroblast under fluorescence microscopy. (a) Fixed cells stained with phalloidin-FITC, before the addition of blebbistatin; (b), at 1 h after the addition of 25 μM of blebbistatin, which inhibits myosin II binding to the actin cytoskeleton (see Table 4.1); Since the balance between microtubules and F-actin was disrupted as the function of myosin II halted by blebbistatin(*2*), the cell morphology changed as shown in (b). (c) 3T3 fibroblast after 25 μM of blebbistatin, followed by wash-out of blebbistatin-containing medium and addition of fresh medium. Scale bars = 20 μm.

Figure 4.5 Measurement of cell dynamics transmitted through focal complexes. (**a–b**) demonstrate force spectra measured at the front of 3T3 fibroblast by actin cytoskeleton, as measured via AFM cantilevered FN-coated spherical probes. Green, purple, and blue curves represent dynamic force before, 1 hr after the addition of 25 μM blebbistatin, and 1 hr after addition of fresh medium, respectively. (**c**) and (**d**) demonstrate force spectra measured on rear regions of 3T3 fibroblasts. Green, red, and blue curves represent dynamic force before, 1 hr after the addition of 25 μM blebbistatin, and after addition of fresh medium. Arrows in (**a**) represent minute-scale oscillations as refer to a reported result by Galbraith et al.(*3*) Red circles indicate regions of measurement on 3T3 fibroblast surfaces. As noted in Materials and Methods, force curves in (**a–d**) were shown, corrected for intrinsic drift (≈ 9 pN/sec, n = 30) due to thermal fluctuations.

Figure 4.6 Summary of 3T3 fibroblast cell-generated force dynamics in response to pharmacological challenges. (a–b) each include five different spectra, where the blue spectrum consistently represents cell responses for fibronectin-functionalized spherical probes before the addition of pharmacological inhibitors. Cell responses were measured at 1 hr after the addition of blebbistatin (25 μM), cytochalsin D (900 nM), and nocodazole (660 nM) on the same cells, to observe any changes in cell responses. BSA-functionalized probes were used as a control for integrin binding-mediated interactions.

(a) time periods of cell-generated forces at cell leading edge; (b) force oscillations at cell leading edges; (c) time periods of cell-generated forces at cell trailing edge; (d) force oscillations at cell trailing edges. Refer to Tables 4.1 and 4.2. Data analyses were conducted with five spectra acquired on each of five cells, for each inhibitor and/or probe functionalization.

Figure 4.7 Biophysical role of intercellularly generated force through FN-integrin pairs. (a–b) are representative areas of FN-conjugated substrata including glass slides and spherical probe surfaces via mapping of FN conjugated on glass substratum with an anti-FN-functionalized cantilever through FFI. (a) is a topography image, which provides height information of substrata; (b) is a recognition image of the same area as (a), where specific interactions are recognized via perturbation of the oscillating cantilever. Dark spots in (b), representing specific binding events between FN and anti-FN, demonstrate the distribution of FN molecules on substrata. The circled dark spot is one example of specific interaction of FN/anti-FN. Scale bar = 200 nm. (a) demonstrates the range of unbinding forces vs. loading rates in FN/integrin complexes. Orange circles represent intracellularly generated cytoskeletal force (Δf_i); blue squares, molecular rupture force of ligand/receptor pairs (F_R) from Li et al.(*6*) If external force exceeds F_R threshold (line), the external force is sufficient to instantaneously rupture ligand-receptor pairs at that effective loading rate. Vertical orange error bars and horizontal black error bars represent standard deviation of F_R (Δf_i) and effective loading rate, respectively. See Materials and Methods for more detail.

Figure 4.8 Schematic of force transmission by actin cytoskeleton against a ligand-presenting surface or probe. Force measurement via a cantilevered spherical probe, with region of interest expanded. Focal complexes and adhesions (dark and purple dots) are created between the plasma membrane and substrata. When finite compressive force is exerted on cells by spherical probes functionalized with FN, this triggers the formation of focal complexes/adhesions and intracellularly generated force. This force generated by cells (green, solid arrow) and by actin polymerization (gray, dotted arrows) are detected via cantilevered probe deflection. Cytoskeletal force may transmit in a form of membrane attachment/detachment force or could directly transmit through physical linkage of focal complexes and the associated actin cytoskeleton as represented in blue letters and arrows. Gray monomers represent actin monomers that constitute actin fibers. Red-yellow complexes are integrin dimers, and blue and light blue objects are adaptor proteins in focal complexes/adhesions; green objects between actin fibers are myosin II

that contract actin fibers.

Figure 5.1 Time-course images of HL-60 cells on substrata coated with P-selectin. Inset schematic in (A) shows how HL-60 cells roll on P-selectin conjugated substrata with respect to shear force exerted by the blood or media. Untreated HL-60 cells exhibit the rolling behavior selectively on the P-selectin coated region (A) and (B), whereas the cells treated with cytochalasin D (1, 20, and 40 μM) do not roll, but instead form static binding on the P-selectin coated region (C) and (D). Note that cytochalasin D excludes the involvement of actin cytoskeleton in various cellular interactions including cell rolling. Scale bar = 50 μm.

Figure 5.2 Fluorescence microscopy images of F-actin in HL-60. (A) F-actin of HL-60 cells that were not activated by P-selectin in suspension was stained with Alexa-phalloidin, with the image focal plane adjusted to approximately the midpoint of cell height. It is well established that actin is concentrated near the perimeter of the plasma membrane for suspended cells. For (B) and (C), the image focal plane was fixed at the interface between HL-60 cells and P-selectin-immobilized slides to visualize the area of contact under two conditions: before (B) and after (C) the addition of cytochalasin D. When HL-60 cells were activated by P-selectin (B), actin became non-uniformly distributed. After the addition of cytochalasin D, which disrupts actin cytoskeleton (C), the distribution of actin was further altered and formed aggregates. Scale bar = 10 μm.

Figure 5.3 Scanning electron micrographs of HL-60 cells. HL-60 cells fixed (*A*) before and (*B*) after the addition of cytochalasin D. Note that there is no gross change in cell morphology or induction of uropoidal substructures upon addition of the inhibitor, and that microvilli substructures are maintained. Scale bar = 5 μm. Arrows in (*A*) and (*B*) indicate microvilli.

Figure 5.4 Schematic of AFM-enabled measurement of cell-generated force dynamics. (A) P-selectin is covalently conjugated to a cantilevered spherical probe (see Materials and Methods and Fig. 4 for density of conjugated P-selectin). HL-60 cells adhere to the glass substratum via specific P-selectin/PSGL-1 binding, where physisorbed P-selectin was used as a "glue" for nonadherent HL-60 cells. Cell dynamics including intracellular force is transmitted via physical connections between PSGL-1 and the cytoskeleton, and is detected as deflection of the cantilevered probe. Mechanical contact is controlled via feedback between a piezoactuator and a photodiode detector of cantilever deflection,

with feedback loop turned off as soon as the probe makes contact with the cell surface. (B) Schematic of real-time measurement of force through cantilever deflection signals converted to force. ΔF_i is defined as force amplitude between sequential force minima ($\Delta F_i > 0$, cell pulling; $\Delta F_i < 0$, cell pushing); τ, time period of force exertion. See Materials and Methods. (C) Optical microscopy image of a P-selectin-functionalized cantilever and HL-60 cells adhered onto the P-selectin-conjugated substratum. Optical microscope-mediated AFM enables the localization of spherical probes on cell surfaces. Scale bar = 20 μm.

Figure 5.5 Cell-generated force measurement with P-selectin-conjugated spherical probes. As in Fig. 2, cantilevered P-selectin-conjugated spherical probes were placed on HL-60 surfaces and bound with PSGL-1 on HL-60 cells. (A) Force generated by the cytoskeletal actin, physically linked directly or indirectly to PSGL-1, deflects the cantilevered probes by magnitudes proportional to force. Solid blue, shaded red, and solid green curves represent cell responses before, after the addition of cytochalasin D, and with BSA-conjugated probes in basal media, respectively. As noted in Materials and Methods, force curves in (A) were shown, corrected for intrinsic drift (average 9 pN/sec, n = 30) caused by cantilever thermal fluctuation was deducted from original force curves. (B) The contractile force generated by cells and measured by cantilevered probes was 2.22 ± 1.53 nN. (C) With BSA probes on normal cells or with P-selectin probes after addition of cytochalasin D, force maxima were reduced to 0.54 ± 0.38 nN and 0.41 ± 0.41 nN, respectively. See Materials and Methods.

Figure 5.6 P-selectin distribution and comparison of cell-generated vs. critical rupture forces on single P-selectin/PSGL-1 complexes under shear flow. (A) Topography image and (B) recognition image of the same area as (A) are representative areas of substrata to which P-selectin is covalently conjugated (See Materials and Methods), including glass slides and spherical probe surfaces. Dark spots in (B) representing specific binding events, demonstrate the distribution of P-selectin molecules on substrata. A circled dark spot is one example of specific interaction. Size of dark spots = 32 ± 4 nm (n >15, where n is the number of AFM images). Scale bar = 250 nm. (C) Range of rupture force vs. loading rates in P-selectin/PSGL-1 complexes. Blue circles represent molecular unbinding force of P-selectin/PSGL-1 complexes(*2*); orange squares, cytoskeletal force as measured by our CFS. If external force exceeds rupture force F_R of molecular pairs (blue circles), external force is larger than resisting force of ligand-receptor complexes, and ligand-receptor pairs are ruptured; if external force is below F_R, it is unlikely that

this force can rupture ligand-receptor pairs. Because calculated unbinding force generated by blood flow (Methods section) is below F_R, blood flow alone cannot induce HL-60 cell rolling. Cytoskeletal force (orange squares) should be added to the force generated by blood flow for cells to roll. F_R = rupture force from molecular force spectroscopy(*2*); F_C = cell generated tensile force. See Materials and Methods for more detail.

Figure 5.7 Schematic of force transmission by actin cytoskeleton. P-selectin is functionalized on spherical probes (light gray); dark gray fibers, actin cytoskeleton; red/yellow objects, PSGL-1 on cell membranes; purple and green objects, cytoplasmic molecules involved in connection between actin cytoskeleton and PSGL-1. (A) and (B) describe that actin cytoskeleton is linked directly or via cytoplasmic molecules to PSGL-1. Two mechanisms underlying a role of actin cytoskeleton in detachment and rolling of HL-60 from P-selectin-conjugated substrata are shown in (C) and (D). (C) Conformational change in PSGL-1 3D structure or microenvironment due to internal force exerted by actin cytoskeleton triggers detachment/attachment of PSGL-1 from substrata. (D) Force transmitted through actin cytoskeleton acts as membrane detachment/attachment force. Plasma membranes of HL-60 detaching from P-selectin-functionalized probes trigger rupture of P-selectin/PSGL-1 pairs; Plasma membranes attaching to P-selectin-functionalized probes triggers binding of P-selectin with PSGL-1. A blue arrow represents the direction of plasma membrane detachment/attachment force created by and transmitted through actin cytoskeleton. (C) and (D) suggest explanations of measurable force exerted by cytoskeleton and of effective detachment of HL-60 rolling on P-selectin-conjugated substrata or endothelial cells. Microvilli omitted for clarity.

Figure 6.1 Overall structure of this thesis. (A) In chapter 2, endothelial cell membrane receptors were mechanically visualized through AFM-based functionalized force imaging. (B) In chapter 3, mechanical interaction between endothelial cells and pericytes that envelop capillary blood vessels was studied through AFM-based indentation and with pharmacological inhibitors. (C) In chapter 4, mechanical interaction between cells and underlying substrata, mediated by focal complexes, was studied through AFM-based real time force spectroscopy and with pharmacological reagents: in the schematic above, two rectangles (C) represent the interaction between pericytes and the basement membrane and interaction between endothelial cells and the basement membrane. (D) In chapter 5, mechanical interaction between endothelial cells

and leukemia cells (HL-60 cells) in cell rolling was studied through AFM-based real time force spectroscopy and with pharmacological inhibitors. This thesis focuses on mechanical interactions in capillary blood vessels: relations among endothelial cells, pericytes, leukemia cells, and underlying substrata of cells.

Figure 6.2 P-selectin conjugation on glass substrata without and with a specific linker. (A) P-selectin is conjugated to a glass substratum via physisorption. Binding sites are spread over the substratum, and P-selectin molecules are aggregated. (B) P-selectin was conjugated with a linker that has a maleimide group at one end. Dark spots (as represented with a white circle), which represent specific P-selectin-PSGL-1 interactions and therefore P-selectin molecules, are distributed with a regular spacing. P-selectin molecules do not aggregate. Scale bars = 300 nm.

Figure 6.3 The actin cytoskeleton and microtubule of pericytes stained with rhodamine-phalloidin and alexa 488-secondary antibody 1 hour after incubation with blebbistatin (25 μM) and nocodazole (1 μM). (A), (D), and (G) represent the actin cytoskeleton stained in red; (B), (E), and (H), microtubule in green; (C), (F), and (I), actin and microtubule images overlapped. (A – C) represent control: pericytes with no pharmacological inhibitors; (D – F) after 1 hour incubation with blebbistatin; (G – I), actin and microtubule overlapped with nocodazole. Blue objects are nuclei stained with DAPI. Scale bars = 20 μm.

Figure A.1 Adhesion and morphology of primary rat hepatocytes on polyelectrolyte multi-layers (PEMs). (A) Schematic depicting coating of tissue culture polystyrene (TCPS) with PEMs comprising interpenetrating poly(acrylic acid), PAA, and poly(allyamine hydrochloride) PAH. (B) Quantification of hepatocyte adhesion on rigid TCPS and PAA/PAH PEMs of varying compliance (assembly pH 6.5, 4.0 and 2.0). All data normalized to hepatocyte adhesion on collagen-coated TCPS. Indentation elastic modulus E for each substratum (measure of stiffness) also shown. Error bars represent SEM (n = 6-8). (C) Phase contrast micrographs showing hepatocyte morphology ~24 hours after seeding onto substrates of varying compliance. Scalebars =100 μm. Error bars represent SEM.

Figure A.2. PEM surface characterization. (*A*) Atomic force microscopy (deflection) image of PEM 2.0 surface hydrated in 150 mM NaCl phosphate buffered saline, pH 7.2. Scalebar = 1 μm. (*B*) Thickness of PEM with/without adsorption of collagen (+decorin)

was measured from corresponding (height) image near a scratched region of the hydrated PEM surface. Scale bar = 10 μm. (*C*) Thickness of PEM substrata is unaltered by protein adsorption (100 μg/mL collagen), indicating that collagen is well-integrated at the PEM surfaces. (*D*) Effective elastic moduli *E* of PEM substrata differ significantly as a function of assembly pH (2.0 or 6.5), but not as a function of subsequent adsorption of collagen (+ decorin). *E* measured via AFM indentation of substrata hydrated in 150 mM NaCl phosphate buffered saline, pH 7.2. Error bars represent standard deviation from mean.

Figure A.3 Confirmation of antibody specificity and access to collagen and decorin. Collagen (100 μg/mL) ± decorin (25 μg/mL) was added to PEM 2.0 and PEM 6.5, and incubated for one hour at 37°C. Primary anti-collagen (for samples +collagen only) or anti-decorin (for samples +decorin) followed by FITC-conjugated secondary antibody (50 μg/mL) were added to each PEM to quantify the specificity and accessibility of antibody to collagen and decorin. With primary and secondary antibody, the fluorescence intensity of PEM 2.0 + collagen, PEM 2.0 + collagen + decorin, PEM 6.5 + collagen, and PEM 6.5 + collagen + decorin was 60.00 ± 13.70, 45.47 ± 16.51, 55.55 ± 22.04, and 45.50 ± 16.22 (arbitrary unit), respectively. These results were compared with control where primary and secondary antibodies were added to unmodified PEMs (-collagen and –decorin). Insets demonstrate the fluorescence signal specificity on PEM 2.0 and on PEM 6.5 (black bars), versus the fully synthetic PEM controls (gray solid line). Error bars represent SEM.

Figure A.4 Adhesion, morphology and phenotypic functions of primary rat hepatocytes on polyelectrolyte multi-layers (PEMs) modified with extracellular matrix proteins. (A) Quantification of hepatocyte adhesion on substrates modified with either type I collagen (100 μg/mL) or collagen mixed with the proteoglycan decorin (25 μg/mL). All data are normalized to hepatocyte adhesion on collagen-coated TCPS. Error bars are SEM (n = 6-8). Pairwise differences among collagen-modified substrates of varying compliance were not statistically significant (n.s.). # $p < 0.01$ vs. 'TCPS+Coll+Dec', ** $p < 0.01$, *** $p < 0.001$, for One-way ANOVA with Tukey's post-hoc test. (B) Quantification of hepatocyte functions on protein-modified substrates: cumulative albumin secretion over two weeks. Error bars are SEM (n=3). Pairwise differences among unmodified surfaces were not statistically significant (n.s.), among collagen-modified surfaces $p < 0.001$, and among collagen+decorin-modified surfaces $p < 0.001$. ** $p < 0.01$, *** $p < 0.001$ for One-way ANOVA with Tukey's post-hoc test.

(C) Hepatocyte morphology on collagen-coated substrata of varying compliance, 2 days post-seeding. Hepatocyte morphology on substrata modified with collagen + decorin was similar. Scalebars = 100 μm. Error bars represent SEM.

Figure A.5 Quantification of hepatocyte DNA on polyelectrolyte multi-layers (PEMs). PEMs of two compliances (stiff PEM 6.5 and compliant PEM 2.0) were used, unmodified or coated with protein (collagen at 100 μg/mL, decorin at 25 μg/mL) followed by seeding of primary rat hepatocytes. Cells were detached from substrates via trypsinization and DNA was quantified using PicoGreen (see Methods for details). Error bars represent SEM (n = 3). 'n.s.' indicates no statistical significance, *** $p < 0.001$ for one-way ANOVA with Tukey's post-hoc test.

Figure A.6 Comparison of hepatocyte morphology and phenotypic functions on tissue culture polystyrene (TCPS) and compliant poly-electrolyte multi-layers (PEM 2.0) modified with type I collagen. (A) Rate of albumin secretion (marker of liver-specific protein synthesis) in hepatocytes on collagen-modified substrates over two weeks. (B) Rate of urea synthesis in hepatocytes on collagen-modified substrates over two weeks. (C) Activity of cytochrome P450 1A (CYP1A, marker of detoxification function) as measured via ethoxy-resorufin O-dealkylation (EROD) in hepatocytes, 4 and 8 days after seeding onto collagen-modified substrates. Error bars represent SEM (n=3). ** $p < 0.05$ vs. 'PEM 2.0 + Collagen (Day 8)' for One-way ANOVA with Tukey's post-hoc test. (D) Morphology of hepatocytes 1 and 13 days after seeding onto collagen-modified substrates. Scalebars = 100 μm. Error bars represent SEM.

Figure B. 1 (A) Fluorescence intensity, normalized by intensity at Day 0 for each sample, and (B) growth of the side length of non-degradable (control, rectangles of PEGDA 30 wt %) and degradable (triangles, PEG-*b*-PLA 30 wt %, 20 wt %, and 10 wt %) hydrogel particles. (C) Elastic modulus E, normalized by E at Day 0 for each sample, for non- (control, rectangles, PEGDA 30 wt %) and degradable hydrogels (triangles, PEG-*b*-PLA 20 wt %) using AFM-enabled nanoindentation. PEG-b-PLA represents for poly(lactic acid)-poly(ethylene glycol)-poly(lactic acid)-poly(ethylene glycol); PEGDA, poly(ethylene glycol) diacrylate.

Figure C. 1 Schematic of interaction between dextran-based biological glue and an amine-functionalized AFM cantilevered probe. Aldehyde groups in the glue binds to amine groups on the spherical AFM probe.

Figure C.2 Unbinding force between dextran-based glues and amine-functionalized probes. (A) shows unbinding forces of four different samples categorized by the density of aldehyde groups. Unbinding force of sample 1 was 0.842 ± 0.231 nN; sample 2, 0.349 ± 0.173 nN; sample 3, 0.252 ± 0.193 nN; and sample 4, 0.225 ± 0.063 nN. Unbinding forces of four samples are statistically different ($p < 0.05$). (B – E) represent frequency vs. unbinding force graphs associated with sample 1 – 4 whose unbinding forces were measured with amine-functionalized probes. Based on the frequency of unbinding forces, Gaussian curves was drawn , and average & standard deviation are calculated as shown in (A).

Figure D.1 Experiments to determine the unbinding force spectrum of biotin-streptavidin have not reached a consensus. Reported data on the unbinding force of biotin-streptavidin is shown as measured by AFM MFS (*diamonds* in *green(2-4)*, *orange(9)* and *yellow(10)*), electric fields (*blue triangles(14)*), magnetic fields (*purple squares(15)*, points overlap), and BFP (*red circles(7)*). Error bars indicating the standard deviation among experimental measurements are shown for all data points, but in some cases are smaller than the symbols. The shaded rectangles highlight measurements at similar loading rates where measured unbinding forces differ by a factor of two and measurements of similar unbinding forces where the loading rate differed by two orders of magnitude.

Figure D.2 (A) Steered Molecular Dynamics simulations were performed on the non-physiological biotin-streptavidin monomer in 1996 by Grubmüller et al. (40). As a starting point for our investigation of the tetramer, we replicated these early results on the monomer. Our results (solid black) agree reasonably well with those of Grubmüller et al. (open, adapted from (40)). Since the spring constant k is the same in all simulations shown, this is equivalent to unbinding force F_R as a function of loading rate F′ on a logarithmic scale. Rupture force at $v = 150$ m/s analyzed via tetramer method, as rupture occurred in less time (4 ps) than the smoothing width time of Ref. (40). (B) An example force-reaction coordinate response during simulated unbinding under conditions $k = 2.8$ N/m, $v = 0.8$ m/s. The unbinding force F_R in this particular trajectory is indicated by the arrow.

Figure D.3 Steered molecular dynamics simulations were performed on nine different biotin-streptavidin complex configurations (some symbols overlap), with three sets of

simulated experiments, differing in loading rate F' (*open*, *solid*, *shaded*). Within each set of experiments the only difference among unbinding trajectories was the starting configuration of the atoms within the complex. Between each set of simulated experiments, the only difference is the velocity v, and therefore the loading rate $F' = kv$ (*open*, v = 0.4 m/s; *solid*, v = 0.8 m/s; and *shaded*, v = 4 m/s). The force transducer stiffness k was 2.8 N/m in all simulations. The large range in observed unbinding force (20%), based only on the initial configuration of the molecular complex, suggests a structural reason for the experimentally observed variation in unbinding force.

Figure D.4 Testing the assumption that loading rate is the controlling variable for unbinding force, we systematically varied force transducer stiffness k (*solid*, 0.83 N/m; *dark shaded*, 1.66 N/m; *light shaded*, 4.15 N/m; *open*, 8.3 N/m) and velocity v to produce three different loading rates (F' = 4.15 N/s, 8.3 N/s, and 16.6 N/s) in SMD simulations of biotin-streptavidin rupture. At the same loading rate, a stiffer force transducer correlated with a higher unbinding force (*open points* are the stiffest force transducers, shading to *black*, which are the most compliant).

Figure D.5 Before performing AFM MFS experiments, the streptavidin-functionalized mica surface was imaged with biotin-functionalized cantilevers in TopMAC mode, allowing for precise placement of the cantilever tip before beginning forced unbinding experiments. The recognition image above (scale bar = 300 nm) demonstrates many streptavidin molecules, which are recognizable by their characteristic dark spots. The cantilever oscillator truncation is the feedback signal voltage and is scaled as 0 V corresponding to large truncation (adhesion). Since these dark spots represent strong binding events between the biotin-functionalized probe and the streptavidin-functionalized mica, positioning the tip near a dark spot significantly increased the probability that each approach-retract cycle would include a biotin-streptavidin binding event.

Figure D.6 (*A*) Experimental measurements of biotin-streptavidin unbinding force F_R were performed via atomic-force microscope-enabled molecular force spectroscopy, utilizing cantilevers of two different spring constants. For each set of loading conditions (effective force transducer stiffness k and retraction rate v) at least 50 force-displacement (F-Δ) responses for single rupture events were recorded, with F_R calculated as indicated. (*Inset*) A single rupture event of F_R = 46 pN, under effective k = 4.12 mN/m and v = 0.073 μm/s. A Gaussian distribution was fit to the histogram of

unbinding forces for each set of conditions (here, k_c = 35 mN/m and v = 0.073 μm/s), and the distribution maximum was reported as F_R. Arrows indicate the FWHM. (*B*) Unbinding force F_R as a function of the logarithm of the loading rate F', as measured by AFM using two different cantilevers: k_c = 35 mN/m (*solid circles*) and k_c = 58mN/m (*open circles*); error bars represent one standard deviation in F_R and effective F', and may appear smaller than symbols. In all cases, the stiffer cantilevers measured higher unbinding forces than the more compliant cantilever, indicating that the dependence of measured F_R on the stiffness of the force transducer k is not limited to the extreme loading rates achieved in simulation.

Figure D.7 The stiffness of the force transducer not only limits the exploration of the ligand in the energy landscape, but also changes the energy landscape the ligand traverses. Here, the effects of stiffness on the biotin-streptavidin energy landscape $E^{**}(F, x)$ (adapted from (*6-8*)) are shown, both before pulling begins (F = 0, *left column*, *gray solid line*) and at an applied load of 100 pN (*right column*, *black solid line*). Compliant cantilevers of k < 1 pN/nm are typical of BFP and optical trap experiments (*top row*). For such small k, the perturbed energy landscape ($E^{**}(F, x)$, *solid*) remains close to the equilibrium energy landscape ($E_0(x)$, *dashed*) in the absence of applied force. Stiff cantilevers of k > 1000 pN/nm are typical of SMD simulations (*bottom row*). Even in the absence of significant applied force of the ligand, the perturbed energy landscape ($E^{**}(F, x)$, *solid*) is far from the equilibrium landscape ($E_0(x)$, *dashed*). AFM cantilevers of $k \approx 10 - 100$ pN/nm are intermediate to these extremes (*middle row*). Since application of a nonzero force inherently implies a nonequilibrium state of the bound complex, no equilibrium landscape is depicted in the right column (F = 100 pN).

Figure D.8 After correcting biotin-streptavidin unbinding forces measured via SMD simulations according to Eq. (D.3), the corrected unbinding force F_C for all for all values of k agree within estimated error ranges (error estimated as ±10%, based on 20% FWHM of force distribution in both simulations and experiments). Uncorrected unbinding forces F_R are shown in Fig. D.3.

Figure D.9 The biotin-streptavidin complex is a tetrameric protein (ribbons) with four biotin molecules (spheres) bound. One subunit (monomer) is indicated in red. The binding pocket for each biotin consists of residues from two of the protein subunits. The blue sphere represents one of the oxygen atoms of the biotin, which is the atom believed

to be linked to the force transducer in forced unbinding experiments.

Figure E. 1 AFM contact mode image of neurons. (A) is an optical image that shows two neurons at the center of a glial cell. (B) two neurons and a glial cells underneath them are imaged in contact mode. (B) shows the same area as (A). Scale bar = 20 μm.

List of Tables

Chapter 1. Introduction

1.1 MOTIVATION

Mechanical properties of materials such as elastic moduli and failure strength are important for design of engineering devices, due to close coupling between material microstructure and mechanical performance under load. Beyond synthetic materials and structures, biological materials including organs, tissues, and cells are all exposed to mechanical cues and stimuli: tissue to tissue, cell to cell, and tissue to cell interactions are examples of such mechanically defined interactions. To maintain structure and function throughout the human body, static, dynamic, and fluid mechanical phenomena continuously occur. It is known that the body maintains homeostasis with the understanding of mechanical properties of, and chemomechanical connections between biological materials at levels of organs, tissues, and cells. However, it is true that mechanical properties and interactions of biological materials have not been as widely studied as biochemical studies in the body. More recently, biologists and biological engineers have become interested in mechanical studies of biological systems, including the structural roles of mechanical elements in cells; the effects of mechanical stimuli on cell-cell contact and interaction; and cellular responses to mechanical stimuli coming from extracellular environment (*2*). Thus, research on mechanical force generation of cells, cellular recognition of mechanical stimuli, and cell-cell mechanical interactions are being published recently with increasing regularity. In particular, atomic force microscopy (AFM) has been recognized as one of the most nondestructive, sensitive mechanical testing and recognition platforms for single molecules and cellular biomechanics. However, the focus of biophysical research using AFM has been limited

to the measurement of molecular unbinding forces or cellular force generated through multimolecular focal contacts, not on biophysical interpretation or functions of such forces. This thesis will discuss the functional roles of cellular force dynamics via advanced approaches through which milli-second level and pN-scale cellular force dynamics are measured in real time in cell systems. In addition, nanometer scale cell surface receptors are visualized, and ligand-receptor binding kinetics and energetics are mapped on cell surfaces through nanomechanical imaging technique, functionalized force imaging (*3*). The cell and molecule types of interest in this thesis are cells that comprise the vascularature and molecules with which these cells interact at the cell-cell, cell-molecule, and cell-tissue interfaces.

1.2 ATOMIC FORCE MICROSCOPY

Since the invention of atomic force microscopy (AFM) (*4*), this tool has enabled the imaging of various materials and surfaces. AFM images are generated through the interaction between cantilevered AFM probes and sample surfaces. As a sample surface that AFM cantilevered probes encounter changes during scanning of the surface, the position of the laser beam reflected by the AFM cantilever surface changes on the photo-detector accordingly (Fig. 1.1). This change in the position of the reflected laser beam with respect to an original location (normally the photodiode center) on the photo-detector is converted to electrical signals, and the electrical signals are processed into pixellated images. Through optics-based microscopes such as optical microscopy and fluorescence microscopy, it is not possible to resolve nanometer-scale molecules due to the wavelength and diffraction of light. However, AFM generates images not via light, but through mechanical interaction between the cantilevered probes and surfaces,

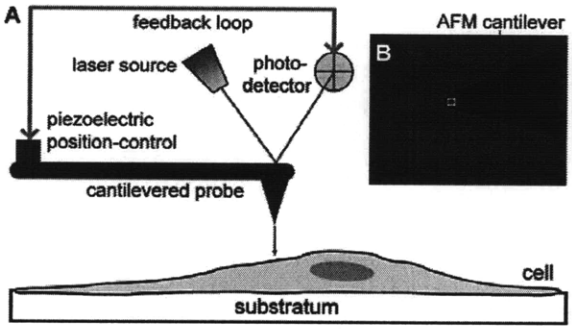

Figure 1.1 Schematic of atomic force microscopy (AFM). (A) Mechanical contact is controlled via feedback loop between a piezo-actuator and a photo-detector that measures the deflection of cantilevered probe(*1*). (B) An example of cell imaging is shown with an AFM cantilever and pericytes that generate wrinkles on underlying silicone rubber substrata. Image courtesy of A. Zeiger.

resulting in the visualization of nanometer-scale surface features. In addition, unlike electron microscopy, sample surfaces are not required to be conductive or to be coated with conductive materials such as gold. This feature of AFM has enabled the imaging of non-conductive materials such as ceramics, polymers, and even living cell surfaces in aqueous media. In addition to surface imaging, AFM has widely been used for other applications such as force spectroscopy and nanoindentation for the measurement of intermolecular forces and elastic moduli, respectively, and the research areas in which AFM is useful are expanding rapidly.

1.2.1 AFM imaging modes

The traditional imaging mode of AFM is called the "contact mode." In contact mode, the force between a cantilevered probe and a sample surface is maintained constant through the feedback loop (Fig. 1.1). The force consists of hydrogen bonding, electrostatic interaction, hydrophobic interaction, and van der Waals interaction between molecules of probes and samples, as well as mechanical force exerted by AFM cantilevers. The interaction between the probe and the sample surface, while the probe

is imaging a sample surface, causes changes in the magnitude of force between the two surfaces. Via the feedback loop, the piezo-actuator that holds the AFM scanner moves to adjust the force, moving the scanner in the vertical or z-direction. This z-directional movement of the piezo-actuator is converted to electrical signals, generating topographical images that provide height information of sample surfaces. The deflection of AFM cantilevers, or deviation from original force set point, caused by the surface/probe interaction generates deflection (or error) images, in which detailed information about sample surfaces is visualized. The contact mode imaging is an original image mode that has been used mainly for solid materials such as ceramics, metals, and polymers.

In addition to physicists and material scientists, other researchers including biologists and biological engineers have begun to use AFM for imaging biological materials such as transmembrane receptors, single or double-stranded DNA chains, and living cell membranes because AFM has enabled imaging samples in liquid. These biological materials are mechanically compliant, compared to metals, ceramics, and polymers. Thus, rigid probes in contact mode imaging, in which probes physically contact samples, tend to modify or damage such samples. Therefore, another imaging mode, tapping mode has been developed. In the tapping mode of AFM, cantilevered probes oscillate at a constant amplitude: the feedback loop works to maintain a constant amplitude set point, whereas force between probes and samples is maintained constant in contact mode. Because cantilevered probes oscillate, this minimizes the time during which rigid probes damage and modify compliant sample features. Topographical and error images are generated in the same manner as in contact mode: the interaction between the oscillating probes and sample features modifies the amplitude of the

oscillating cantilevered probes, and the amplitude deviation from the set point is converted to error signal, as force deviation is to error signal in contact mode. Height (or topography) information is provided by the movement of the piezo-actuator moving in the z-direction to maintain the amplitude set point. Another mechanical image is provided in tapping mode: a phase image. The AFM cantilevered probes are driven by the external electrical or magnetic fields. However, the interaction between samples and oscillating probes creates a phase lag between the oscillation of cantilevered probes and that of initial electrical or magnetic fields. Phase lags are especially influenced by the sample compliance, and therefore, phase images are useful to distinguish samples, based on mechanical properties, for example in block copolymers. Researchers including myself and others in the Van Vliet group, Peter Hinterdorfer at Johannes Kepler University of Linz, and Stuart Lindsay at Arizona State University, use another type of tapping mode called the "recognition imaging(*5*)," or "functionalized force imaging(*3*)." The traditional tapping mode drives the whole body of AFM cantilevers, which may reduce the imaging quality and recognition sensitivity in fluids. Only the tip of cantilevers is, therefore, coated with magnetic materials, and magnetic field drives the oscillation of the free-end of the AFM cantilevers. It is known that this type of tapping mode reduces damping created by friction between the liquid and oscillating cantilevers, optimized for compliant and fragile biological materials. Detailed information about AFM imaging, especially recognition imaging (or functionalized force imaging) and specific examples will be discussed in Chapter 2.

1.2.2 AFM force spectroscopy analysis and nanoindentation

AFM is based on interaction force at surfaces, and the deflection of cantilevers caused

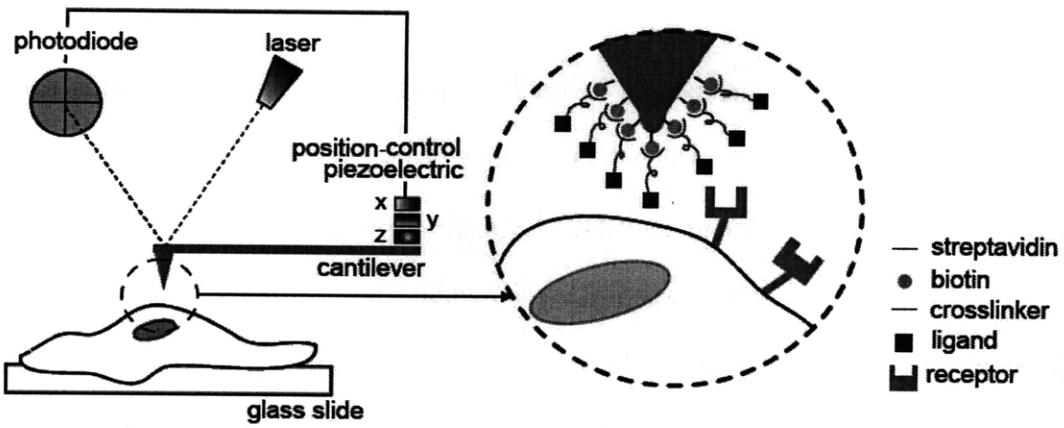

Figure 1.2 Schematic of an AFM cantilever conjugated with ligands via biotin-streptavidin bond for imaging transmembrane receptors for functionalized force imaging, molecular force spectroscopy, and nano-indentation (*1*).

by the interaction between probes and samples is proportional to force. Therefore, beyond obtaining surface images, it is also possible to measure unbinding force between probes and samples. This is called "force spectroscopy"; if it is used for measuring intermolecular forces, it is called "molecular" force spectroscopy. Many biophysicists have used force spectroscopy analysis to measure the unbinding force between complementary molecules: ligand-receptor pairs, complementary DNA strands, antibody-antigen pairs, and biological glues such as avidin-biotin or streptavidin-biotin pairs(*6*). The unbinding force between these molecules is in a range of 20 pN – 1,000 pN(*3, 7-9*), and AFM force spectroscopy with the force resolution of below 10 pN enables the measurement of single molecular force(*1, 3*). One example is the measurement of ligand-receptor unbinding force as shown in Fig. 1.2(*1*). Ligands or antibodies are chemically immobilized on cantilevered probes, and transmembrane receptors on the plasma membrane are recognized via specific ligand (antibody)-receptor (antigen) interaction while AFM cantilevered probes are imaging cell surfaces. In addition, the revelation of locations of receptors through AFM imaging enables the

measurement of unbinding force by the ligand-immobilized probe being placed on the receptor, followed by detachment at a specific loading rate. The pair is ruptured, and associated unbinding force, which is a function of loading rate according to Bell's model(*10*), is measured through molecular force spectroscopy.

Molecular force spectroscopy, in which unbinding force is measured at specific loading rates, can be considered an "active" measurement of force, in which cantilevered probes are "actively" detached from sample surfaces and the feedback loop via the piezo-actuator is turned on. This type of force spectroscopy has been a main tool for biophysics research over decades. Examples of the force spectroscopy analysis are given in Chapter 2.

The author of this thesis is one of the few researchers that have developed and used "passive" force spectroscopy analysis. Whereas the force spectroscopy analysis mentioned above perturbs complementary binding pairs and actively triggers unbinding events to measure unbinding force, biological system-generated forces are "passively" measured by AFM cantilevered probes in this type of force spectroscopy. The piezo-actuator and the associated feedback loop are turned off to fix the position of the "active" piezo-actuator, measuring only system-generated forces that cause AFM cantilever deflection. Examples of this force spectroscopy are discussed in detail in Chapters 4 and 5.

Nanoindentation is an approach that measures the quantitative stiffness and quantitative elastic modulus of a sample. When a sample surface is indented with a cantilevered probe of known geometry, the AFM cantilever is deflected as in force spectroscopy analysis. The deflection vs. displacement of the cantilever and the piezo-actuator is recorded, followed by the conversion of deflection to force. Because elastic

moduli of materials are calculated from the load vs. displacement curve, geometrical details of contacting probes are required: the shape and radius of probes. Many researchers have developed models and methods with which to calculate elastic moduli, one of which is the modified Hertzian model discussed further by Thompson et al(*11, 12*). The author of this thesis has also utilized nanoindentation and the Herzian model to measure the elastic moduli of materials: elastic moduli of polymers in Appendices A and B and those of living cell membranes in Chapter 3.

1.3 INSTRUMENTAL ANALYSIS OF MOLECULAR AND CELLULAR FORCE MEASUREMENT

Many experimental tools have been used to measure pico-Newton (pN) to nano-Newton (nN) scale forces generated by molecule-molecule interaction or intra- and intercellular interaction. In particular, three experimental approaches have been widely used: atomic force microscopy (AFM)(*13-16*), optical tweezers(*17-19*), and magnetic tweezers(*20-22*). In addition to measuring system-generated forces, these approaches enable force exertion to the system, simultaneously measuring the responses of the system against force exertion. The main reason that these instrumental analyses are widely used is that the range of molecular and cellular force (pN to nN) is within the range of forces that can be resolved by these instrumental platforms (*23-25*).

As discussed above, AFM exerts normal force to systems because probes are cantilevered vertically to sample surfaces and the piezo-actuator moves in the z-direction(*1*). Typically, normal forces are applied to cells that are sensitive to mechanical stimuli, and the cytoskeleton (whose three main components are the actin cytoskeleton, microtubules, and intermediate filaments) and mechano-receptors such as

integrin dimers respond and exert mechanical forces against this external normal force(*26-28*). Therefore, the deflection of AFM cantilevered probes resulted from cellular responses transmitted through cytoskeleton and mechano-receptors is recorded and converted to force. In optical tweezers and magnetic tweezers, electrical field and magnetic field are used for exerting traction and rotational forces to dielectric particles and magnetic particles, respectively(*17-22*). The molecules of interests can be conjugated on the particle surface(*22, 24*), and this enables the measurement and tracing of responsive signals caused by interaction with complementary molecules, which may be an isolated DNA strand or transmembrane receptors.

Although many researchers have measured cell-generated forces using optical and magnetic tweezers (traction and rotational forces), past research has focused on what to measure (the range of magnitude of force or the periodicity of the forces)(*23, 24, 29-31*), not on the biophysical meanings and functions of underlying forces. AFM has been widely used for the measurement of unbinding forces between single molecular pairs, but research topics have been also limited to the measuring unbinding force with respect to loading rate(*5, 6, 8, 10, 15, 32, 33*). In this thesis, however, by measuring cellular signals that have not been measured before due to the limit of imaging resolution, the author aims to interpret the biological roles of cell-generated forces and relate the forces to cellular mechanisms that cells employ for communication with external environments including other cells (Chapters 3 and 5) or extracellular matrices (Chapter 4).

1.4 MECHANOTRANSDUCTION

Cells interact with other cells or extracellular environment via chemical and mechanical

signals. Although chemical interactions via growth factors and ions have been studied by many researchers, it has not been long since mechanical interaction between cells and extracellular environment became major research topics. Therefore, a concept, which is called mechanotransduction, that cells sense their physical or mechanical environment and translate mechanical forces and deformations into biochemical signals is a relatively new concept that is now being quantified and detailed(*34, 35*). There are numerous systems throughout the body in which physical and mechanical phenomena are involved, including endothelial cells and blood vessels that are sensitive to blood flow(*36, 37*) and neurons that sense specific mechanical signals(*38*). In addition, mechanotransduction spans from adhesion molecules such as focal adhesions(*34, 35, 39, 40*) and ion channels(*38, 41*) to embryogenesis(*42-44*). However, more research on intracellular dynamics and cell-cell and cell-tissue interaction mediated by the actin cytoskeleton, microtubules, and intermediate filaments is to be conducted, especially in light of combinational roles of three cytoskeletal components. In addition to this, chemical signals to which mechanical signals are converted in the process of cytoskeletal mechanotransduction and signal pathways need more attention for further understanding of mechanotransduction.

1.5 THESIS OBJECTIVES AND OUTLINE

The main goal of this thesis is to study the interaction between chemically or mechanically characterized materials and cells. In particular, the mechanical responses of cells are recognized via various AFM imaging techniques with maximum spatial resolution on the sub-nanometer scale, and force spectroscopy analysis with resolution on the pN to nN scales. The recognition of mechanical responses of cells or mapping of

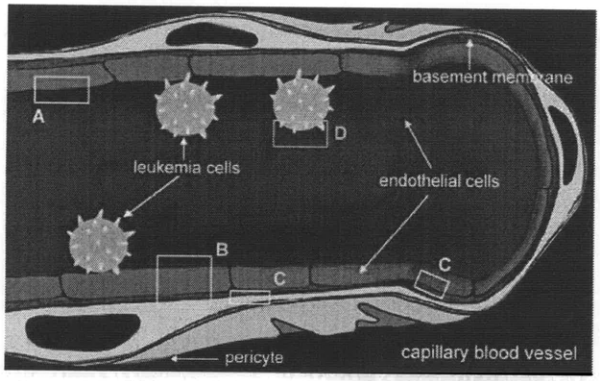

Figure 1.3 Overall structure of this thesis and cellular parts in which mechanotransduction is involved. (A) In chapter 2, endothelial cell membrane receptors were mechanically visualized through AFM-based functionalized force imaging. (B) In chapter 3, mechanical interaction between endothelial cells and pericytes that envelop capillary blood vessels was studied through AFM-based indentation and with pharmacological inhibitors. (C) In chapter 4, mechanical interaction between cells and underlying substrata, mediated by focal complexes, was studied through AFM-based real time force spectroscopy and with pharmacological reagents: in the schematic above, two rectangles (C) represent the interaction between pericytes and the basement membrane and interaction between endothelial cells and the basement membrane. (D) In chapter 5, mechanical interaction between endothelial cells and leukemia cells (HL-60 cells) in cell rolling was studied through AFM-based real time force spectroscopy and with pharmacological inhibitors. This thesis focuses on mechanical interactions in capillary blood vessels: relations among endothelial cells, pericytes, leukemia cells, and underlying substrata of cells.

cell surface receptors is mediated by chemically (conjugation of ligands and antibodies) and mechanically characterized AFM cantilevers (i.e., spring constant and InvOLS). Higher spatial and force resolution of AFM imaging techniques and force spectroscopy analysis enabled the mapping of specific receptors on endothelial cell surfaces and the detection of pN-scale force transmission through ligand-receptor pairs on the plasma membrane with biophysical interpretation of cellular force generation. This thesis consists of four major chapters: (1) receptor recognition on endothelial cell membranes, (2) mechanical interaction between endothelial cells and pericytes that encompass capillary blood vessels, (3) cell-matrix contact via focal adhesions, and (4) leukemia cells rolling on endothelial cell surfaces and P-selectin-conjugated glass substrata (see Fig. 1.3) This thesis also includes appendices that detail the effect of force transducer

stiffness on the measurement of unbinding force, nerve cell imaging to observe the connection between axons and dendrites, and chemomechanical characterization of polyelectrolyte multilayers, biodegradable hydrogels, and biological glues.

The first part of this thesis, Chapter 2 includes the mapping of transmembrane receptors and associated binding kinetic/thermodynamic analyses via AFM functionalized force imaging (single-molecule recognition imaging): Vascular endothelial growth factor receptor 2 (VEGFR2) is visualized with anti-VEGFR2 antibody-conjugated AFM cantilevers. This mapping of cell membrane receptors enable the calculation of binding kinetics and energetics between VEGFR2 and its antibody via real-time functionalized force imaging on temperature-controlled AFM. The existence of specific receptors for an oligopeptide isolated from tissue inhibitor of metalloproteinase-2 (TIMP-2), called loop 6, is verified via functionalized force imaging, and the receptors for loop 6 are identified with blocking experiments.

Chapter 3 discusses the mechanical interaction between endothelial cells and pericytes that line and envelop capillary blood vessels, respectively. Pericytes exert mechanical force, and actin-specific pharmacological inhibitors are introduced to confirm a role of the actin cytoskeleton in exerting mechanical force to underlying substrata. Specifically, it is demonstrated that pericytes exert MPa-range stress to substrata, stresses larger by ten to hundred times than that exerted by other cell types such as endothelial cells and fibroblasts.

Chapter 4 introduces focal adhesion dynamics of cells using AFM force spectroscopy analysis. Pharmacological inhibitors targeting different actin-mediated mechanisms decouple force generation by actin (de)polymerization and actomyosin contraction. It is observed that pN-scale force dynamics exhibit milli-second temporal

periodicity that is transmitted through individual integrin-fibronectin pairs in focal complexes, and this force is sufficient to immediately rupture the pairs. We suggest from this observation that cells use mechanical force to rupture ligand-receptor pairs in focal complexes for migration and attachment, in addition to chemical-enzymatic mechanisms to detach cell surfaces from underlying substrata (*45, 46*).

Chapter 5 discusses the role of actin-mediated force in leukemia cell (HL-60) rolling on endothelial cell surfaces. It has been known that the rolling of HL-60 cells is mediated by molecular interaction between P-selectin on endothelial cell surfaces and P-selectin glycoprotein ligand-1 (PSGL-1) on HL-60 cells (*47*). However, we demonstrate that the cell rolling do not occur when actin polymerization is inhibited by an actin-specific pharmacological inhibitor. In addition, we also show that actin-mediated cellular dynamics disappear with the actomyosin-inhibitor treatment. From these observations, it is suggested that, in addition to drag force exerted by blood flow, cytoskeletal force dynamics are required to induce cell rolling. This observation suggests that mechanical force dynamics play an important role in cell rolling in the blood vessel.

In the appendices, chemical and mechanical properties of materials are characterized using AFM-enabled force spectroscopy and nanoindentation. In Appendix A, these methods are used to show that hepatocyte attachment is influenced by the polyelectrolyte multilayer substrata stiffness (*48*). In separate studies using AFM nanoindentation methods, it is shown that the elastic modulus of biodegradable hydrogel particles decrease over time in Appendix B (*49*). In Appendix C, the density of aldehyde groups on novel wet adhesives is quantified using amine-functionalized spherical probes via AFM force spectroscopy analysis, and it is suggested that the

biological glues bind to intestinal tissues via amine-aldehyde binding. The effect of force transducer stiffness on the measurement of intermolecular unbinding force is studied through biotin-streptavidin pairs in Appendix D. Finally, as demonstration of large scale AFM imaging, the connection between axons and dendrites is visualized using AFM contact mode imaging in Appendix E.

REFERENCES

1. K. J. Van Vliet, Bao, G., Suresh, S., *Acta Materialia* **51**, 5881 (2003).
2. D. E. Ingber, and Jamieson, J. D., *Cells as tensegrity structures: architectural regulation of histodifferentiation by physical forces tranduced over basement membrane*. G. E. D. N. a. M. Differentiation, Ed. (Academic Press, Orlando, 1985), pp. 13-32.
3. S. Lee, Mandic, J., and Van Vliet, K. J., *Proceedings of the National Academy of Sciences of the United States of America* **104**, 9609–9614 (2007).
4. G. Binnig, Quate, C.F., and Gerber, C., *Physical Review Letters* **56**, 930 (1986).
5. C. Stroh, Wang, H., Bash, R., Ashcroft, B., Nelson, J., Gruber, H., Lohr, D., Lindsay, S. M., and Hinterdorfer, P., *Proceedings of the National Academy of Sciences of the United States of America* **101**, 12503 (2004).
6. E. B. Walton, Lee, S., and Van Vliet, K.J., *Biophysical Journal* **94**, 2621–2630 (2008).
7. F. Li, Redick, S.D., Erickson, H.P., and Moy, V.T., *Biophys J* **84**, 1252–1262 (2003).
8. L. Li, Chen, S., Oh, S., Jiang, S., *Analytical Chemistry* **74**, 6017 (2002).
9. K. R. Snapp, Heitzig, C.E., and Kansas, G.S., *Blood* **99**, 4494 (2002).
10. R. Merkel, Nassoy, P., Leung, A., Ritchie, K., and Evans, E., *Nature* **397**, 50 (1997).
11. M. T. Thompson, Berg, M. C., Tobias, I. S., Rubner, M. F., and Van Vliet, K. J., *Biomaterials* **26**, 6836 (2005).
12. M. T. Thompson, Berg, M. C., Tobias, I. S., Lichter, J. A., Rubner, M. F., Van Vliet, K. J., *Biomacromolecules* **7**, 1990 (2006).

13. W. Baumgartner, Hinterdorfer, P., Ness, W., Raab, A., Vestweber, D., Schindler, H., and Drenckhahn, D., *Proceedings of the National Academy of Sciences of the United States of America* **97**, 4005 (2000).

14. W. Baumgartner, Hinterdorfer, P. & Schindler, H. , *Ultramicroscopy* **82**, 85 (2000).

15. P. Hinterdorfer, Gruber, H. J., Kienberger, F., Kada, G.,Riener, C., Borken, C., Schindler, H., *Ultramicroscopy* **23**, 115 (2002).

16. P. e. a. Hinterdorfer, *Ultramicroscopy* **23**, 115 (2002).

17. A. Ashkin, *Physical Review Letters* **24**, 156 (1970).

18. M. P. Macdonald, Spalding, G. C., Dholakia, K., *Nature* **421**, 421 (2003).

19. J. W. Shaevitz, (August 22, 2006).

20. F. J. Alenghat, Fabry, B., Tsai, K., Goldmann, W. H., Ingber, D. E., *Biochem. Biophys. Res. Comm.* **277**, 93 (2000).

21. D. R. Overby, Matthews, B. D., Alsberg, E., and Ingber, D. E., *Acta Biomaterialia* **1**, 295 (2005).

22. N. Wang, and Ingber, D. E., *Biochem. Cell Biol.* **73**, 1 (1995).

23. C. Galbraith, & Sheetz, M.P., *Proc Natl Acad Sci USA* **94**, 9114–9118 (1997).

24. C. G. Galbraith, Yamada, K.M., and Sheetz, M.P., *The Journal of Cell Biology* **159**, 695–705 (2002).

25. D. E. Ingber, *Proc Natl Acad Sci USA* **100**, 1472–1474 (2003).

26. S. Lee, Kotecki, M., Zeiger, A., Van Vliet, K. J., and Herman, I. M., *Submitted* (2009).

27. S. Lee, Nikova, D., Herman, I. M., and Van Vliet, K. J., *Submitted* (2009).

28. Z. Sun, Martinez-Lemus, L. A., Hill, M. A., and Meininger, G. A., *Am J Physiol*

Cell Physiol **295**, 268 (2008).

29. J. T. Finer, Simmons, R.M., Spudich, J.A., *Nature* **368**, 113–119 (1994).

30. G. Giannone, Dubin-Thaler, B.J., Rossier, O., Cai, Y., Chaga, O., Jiang, G., Beaver, W., Dobereiner, H.-G., Freund, Y., Borisy, G., and Sheetz, M.P., *Cell* **128**, 561 (2007).

31. J. E. Molloy, Burns, J.E., Kendrick-Jones, J., Tregear, R.T., White, D.C., *Nature* **378**, 209–212 (1995).

32. P. Hinterdorfer, and Dufrêne, Y.F., *Nature Methods* **3**, 347 (2006).

33. G. Li, Xi, N., and Wang, D.H., *Journal of Cellular Biochemistry* **97**, 1191 (2006).

34. E. E. Jaalouk, and Lammerding, J., *Nature Reviews Molecular Cell Biology* **10**, 63 (2009).

35. A. Katsumi, Orr, A. W., Tzima, E., and Schwartz, M. A., *Journal of Biological Chemistry* **279**, 12001 (2004).

36. G. Dai, Kaazempur-Mofrad, K. R., Natarajan, S., Zhang, Y., Vaughn, S., Blackman, B. R., Kamm, R. D., Garcia-Cardena, G., and Gimbrone, M. A., *Proceedings of the National Academy of Sciences of the United States of America* **101**, 14871–14876 (2004).

37. K. B. Vartanian, Kirkpatricka, S. J., Hansona, S. R., and Hinds, M. T., *Biochemical and Biophysical Research Communications* **371**, 787 (2008).

38. M. Chalfie, *Nature Review Molecular Cell Biology* **10**, 44 (2009).

39. B. Geiger, and Bershadsky, A., *Current Opinion in Cell Biology* **13**, 584–592 (2001).

40. B. Geiger, Spatz, J. P., and Bershadsky, A. D., *Nature Review Molecular Cell Biology* **10**, 21 (2009).

41. S. I. Sukharev, Blount, P., Martinac, B., Blattner, F. R., and Kung, C., *Nature* **368**, 265 (1994).

42. D. W. Thompson, *Growth and Form* (Cambridge University Press, Cambridge, 1917), pp.

43. V. Vogel, and Sheetz, M., *Nature Review Molecular Cell Biology* **7**, 265 (2006).

44. M. A. Wozniak, and Chen, C. S., *Nature Review Molecular Cell Biology* **10**, 34 (2009).

45. S. J. Franco, Rodgers, M. A., Perrin, B. J., Han, J., Bennin, D. A., Critchley, D. R., and Huttenlocher, A., *Nature Cell Biology* **6**, 977 (2004).

46. S. J. Franco, and Huttenlocher, A., *J Cell Sci* **118**, 3829 (2005).

47. D. A. Hammer, and Apte, S.M., *Biophysical Journal* **63**, 35 (1992).

48. A. A. Chen, Khetani, S. R., Lee, S., Bhatia, S. N., Van Vliet, K. J. , *Biomaterials* **30**, 1113 (2008).

49. D. K. Hwang, Oakey, J., Toner, M., Arthur, J. A., Anseth, K. S., Lee, S., Zeiger, A., Van Vliet, K. J., Doyle, P. S., *Journal of American Chemical Society* **Accepted** (2009).

Chapter 2

AFM-based Functionalized Force Imaging

2.1 INTRODUCTION

This chapter describes mapping of cell surface receptors and their binding kinetics using AFM-based functionalized force imaging. As introduced in Chapter 1, membrane-bound or transmembrane molecules that are smaller than a half the wavelength of visible light cannot be visualized easily via optics-based microscopy. Therefore, the main goal of this chapter is to selectively visualize transmembrane receptors of interest, not via light but via mechanical force: individual receptors are mapped on cell surfaces using force-based imaging, termed functionalized force imaging or recognition imaging. In Section 2.2, anti-vascular endothelial growth factor receptor 2 (VEGFR2) antibody is conjugated on the magnetic material-coated AFM cantilevers, and the number and distribution of VEGFR2 are visualized on the surface of human umbilical vein endothelial cells. Calculation of binding kinetics and energetics from such images is verified in Section 2.3 for both the VEGFR2-antibody on intact cells and the biotin-streptavidin model ligand-receptor system. In Section 2.4, the existence of specific receptors for an oligopeptide isolated from tissue inhibitor of metalloproteinase-2 (TIMP-2), called Loop 6, is identified via functionalized force imaging, and receptors for Loop 6 are identified by competitive inhibition imaging with antibody against a potential receptor for Loop 6.

2.2 CHEMOMECHANICAL MAPPING OF LIGAND-RECEPTOR BINDING KINETICS ON CELLS

Parts of the following study were published in 2007 with co-author J Mandic [1].

2.2.1 INTRODUCTION

Molecular receptors at the living cell surface drive critical cell behaviors ranging from adhesion to differentiation, primarily via structural/functional changes induced by binding to extracellular molecules or ligands. Both the receptor location and the kinetics of ligand binding are important to the understanding of receptor-driven functions within cells, but few experimental approaches provide simultaneous access to spatial, temporal, and intermolecular force dynamics in individual, whole cells [2]. Such quantification is crucial to understanding how cells within or among subpopulations may respond differentially to the same ligand (e.g., drug responsivity [3] and differentiation [4]), and how ligand binding can depend on clustering of multiple molecules (e.g., synapse formation [5]) or cytoskeletal association (e.g., focal adhesion formation [6]). Several impressive experimental approaches including flow cytometry, immunocytochemical staining, Förster resonance energy transfer, or FRET, and fluorescence recovery after photobleaching, or FRAP are based on optical signals that require either fluorophore-labeling or genetic modification of cell surface proteins [2]. Binding affinity and kinetics among ligands and cell surface receptors are typically extracted from time course monitoring of total radio- or fluorophore-labeled ligand levels in the presence of unlabeled ligand counterparts, and thus the spatial distribution of active receptors during such competitive ligand binding is not accessed. Measurement of intermolecular interaction forces and associated binding kinetics of several antibody-antigen and

ligand-receptor pairs has been demonstrated via atomic force microscopy (AFM) on purified proteins adhered to flat, rigid surfaces [7-12], and through discretized "blind" mapping of adhesion forces between the ligand-coated AFM probe and the cell surface [13-19]. However, leveraging such picoNewton-scale molecular interaction forces to image individual receptors and infer ligand-binding kinetics on intact, topographically rough cells has remained challenging.

In addition to the fundamental understanding of cell signaling enabled by direct imaging and kinetic analysis, ligand binding affinity as quantified by the equilibrium dissociation constant K_D is pertinent to clinical therapies that regulate signal transduction via direct receptor binding. Vascular endothelial growth factor receptors (VEGFRs), transmembrane receptor tyrosine kinases primarily expressed by VE cells [20], are key targets due to the apparent role of these receptors in mechanosensory functions such as focal adhesion turnover, actin cytoskeletal remodeling, and angiogenesis [21-24]. Intermittent blocking of VEGFR2 in VE cells promotes rapid blood-vessel regression in animal models [4], but new strategies to inhibit/promote this signaling require enhanced understanding of VEGFR2 distribution and binding kinetics with biological or synthetic molecules. Here we develop and apply an approach through which receptor location and binding kinetics to extracellular biomolecules are achieved at the single molecule and single cell levels, respectively. Through this chemomechanical imaging on living and fixed VECs, we find that available VEGFR2s are non-uniformly distributed, in close spatial association with the underlying cortical cytoskeleton, and that equilibrium rate constants can be accessed on intact cells to correlate binding affinity with subcellular location.

2.2.2 RESULTS

2.2.2.1 Determination of receptor location and binding specificity

Direct mechanical imaging of cell surface receptor location can elucidate non-uniform distributions of receptors with respect to other structural features, and provides access to whole-cell binding kinetics. By maintaining constant or intermittent contact with a cantilevered probe while scanning the cell surface, AFM feedback voltages create image contrast via differential height or stiffness (Fig. 2.1A); or via reversible adhesion between molecules tethered to the scanning probe and molecules bound to rigid, flat surfaces [12,25]. By displacing the probe normal to the surface at discrete points and analyzing the force-displacement responses, interaction force spectra can also be measured on rigid surfaces and on chemically fixed or living cells to construct two dimensional grids of pixels indicating either stiff/compliant or strong/weak binding regions (e.g., [26-28]). Although such molecular interactions are far from equilibrium, the spectrum of picoNewton-scale unbinding or rupture forces between probe-bound ligands and adsorbed monolayers of purified receptors has been employed to estimate the equilibrium dissociation rate k_{off} between antigen/antibody and ligand/receptor pairs [29,30], and has been reported to agree reasonably well with surface plasmon resonance measurements of population-averaged rates for rigidly bound, purified proteins [31]. However, pointwise acquisition of such profiles on cell surfaces has thus far proven too spatially coarse (pixels of ~500 nm size [24,28]) or slow (e.g., 45 min to acquire 32 × 32 pixels of 20 nm size [13]) to resolve both the nanoscale location and binding kinetics of individual cell surface receptors [32].

To both visualize and measure the binding kinetics of VEGFR2 receptors on vascular endothelial cells, we employed chemomechanical imaging of chemically fixed

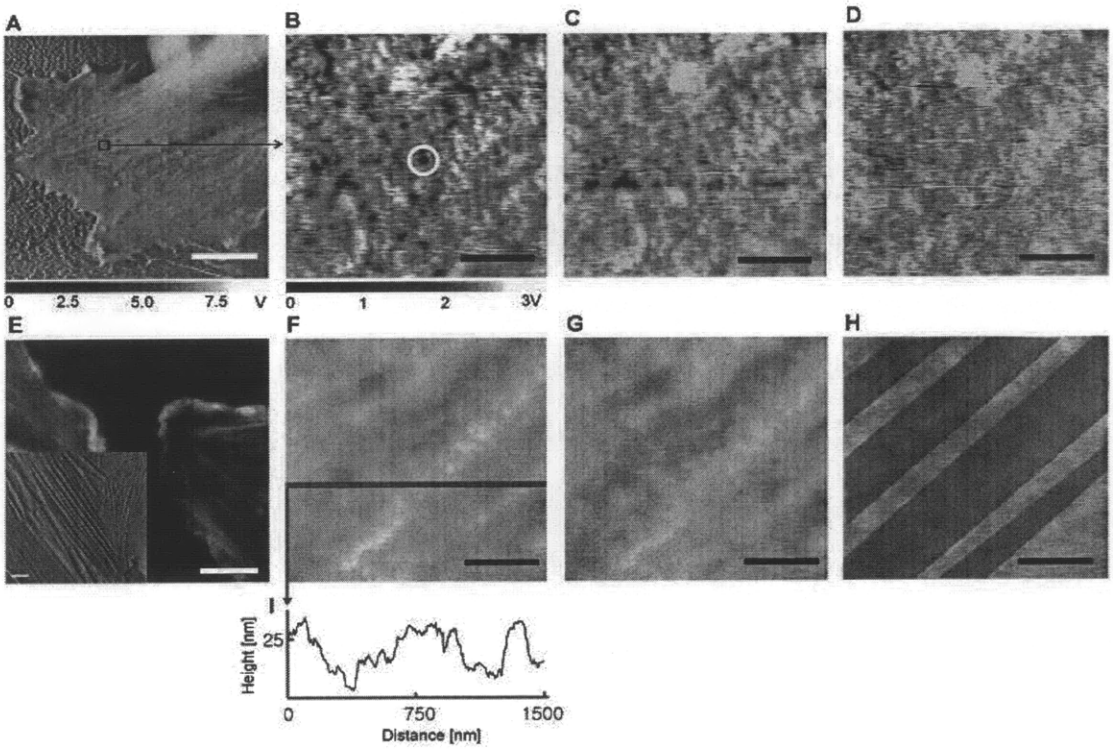

Figure 2.1 Time-lapsed functionalized force imaging. Fixed human umbilical vein endothelial cell (HUVEC) surface imaged with anti-VEGFR2- functionalized probe via magnetic AC mode in HEPES buffer at pH = 7.2 and 27°C. (A) Phase image of cell body and periphery; scan rate = 10 μm/sec. Scalebar = 10 μm. Recognition image over indicated area in A before addition of 5 μg/mL soluble anti-VEGFR2 (B), at times post-blocking of t_{pb} = 12 min (C), and t_{pb} = 60 min (D) indicates reduction in number of recognition events with increasing tpb. White circle in (B) indicates one such recognition event, and output voltage scale applies to (B – D). (F - H) Topography images of (B – D) indicate that there is no degradation of the surface topography over this timescale. Scan rate = 1 μm/sec; scalebars = 500 nm. (E) demonstrates cytoskeletal bundles represented in a fluorescence image of FITC-phalloidin-stained F-actin and an AFM contact mode image (inset); scalebars = 10 μm. Four cytoskeletal bundles are manifest as lighter (high) regions in (F – I); for visual clarity, the position and apparent width of these bundles is shown only in (H), where blue bands are reconstructed from height traces as shown in (I). (I) Indicated line trace of the height image in (F) shows the apparent position and width of three cytoskeletal bundles that deflect the cantilever due to their comparatively higher stiffness; this width agrees reasonably well with that measured in fluorescence optical images such as (E).

and living human umbilical vein endothelial cells (HUVECs) that endogenously express VEGFR2. By scanning the cell surface with a magnetically driven oscillating, cantilevered probe to which monoclonal anti-VEGFR2 antibodies were tethered at a

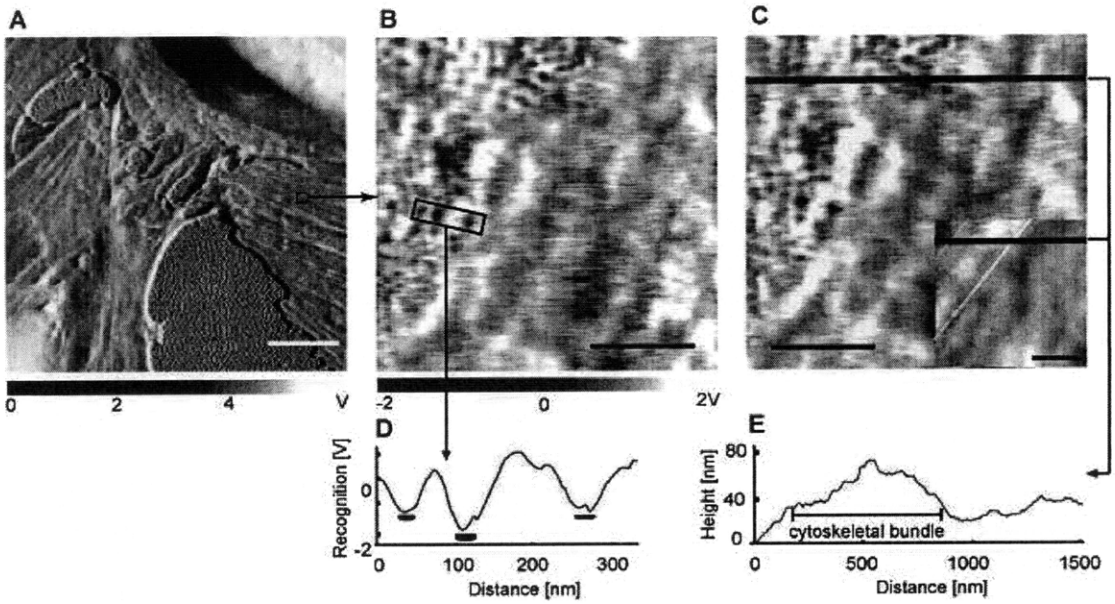

Figure 2.2 Confirmation of anti-VEGFR2 binding specificity on cell surfaces. After imaging fixed HUVECs with anti-VEGFR2-functionalized probe ((A) phase image; (B, C) magnetic AC mode recognition image in indicated region of interest). Thirty minutes after the addition of 5 μg/mL soluble mouse monoclonal anti-human anti-CD31 IgG1 (C), no competitive blocking of recognition events was observed. This indicates these recognition events represent specific binding between probe-bound anti-VEGFR2 and VEGFR2 on the HUVEC surface. The height image corresponding to this region (inset) indicates the position of cytoskeletal bundles beneath the cell membrane; the white lines marking the bundle edges were constructed from height traces of the region, as shown in (E). (D) Output voltage scale for (B) and (C) demonstrates recognition signal compared to background in a line scan over a region including three binding events. Black discs just below the line trace minima indicate the position of strong recognition events. (E) This height trace of the line indicated in (C) enables comparison of the position of the underlying cytoskeletal bundles with respective to recognition events attributed to VEGFR2 locations. (B – E) demonstrate that VEGFR2 is non-uniformly distributed near cytoskeletal bundles beneath the plasma membrane. Scan rate = 10 μm/sec in (A); 1 μm/sec in (B, C). White scale bars = 10 μm; black scale bars = 500 nm.

concentration of approximately one antibody per probe (Materials and Methods, Fig. 2.3), retardation of full-amplitude oscillations indicative of pN-scale unbinding force between the probe and the cell surface creates image contrast [33] in the form of punctate, dark regions of diameters ranging 45.9 ± 8.9 nm (Figs. 2.1A-D, Figs. 2.2B,C); see Materials and Methods regarding image resolution. This molecular recognition imaging has been demonstrated for rigid surface-bound molecular pairs [34], so we

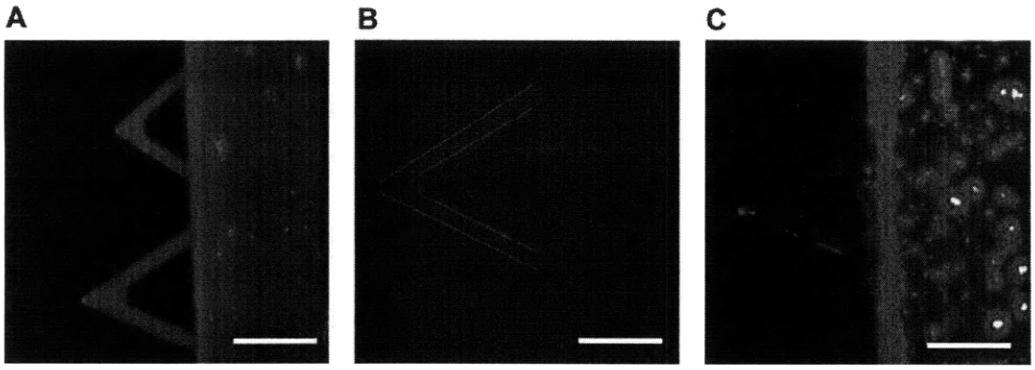

Figure 2.3. Confirmation of probe functionalization. FITC-labeled anti-IgG1 binds to Si_3N_4 probes functionalized with primary antibody, anti-VEGFR2 (A), but does not bind to Si_3N_4 probes functionalized with only the distensible poly(ethylene glycol)-based linker (B). In the absence of this linker, the primary antibody can bind nonspecifically and aggregate on the Si_3N_4 surface, as visualized in (C) via subsequent binding of the FITC-labeled anti-IgG1. Scale bars = 50 μm.

refer to these regions of strong binding as recognition sites which are assumed as putative receptor locations that can be confirmed via demonstration of binding specificity. We demonstrated specificity of this interaction via competitive binding, introduction of the soluble anti-VEGFR2 to the imaging solution; binding of these soluble antibodies to VEGFR2 on the cell surface should block specific interaction forces between the anti-VEGFR2 probe and the cell over time scales comparable to those employed for immunocytochemical staining. Figures 2.1B–D show this competitive inhibition over 60 min post-blocking, as the number of observable binding sites in these images is diminished without concurrent degradation of the cell surface topography (Figs. 2.1F-H). In contrast, the number of recognition sites did not decrease over the same imaging duration upon the addition of 5 μg/mL monoclonal anti-CD31, an antibody specific to these cells as confirmed by flow cytometry and immunocytochemistry (Fig. 2.2); and no recognition sites were observed in repeated,

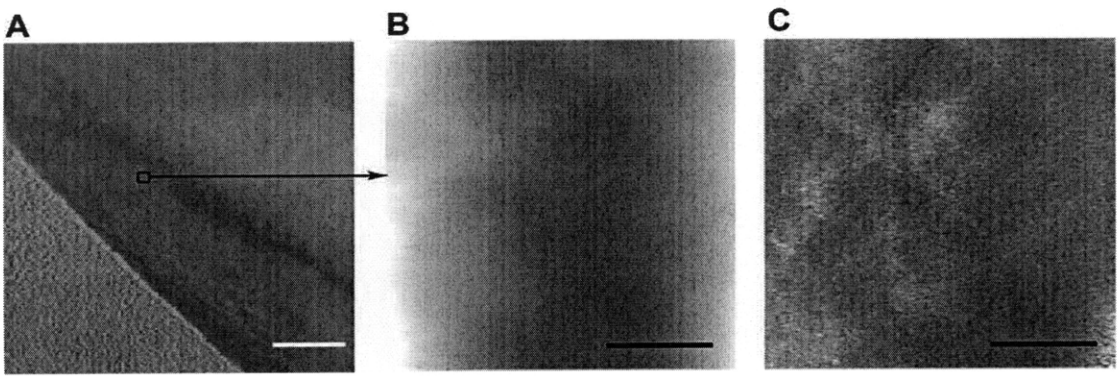

Figure 2.4 Confirmation of anti-VEGFR2 binding specificity on HUVECs. (A) Functionalized force imaging of human 3T3 fibroblast cells (phase image) with anti-VEGFR2-functionalized probe does not indicate binding in either the topography image (B) or recognition image (C) of these cells, which do not to endogenously express VEGFR2 as shown in Fig. 8. Scan rate = 10 μm/sec in A and 1 μm/sec in (B, C). White scalebar = 10 μm; black scalebars = 500 nm.

identical experiments on human NIH 3T3 fibroblasts that do not express VEGFR2, as confirmed by flow cytometry (Figs. 2.4 and 2.5). The specificity of this antibody for VEGFR2 in these cells is further supported by flow cytometry for HUVECs cultured under identical conditions (Fig. 2.5). Note that, in these oscillatory interaction imaging modes, the output voltage signals of Fig. 2.1B-D are related to but not convertible to force or displacement in a straightforward manner.

Analysis of fixed-cell images such as Fig. 2.1B and Fig. 2.2B indicate $1.47 \pm 0.38 \times 10^5$ VEGFR2/cell (n = 60; see Materials and Methods). This determination among individual cells agrees well with HUVEC population-averaged measurements via radiolabeled ligands (1.1×10^5 [35] and 1.5×10^5 VEGFR2/cell [36]). Additionally, this nanoscale imaging indicates the non-uniform receptor distribution over ~2 μm^2 regions and the close cytoskeletal association of these receptors (Fig. 2.1B – I, Fig. 2.2B – E).

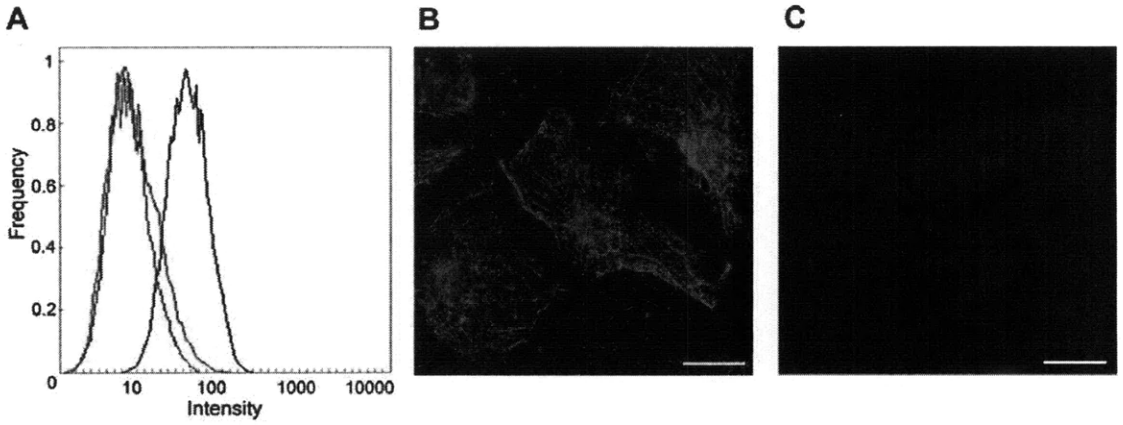

Figure 2.5 Identification of VEGFR 2 on HUVECs and human 3T3 fibroblasts. (A) Flow cytometry confirms significant presentation of VEGFR2 on HUVECs (blue), but not on 3T3 fibroblasts (green), using the same antibodies as in functionalized force imaging. IgG isotype control on HUVECs also demonstrates anti-VEGFR2 specificity (red). (B - C) Immunocytochemistry using the same antibodies as in functionalized force imaging confirms gross spatial distribution of VEGFR2 on HUVECs in B, but the absence of VEGFR2 on 3T3 fibroblasts in (C). Scalebars = 10 μm.

2.2.2.2 Binding kinetics analysis

Imaging via intermolecular forces also gives access to ligand binding affinities on individual cells. To determine the dissociation rate k_{off} between the probe-bound antibody and cell surface receptors, we acquired force-displacement spectra on imaged cell regions such as Fig. 2.1B. This enabled us to efficiently sample unbinding or rupture forces F_R at recognition sites (ostensible receptor locations), before and after blocking with soluble antibody. As shown in Fig. 2.6A, each force-displacement retraction profile represents (on average) a single ligand-receptor unbinding event from which rupture force F_R and unbinding width l (proportional to the characteristic unbinding time τ) are determined [9,37]. Figure 2.6B shows the distribution of these F_R, with maxima at 32.5 ± 2.5 pN and 64.1 ± 5.4 pN; these significantly exceed nonspecific unbinding forces measured at cell surface regions of low recognition image contrast or

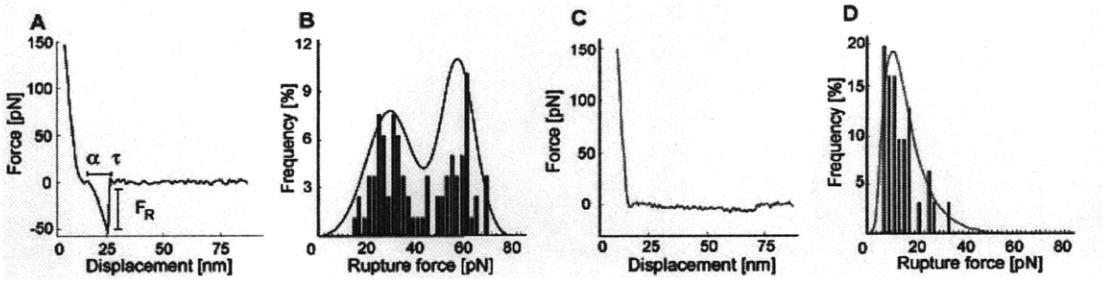

Figure 2.6 Force spectroscopy analysis of binding events on fixed HUVECs. (A - B) Representative specific ligand-receptor unbinding trajectory (force-displacement response) at recognition sites included in the probability density function of >600 rupture forces indicating two maxima of 33 pN and 64 pN. (C - D) Representative nonspecific unbinding trajectories (force-displacement curve) at >400 non-recognition sites on the cell surface indicate a nonspecific rupture force level of ~13 pN. Effective loading rate = 11.7 nN/sec. Bond lifetime τ in (A) is proportional to the binding displacement and is used to calculate binding constants (see Materials and Methods).

after blocking (Fig. 2.6D, 12.5 ± 2.1 pN). Multiple force maxima indicate a non-zero probability of binding two receptors (homodimers) with a single antibody or, more likely, binding of two antibodies on the probe to a pair of closely spaced receptors [29]. From these F_R and τ acquired on cells, the equilibrium dissociation rate k_{off} can be determined directly via Bell's model [37,38]; see Materials and Methods. For anti-VEGFR2 / VEGFR2 on HUVECs, we found that $k_{off} = 1.05 \pm 0.6 \times 10^{-4}$ s^{-1}.

To determine the equilibrium association rate k_{on}, we imaged cell surfaces during competitive inhibition with soluble anti-VEGFR2. The number of observable binding sites in images such as Figs. 2.1B-D decreased with time as soluble antibodies bound to VEGFR2 on the cell surface and blocked probe-receptor binding. We analyzed this temporal increase in bound receptors according to a monovalent binding kinetic model [2] to obtain $k_{on} = 5.83 \pm 1.48 \times 10^4$ s^{-1}M^{-1}, corresponding to an equilibrium dissociation constant $K_D = k_{off} / k_{on}$ of $1.80 \pm 0.87 \times 10^{-9}$ M (n = 6).[1] Here, k_{off} was

[1] The off-rate, on-rate, and dissociation constant determined from a best fit of this competitive binding response result in a difference of only -24%, -55%, and +41% from those calculated above: $k_{off} = 7.98$

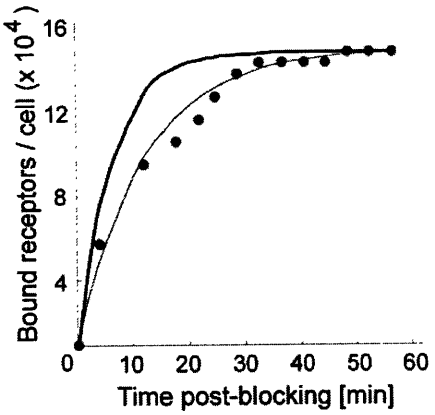

Figure 2.7 Time course of competitive binding to HUVEC surface. Recognition sites from images such as Fig. 1B decrease with time post-blocking via addition of 5 μg/mL soluble anti-VEGFR2 during sustained functionalized force imaging of the cell surface with an antibody-functionalized probe at 27°C. As the number of observable binding sites decreases during blocking, the number of receptors bound by the soluble antibodies correspondingly increases (•). Kinetic constants can be determined by application of a binding kinetic model for which k_{off} is assumed from independent force spectroscopy experiments (—), or by a least-squares best fit to the experimental data (—). See Materials and Methods for detailed calculation of binding kinetic constants.

assumed from force spectroscopy, rather than a best fit to the response in Fig. 2.7; see Materials and Methods for comparison. Deviations from the model at early times post-blocking are attributed in part to the model assumption of uniformly distributed ligand; in practice, diffusion of the ligand upon injection is required. These binding kinetics, measured directly on intact cells, represent the rate at which an ensemble of receptors on an individual cell surface is occupied, as distinct from existing technologies that infer equilibrium constants through cell population-averages or on purified proteins. *** K_D is well within the range of antibody-antigen interactions (K_D = 10^{-4} – 10^{-12} M) measured by various approaches for purified antigens [39,40], and the rates k_{off} and k_{on}

$\times 10^{-5}$ s^{-1}, k_{on} = 2.60×10^4 $M^{-1}s^{-1}$, and K_D = 3.07×10^{-9} M; see Materials and Methods for detailed comparison of these kinetic analyses.

inferred from surface plasmon resonance for anti-VEGFR2/purified humanVEGFR2 [41]; see Materials and Methods.

2.2.2.3 Visualization of receptors on living cell surfaces

Although biological receptor diffusivity and internalization are typically retarded in kinetic and structural analysis through processes such as chemical fixation [42-44], we note that this imaging via reversible intermolecular binding also provides direct access to receptor dynamics on living cell surfaces. Figure 2.8 shows specific, punctate unbinding events between an anti-VEGFR2-functionalized probe and the living HUVEC cell surface: un/binding events are detectable as marked phase lag of cantilevered probe oscillation over the compliant, mechanically heterogeneous surface of the living cell.

In contrast to fixed-cell surface imaging, here the position and number of putative receptors vary over time in the absence of competitive binding. This variation is due ostensibly to lateral diffusion along and recycling through the membrane. The diffusion coefficients D measured by FRAP for other receptors over cell membrane areas of comparable size (0.001 to 0.1 $\mu m^2/sec$ [2]) are comparable to imaging scan rates (here ~0.02 $\mu m^2/sec$ at 2 min/image). This means that a receptor could diffuse across the region of Fig. 2.8B over a period $t \sim \langle x^2 \rangle / 4D$ ranging from 6 sec to 10 min; thus, receptors may not be observed in sequential images of the same region acquired minutes apart. However, in sequential images such as Figs. 2.8B and C, we observed that receptors adjacent to cortical cytoskeletal filaments displaced only 178 ± 49 nm (n = 12) with respect to the moving cytoskeleton. This compartmentalized motion near filaments is consistent with the root mean squared displacement of other membrane

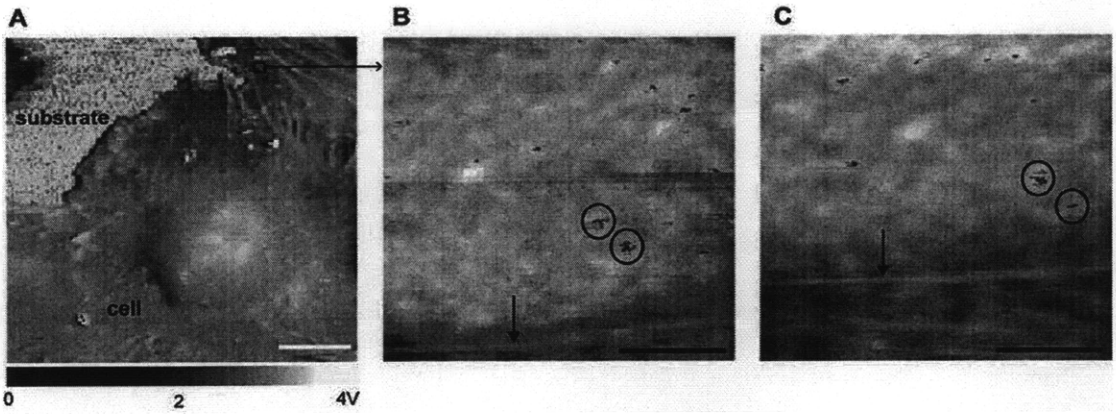

Figure 2.8 Single receptor imaging on living HUVEC surface. (A) Portion of living cell imaged with anti-VEGFR2-functionalized probe in magnetic AC mode at 27°C, phase image. Scan rate = 10 μm/sec; scalebar = 10 μm. Ligand-receptor binding results in punctate image contrast (circled regions indicate a subset of the observed receptors) in phase lag images (B, C) that is competitively inhibited by addition of soluble anti-VEGFR2 antibody (data not shown). Scan rate = 1 μm/sec; scalebars = 500 nm. The time lapse between (B) and (C) is 30 min. Note the mechanical contrast and displacement of the underlying cytoskeletal actin (normal to arrow) over this timescale. These images indicate $1.32 \pm 0.44 \times 10^5$ receptors/cell (n = 6).

proteins (30 - 700 nm) that has been attributed to cortical cytoskeletal confinement and steric hindrance [42,44,45].

2.2.3 DISCUSSION

Through this functionalized force imaging approach, we found that individual VEGFR2 can be imaged on intact, fixed and living cell surfaces with molecular resolution via reversible, intermolecular binding events (Fig. 2.1). We also showed that the specificity of these binding events can be demonstrated via competitive binding of soluble molecules (Figs. 2.1, 2.2, 2.6, and 2.7) and associated control experiments (Figs. 2.3 – 2.5). As the number of receptors per cell compared well with that estimated from cell population-averaged approaches, we infer that the efficiency of this force-based imaging approach is sufficiently high to provide an accurate depiction of receptor location. Further, we found that the equilibrium binding kinetics could be measured on

an individual cell basis via a combination of molecular force spectroscopy of putative receptors (k_{off}) and real-time image acquisition during competitive binding (k_{on}). Moreover, our approach provides the opportunity to correlate binding kinetics with structural features such as cytoskeletal association of the receptor.

From direct analysis of corresponding recognition and height images (e.g., Figs. 2.1 and 2.2), we can consider the distribution of individual VEGFR2 with respect to the center and apparent edge of subsurface cytoskeletal bundles; the staining and dimensions of these bundles are consistent with linear bundles of actin filaments termed stress fibers. The majority of recognition sites were located directly adjacent to these underlying cytoskeletal bundles: 61% were above the cytoskeletal bundles (i.e., "on" 2D projections of the bundle height traces); 34% were located within 72 ± 49 nm from apparent bundle edges and thus within the subsurface bundle width; and <5% were observed at distances >500 nm from bundle edges. The observed VEGFR2 were uniformly distributed along the bundle length and width (bundle diameter-normalized distance of 0.53 ± 0.31 from the bundle center). This finding supports the current hypothesis that VEGFR2 function is intimately related with that of transmembrane integrin complexes that transmit force from the extracellular matrix to the actin cytoskeleton [20,46,47]. These results also lay the groundwork for important and open questions, including whether this imaging approach and/or the binding kinetics are altered in mechanically stiff regions of cell surfaces; this work is ongoing. However, reasonable agreement of VEGFR2/cell with cell population-averaged levels [35,36] suggests that total receptor number is not grossly underestimated.

We note that, although functionalized force imaging can identify the existence and distribution of receptors, full analysis of binding kinetics requires that the diffusion

and recycling of receptors must be suppressed to maintain a constant receptor population, e.g., via light fixation of the membrane proteins. Despite the potential to alter binding kinetics through modification of membrane protein structure, such chemomechanical imaging provides the capacity to compare ligand-binding properties for a given receptor in the presence of drug ant/agonists, or among cells within an inherently mixed population (e.g., tumors or differentiating progenitor cells). Further, chemical fixation is a well accepted approach to enable lower resolution visualization (optics-based imaging) of cell structure and gross spatial distributions of proteins. In fact, our claim of antibody-receptor binding specificity is supported by standard immunocytochemical staining practices: incubation of primary antibodies with fixed cells over the same duration as our competitive binding experiments (~60 min) is considered sufficient to saturate receptors.

The dual access to chemically informed, subcellular structure and to ligand-receptor binding kinetics enabled by this imaging approach allows us to ask new questions about how co-localization of subcellular structures affects receptor function and physiological / pathological cell processes. In the present case, we observed that VEGFR2 is accessible to functionalized force imaging, and that these imaged receptors are spatially associated with the underlying cytoskeleton. However, this is a general and versatile approach for interrogation of other receptors or molecules presented at the cell surface; it is limited chiefly by the capacity to functionalize probe surfaces with active biomolecules including proteins, polysaccharides, and synthetic drugs. We anticipate that the fundamental measurements of individual cell surface molecules and their ligand-binding properties enabled by this approach will enable predictions of key dynamic interactions between extracellular molecules and the intact cell surface,

especially as these relate to ligand-induced clustering and the association of transmembrane receptors with mechanically dynamic structures such as the cytoskeleton.

2.2.4 MATERIALS AND METHODS

2.2.4.1 Cell culture

Human umbilical vein endothelial cells (HUVECs) were cultured in endothelial basal medium-2 (EBM-2, Cambrex Bio Science). 3T3 fibroblast cells (ATCC) were cultured in Dulbecco's Modified Eagle Medium, 10% calf serum, 1% penicillin-streptomycin, 1% glutamine (Invitrogen), on tissue culture treated coverslips (NalgeNunc).

2.2.4.2 Functionalized force imaging

Living and fixed (3% formaldehyde and 0.1% glutaraldehyde, Sigma-Aldrich, followed by rinsing with 0.05 M, pH = 7.4 Tris buffer) HUVECs were imaged in TopMAC mode within a fluid cell (PicoPlus scanning probe microscope (SPM), Agilent/Molecular Imaging) [12], using backside magnetically-coated Si_3N_4 cantilevers functionalized with monoclonal anti-VEGFR2 antibody; see Materials and Methods. Living HUVECs were rinsed well and imaged in HEPES containing Ca^{2+} at 27°C. All images were acquired using a closed loop piezoscanner for which positional stability was better than 0.3 nm/min, as confirmed via elapsed imaging of avidin adsorbed to mica. All measurements are expressed as average ± standard deviation.

The number of binding events per cell was determined by direct image analysis (summing of the number of closed regions at least one order of magnitude darker than background threshold) of a given cell area, obtaining 22 ± 6 sites per 1.5 × 1.5 μm^2

recognition image, or 9.8 sites/μm^2 in fixed HUVECs (n = 11); these regions were considered representative of the cell surface, as supported by immunohistochemistry shown in Figure 2.5B. Surface area per cell was determined by three dimensional analysis of via magnetic AC mode images of 60 images including at least one HUVEC, where for each cell the area was calculated as the sum of an ellipsoid surface area (based on known maximum cell height and long/short axis of the organelle-containing region) and an annulus surface area of the comparably flat cell body perimeter: 10,400 ± 2,700 μm^2 (n = 60). The probability density functional of molecular force spectroscopy indicated a finite probability of encountering either one receptor (33 pN, 58.4%) or two receptors (64 pN, 42.6%). The total number of receptors per cell was then determined as the product of the probability-weighted number of sites per cell surface area and the average cell surface area ($1.47 \pm 0.38 \times 10^5$ VEGFR2/cell).

2.2.4.3 Molecular force spectroscopy

Directly following SPM imaging in MAC mode, molecular force spectroscopy was conducted on 600 locations of strong binding (dark in recognition image) and 400 locations of weak binding (light in recognition image) for each cell area imaged (n=11). Cantilever force constant [nN/nm] and photodiode optical lever sensitivity [nm/V] were determined experimentally in air for each cantilever prior to functionalization [48], and confirmed as unchanged at the conclusion of each experiment. Unbinding or rupture force F_R was determined for each event from the calibrated force-displacement response [37], and non-specific unbinding events were excluded from the calculated probability density functions. Topographic images were recorded subsequently to verify non-destructive interrogation of the surface.

2.2.4.4 Binding kinetics analysis

As shown in Figure 2.7, direct imaging of the number of unbound receptors indicates the velocity of this association as k_{on} = 5.83 ± 1.48 × 10^4 $s^{-1}M^{-1}$, corresponding to an equilibrium dissociation constant $K_D = k_{off} / k_{on}$ of 1.80 ± 0.87 ×10^{-9} M (n = 6). Deviations at early times post-blocking can be attributed in part to the model assumption of uniformly distributed ligand; in practice, diffusion of the ligand upon injection is required. Our results, measured directly on intact cell surfaces, are well within the range of antibody-antigen interactions (10^{-4} to 10^{-12} M) measured by various approaches for purified antigens, including molecular force spectroscopy on rigid surfaces [39,40] and by surface plasmon resonance for purified human VEGFR2 [41]. Detailed calculation of binding constants is as follows:

The lifetime of a bond can be expressed [29,38,40] as:

$$\tau = \tau_0 \exp(-\frac{l \cdot F_R}{k \cdot T}) \qquad (2.1)$$

where τ_0 is the lifetime of unstressed bonds; l is the binding cleft of or the unbinding width on an antibody; F_R is the rupture force between the antibody on the probe and the surface receptor; k is Boltzmann's constant; T is the absolute temperature. The dissociation rate constant is calculated as $k_{off} = \tau_0^{-1}$. Taking the natural logarithm of Eq. (2.1), the resulting slope is equivalent to the unbinding width l and the intercept is directly related to the dissociation rate constant k_{off}. Bond lifetime τ can be calculated from data shown in Figure 2.6A [29,40] because the lengthscale of ligand-receptor binding

curve can be converted to the timescale of the binding for a constant displacement rate of the probe:

$$\ln \tau = \ln \tau_0 - l \cdot \frac{F_R}{k \cdot T} \tag{2.2a}$$

$$\ln \tau = 9.1633 - 0.9309 \cdot \frac{F_R}{k \cdot T} \tag{2.2b}$$

where the intercept is 9.1633, so $k_{off} = \frac{1}{\tau_0} = \frac{1}{e^{9.1633}} = 1.05 \times 10^{-4}\ s^{-1}$, and $l_0 = 0.93$ nm. The observed range of k_{off} (n = 11) was $1.05 \pm 0.6 \times 10^{-4}\ s^{-1}$.

For reversible binding of a ligand to a receptor in the formation of a ligand-receptor complex, the reaction can be expressed as follows [2]:

$$\text{Ligand (L)} + \text{Receptor (R)} \underset{koff}{\overset{kon}{\rightleftharpoons}} \text{Ligand-receptor complex (C)}$$

The system considered in this calculation is one tissue culture-treated polystyrene coverslip onto which 2×10^5 cells were adhered. The rate of change of the complex is:

$$\frac{dC}{dt} = k_{on} \cdot R \cdot L - k_{off} \cdot C \tag{2.3}$$

where L, R, and C represent the concentration of ligand, receptor, and ligand-receptor complex, respectively. Because excess of ligand molecules relative to the estimated number of receptors was added, L can be considered constant ($L = L_0$ = constant = 5

μg/mL = 47 nM). The total number (here, concentration) of receptors R_T (78.34 pM) is composed of unbound receptors (R) and bound receptors (C), $R_T = R + C$. Thus, equation can be simplified as:

$$\frac{dC}{dt} = k_{on} \cdot (R_T - C) \cdot L_0 - k_{off} \cdot C \tag{2.4}$$

where the boundary condition is $C(0) = 0$ (at $t = 0$). The solution of this differential equation is:

$$C(t) = \frac{k_{on} \cdot L_0 \cdot R_T}{k_{on} \cdot L_0 + k_{off}} \left[1 - \exp\left\{-(k_{on} \cdot L_0 + k_{off}) \cdot t\right\}\right] \tag{2.5}$$

The number of bound receptors per cell is equivalent to 141,482 (146,924 – 5,442) according to the result of our blocking experiment. Therefore, the saturated concentration of ligand-receptor complexes, $\frac{k_{on} \cdot L_0 \cdot R_T}{k_{on} \cdot L_0 + k_{off}}$ should also be equal to 7.83×10^{-11} M (or 141,482 bound receptors over 2×10^5 cells). Because k_{off}, L_0, and R_T are known, k_{on} can be calculated from this molar equivalence as $5.83 \pm 1.48 \times 10^4$ $s^{-1}M^{-1}$ (n = 6). In addition, the dissociation constant between the VEGFR2 and its monoclonal antibody is obtained as $K_D = k_{off}/k_{on} = 1.80 \pm 0.87 \times 10^{-9}$ M (n = 6). As point of reference, Lu et al. measured binding kinetics between three different monoclonal anti-VEGFR2 and purified human VEGFR2 using surface plasmon resonance, and obtained average values of k_{off}, k_{on}, and K_D as 3.95×10^{-4} s^{-1}, 1.14×10^5 $M^{-1}s^{-1}$, and 3.46×10^{-9} M, respectively [41].

2.3 CHEMOMECHANICAL MAPPING OF LOOP 6 RECEPTORS ON CELLS

Over the course of this study detailed below, the identity of a cell surface receptor for Loop 6 was established by both FFI and complementary methods conducted by our collaborators C. Fernandez, M.A. Moses et al. As the papers identifying this receptor (co-authored by our collaborators and ourselves) are currently under review, the name of this receptor is omitted from this thesis document. Parts of the following study were submitted in 2009 with co-authors Cecilia A. Fernandez and Marsha A. Moses [49].

2.3.1 INTRODUCTION

In this section, we demonstrate functionalized force imaging of receptors on the surface of cells by investigating specific binding of a potent small molecule, Loop 6, to the surface of microvascular endothelial cells. Whether a specific receptor for an oligopeptide, Loop 6 exists on the plasma membrane of surface, and what receptors Loop 6 binds to have been explored. Loop 6, consisting of 24 amino acids as a portion of tissue inhibitor of metalloprotease-II (TIMP-II), inhibits both normal and mitogen-driven angiogenesis *in vivo* and *in vitro* in endothelial cell systems by the inhibition of endothelial cell proliferation [50]. Even though Loop 6 resulted in the inhibition of embryonic neovascularization, the starting point of its anti-angiogenic mechanism was unknown. By imaging the surfaces of human dermal microvascular endothelial cells (hdMVECs) with Loop 6-functionalized AFM probes, we demonstrated the existence and identity of the specific receptor for Loop 6. This functionalized force imaging verification was complementary to other, more traditional biochemical approaches including surface plasmon resonance and colocalization imaging.

2.3.2 RESULTS AND DISCUSSION

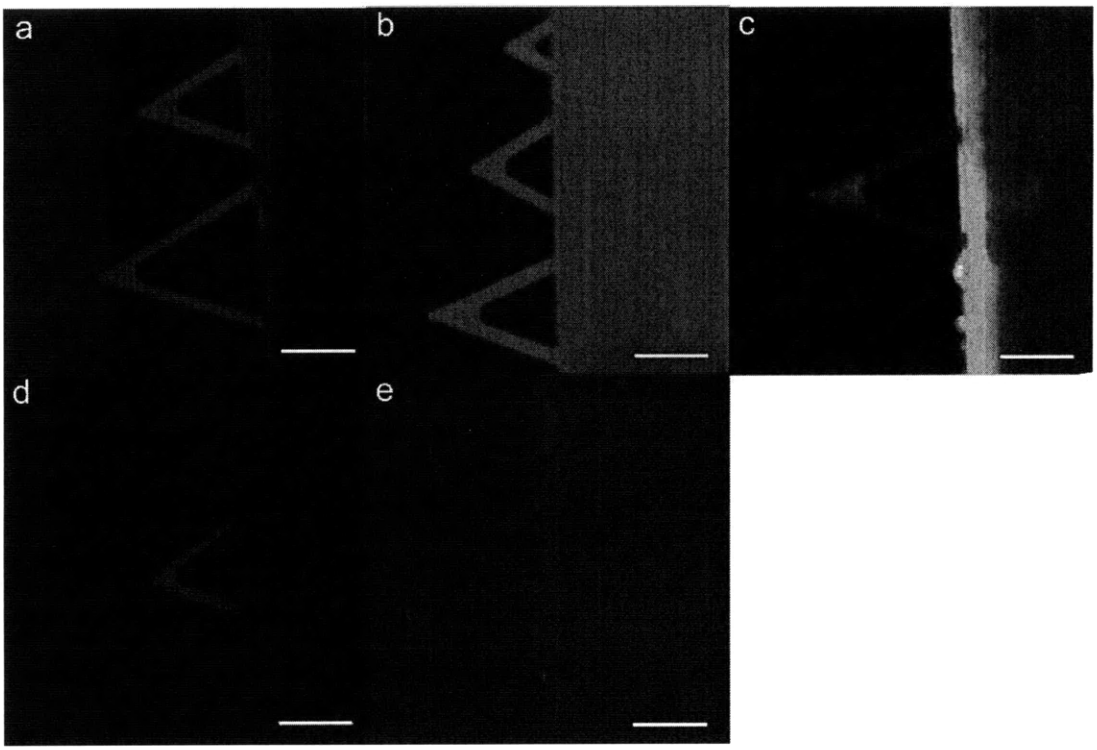

Figure 2.9 Loop 6 functionalization on the silicon nitride probe and its verification. (a) Bare silicon nitride cantilever treated with streptavidin-fluorescein - no specific bindings. (b) BSA-biotin-adsorbed silicon nitride cantilever treated with Texas red-streptavidin - specific bindings, which confirmed BSA-biotin molecules were active. (c) BSA-biotin-adsorbed silicon nitride cantilever, followed by streptavidin immobilization, treated with biotin-fluorescein - specific bindings, which confirmed streptavidin attached to BSA-biotin molecules was active. (d) BSA-biotin-adsorbed silicon nitride cantilever, followed by streptavidin immobilization treated with Texas red-streptavidin – no specific binding. (e) BSA-biotin-adsorbed silicon nitride cantilever, followed by streptavidin immobilization, and biotinylated Loop 6 treated with biotin-fluorescein. No specific binding is observed because biotinylated Loop 6 occupied the binding position to biotin-fluorescein. Scale bars = 50 μm.

Loop 6 molecules were tethered onto the silicon nitride AFM probes, and probe modification chemistry was confirmed with epifluorescence microscopy (Fig. 2.9). Visualization of specific intermolecular binding is enabled by specific AFM signal deconvolution modes such as recognition mode [12]. Flow cytometry result (Fig. 2.13b)

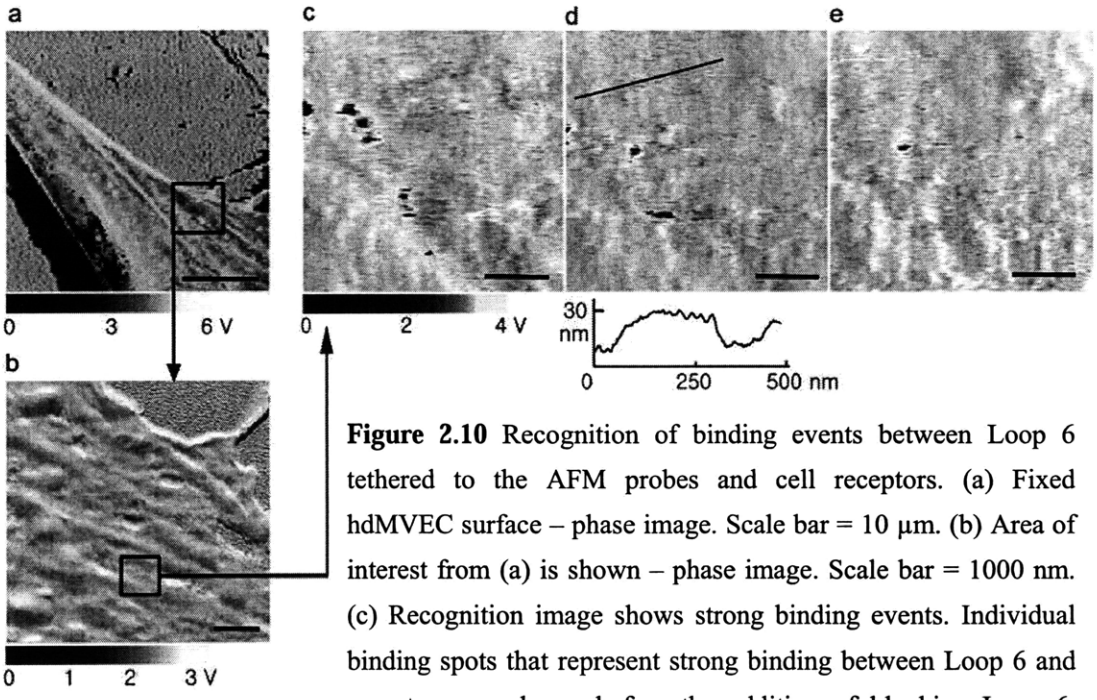

Figure 2.10 Recognition of binding events between Loop 6 tethered to the AFM probes and cell receptors. (a) Fixed hdMVEC surface – phase image. Scale bar = 10 μm. (b) Area of interest from (a) is shown – phase image. Scale bar = 1000 nm. (c) Recognition image shows strong binding events. Individual binding spots that represent strong binding between Loop 6 and receptors are shown before the addition of blocking Loop 6. (d) The same area as (c) at 10 minutes after the addition of soluble Loop 6. Height cross-section (black line) shows height trace and cytoskeletal fiber beneath the plasma membrane. (d) The same area as (c) and (d) is shown at post blocking time of 30 minutes. (c), (d), and (e) are all recognition images. Scale bars = 200 nm.

demonstrates the specificity of Loop 6 only to hdMVECs, not to 3T3 fibroblast cells. As shown in Fig. 2.10, the surface of hdMVECs was imaged with a Loop 6-functionalized probe, and binding specificity was confirmed by adding soluble Loop 6 to occlude the binding pockets of receptors. With increasing time post-blocking, the location and the number of binding sites changed, and the number of binding sites decreased. This decrease in the number of binding sites demonstrates the existence of receptors for Loop 6 and specificity of receptors with Loop 6 tethered to the AFM probes.

The rupture force histogram demonstrates a strong interaction between receptors and Loop 6 with rupture force of 31 ± 8 pN (Fig. 2.11a), which causes strong binding force in the force vs. displacement curve as shown in Fig. 2.11b. As control

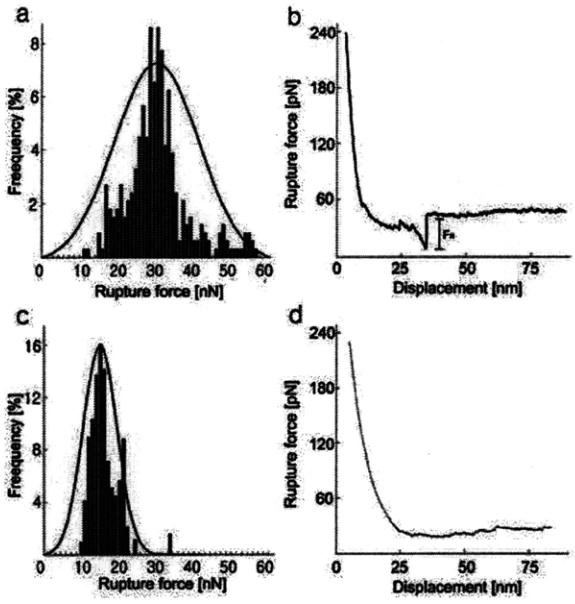

Figure 2.11 Force spectroscopy analysis of binding events. (a) Measurement of rupture force from 337 force curves on the binding spots. Histogram and Gaussian curve reveals that rupture force between Loop 6 and its receptor is 30.92 ± 8.41 pN. (b) Rupture force vs. displacement curve shows the specificity of binding events. (c) Measurement of binding force from 145 force curves was made on the areas that didn't show binding spots. Histogram and Gaussian curve shows that noise force was 15.38 ± 3.28 pN. (d) Compared to (b), strong binding is not shown in the rupture force vs. displacement curve. All the curves were obtained with a loading rate of 4,400 pN/sec.

experiments, force spectroscopy analysis was done on the regions where dark spots did not appear (Fig. 2.11c). Non-specific binding force measured on these regions was 15 ± 3 pN, which is in the error range of AFM force resolution. When Fig. 2.11b is compared with Fig. 2.11d, it is validated that rupture force measured with Loop 6-functionalized probes is specific.

Figure 2.12 demonstrates the number of binding sites as a function of time post-blocking. The tootal number of receptors per cell, $5.6 \pm 0.8 \times 10^4$ was estimated based on images such as Figs. 2.10 and 2.15, and the calculation of the total surface area of hdMVECs (5,020 ± 760 μm^2 per cell, calculated from 23 AFM images of these cells). Other researchers have demonstrated from radio-labeling experiments that the number of a potential receptor for Loop 6 on endothelial cells and R600 fibroblast cells is $3.9 \pm 0.6 \times 10^4$ / cell and 3.0×10^4 / cell, respectively. This number of receptors per cell previously reported confirms that the number of receptors calculated from AFM images lies within the same order of magnitude.

A specific receptor that we consider as a potential receptor for Loop 6, a

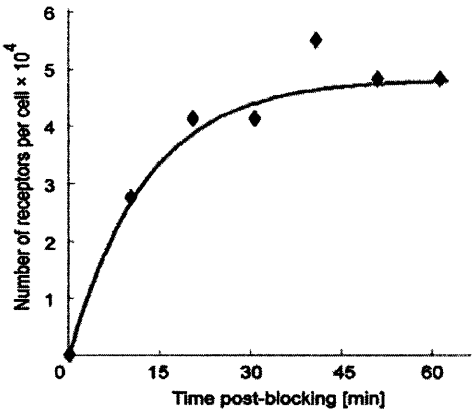

Figure 2.12 Analysis of the number of binding sites. Change in the number of binding sites, which is visualized in Fig. 1 on hdMVEC surface, is shown in real time. The number of binding sites is decreasing after the addition of soluble Loop 6, which verify the specificity of Loop 6 binding to receptors. Purple dots represent experimental data, and a solid line comes from fitting as shown in supporting information.

tyrosine kinase-associated receptor, is known to be involved in cell growth, transformation, and apoptosis. As Fig. 2.13 demonstrates, this receptor was expected to be the receptor for Loop 6 from previous experiments in the Moses group; this specificity was proven from AFM blocking experiments shown in Fig. 2.15. Here, antibody against the receptor was added to the imaging solution as a blocking agent; binding characteristics over time were compared with those images that used soluble Loop 6 as blocking agent. The occlusion of the receptor by the antibody caused the decrease in the binding sites over imaging time post-blocking. In contrast to Fig. 2.15, the number of binding sites did not decrease over imaging duration upon the addition of monoclonal anti-CD31, an antibody specific to endothelial cells (data not shown). Comparison of experiments where two separate antibodies were added (antibody against a potential receptor for Loop 6 and anti-CD31) confirms the capability of Loop 6 on the probe to specifically bind to the receptor on the cell surfaces.

While the addition of antibodies to the imaging media confirms the specificity of binding spots on the cell surfaces, the activity of the probe that was used for recognition events was also verified. Upon manifesting specific binding sites in Fig. 2.15, the same tip was used again to recognize another set of binding events on another

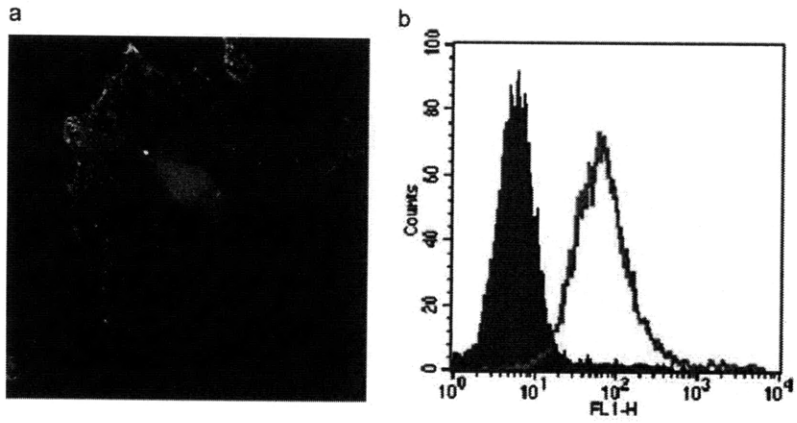

Figure 2.13 (a) Suggested colocalization of a potential receptor for Loop 6 and Loop 6 receptor on hdMVECs, via immunocytological staining (antibody against the potential receptor) and fluorescently labeled Loop 6 (provided by C. Fernandez). (b) Flow cytometry (FACS) confirmation of specificity of Loop 6 to hdMVECs (green) as compared to NIH-3T3 fibroblasts (purple).

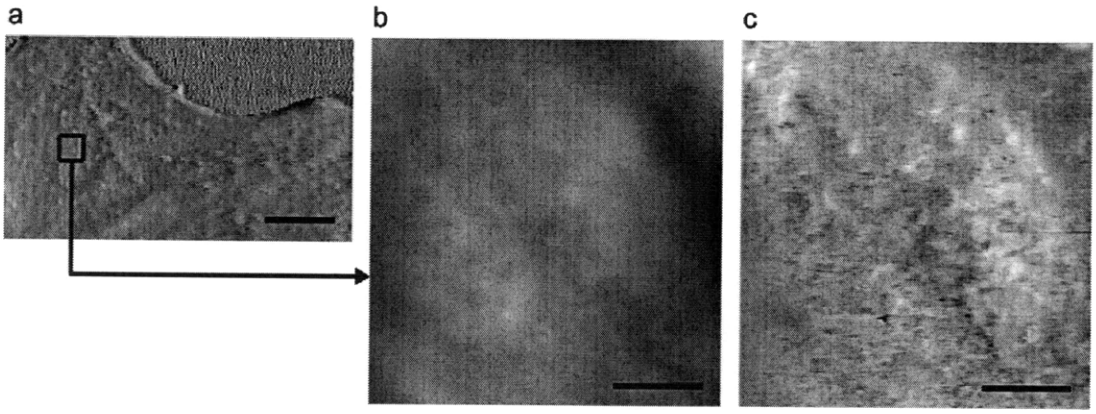

Figure 2.14 Fixed cell surface with bare probe. (a) hdMVEC surface was imaged with a bare probe. Scale bare = 5 μm. (b) The topography image of the area marked in (a) was shown. (c) is the recognition image of the same area as (b). No binding events were recognized when the cell surface was imaged with the bare probe.

cell surface of a different cell sample. The activity of the probe was maintained even after the addition of antibody against the potential receptor and the switch to another cell sample. Importantly, these cells did not exhibit any specific binding sites when the cell surfaces were imaged with a bare probe (Fig. 2.14).

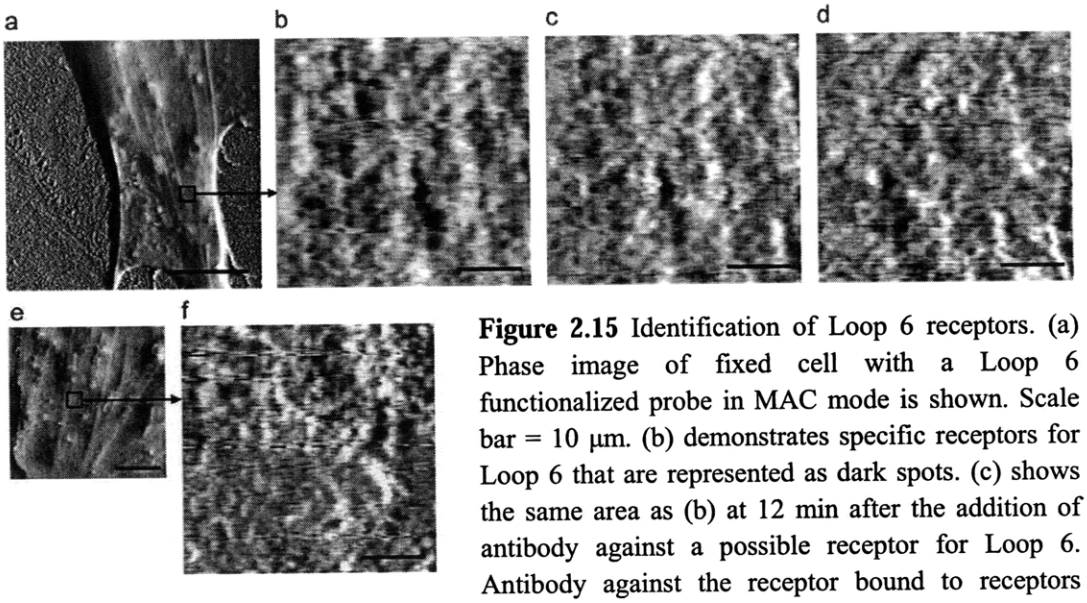

Figure 2.15 Identification of Loop 6 receptors. (a) Phase image of fixed cell with a Loop 6 functionalized probe in MAC mode is shown. Scale bar = 10 μm. (b) demonstrates specific receptors for Loop 6 that are represented as dark spots. (c) shows the same area as (b) at 12 min after the addition of antibody against a possible receptor for Loop 6. Antibody against the receptor bound to receptors occludes binding sites. (d) is the cell image at 42 minutes after the addition of the antibody. Scale bars of b, c, and d = 500 nm. (e) is an image of another fixed cell with the same probe used to get images of a – d after one set of experiment (a – d) was conducted to verify the activity of the probe through which specificity of ligand-receptor binding was confirmed. Scale bar = 10 μm. (f) demonstrates another binding event on a cell surface of different cell sample. Scale bar = 500 nm.

2.3.3 METHODS

2.3.3.1 Cell culture

Human dermal microvascular endothelial cells were cultured in endothelial basal medium-2 (EBM-2, Cambrex Bio Science, Walkersville, MD) containing the following supplements (Cambrex Bio Science); 5% fetal bovine serum (FBS), 0.1% epidermal growth factor (rhEGF), 0.1% ascorbic acid, 0.04% Hydrocortisone, 0.1% potential receptor for Loop 6, 0.1% gentamicin sulfate amphotericin-B (GA-100), 0.4% human fibroblast growth factor-B (hFGF-B), and 0.1% vascular endothelial growth factor (VEGF). 3T3 fibroblast cells were cultured in Dulbecco's Modified Eagle Medium, 10% Donor Calf Serum with Iron, 1% Penicillin-Streptomycin, 1% Glutamine (Invitrogen Corporation). Cells were grown on tissue culture treated coverslips (Nalge

Nunc International).

2.3.3.2 AFM probe chemistry

Silicon nitride AFM cantilevers (MLCT-AUHW, Veeco Instruments) were cleaned in piranha solution (30% hydrogen peroxide: 70% sulfuric acid) for 30 minutes, followed by rinsing in deionized water. Cantilevers were rinsed in ethanol (10 minutes), acetone (10 minutes) and dichloromethane (10 minutes), all of which were obtained from Sigma-Aldrich Corporation, then dried in a stream of nitrogen. Cantilevers were exposed to UV light for one hour. N,N-Diisopropylethylamine (300 μL, Sigma-Aldrich Corporation) and 3-Aminopropyltriethoxysilane (900 μL, Sigma-Aldrich Corporation) were used in a vacuum dessicator via chemical vapor deposition for two hours. Biotinylated BSA (B-BSA, Pierce Biotechnology, Rockford, Il) in sodium bicarbonate (pH = 8.9, 0.5 mg/mL) was added to cleaned cantilevers, and the adsorption reaction proceeded overnight at 37°C [51]. Cantilevers were rinsed with 150mM phosphate buffered saline (PBS) twice, followed by covalent attachment of B-BSA to the cantilevers with 52mM 1-Ethyl-3-[3-dimethylaminopropyl] carbodiimide Hydrochloride (EDC, Pierce Biotechnology) for two hours. EDC cantilevers were rinsed five times with PBS. B-BSA cantilevers were incubated with 100 μL of streptavidin (Pierce Biotechnology) in PBS (1 mg/mL) for 20 minutes, then rinsed ten times with PBS. Streptavidin-treated cantilevers were incubated with 150 μL of Biotinylated Loop 6 (30 μg/mL) for 20 minutes, and finally cleaned ten times with PBS. When AFM imaging is done in tapping mode, the optimal length of linkers is crucial with respect to the probe oscillation amplitude. Especially, polyethylene glycol (PEG) linkers, which are 5-15nm long, are used for tapping mode imaging. In contact mode,

however, short linkers are better than long tethers because probes are almost touching the surfaces.

2.3.3.3 AFM imaging of living hdMVECs

Pico Plus AFM (Agilent Technology/Molecular Imaging Company, Tempe, AZ) was used for living cell imaging. hdMVECs grown on tissue culture treated coverslips were removed from the 5% CO_2 incubator just before imaging. hdMVECs were maintained in 600 μL of filtered EBM-2 (live cell imaging) and in HEPES (fixed cell imaging) during AFM imaging at room temperature. Loop 6-functionalized cantilevers were not dried before use, and cells were imaged in contact mode and magnetic AC (MAC) mode at a nominal contact force and amplitude according to specific experimental conditions such as how big cell are and which cells were chosen with a cantilever of spring constant k = 0.0293 N/m for contact mode and 0.0834 N/m for MAC mode. Soluble Loop 6 and antibody against a potential receptor for Loop 6 were added via the peristaltic pump through tubing integrated into the fluid cell damping plate. Force spectroscopy pulling was conducted with sweep duration of 0.1s. Imaging rate was 800 nm/sec to 70 μm/sec, depending on the size of target samples. When large portions of cell surfaces were imaged, the fast rate was used; for small portions, the slow imaging rate was used to maximize the binding interaction time.

2.3.3.4 Fluorescence microscopy imaging of AFM cantilevers

B-BSA adsorbed, streptavidin treated, and Loop 6-bound cantilevers were treated with fluorescein-conjugated biotin and Texas Red-conjugated streptavidin (0.2 mg/mL, Invitrogen) for 30 minutes, then rinsed ten times with filtered 150 mM PBS before

optical imaging (Zeiss Axioplan2, Carl Zeiss International) at 20X. A customized PDMS fluid chamber was devised to image the cantilevers immersed in buffered solution.

2.4 BINDING AND ACTIVATION ENERGY MEASUREMENT ON CELLS VIA SINGLE MOLECULE RECOGNITION IMAGING

Parts of the following study were submitted for publication in 2009 [52].

2.4.1 INTRODUCTION

Thermodynamics and kinetic binding parameters between biomolecules are key to predicting the stability and lifetime of interactions among molecular pairs including ligand-receptor, enzyme-substrate, antigen-antibody, complementary DNA strands, and molecular glues such as biotin-streptavidin. These parameters include association/dissociation rate constants, free energy, enthalpy, and entropy. In particular, the measurement of binding energy for the elucidation of free energy landscapes and associated activation energy in drug-epitope systems is considered to be a starting point to design effective drugs and resolve the mechanism underlying observed binding events [53]. Therefore, various experimental methods to measure binding/activation energy have been explored such as isothermal titration calorimetry, atomic force microscopy (AFM) force spectroscopy analysis, and grand canonical monte carlo simulation. Isothermal titration calorimetry, in which the binding energy of macromolecules is measured in terms of power required to maintain constant temperature, is especially useful for the measurement of isolated macromolecules. Atomic force microscopy (AFM)-enabled molecular force spectroscopy (MFS) analysis is well-suited for the measurement of unbinding force and dissociation rate constant (k_{off}) between binding pairs, both of which are closely related to internal energy involved in rupture events [10,53-55]. Both measurement techniques have been useful specifically for the determination of key amino acids in "hot" binding spots by

comparing binding energy of wild type with that of point-mutated proteins where candidate amino acids in binding sites are replaced to demonstrate key thermodynamic properties [54,56-59].

Although AFM-MFS enables direct measurement of unbinding force in binding pair systems, it is known that measured force between tethered molecules at the cantilevered probes and complementary molecules conjugated to substrates is not absolute, but rather is affected by experimental conditions such as the spring constant and loading rate of cantilevered probes [60]. To date, this analysis has been reported as a direct measurement of only the change in enthalpy (ΔH) associated with bond-breaking processes, not the change in entropy (ΔS), which involves translational/rotational degrees of freedom of molecules, effects of solvents, and protein conformation [54]. Because force spectroscopy analysis can be executed under near physiological conditions on the AFM and does not require isolation of trans-membrane molecules on cell surfaces[61,62], AFM-MFS has enabled measurement of the unbinding force of biological macromolecules at a molecular level. However, it is not yet possible to measure free energy change (ΔG) because this property is the combination of enthalpy change (ΔH) and entropy change (ΔS). Isothermal titration calorimetry is a standard experiment to directly measure binding energy of biological macromolecules, but requires that molecules for isothermal titration calorimetry should be isolated or synthesized at high concentration; these constraints increase the possibility that measured energy deviates from actual energy under physiological conditions, and are not amenable to unpurified transmembrane protein receptors. The factors that are involved in determining free energy in biological systems are solution effects, protein conformational degree of freedom, and affinity change with respect to

monomeric/dimerized receptors [63]. Therefore, it is important to measure unbinding force or energy on intact cell surfaces at the single-molecule level, where the relation between environment and transmembrane molecules as well as the factors mentioned above are well maintained.

Functionalized force imaging [62] or recognition imaging [12] can facilitate such experiments, by using the AFM to first image the position of molecules complementary to those conjugated on the cantilevered probes via specific intermolecular interactions. Van Vliet et al. [64] proposed that functionalized force imaging could be useful for recognizing specific receptors on the cell surfaces via conjugation of antibodies or ligands that specifically bind to cell surface receptors. Researchers [12,34] have demonstrated the possibility of antigen detection with antibody-conjugated probes and of confirmation of the existence of receptors via functionalized force imaging. However, to date no results on the measurement of binding energy on real, intact cell surfaces have been reported.

Here, we present a nanomechanical contact measurement of binding energy (ΔG, ΔH, and ΔS) and activation energy barrier ($\Delta G^{\ddagger}$, $\Delta H^{\ddagger}$, and $\Delta S^{\ddagger}$) simultaneously via AFM functionalized force imaging. These estimations of thermodynamic properties via nanomechanical binding between molecules were derived from molecular-resolution images of both protein-functionalized surfaces (controls) and intact cell surfaces. Efficiency of energy measurement by functionalized force imaging of a control system, biotin-streptavidin, was compared with the results from isothermal titration calorimetry and expanded to include a wider range of temperature than reported previously for this well-studied complex. This approach was then applied to a biological system (vascular endothelial cell system) to calculate the binding and activation energies of vascular

endothelial growth factor receptor 2 (VEGFR2), expressed endogenously on human umbilical vein endothelial cell (HUVEC) surfaces.

2.4.2 RESULTS

2.4.2.1 Biotin-streptavidin analysis

One of the most well studied molecular pairs via AFM or other technological platforms is the biotin-streptavidin system, a well-known biological glue that is one of the strongest noncovalent binding pairs ($K_a \sim 10^{13}$ M^{-1}) [56,65]. Binding characteristics of this system, including unbinding force or rupture forces at defined loading rates [60,66] and unbinding energy [57,58,67] have been reported since Weber et al. [68] first performed the measurement of free energy via titration calorimetry. In particular, the comparison between wild type streptavidin-biotin and mutated streptavidin-biotin systems via isothermal titration calorimetry and AFM force spectroscopy analysis has been useful to find the key amino acids crucial to generating strong unbinding forces and the internal energy of this system.

Here, the biotin-streptavidin system was chosen to validate the efficiency of energy measurements of this pair via functionalized force imaging (FFI) or recognition imaging. Streptavidin was conjugated to flat mica, and biotinylated bovine serum albumin was conjugated to AFM cantilevered probes (see Materials and Methods).

As Figs. 2.16 A-C demonstrate, specific binding events are represented as dark spots in FFI images. From these images, it is possible to identify the location, number, and distribution of streptavidin molecules attached on the substrates. Instead of population-averaged methods such as radiolabeling experiments or surface plasmon resonance, individual molecules via specific binding events were traced, which enables

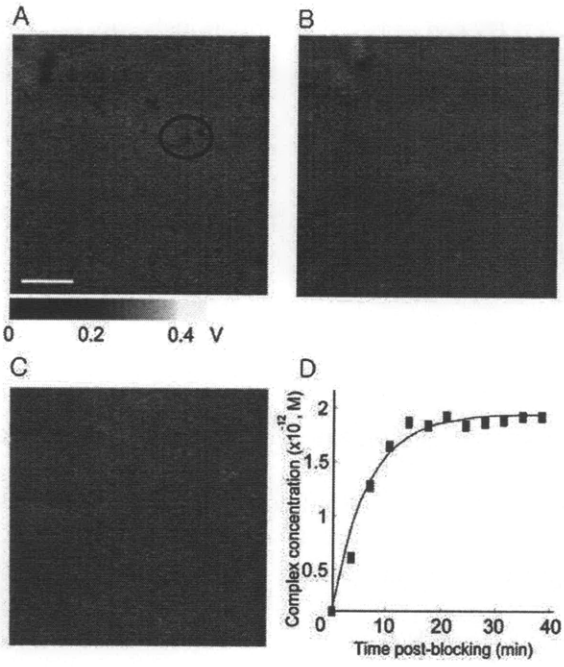

Figure 2.16. (A – C) Time-lapsed functionalized force imaging of streptavidin conjugated mica with biotin-conjugated probe at 4°C (277 K). (A) Recognition image of streptavidin molecules with biotin-conjugated probe (t_{pb} = 0 min) before the addition of blocking biotin shows dark spots that represent specific binding between biotin and streptavidin. One example of specific binding events is represented in the circle. Scale bar = 300 μm. (B) Same region as (A) at t_{pb} = 7 min after the addition of biotin and (C) at t_{pb} = 38 min. Scan rate of (A), (B), and (C) = 1,5 μm/sec. (D) Time course of competitive binding of biotin to streptavidin mica. The number of biotin-streptavidin complexes increases with the function modeled above with respect to time post-blocking at 4°C (277 K). Square (■) indicates observed data, and line (–) represents best fit. Kinetic constants/energy were calculated from the best fit, as described in the text.

the analysis of single molecule binding kinetics, although kinetic constants and energy were averaged for statistical analyses. To check the specificity of binding events, biotin, as a blocking agent, was added to streptavidin-conjugated mica. As biotin added to the imaging solution, the number of specific binding events decreased, indicating formation of biotin-streptavidin complexes over time. Note that the number of dark spots decreased, demonstrating that the binding of biotin on the cantilever probes to streptavidin on mica was specific. In addition, as AFM enables the real time imaging of the same locations, the observation of the change in the number of binding spots provides valuable kinetic information. Kinetic constants (k_{on} and k_{off}), binding energy, and activation energy were calculated from these time-lapsed FFI images as discussed above. The calculated constants and parameters are summarized in Table 2.1.

As shown in Table 2.1, k_{off} is more sensitive to temperature variation than k_{on}. Absolute values of both enthalpy and entropy changes increased as temperature

Table 2.1 Binding kinetics and thermodynamic parameters in biotin-streptavidin system

Kinetic/thermodynamic parameters	Temperature			
	277 K	298 K	303 K	310 K
k_{off} ($\times 10^{-5}$, s^{-1})	0.010 ± 0.012	0.55 ± 0.24	1.28 ± 0.29	7.83 ± 2.67
k_{on} ($\times 10^{8}$, $s^{-1}M^{-1}$)	0.64 ± 0.12	1.12 ± 0.45	2.34 ± 0.83	4.48 ± 1.17
K_D ($\times 10^{-13}$, M)	0.016 ± 0.003	0.49 ± 0.32	0.55 ± 0.43	1.75 ± 0.85
ΔG (kcal/mol)	-18.76 ± 1.17	-18.15 ± 0.29	-18.38 ± 0.92	-18.09 ± 0.41
ΔH (kcal/mol)	-21.62 ± 2.32	-25.02 ± 3.38	-25.86 ± 2.93	-27.07 ± 3.24
-TΔS (kcal/mol)	2.86 ± 1.13	6.87 ± 3.09	7.48 ± 3.11	8.98 ± 2.83

increased (Fig. 2.17A). The magnitudes of ΔG, ΔH, and ΔS calculated in functional force imaging agree within 20.4 % range with previous reports at 298 K and 310 K [54,56-59,68], confirms the efficiency of this AFM measurement. However, to our knowledge, these parameters have not been reported over the full range of temperatures considered here. As shown in Table 2.1 and Fig. 2.17, high affinity of biotin to streptavidin corresponds to large negative enthalpy at all the temperature ranges measured in this experiment. This was expected based on the fact that binding between biotin and streptavidin comprises a network of hydrogen bonds [59]. Slow increases in large negative enthalpy changes with increasing temperature are the hallmark of stable biotin-streptavidin binding even at higher temperatures. Entropy changes increased more rapidly with increasing temperature, as compared to enthalpy changes. From the experimental data in Fig. 2.17, the best fits of enthalpy and entropy were estimated: entropy, $E_{-T\Delta S} = 2.5704 \cdot e^{0.0355 \cdot T}$ (R^2 = 0.9816); and enthalpy, $E_{\Delta H} = -21.053 \cdot e^{0.00685 \cdot T}$ (R^2 = 0.9998) where unit of $E_{-T\Delta S}$ and $E_{\Delta H}$ is kcal/mol, and the unit of T is Kelvin. The temperature where $T\Delta S$ exceeds ΔH ($\Delta G = 0$) is the temperature at which the rates of binding and unbinding are equal:

Table 2.2 Activation energy in biotin-steptavidin system at 25°C (298K)

Activation Energy	Value (kcal/mol)
$\Delta G^{\ddagger}$	24.52 ± 0.59
$\Delta H^{\ddagger}$	32.73 ± 1.15
$T\Delta S^{\ddagger}$	8.21 ± 1.73

$E_{-T\Delta S} + E_{\Delta H} = E_{\Delta G} = 2.5704 \cdot e^{0.0355 \cdot T} - 21.053 \cdot e^{0.00685 \cdot T} = 0$. This temperature was calculated as 73°C, which implicitly assures that streptavidin is stable at this temperature. Above this temperature, the dominant binding state will be shifted from association to dissociation, which, however, does not imply that every biotin-streptavidin pair will necessarily rupture. Figure 2.17C describes the thermal stability and temperature-related binding characteristics of biotin-streptavidin binding in terms of heat capacity. Some protein-protein interactions [69] and DNA-protein interactions [70] are characterized by different heat capacities ($\Delta C = \Delta H/T$): heat capacity is the gradient of the enthalpy vs. temperature graph. Since heat capacity is the heat required to increase one mole of a sample by one degree, this variation of heat capacity demonstrates the conformational change of molecules (e.g., protein or DNA) to optimize and strengthen the interactions at a certain temperature (e.g., at physiological temperature of 37°C). However, biotin-streptavidin binding does not show this variation of heat capacity within 4 - 37 °C, which implies that strong hydrogen bond network maintains the conformation of streptavidin, unlike molecular systems (e.g., site specific binding of proteins to DNA) in which local folding is coupled to binding as previously reported under physiological conditions [70].

Table 2.2 and Fig. 2.17B summarize the biotin-streptavidin activation barrier calculated from the Eyring equation (2.10). Activation barriers of free energy, enthalpy,

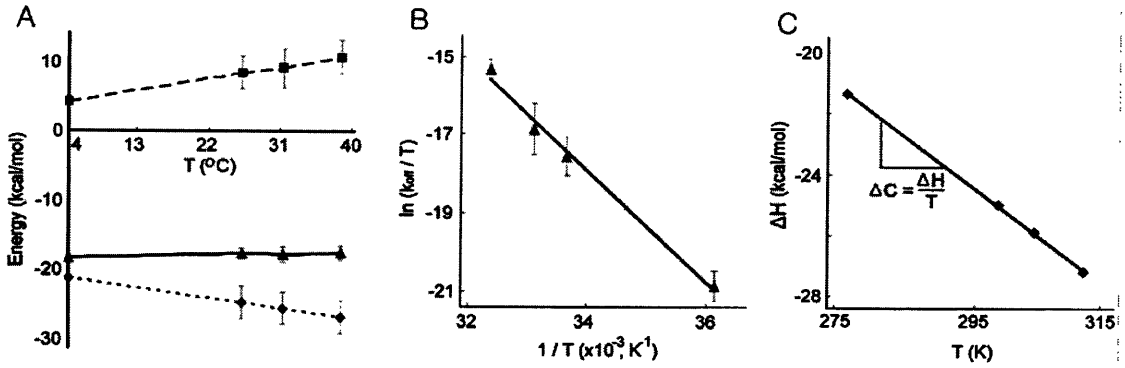

Figure 2.17 Calculation of (A) binding and (B) activation energy in biotin-streptavidin system. (A) Entropy (■), enthalpy (♦), and free energy (▲) show different time-dependence. Magnitude of both entropy and enthalpy increases as temperature increases, whereas free energy, which is the combination of entropy and enthalpy, increases slowly. (B) Plot of the Eyring equation of biotin-streptavidin binding system. From the slope and intercept are activation entropy, enthalpy, and associated free energy calculated as discussed above. (C) The slope of enthalpy vs. temperature graph represents heat capacity. Heat capacity of biotin-streptavidin system is barely dependent on temperature within the temperature range of 277- 310 K. This independence of temperature implies that biotin-streptavidin binding is not coupled with local folding.

and entropy agree within 15% with previously published data [54,56]. Biotin must overcome a large enthalpy barrier; that is, enthalpy dominates over entropy in binding dissociation. A large, positive enthalpy implies that the breaking of internal bonds is endothermic, and a positive entropy means that the transition state in which strong internal bonds are broken is entropically favored [56].

The binding energy (ΔG, ΔH, and ΔS) and activation energy barrier ($\Delta G^{\ddagger}$, $\Delta H^{\ddagger}$, and $\Delta S^{\ddagger}$) were calculated for the biotin-streptavidin system and agreed reasonably with values obtained via established methods for purified molecules. Having thus confirmed the accuracy of this method for isolated proteins, we then considered analysis of cell surface-bound proteins.

2.4.2.2 Analysis of VEGFR2 and anti-VEGFR2 system on cells

Vascular endothelial growth factor receptors (VEGFRs) are a family of receptor tyrosine

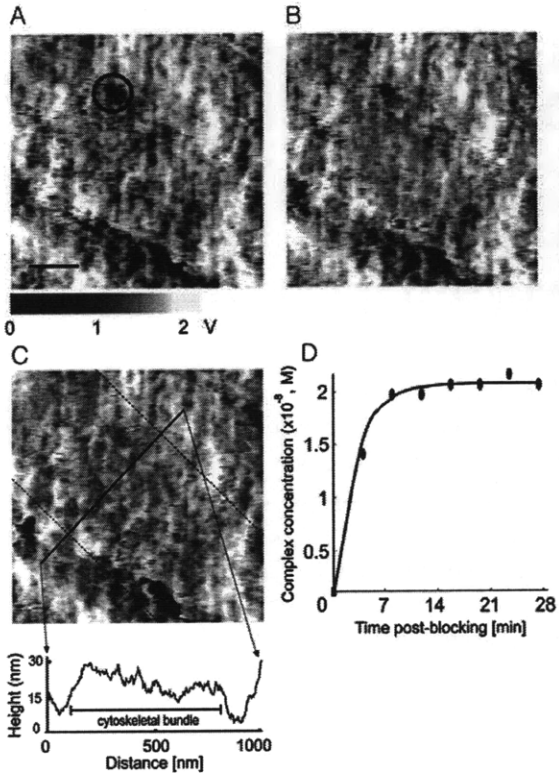

Figure 2.18 (A – C) Time-lapsed functionalized force imaging of VEGFR2 and anti-VEGFR2 on fixed HUVECs at 37°C (310 K). (A) Recognition image of cell surface with anti-VEGFR2-conjugated probe (t_{pb} = 0 min) before the addition of blocking antibody shows dark spots that represent specific binding between receptor and antibody. One example of specific binding events is represented in the circle. Scale bar = 200 nm. (B) Same region as (A) at t_{pb} = 3.5 min after the addition of anti-VEGFR2 and (C) at t_{pb} = 25 min. Scan rate of (A), (B), and (C) = 1,000 nm/sec. Line-trace from height image (image not shown here) in (C) demonstrates that receptors are concentrated near/above cytoskeleton underneath the plasma membrane. The area between two dotted lines represents cytoskeletal bundle. (D) Time course of competitive binding on the cell surface. The number of antibody-receptor complexes increases with the modeled function with respect to time post-blocking at 37°C (310 K). Circle (•) indicates observed data, and line (–) represents best fit. Kinetic constants/energy were calculated from the best fit, which was discussed in Materials and Methods.

kinases that play a key role in cytoskeleton remodeling, endothelial cell proliferation/migration, and angiogenesis [20]. As a result, VEGFRs have been a target for anti-angiogenic treatments, cancer therapies, and drug design. In this ligand-receptor system, the binding energy and force can provide quantitative predictions of binding efficiency on cell membranes [53]. In addition, the spatial distribution of VEGF receptors with respect to other cellular features such as the actin cytoskeleton will be important parameters for drug designs and for understanding the mechanisms underlying drug activity.

The functionalized force imaging (FFI) technique that was demonstrated with the biotin-streptavidin system was utilized for the measurement of binding and activation energy between vascular endothelial growth factor receptor 2 (VEGFR2) and

Table 2.3 Binding kinetics and thermodynamic parameters in VEGFR2 and anti-VEGFR2 system

Kinetic/thermodynamic parameters	Temperature		
	277 K	300 K	310 K
k_{off} ($\times 10^{-4}$, s^{-1})	0.0656 ± 0.0244	1.05 ± 0.6	6.33 ± 2.81
k_{on} ($\times 10^{4}$, $s^{-1}M^{-1}$)	2.48 ± 0.72	5.83 ± 1.48	8.34 ± 1.89
K_D ($\times 10^{-9}$, M)	0.264 ± 0.023	1.80 ± 0.46	7.59 ± 1.34
ΔG (kcal/mol)	-12.14 ± 0.04	-12.00 ± 0.13	-11.52 ± 0.10
ΔH (kcal/mol)	-15.03 ± 0.58	-17.63 ± 0.60	-18.82 ± 0.69
-TΔS (kcal/mol)	2.89 ± 0.61	5.63 ± 0.81	7.30 ± 0.82

antibody against VEGFR2 (anti-VEGFR2) on cell membranes. Monoclonal anti-VEGFR2 was conjugated to magnetically coated cantilevers used for imaging in TopMAC mode as described in Materials and Methods. Human umbilical vein endothelial cells (HUVECs) were lightly fixed so that FFI could be performed without the complications due to receptor trafficking processes such as lateral diffusion, endocytosis, and recycling.

As shown in Figs. 2.18 A-C, dark spots in the images represent specific binding events between VEGFR2 on the cell surface and anti-VEGFR2 on the probe. Specificity was demonstrated with a blocking experiment in which soluble anti-VEGFR2 was added to block VEGFR2 binding sites, consequently decreasing the number of observed receptors (Figs. 2.18 B-C). This information was used to calculate ligand-receptor binding kinetics via the procedure discussed for the biotin-streptavidin system. Since FFI exerts oscillation force onto the sample surface, imaging also showed the locations of rigid actin fibers under the soft, thin plasma membrane, enabling observation of the spatial correlation of VEGFR2 with actin bundles (Fig. 2.18C) as previously described [62]. These results confirmed our previous findings [62] that VEGFR2 was non-

Table 2.4 Activation energy in VEGFR2 and anti-VEGFR2 system at 27°C (300 K)

Activation Energy	Value (kcal/mol)
$\Delta G^{\ddagger}$	22.83 ± 0.23
$\Delta H^{\ddagger}$	22.30 ± 0.41
$T\Delta S^{\ddagger}$	-0.53 ± 0.64

uniformly distributed near the actin cytoskeleton.

Binding constants k_{on} and k_{off} measured with FFI were used for the calculation of binding energy via the Gibbs-Helmholtz equation (2.11), and activation energy via the Eyring Equation (2.10), as discussed in Materials and Methods. Calculated constants and parameters are summarized in Table 2.3. As with the biotin-streptavidin system, both k_{on} and k_{off} increased as temperature increased, and the temperature dependence of k_{off} was greater than that of k_{on}. Energetic parameters (Table 2.3) provided qualitative insight into the change in the structure of antibody-receptor binding sites: at higher temperature, more internal bonds between the antibody and VEGFR2 epitope are generated (magnitude of ΔH increases), but the degree of freedom increases as well (magnitude of ΔS increases). The rate of $T\Delta S$ increase is faster than that of ΔH increase. Therefore, free energy will reach zero at the temperature at which entropy effects exceed enthalpy effects as shown in the biotin-streptavidin system. The fact that heat capacity of binding (ΔC_p) does not change within this temperature range (Fig. 2.19C) implies that transmembrane VEGFR2 does not require a conformational change for active binding with this anti-VEGFR2 antibody, as was also the case in the biotin-streptavidin system. As shown in Table 2.4 and Fig. 2.19B, information on the transition state is provided by the activation enthalpy ($\Delta H^{\ddagger}$) and entropy ($T\Delta S^{\ddagger}$). This molecular system has positive activation enthalpy, which implies that the bonds that are strong

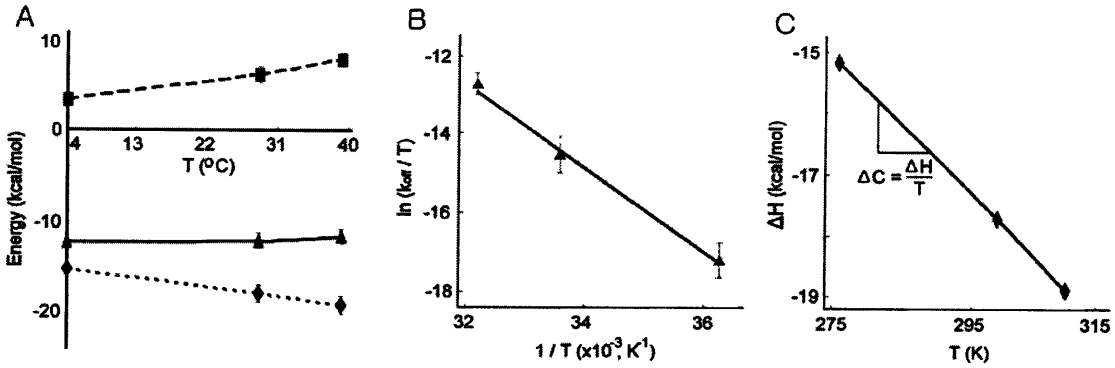

Figure 2.19 Calculation of binding (A) and activation energy (B) in the VEGFR2-anti-VEGFR2 system. (A) Entropy (■), enthalpy (♦), and free energy (▲) each show different dependence on time. The magnitude of both entropy and enthalpy increases as temperature increases, whereas free energy, which is the combination of entropy and enthalpy, increases slowly. (B) Plot of the Eyring equation for the antibody-receptor system. Activation entropy, enthalpy, and associated free energy are calculated from the slope and intercept, as discussed above. (C) The slope of the enthalpy vs. temperature graph represents heat capacity. The heat capacity of VEGFR2 and anti-VEGFRs is barely dependent on temperature within the temperature range of 277- 310 K. This temperature independence implies that antibody-receptor binding is not coupled with local folding like in the biotin-streptavidin system discussed above.

enough to show large binding enthalpy (ΔH) are significantly weakened or broken at the transition state. Small, negative activation entropy ($T\Delta S^{\ddagger}$) means that the degree of freedom of the antibody-receptor pair is reduced at the transition state, implying that the transition state is entropically unfavorable. However, the extent to which the conformational degree of freedom is reduced is small. Overall activation free energy is positive due to the large positive activation enthalpy. Therefore, the antibody bound to the probe must overcome the activation energy barrier ($\Delta G^{\ddagger}$) of 22.83 kcal/mol in order to be pulled off of the receptor epitopes.

2.4.3 DISCUSSION AND CONCLUSION

Beyond the surface imaging and unbinding forces that have been major applications of AFM, functionalized force imaging (FFI) also facilitates the calculation of binding and activation energies as well as visualization of individual receptors on intact cell surfaces.

Specificity of binding events was verified in biotin-streptavidin and antibody-receptor systems through competitive inhibition (blocking) experiments with soluble ligands or antibodies. Binding kinetics and energetics were investigated in the well-known biotin/streptavidin system. Whether or not this pair undergoes conformational change during specific interactions across various temperatures was explored through the calculation of heat capacity. FFI enabled the recognition of a transitional state between the association-preferred to the dissociation-preferred states through the best-fit analysis of enthalpy and entropy changes. The calculations and estimations in this well-studied system were verified with previously published reports. In the same manner, the same experiments were conducted on intact cell surfaces for the measurement of binding kinetics and energies in the vascular endothelial growth factor receptor 2 (VEGFR2) and anti-VEGFR2 antibody system. Different batches of antibodies have different binding epitopes. Therefore, there are no published reports with which to confirm the result of binding kinetics and energetics in the VEGFR2/anti-VEGFR2 antibody system. However, because we first validated our technical efficacy of FFI through the biotin-streptavidin system, we applied the same approach to the antibody-receptor system and obtained detailed information on binding kinetics and energy parameters on intact cell surfaces. Simultaneously, specific recognition of individual receptors as well as the revelation of other cellular features such as the underlying cytoskeleton implies the functional correlation of VEGFR2 and actin fibers, which has been suggested by many researchers[20,46,47].

Binding kinetics and associated binding/unbinding energetics involved are important factors that should be considered for drug design, because this information provides clues to the characteristics of binding events such as energy flow, transition

state, and ultimately the mechanisms of drug action. Drug molecules have the potential to interact with other receptors besides target surface molecules in physiological conditions. These possibilities increase the importance of measuring binding kinetics/energetics on intact cell surfaces, which is one of the major strengths of FFI. FFI, through visualizing nanometer scale receptors, enables the direct measurement of both binding kinetics and enegetics at the same time on intact cell surfaces and does not require receptor purification required other technical platforms (e.g., isothermal titration calorimetry). Many drugs act through via drug-receptor interaction, which competes with interactions between growth factors (or ligands) and receptors[71]. In other words, drug molecules preclude available binding sites of receptors to which growth factors or ligands should bind resulting in the activation of receptors and sequential signal cascades. Binding kinetics and energetics involved in the competition between drugs and ligands are key factors on intact cell membranes. Therefore, the investigation of drug binding kinetics through FFI would be the starting point for understanding drug efficiency before further exploration of signal transduction underlying drug-receptor interaction.

Note that we chemically fixed cell surfaces to suppress the lateral diffusion and recycling of membrane molecules. This approach is similar to established methods: chemical fixation and associated immunocytochemistry with antibodies have been a standard way to validate the existence of tagged molecules of interest. Researchers have used standardized antibody conjugation protocols to determine how long it takes for antibodies to bind to epitopes. This was confirmed by FFI by visualizing ligand-receptor binding events (Figs 2.16 and 2.18) over time. The imaging of single receptor molecules and real-time occupation of previously imaged receptors with incoming antibodies

reveals the detailed temporal information. Functionalized force imaging and associated binding models introduced in this paper have the potential for the characterization of other biological binding pairs such as DNA/DNA pairs, polysaccharide/lipid pairs, antibody/antigen pairs, and growth factor/receptor pairs, requiring modified chemistry for the conjugation of molecules to cantilevered probes in each case.

2.4.4 MATERIALS AND METHODS

2.4.4.1 Binding kinetics

For reversible binding of ligands (biotin or anti-VEGFR2 antibody) to receptors (streptavidin or VEGFR2) in the formation of a ligand-receptor complex, the reaction can be expressed as follows [2]:

$$\text{Ligand (L)} + \text{Receptor (R)} \underset{koff}{\overset{kon}{\rightleftharpoons}} \text{Ligand-receptor complex (C)} \qquad (2.6)$$

The systems considered in this calculation were a mica surface to which streptavidin was conjugated (control) and human umbilical vein endothelial cells (HUVECs) cultured on tissue culture-treated polystyrene coverslip. The rate of change of these ligand-receptor interactions can be expressed as follows:

$$\frac{dC}{dt} = k_{on} \cdot R \cdot L - k_{off} \cdot C \qquad (2.7)$$

where L, R, and C represent the concentration of anti-VEGFR2 antibody/biotin, VEGFR2/streptavidin, and antibody-receptor/biotin-streptavidin complex, respectively.

The total number (here, concentration) of VEGFR2/streptavidin R_T is comprised of unbound VEGFR2/streptavidin (R) and bound VEGFR2/streptavidin (C), $R_T = R + C$; the total number of (here, concentration) of anti-VEGFR2/biotin L_T, $L_T = L + C$. Thus, the equation can be expressed as:

$$\frac{dC}{dt} = k_{on} \cdot (R_T - C) \cdot (L_T - C) - k_{off} \cdot C \tag{2.8}$$

where the boundary condition is $C(0) = 0$ (at $t = 0$). The solution of this differential equation is:

$$C(t) = \frac{\left(\frac{A^2 - B}{A}\right) \cdot \left[\exp\left\{k_{on} \cdot \left(A - \frac{2B}{A}\right) \cdot t\right\} - 1\right]}{\left(\frac{A^2 - B}{B}\right) \cdot \exp\left\{k_{on} \cdot \left(A - \frac{2B}{A}\right) \cdot t\right\} - 1} \tag{2.9}$$

where $A = L_T + R_T + \frac{k_{off}}{k_{on}}$ and $B = L_T \cdot R_T$ with the assumption that $\left(1 - \frac{4B}{A^2}\right)^2 \cong 1 - \frac{1}{2} \cdot \frac{4B}{A^2} = 1 - \frac{2B}{A^2}$ (high order terms were ignored) and $A >> B$.

Coefficients were calculated from each graph of time vs. number of ligand-receptor complex, followed by the calculation of k_{on} and k_{off} at each temperature.

Diffusion of soluble biotin or anti-VEGFR2 in imaging medium during competitive inhibitor was estimated from the Stokes-Einstein relation [72]. For spherical particles of radius r and medium viscosity η, the diffusion coefficient is expressed as $D = \frac{k_B \cdot T}{6\pi \cdot \eta \cdot r}$, where k_B is Boltzmann constant and T is absolute temperature. Within

the temperature range of 270 – 310 K, the diffusion coefficient of biotin (MW: 244.31 g mol^{-1}) is 371 – $\mu m^2 s^{-1}$, and that of the antibody (MW: 120 kDa, IgG1) is 88 – 98 $\mu m^2 s^{-1}$. Thus, the diffusion coefficient of biotin or antibody within this temperature range can be assumed not to affect the binding kinetics analysis, in that biotin and antibody spread uniformly before the beginning of the first FFI image acquisition.

2.4.4.2 Calculation of activation energy and binding energy

Association and dissociation rate constants (k_{on} and k_{off}) were determined using Equation (4). Both k_{on} and k_{off} are sensitive to temperature. These values increase as temperature increases since the ligands that have higher energy at higher temperatures have more chances to collide with receptors. This temperature-dependence of rate constants, especially dissociation rate constant k_{off}, is well described with the Arrhenius equation or the Eyring equation [58] from which activation free energy ($\Delta G^{\ddagger}$), enthalpy ($\Delta H^{\ddagger}$), and entropy ($\Delta S^{\ddagger}$) are calculated. The Eyring equation is as follows:

$$\ln\left(\frac{k_{off}}{T}\right) = -\frac{\Delta H^{\ddagger}}{R}\left(\frac{1}{T}\right) + \left[\ln\left(\frac{k_B}{h}\right) + \frac{\Delta S^{\ddagger}}{R}\right] \tag{2.10}$$

where k_B, and h are the Boltzmann constant and Planck's constant, respectively.

Since k_{on} , k_{off} , and $K_D = k_{off} / k_{on}$ (or $K_A = k_{on} / k_{off}$) were measured at different temperature, binding free energy (ΔG) was calculated by $\Delta G = -R \cdot T \cdot \ln(K_A)$. Note that units of units of k_{on} and k_{off} should be expressed as [s^{-1} M^{-1}] and [s^{-1}], respectively for the calculation of free energy. K_A is expressed in units of M^{-1} because the other logarithm contains 1 M of ligand (L), receptor (R), and ligand-receptor complex (C)

which was subtracted, yielding zero in the logarithm. From the free energy at each temperature calculated as described, the Gibbs-Helmholtz equation [69] was then used to calculate binding enthalpy (ΔH):

$$\left(\frac{\partial(\Delta G/T)}{\partial T}\right)_P = -\frac{\Delta H}{T^2} \tag{2.11}$$

assuming constant atmospheric pressure. Gradients of $\Delta G/T$ vs. T graphs at each temperature represent $-\Delta H/T^2$. From a least-squares linear regression fit to these piecewise slopes, binding enthalpy (ΔH) at each temperature was calculated.

2.4.4.3 AFM cantilever chemistry

2.4.4.3.1 Chemistry for the conjugation in biotin-streptavidin pairs

Silicon nitride cantilevers (MAC-IV levers, Agilent/Molecular Imaging) were rinsed in dichloromethane for 10 min, followed by cleaning with the oxygen plasma cleaner for 10 min. N,N-Diisopropylethylamine (300 μL, Sigma-Aldrich Corporation) and 3-Aminopropyltriethoxysilane (900 μL, Sigma-Aldrich) were used for amine derivitization of cleaned cantilevers and freshly cleaved mica in a vacuum desiccator via chemical vapor deposition for 2 hr. Bovine serum albumin-LC-BSA (Biotin-LC-BSA, Pierce Biotechnology) in sodium bicarbonate (pH = 8.9, 0.5 mg/mL) was added to cantilevers and Biotin-BSA (0.015 mg/mL) to mica, and the adsorption reaction proceeded overnight at 37°C. [51] Cantilevers and mica were rinsed with 150 mM phosphate buffered saline (PBS) twice, followed by covalent attachment of Biotinylated BSA to the cantilevers and mica with 52 mM 1-Ethyl-3-[3-dimethylaminopropyl]carbodiimide hydrochloride (EDC, Pierce Biotechnology) for 2 hr.

After the covalent conjugation of Biotinylated BSA via EDC, cantilevers and mica were rinsed five times with PBS. Biotin-BSA conjugated mica was incubated with 100 μL of streptavidin (Pierce Biotechnology) in PBS (0.5 mg/mL) for 20 min, followed by rinsing ten times with PBS.

2.4.4.3.2 Chemistry for the conjugation in anti-VEGFR2 and VEGFR2 system

Si_3N_4 cantilevers, backside-magnetically coated by the manufacturer (MAC-IV levers, Agilent/Molecular Imaging) were rinsed in dichloromethane for 10 min, followed by oxygen plasma cleaning for 10 min. Chemical vapor deposition of 1:3 N,N-diisopropylethylamine and 3-aminopropyltriethoxysilane (Sigma-Aldrich Corporation) was achieved in a vacuum dessicator for 2 hrs, followed by conjugation of pyridyl dithio-polyethylene glycolsuccinimidylpropionate (5 mg, PDP-PEG, Agilent/Molecular Imaging) in 0.5 mL of dichloromethane and 7 μL of triethylamine (Sigma-Aldrich Corporation). Mouse antihuman monoclonal anti-vascular endothelial growth factor receptor 2 (1 mg/mL, anti-VEGFR2, IgG1, Abcam) was conjugated with a 15-fold molar excess of N-Succinimidyl 3-(Acetylthio)propionate (sATP, Pierce Biotechnology) in dimethylsulfoxide (Sigma-Aldrich Corporation). This conjugated antibody was bound to PDP-PEG-treated cantilevers for 2 hr via deacetylation with 0.5 M hydroxylamine (Sigma-Aldrich Corporation), 25 mM ethylene diamine tetraacetic acid (EDTA, Pierce Biotechnology) in 150 mM phosphate buffered saline at pH = 7.36 [12].

2.4.4.4 Functionalized force imaging or recognition imaging

Living and fixed (3 % formaldehyde and 0.1% glutaraldehyde, Sigma-Aldrich Corporation, followed by rinsing with 0.05 M, pH = 7.4 Tris buffer) HUVECs were imaged in TopMAC mode within a fluid cell (PicoPlus AFM, Agilent Technologies)[73], using backside magnetically-coated Si_3N_4 cantilevers described above (Agilent Technologies).

The number of binding events per cell was determined by direct image analysis (summing of the number of closed regions at least one order of magnitude darker than background threshold) of a given cell area; these regions were considered representative of the cell surface, as supported by immunohistochemistry shown in the previously published report [62]. The HUVEC surface area per cell was determined three-dimensional analysis of via magnetic AC mode images including at least one HUVEC, where for each cell the area was calculated as the sum of an ellipsoid surface area (based on known maximum cell height and long/short axis of the organelle-containing region) and an annulus surface area of the comparably flat cell body perimeter: 10,400 ± 2,700 μm^2 (n = 50). The total number of receptors per cell was then determined as the product of the probability-weighted number of sites per cell surface area and the average cell surface area. All images were acquired using a closed loop piezoscanner (Agilent Technologies); we have confirmed through silicon calibration grids that the image area does not translate appreciably over the timescales considered here.

The calculated number of total receptors per cell was compared to previously published results[35,36,62]. For the calculation of number of biotin to block the streptavidin in the ligand-receptor model, k_{off} and k_{on} estimated from functional force imaging were compared with previously published data [54,56-59,68]. Dark regions in MAC mode images had diameters ranging 42 ± 6.2 nm (n = 20), as compared with previously published

data [62]. The temperature controller and the temperature-controlled heating stage (Agilent Technologies) on which fixed cells were mounted was used to change and control temperature during the AFM imaging of cell surfaces. As it is known that two additional binding sites of streptavidin to biotin after the conjugation to biotin-BSA are open to incoming biotin, 1.8 binding sites of streptavidin to biotin resulted in the most accurate calculation of kinetic constants, which could be estimated from the fact that molecular weight and size of BSA (66 kDa) and streptavidin (53 kDa) are similar and that a portion of binding sites of streptavidin is shielded by steric hindrance between streptavidin and BSA.

2.5 CONCLUSION

This chapter demonstrated a force-based imaging technique, functionalized force imaging using atomic force microscopy (AFM), through which individual receptors can be mapped on cell surfaces with whole cell binding kinetics. The number, distribution, and association / dissociation rate constants of vascular endothelial growth factor receptor-2 (VEGFR2) were quantified with respect to anti-VEGFR2 antibody on both living and fixed human umbilical vein endothelial cells. The direct receptor imaging via functionalized force imaging provided a way to calculate the binding kinetics through blocking experiment, which also confirmed the specificity of ligand-receptor binding, and visualized the non-uniform distribution of VEGFR2 with respect to the underlying cytoskeleton, providing spatiotemporal visualization of cell surface dynamics. The existence of specific receptors on these vascular endothelial cells for a new drug molecule, Loop 6, was verified via functionalized force imaging using Loop 6-functionalized AFM cantilevers, followed by the identification of Loop 6 receptors, with blocking experiments with antibody against a potential receptor for Loop 6. In addition, a quantification method was developed to calculate the thermodynamic parameters of ligand-receptor pairs including biotin-streptavidin and VEGFR2-anti-VEGFR2 pairs using the temperature-controlled AFM approach, together with functionalized force imaging. Functionalized force imaging and kinetic models introduced in this chapter have the potential for the characterization of other biological binding pairs such as antigen-antibody pairs and DNA/DNA pairs, with modification of conjugation chemistry that was introduced in this chapter.

REFERENCES

1. Lee S, Mandic, J., and Van Vliet, K. J. Chemomechanical mapping of ligand - receptor binding kinetics on cells. Proceedings of the National Academy of Sciences of the United States of America 2007;104:9609–9614.
2. Lauffenburger DA, and Linderman, J. J. Receptors: Models for Binding, Trafficking, and Signaling: Oxford University Press; 1993.
3. Rotsch C, and Radmacher, M. Drug-induced changes of cytoskeletal structure and mechanics in fibroblasts: an atomic force microscopy study. Biophysical Journal 2000;78:520-535.
4. Kamba T, Tam, B. Y. Y., Hashizume, H., Haskell, A., Sennino, B., Mancuso, M. R., Norberg, S. M., O'Brien, S. M., Davis, R. B., Gowen, L. C., Anderson, K. D., Thurston, G., Joho, S., Springer, M. L., Kuo, K. J., and McDonald, D. M. VEGF-dependent plasticity of fenestrated capillaries in the normal adult microvasculature. Am J Physiol Heart Circ Physiol 2006;290:H560-576.
5. Vyas YM, Maniar, H., Lyddane, C. E., Sadelain, M. & Dupont, B. Ligand binding to inhibitory killer cell Ig-like receptors induce colocalization with Src homology domain 2-containing protein tyrosine phosphatase 1 and interruption of ongoing activation signals. The Journal of Immunology 2004;173:1571-1578.
6. Avalos AM, Arthur, W. T., Schneider, P., Quest, A. F. G., Burridge, K., and Leyton, L. Aggregation of integrins and RhoA activation are required for Thy-1-induced morphological changes in astrocytes. Journal of Biological Chemistry 2004;279:39139-39145.
7. Browning-Kelley ME, Wadu-Mesthrige, K., Hari, V., and Liu, G.Y. Atomic Force Microscopic Study of Specific Antigen/Antibody Binding. Langmuir 1997;13:343-350.
8. Li L, Chen, S., Oh, S., Jiang, S. In situ single-molecule detection of antibody-antigen binding by tapping-mode atomic force microscopy. Analytical Chemistry 2002;74:6017-6022.
9. Merkel R, Nassoy P, Leung A, Ritchie K, Evans E. Energy landscapes of receptor - ligand bonds explored with dynamic force spectroscopy. Nature 1999;397:50-53.
10. Moy VT, Florin, E.L., Gaub, H.E. Intermolecular forces and energies between ligands and receptors. Science 1994;266:257-259.
11. Schwesinger F, Ros, R., Strunz, T., Anselmetti, D., Guntherodt, H.-J., Honegger, A., Jermutus, L., Tiefenauer, L., and Pluckthun, A. Unbinding forces of single antibody-antigen complexes correlate with their thermal dissociation rates.

Proceedings of the National Academy of Sciences of the United States of America 2000;97:9972-9977.

12. Stroh C, Wang, H., Bash, R., Ashcroft, B., Nelson, J., Gruber, H., Lohr, D., Lindsay, S.M., and Hinterdorfer, P. Single-molecule recognition imaging microscopy. Proceedings of the National Academy of Sciences of the United States of America 2004;101:12503-12507.
13. Dupres V, Monozzi, F.D., Locht, C., Clare, B.H., Abbott, N.L., Cuenot, S., Bampard, C., Raze, D., Duprene, Y.F. Nanoscale mapping and functional analysis of individual adhesions on living bacteria. Nature Methods 2005;2:515-520.
14. Gad M, Itoh, A., and Ikai, A. Mapping cell wall polysaccharides of living microbial cells using atomic force microscopy. Cell Biology International 1997;21:697-706.
15. Horton M, Charras, G., and Lehenkari, P. Analysis of ligand-receptor interactions in cells by atomic force microscopy. Journal of Receptors and Signal Transduction 2002;22: 169-190.
16. Nonaka M, Doi, T., Fujiyoshi, Y., Takemoto-Kimura, S. & Bito. Essential contribution of the ligand-binding beta B/beta C loop of PDZ1 and PDZ2 in the regulation of postsynaptic clustering, scaffolding, and localization of postsynaptic density-95. Journal of Neuroscience 2006;26:763-774.
17. Lehenkari PP, and Horton, M.A. Single Integrin Molecule Adhesion Forces in Intact Cells Measured by Atomic Force Microscopy. Biochemical and Biophysical Research Communications 1999;259:645-650.
18. Madl J, Rhode, S., Stangl, H., Stockinger, H., Hinterdorfer, P., Schutz, G. J., Kada, G. A combined optical and atomic force microscope for living cell investigations. Ultramicroscopy 2006;106:645-651.
19. Puntheeranurak T, Wildling, L., Gruber, H. J., Kinne, R. K. H., and Hinterdorfer, P. . Ligands on the string: single-molecule AFM studies on the interaction of antibodies and substrates with the Na+-glucose co-transporter SGLT1 in living cells. Journal of Cell Science 2006;119:2960-2967.
20. Olsson A-K, Dimberg, A., Kreuger, J. & Claesson-Welsh, L. VEGF receptor signalling - in control of vascular function. Nature Reviews | Molecular Cell Biology 2006;7:359-371.
21. Izumi Y, di Tomaso, E., Hooper, A., Huang, P., Huber, J., Hicklin, D. J., Fukumura, D., Jain, R. K., and Suit, H. D. Responses to Antiangiogenesis

Treatment of Spontaneous Autochthonous Tumors and Their Isografts. Cancer Research 2003;63:747-751.

22. Posadas E, Davidson, B. & Kohn, E. Proteomics and Ovarian Cancer: Implications for Diagnosis and Treatment: A critical review of the recent literature. Current Opinion in Oncology 2004;6:478-484.

23. Rakhmilevich A, Hooper, A., Hicklin, D. & Sondel, P. Treatment of experimental breast cancer using interleukin-12 gene therapy combined with anti-vascular endothelial growth factor receptor-2 antibody. Molecular Cancer Therapeutics 2004;3:969-976.

24. Almqvist N, Bhatia, R., Primbs, G., Desai, N., Banerjee, S., and Lal, R. Elasticity and adhesion force mapping reveals real-time clustering of growth factor receptors and associated changes in cellular rheological properties. Biophysical Journal 2004;86:1753-1762.

25. Thomson NH, Fritz, M., Radmacher, M., Cleveland, J. P., Schmidt, C. F., and Hansma, P. K. Protein tracking and detection of protein motion using atomic force microscopy. Biophysical Journal 1996;70:2421-2431.

26. Charras G, Horton, M. . Single Cell Mechanotransduction and Its Modulation Analyzed by Atomic Force Microscope Indentation. Biophysical Journal 2002;82:2970-2981.

27. Ikai A, Afrin, R., Itoh, A., Thogersen, H. C., Hayashi, Y., Osada, T. Force measurements for membrane protein manipulation. . Colloids and Surfaces B-Biointerfaces 2002;23:165-171.

28. Pfister G, Stroh, C. M., Perschinka, H., Kind, M., Knoflach, M., Hinterdorfer, P., and Wick, G. Detection of HSP60 on the membrane surface of stressed human endothelial cells by atomic force and confocal microscopy. Journal of Cell Science 2005;118:1587-1594.

29. Baumgartner W, Hinterdorfer, P., Ness, W., Raab, A., Vestweber, D., Schindler, H., and Drenckhahn, D. Cadherin interaction probed by atomic force microscopy. Proceedings of the National Academy of Sciences of the United States of America 2000;97(8):4005-4010.

30. Kienberger F, Ebner, A., Gruber, H. J. & Hinterdorfer, P. Molecular recognition imaging and force spectroscopy of single biomolecules. Accounts of Chemical Research 2006;39:29-36.

31. Green RJ, Davies, J., Davies, M. C., Roberts, C. J. & Tendler, S. J. . Surface plasmon resonance for real time in situ analysis of protein adsorption to polymer surfaces. Biomaterials 1997;18:405-413.

32. Van Vliet K, and Hinterdorfer, P. Probing drug-cell interactions. Nano Today 2006;1:18-25.
33. Saxton MJ. Anomalous Subdiffusion in Fluorescence Photobleaching Recovery: A Monte Carlo Study. Biophysical Journal 2001;81: 2226-2240.
34. Hinterdorfer P, and Dufrene, Y. F. Detection and localization of single molecular recognition events using atomic force microscopy. Nature Methods 2006;3:347-355.
35. Waltenberger J, Claesson-Welsh, L., Siegbahnll, A., Shibuya, M. & Heldin, C.-H. Receptors for Vascular Endothelial Growth Factor. Journal of Biological Chemistry 1994;269:26988-26995.
36. Scheidegger P, Weiglhofer, W., Suarez, S., Console, S., Waltenberger, J., Pepper, M. S., Jaussi, R., and Ballmer-Hofer, K. Signalling properties of an HIV-encoded angiogenic peptide mimicking vascular endothelial growth factor activity. Biochemical Journal 2001;353:569-578.
37. Baumgartner W, Hinterdorfer, P. & Schindler, H. . Data analysis of interaction forces measured with the atomic force microscope. Ultramicroscopy 2000;82:85-95.
38. Bell GI. Models for the specific adhesion of cells to cells. Science 1978;200(12):618-627.
39. Dill K, Lin, M., Poteras, C., Fraser, C., Hafeman, D.G., Owicki, J.C., Olson, J.D. Antibody-Antigen Binding Constants Determined in Solution-Phase with the Threshold Membrane-Capture System: Binding Constants for Antifluorescein, Anti-Saxitoxin, and Anti-Ricin Antibodies. Analytical Biochemistry 1994;217:128-138.
40. Hinterdorfer P, Baumgartner, W., Gruber, H. J., Schilcher, K., and Schindler, H. Detection and localization of individual antibody-antigen recognition events by atomic force microscopy. Proceedings of the National Academy of Sciences of the United States of America 1996;93:3477-3481.
41. Lu D, Jimenez, Z., Zhang, H., Bohlen, P., Witte, L., and Zhu, Z. Selection of high affinity human neutralizing antibodies to VEGFR2 from a large antibody phage display library for antiangiogenesis therapy. International Journal of Cancer 2002;97:393-399.
42. Murase K, Fujiwara, T., Umemura, Y., Suzuki, K., Iino, R., Yamashita, H., Saito, M., Murakoshi, H., Ritchie, K., and Kusumi, A. . Ultrafine Membrane Compartments for Molecular Diffusion as Revealed by Single Molecule Techniques. Biophysical Journal 2004;86:4075-4093.

43. Ritchie K, Shan X.-Y., Kondo, J., Iwasawa, K., Fujiwara, T., and Kusumi, A. . Detection of Non-Brownian Diffusion in the Cell Membrane in Single Molecule Tracking. Biophysical Journal 2005;88:2266-2277.
44. Sako Y, and Kusumi, A. Barriers for lateral diffusion of transferrin receptor in the plasma membrane as characterized by receptor dragging by laser tweezers: fence versus tether. Journal of Cell Biology 1995;129:1559-1574.
45. Sheetz MP. Glycoprotein motility and dynamic domains in fluid plasma membranes. Annu Rev Biophys Biomol Struct 1993;22:417-431.
46. Choquet D, Felsenfeld, D. P., Sheetz, M. P. Extracellular Matrix Rigidity Causes Strengthening of Integrin–Cytoskeleton Linkages. Cell 1997;88:39–48.
47. Veikkola T, Karkkainen, M., Claesson-Welsh, L., and Alitalo, K. Regulation of Angiogenesis via Vascular Endothelial Growth Factor Receptors. Cancer Research 2000;60:203-212.
48. Cleveland JP, Manne, S., Bocek, D. & Hansma, P. K. A Nondestructive Method for Determining the Spring Constant of Cantilevers for Scanning Force Microscopy. Rev Sci Instrum 1993;64:403-405.
49. Lee S, Fernandez, C. A., Moses, M. A., and Van Vliet, K. J. Chemomechanical mapping of loop 6 receptors on cells. Submitted 2009.
50. Fernandez CA, Butterfield, C., Jackson, G., and Moses, M.A. Structural and Functional Uncoupling of the Enzymatic and Angiogenic Inhibitory Activities of Tissue Inhibitor of Metalloproteinase-2 (TIMP-2). The Journal of Biological Chemistry 2003;278:40989-40995.
51. Chen A, and Moy, V.T. Single molecule force measurements. Methods in Cell Biology 2000;68:301-309.
52. Lee S, and Van Vliet, K. J. Binding and activation energy measurement on cells via single molecule recognition imaging. Submitted 2009.
53. Clark M, Guarnieri, F., Shkurko, I., and Wiseman, J. Grand Canonical Monte Carlo Simulation of Ligand-Protein Binding. Journal of Chemical Information and Modeling 2006;46:231-242.
54. Chilkoti A, Boland, T., Ratner, B.D., and Stayton, P.S. The Relationship Between Ligand-Binding Thermodynamics and Protein-Ligand Interaction Forces Measured by Atomic Force Microscopy. Biophysical Journal 1995;69:2125-2130.
55. Davis-Harrison RL, Armstrong, K. M., and Baker, B. M. Two Different T Cell Receptors use Different Thermodynamic Strategies to Recognize the Same Peptide/MHC Ligand. Journal of Molecular Biology 2005;346:533-550.

56. Chilkoti A, and Stayton, P.S. Molecular Origins of the Slow Streptavidin-Biotin Dissociation Kinetics. Journal of American Chemical Society 1995;117:10622-10628.

57. Chu V, Freitag, S., Trong, I.L., Stenkamp, R.E., Stayton, P.S. Thermodynamic and structural consequences of flexible loop deletion by circular permutation in the streptavidin-biotin system. Protein Science 1998;7:848-859.

58. Freitag S, Chu, V., Chu, V.. Penzotti, J.E., Klumb, L.A., To, R., Hyre, D., Trong, I.L., Lybrand, T.P., Stenkamp, R.E., and Stayton, P.S. A structural snapshot of an intermediate on the streptavidin - biotin dissociation pathway. Proceedings of the National Academy of Sciences of the United States of America 1999;96:8384–8389.

59. Klumb LA, Chu, V., and Stayton, P. S. Energetic roles of hydrogen bonds at the ureido oxygen binding pocket in the streptavidin-biotin complex. Biochemistry 1998;26:7657-7663.

60. Merkel R, Nassoy, P., Leung, A., Ritchie, K., and Evans, E. Energy landscapes of receptor - ligand bonds explored with dynamic force spectroscopy. Nature 1999;397:50-53.

61. Chtcheglova LA, Waschke, J., Wildling, L., Drenckhahn, D., and Hinterdorfer, P. Nano-Scale Dynamic Recognition Imaging on Vascular Endothelial Cells. Biophysical Journal 2007;93:L11-L13.

62. Lee S, Mandic, J, and Van Vliet, K.J. Chemomechanical mapping of ligand–receptor binding kinetics on cells. Proc Natl Acad Sci USA 2007;104:9609–9614.

63. Gabhann FM, Popel, A.S. Model of competitive binding of vascular endothelial growth factor and placental growth factor to VEGF receptors on endothelial cells. Am J Physiol Heart Circ Physiol 2003;286:H153–H164.

64. Van Vliet KJ, Bao, G., Suresh, S. The biomechanics toolbox: experimental approaches for living cells and biomolecules. Acta Materialia 2003;51:5881-5905.

65. Ding Z, Fong, R.B., Long, C.J., Stayton, P.S., and Hoffman, A.S. Size-dependent control of the binding of biotinylated proteins to streptavidin using a polymer shield. Nature 2001;411:59-62.

66. Yuan C, Chen, A., Kolb, P., and Moy, V.T. Energy Landscape of Streptavidin-Biotin Complexes Measured by Atomic Force Microscopy. Biochemistry 2000;39:10219-10223.

67. Dixit SB, and Chipot, C. Can Absolute Free Energies of Association Be Estimated from Molecular Mechanical Simulations? The Biotin-Streptavidin System Revisited. Journal of Physical Chemistry A 2001;105:9795-9799.
68. Weber PC, Wendoloski, J.J., Pantoliano, M.W., and Salemmet, F.R. Crystallographic and Thermodynamic Comparison of Natural and Synthetic Ligands Bound to Streptavidin. Journal of American Chemical Society 1992;114:3197-3200.
69. Cliff MJ, Williams, M.A., Brooke-Smith, J., Barford, D., and Ladbury, J.E. Molecular Recognition via Coupled Folding and Binding in a TPR Domain. Journal of Molecular Biology 2005;346:717–732.
70. Spolar RS, Record Jr, M. T. . Coupling of local folding to site-specific binding of proteins to DNA. Science 1994 263:777-784.
71. Maehle A-H, Prüll, C.-R., and Halliwell, R. F. The emergence of the drug receptor theory. Nature Reviews Drug Discovery 2002;1:637-641.
72. Reid RC, Prausnitz, J. M., Poling, B. E. The Properties of Gases & Liquids: McGraw-Hill; 1988.
73. Stroh C, Wang, H., Bash, R., Ashcroft, B., Nelson, J., Gruber, H., Lohr, D., Lindsay, S. M., and Hinterdorfer, P. Single-molecule recognition imaging microscopy. Proceedings of the National Academy of Sciences of the United States of America 2004;101(34):12503-12507.

Chapter 3

Actin-mediated force exertion: Microvascular pericyte-dependent substrata deformation

Parts of the following study were submitted for publication in 2009 with co-authors Maciej Kotecki, Adam Zeiger, and Ira M. Herman[1].

3.1 INTRODUCTION

Perivascular cells such as pericytes (PC) and vascular smooth muscle cells (SMC) are mural cells that surround capillaries and post-capillary venules[3]. As a growing scientific literature indicates, pericytes play key roles in microvascular physiology and pathophysiology, including regulating microvascular remodeling, maturation, and stabilization during angiogenesis (growth of new blood vessels) and lymphangiogenesis[5,6]. Unlike SMCs, however, pericytes are actually embedded within the basement membrane, an extracellular matrix comprised of proteins such as fibronectin and collagen, which they help to co-create in direct association with the capillary- and venular-derived endothelial cells. However, both pericytes and SMCs of arterioles, veins and arteries establish intimate cell-cell contacts that serve to coordinate vascular tonus and differentiation during development, adult life, and progession of vascular disease[5,6]. Recently, it has been demonstrated that pericyte-endothelial cell interactions play a critical role in physiologic and pathologic angiogenesis [5,10,11]. However, these researchers have focused primarily on the chemical interactions between endothelial cells and pericytes, including (i) the roles that basement membrane protein components play in modulating microvascular cell growth and contractile

phenotype, or (ii) the regulatory roles that survival agents and growth factors play in signaling adaptive responses in cell-matrix associations via the serine/threonine and tyrosine kinase-dependent signaling pathways that modulate endothelial cell cycle kinetics, cell growth or proliferative phenotype. Further, it has been shown that endothelial-pericyte interactions at gap junctions regulate microvascular dynamics during developmental or disease-associated phenomena[6]. However, despite this recent and deepened understanding of the biochemical signal transduction regulating such varied phenomena as growth factor-receptor interactions, matrix adhesion, or electrochemical ion signaling via gap junctions[5,6,14,15], little is known regarding the regulatory role of mechanotransduction or mechanical interactions between pericytes and endothelial cells.

Recently a report by Sun et al.[16], one of few reports on mechanical responses of perivascular cells[17-19], demonstrated that SMCs responded to extracellular mechanical stimuli. These researchers used extracellular matrix (ECM) ligand-conjugated spherical AFM probes (specifically, collagen). These results strongly support the idea that pericytes and SMCs are chemomechanically active cells and that mechanotransduction may play an important role in pericyte (SMC)-endothelial interactions as well as angiogenesis. Mechanotransduction in pericyte and SMC systems, however, has not yet been considered to be a major contributive factor in the regulatory roles of perivascular cells.

Mechanical contact between pericytes and endothelial cells has been implied by an analysis of the cytoskeleton-dependent signaling pathways that are controlled and reciprocally regulate the physical or chemical interconnections that exist amongst the actin network, plasma membrane and the associating extracellular matrix[6,20,21]. Each cell

is in communication with its microenvironment, transducing signals via basement membrane contacts, focal adhesions, or cell-cell associations[22]. For example, focal adhesion-associated integrins bind to ECM ligands, such as collagen or fibronectin, and signal via membrane kinases, and cytoskeletal-associated effectors. ECM-bound and integrin-associated plasma membrane domains that ligate crosslinked actin filament arrays to the plasma membrane. Downstream, Rho GTP-dependent pathways[6] exert their influence on the actin-mediated mechanical force transduction by a multitude of effectors that incude actomyosin- and actin-associated phosphoprotein kinases. Through these downstream effectors, mechanical forces are generated or de-stabilized, perhaps through actin filament-specific (de)polymerization, or via the inhibition of actomyosin-based contraction[23-25]. Therefore, integrins physically connect intracellular actin stress fibers with extracellular matrix and transmit actin-mediated forces to the extracellular environment. Integrin involvement in mechanotransduction has been studied in SMCs[16,26] and pericytes[20,21]. For example, Kutcher et al.[6], using compliant silicone rubber substrata (poly(dimethyl siloxane), or PDMS), showed that silicone rubber wrinkled as a result of the attachment force transmitted from the actin cytoskeleton via integrins experess on pericytes.

Here, we demonstrate that actin filament assembly processes, including filament (de)polymerization and actomyosin-based contraction play critical roles in regulating pericyte shape, contractility, cell-substrate attachment, force generation, and substrate deformation. As evidenced by the dynamic deformation of PDMS substrata[6], creation of wrinkles on ECM ligand-coated substrata implies that mechanotransduction is crucial to pericyte adhesion to and contraction of underlying substrata. AFM-based imaging of living pericyte behavior, including contraction of deformable substrata, demonstrate the

regulatory role of the actin cytoskeleton: actin filaments and actomyosin contractions play in generation of mechanical forces required for cells to sustain their shape, control motility and sustain contractile phenotype. Further, using pharmacological inhibitors of the actin cytoskeleton: latrunculin A, blebbistatin, ML-7, nocodazole, and jasplakinolide, we have dissected the relative contributory roles of actin dynamics and actin-myosin interactions in regulating pericyte-deformation of PDMS substrata, including the local cell stiffness as measured by AFM-enabled indentation. These results indicate that the actin cytoskeleton is a critical cellular integrator required to sustain pericyte morphology and membrane tension. Further, quantification of this strain on the PDMS substrata suggests that pericyte-generated traction significantly exceeds that exerted by other cell types. In turn, we ascertain that these mechanical forces can be sufficient to reciprocally modify the effective mechanical stiffness of underlying substrata. These findings point to an important and previously unrecognized role for mechanical force transduction in regulating cell-matrix and microvascular cell-cell dynamics during physiologic or pathologic angiogenesis.

3.2 RESULTS

Local elastic moduli of pericyte surfaces were measured through the AFM-enabled nanoindentation (see Materials and Methods). Pericytes were grown on collagen-conjugated PDMS (Fig. 3.1A), and AFM probes of radius R = 25 nm were placed at specific positions, such as pericyte plasma membranes positioned over regions of substrata deformation, e.g., over PDMS domains where force deformation is sufficient to generate visible wrinkles. In contrast, AFM probes can also be placed upon plasma membrane domains where cell-derived mechanical forces are incapable of creating

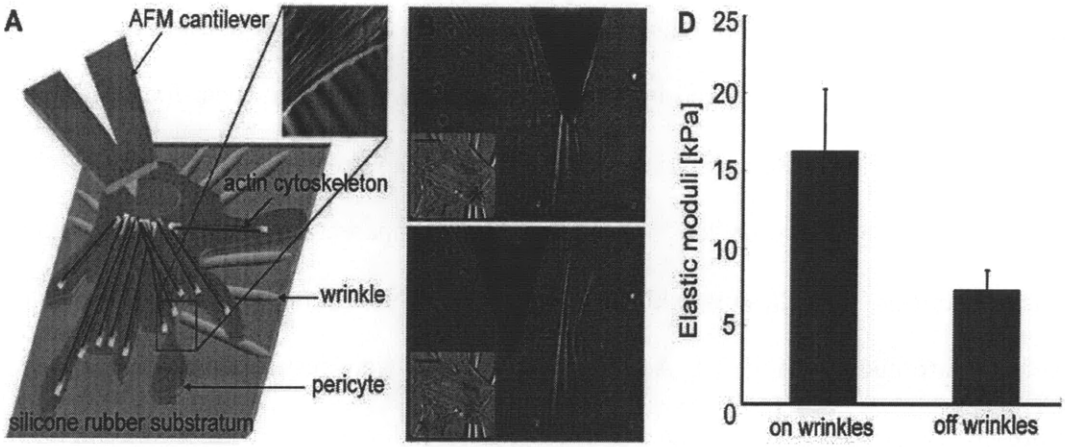

Figure 3.1 Schematic of AFM-enabled imaging and cellular mechanical analyses. Pericytes are grown on silicone rubber (see Materials and Methods for substrata preparation). (A) Cellular mechanics are detected as a quantifiable deflection of the cantilevered probe, while mechanical contacts within AFM imaging mode and mechanical analyses are aided by optical microscopy-incorporated AFM. Using the closed loop scanner, the cantilevered probe is placed at specific positions of interest as shown in (B) and (C). (B) and (C) optical microscopy images show mechanical tests at pericyte membranes on and off the substrata wrinkles, respectively. Inset images in (B) and (C) are AFM deflection images, and blue asterisks (*) represent specific points at which mechanical tests are conducted at current positions of AFM cantilevered probes in optical images. (D) summarizes the cell elastic moduli on (16.3 kPa) and off (7.4 kPa) these wrinkles, measured as schematized in (A). Scale bar = 20 μm.

wrinkles within the PDMS substrata (Fig. 3.1). To increase the efficiency of the positioning of AFM probes on specific regions of the cells, live pericytes were first imaged in AFM contact mode. Using a closed loop piezo scanner, the positions of AFM probes on pericyte membranes were chosen to enable the measurement of local elastic moduli at positions both on and off the "wrinkles" generated by the cell contraction of the PDMS substrata (Figs. 3.1 – 3.3). See Materials and Methods for detailed information about AFM imaging and measurement. Figure 3.1B and C illustrates the integrated optical microscopy and AFM imaging of pericytes. We hypothesized that the pericytes generated wrinkles on the PDMS substrata via actin-mediated force exertion due to mechanisms such as actin (de)polymerization and actomyosin contraction. Thus, we reasoned that the pericytes would exhibit greater stiffness near the wrinkles, likely

due to the force transduction transferred from bundled actin arrays that are crosslinked to membrane domains anchored in the extracellular matrix via integrin-focal adhesion protein assemblies. The effective elastic moduli (E) of the pericyte membranes measured directly above or "on" wrinkles, near the apparent origin of these wrinkles, and far from or "off" these wrinkles were measured through optical microscopy-aided AFM as introduced in Fig. 3.1. As indentation depths were restricted to < 25 nm, E is representative of the microdomain stiffness of the cell's cortical actin and cytoplasm. Mechanical tests with AFM (Figs. 3.1A, 3.2, and 3.3) showed that the effective (average) elastic moduli at off-wrinkle locations of the pericytes were 45.4 % less than that at on-wrinkle positions (n = 150, Fig. 3.1D and Table 3.2). Here, pericytes that changed the number of wrinkles, attachment to substrata, or cell morphology during the course of such mechanical tests were excluded in analyses. To consider the possibility that this increased E of the cell on locations of PDMS wrinkles could be due to an increase in the effective mechanical stiffness of wrinkled PDMS itself, elastic moduli of wrinkled and unwrinkled PDMS were measured at locations outside the cell perimeter; E_{PDMS} on and off such wrinkles were not statistically significantly different (n = 4, $p < 0.05$).

We hypothesized that PDMS substrata deformation by pericytes and the change in the elastic moduli of local pericyte membrane microdomains were attributable to the organization and contraction of the actin cytoskeleton: internally generated mechanical forces are transduced across the plasma membrane to the underlying substrata via filmanet assembly/disassembly, membrane-associated crosslinking, and, possibly, actomyosin-based contraction. As reported by Shlomovitz et al.[27], these actin-based forces are closely coupled. As has also been reported, integrin receptors can physically

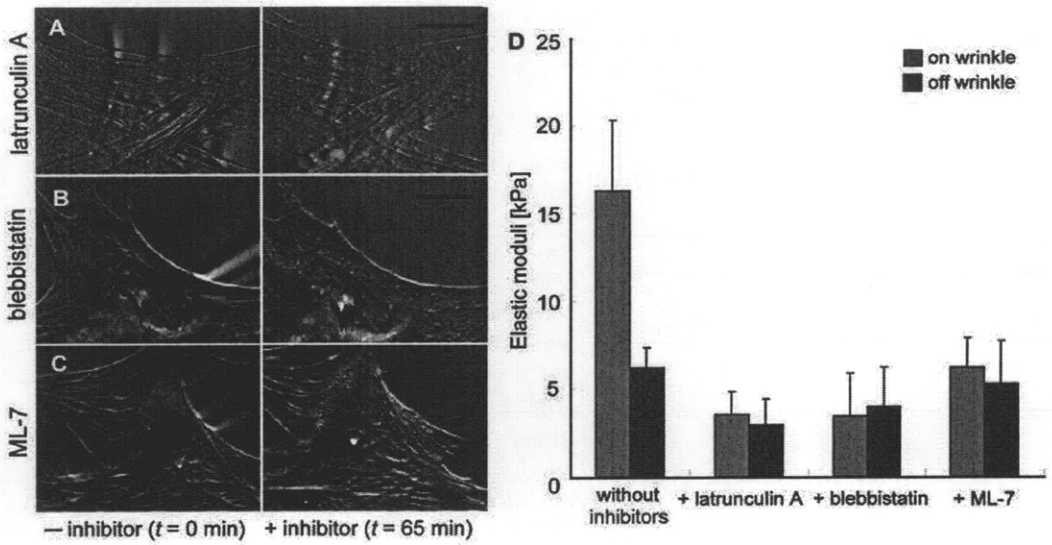

Figure 3.2 Actin-dependent alterations in pericyte shape, contractile phenotype and elastic moduli. In (A), (B), and (C), AFM deflection images demonstrate changes in pericyte shape. Concomitantly, cell shape and PDMS deformation, either before or 65 min after the addition of pharmacological inhibitors specifically impact actin (de)polymerization and/or actomyosin contraction: (A), latrunculin A (1 μM); (B), blebbistatin (25 μM); (C), ML-7 (300 nM), respectively (see Table 3.1). (D) demonstrates the elastic moduli of pericyte membranes, as schematized in Fig. 1 (see Materials and Methods for elastic moduli measurement), before and after inhibitors, at pericyte membranes on and off deformed (wrinkled) PDMS substrate domains. Table 3.2 summarizes elastic moduli with inhibitors. Scale bars = 20 μm. All the mechanical tests were conducted with more than five cells (n = 5) and 30 mechanical tests at each point.

link ECM ligands and the actin cytoskeleton, generating mechanical forces that are apparently sufficient to deform PDMS substrata to create wrinkles. To verify this hypothesis, we measured the stiffness of pericyte microdomains before and after actin-disrupting pharmacological inhibitors: latrunculin A, blebbistatin, and ML-7, as well as pharmacological agents capable of reversibly regulating actin polymerization and actomyosin contraction, nocodazole and jasplakinolide[2,4,7,8] (see Table 3.1). First AFM imaging and subsequent mechanical testing of elastic moduli on pericyte microdomains, was conducted before and after the addition of latrunculin A (1 μM), blebbistatin (25 μM), and ML-7 (300 nM). Reduced force transduction and substrata deformation are

Table 3.1 Pharmacological inhibitors used in this study.

Inhibitors	Binding target	Mechanisms and consequences
Latrunculin A	Monomeric G-actin	Binds to actin monomers, making 1:1 complexes with monomers. This thus inhibits actin polymerization and disruption of the actin cytoskeleton[2].
Blebbistatin	Myosin ATPase	Binds to myosin ATPase and thus blocks force exertion by actomyosin contraction. Cellular consequence is that microtubules dominate over the actin cytoskeleton in maintentance of cell morphology and force generation in contrast to the effects from nocodazole[4].
ML-7	Myosin light chain kinase	Binds to myosin light chain kinase, thus blocks the force generation of actomyosin contraction, inhibiting myosin light chain phosphorylation. Therefor, ML-7 acts as a competitive inhibitor against ATP for actomyosin contraction[7,8].
Nocodazole	β-tubulin	Binds to β-tubulin and thus blocks microtubule assembly, disrupting microtubule dynamics during interphase and inhibits spindle formation during mitosis. Cellular consequences include inhibition of karyokinesis during M-phase while altering the actin-dependent contribution to cell morphology and force generation during interphase by disrupting cellular balance between actin and microtubule networks[4,9].
Jasplakinolide	Actin filament (F-actin)	Binds to actin filaments, inducing large F-actin aggregates. Cellular consequences include the enhancement of the rate of actin polymerization, stabilizing actin filaments *in vitro*[12,13].

Table 3.2 Elastic moduli of pericyte microdomains with pharmacological inhibitors.

Elastic modulus [kPa]	no inhibitors	latrunculin A	blebbistatin	ML-7	nocodazole	jasplakinolide
on wrinkles	16.3 ± 3.9	3.5 ± 1.3	3.5 ± 2.4	6.3 ± 1.6	16.8 ± 6.9	18.1 ± 6.4
off wrinkles	6.3 ± 1.1	2.9 ± 1.5	4.0 ± 2.2	5.3 ± 2.4	7.2 ± 2.8	7.4 ± 3.1

observable in the decreased number of wrinkles that pericytes generate due to the inhibition effect of these agents, as shown in Fig. 3.2; in the absence of actin-specific agents, however, the number of wrinkles did not decrease over time. This confirms that the force with which pericytes held underlying substrata decreased, and eventually the force generated via the actin network and cytoskeleton (latrunculin A) and actomyosin

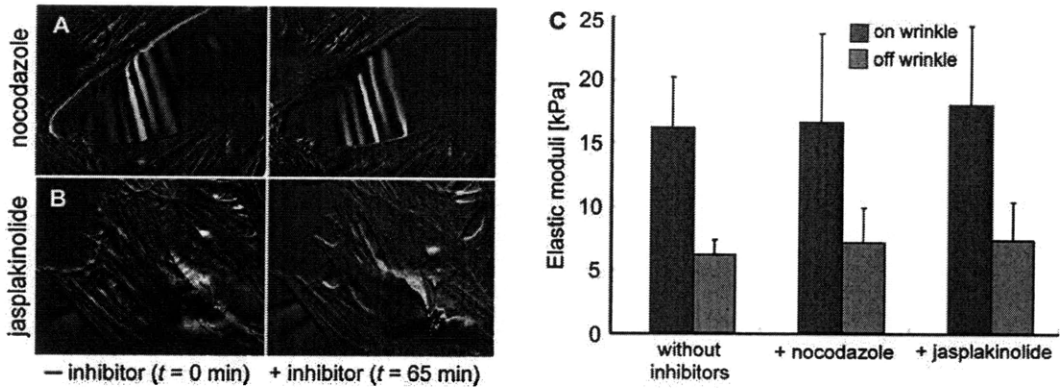

Figure 3.3 Change in elastic moduli and cell shape with addition of cytoskeletal-specific agents. The same set of experiments as shown in Fig. 2 was conducted with pharmacological reagents that increase the activity of the actin cyskeleton: nodozale (670 nM) (A) and jasplakinolide (670 nM) (B): see Table 1. (C) Mechanical tests were conducted before and after addition of these reagents at cell membranes on and off PDMS wrinkles. See Table for summary of elastic moduli with nocodazole and jasplakinolide. All the mechanical tests were conducted with more than five cells (N = 5) and 30 mechanical tests (n = 30) on and off wrinkles. Scale bars = 20 μm.

contraction (blebbistatin and ML-7) also decreased. Correspondingly, the elastic moduli of the pericyte microdomains both on- and off-wrinkles due to the pharmacological inhibitors (see Table 3.2 for summary of elastic moduli ± inhibitors). This effect on the local stiffness of pericytes was caused by the reduced membrane tension due to decreased density (by 25%) and thickness (by 13%) of actin stress fibers, as quantified by AFM contact-mode height images of these cells. At 65 minutes after the addition of latrunculin A, blebbistatin, and ML-7 at room temperature, elastic moduli on-wrinkles and off-wrinkles were not statistically different, which indicates the dominant effect of the actin cytoskeleton on the local stiffness of the pericyte surface. Fluorescent images of phalloidin-stained F-actin within the pericytes (Fig. 3.4) after the addition of latrunculin A, blebbistatin, and ML-7 reveal cytoskeletal reorganization as the cell cortex blebs and peripheral membrane domains are observed to bulge into irregular, rounded membrane structures. Comparisons among the different actin inhibitors show

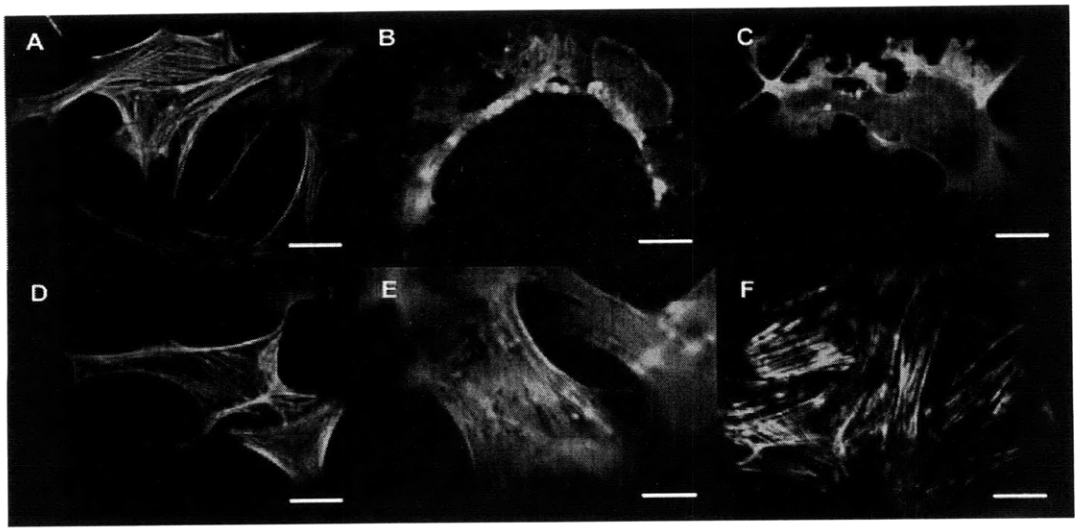

Figure 3.4 Fluorescent images of actin-stained pericytes with pharmacological inhibitors. Fixed pericytes were stained with Alexa 488 phalloidin at 37°C: (A), untreated pericytes; (B), those treated with latrunculin A (1 μM); (C), blebbistatin (25 μM); (D), ML-7 (300 nM); (E), nocodazole (670 nM); and (F), jasplakinolide (670 nM). Scale bars = 20 μm.

that the actin stress fibers still remained visible after treatment with ML-7 (300 nM, 1h) and latrunculin A (1 μM, 1h), while pericyte morphology and the number of actin stress fibers changed dramatically with blebbistatin, both of which indicate the loss/decrease of actin-mediated intracellular force.

When inhibitors were washed out via replacement with fresh media, pericytes recovered these substrata wrinkles within 45 min at 37°C (data not shown). Pericytes that were not treated with pharmacological inhibitors did not lose wrinkles, and local membrane stiffnesses did not change over this same imaging duration, showing distinct actin stress fibers in fluorescent images of actin-stained pericytes (Fig. 3.4).

Nocodazole (670 nM) and jasplakinolide (670 nM) were next considered as indirect, positive modulators of actomyosin contraction. Nocodazole, which binds to microtubule monomers (β-tubulin) and inhibits the microtubule polymerization, is a pharmacological inhibitor that indirectly activates the actin cytoskeleton by binding to

microtubule, while jasplakinolide triggers the nucleation and polymerization of the actin cytoskeleton (see Table 3.1). We hypothesized that both nocodazole and jasplakinolide might enhance the ability of pericytes to generate mechanical forces sufficient for substrate deformation- and alter local elastic moduli because our results from latrunculin A, blebbistatin, and ML-7 demonstrated the critical contribution of the actin cytoskeleton in the creation of wrinkles on substrata. Pericytes were imaged in AFM contact mode, followed by the mechanical measurements of elastic moduli of pericyte microdomains on- and off-wrinkles, before and 65 min after the addition of these inhibitors. These local elastic moduli showing wrinkles either increased or remained unchanged in response to nocodazole and jasplakinolide (See Table 3.2 for summary of elastic moduli with inhibitors). Fluorescent images with actin-stained pericytes after incubation with nocodazole demonstrated that the thickness of actin stress fibers increased with decreased spacing between actin stress fibers (Fig. 3.4), whereas jasplakinolide-treated pericytes showed brighter, thickened actin-concentrated patches on stress fibers. Statistically similar or increased elastic moduli with nocodazole and jasplakinolide (Fig. 3.3C and Table 3.1) were consistent with the finding that the number of pericyte-generating wrinkles increased or did not change under optical microscopy and AFM imaging. Together, these results show that the mechanism under which pericytes generate wrinkles on the PDMS substrata was directly related to the force-generating potential of actin cytoskeletal dynamics.

When live pericytes are imaged via AFM, the topography of the wrinkled PDMS substrata can also quantified simultaneously. Such topographical information provided by height images as shown in Fig. 3.5 is important for the estimate of strain exerted by pericytes. We computed the average strain indicated by each wrinkle as the

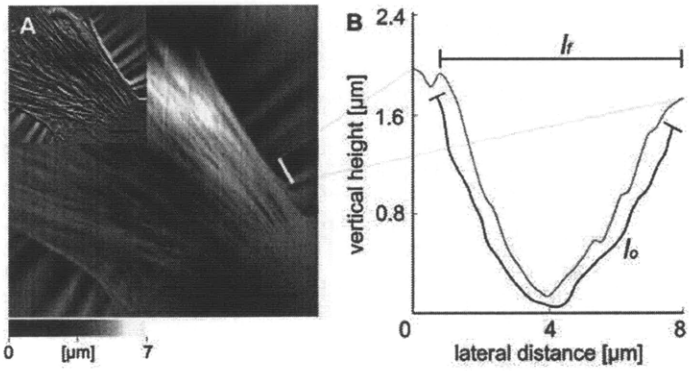

Figure 3.5 Calculation of strain exerted by pericyte and PDMS elastic moduli. (A) is a topographic AFM image, and an inset image is a deflection image associated with the topography image obtained in AFM contact mode. From height information provided by topography images, PDMS strain exerted by pericytes can be calculated as shown in (B). (B) is a height trace of a white line in (A). For the calculation of strain ε, l_f of substrata and the original length (l_o) of a green trace were measured from an AFM height image, from which nominal engineering strain was measured (see Materials and Methods). Over 30 wrinkles (n = 30) were considered for the strain calculation, and the range of PDMS strain that pericytes exerted ranged from 1.3 – 38 % (average 16 ± 12 %). Scale bars = 20 μm.

change in contour length Δl of each wrinkled region $\Delta l / l_o$, where l_o is the unwrinkled substrata span (see Materials and Methods). This analysis indicated that pericytes exerted strains of 16 ± 12 %, with a range from 1.3 – 38 %.

3.3 DISCUSSION

Microvascular pericytes are mural cells that modulate capillary tonus and endothelial growth potential, events that are critical to physiologic and pathological angiogenic phenomena during human development and vascular disease states. AFM-based mechanical testing enabled the quantification of microvascular pericyte bio-mechanical force transduction, including effective stiffness of cell microdomains and near and far from regions of substrata wrinkling. Quantitative analysis of pericyte-generated force transduction and substrate deformation were directly interrogated by the addition of cytoskeletal-specific pharmacological disrupting agents/inhibitors. F-actin-mediated

dependence o substrata deformation was observable via changes in cell shape and membrane stiffness, which corresponded to F-actin (de)polymerization and/or inhibition of actomyosin ATPase-mediated contraction.

In our model, pericytes are capable of generating sufficient force to underlying PDMS substrata, inducing wrinkles on collagen-coated PDMS substrata as shown in Fig. 3.1. We hypothesized that these wrinkles were generated by mechanical forces via the actin cytoskeleton: actin (de)polymerization and actomyosin contraction. To verify this hypothesis, we tested elastic moduli of pericyte membranes over PDMS wrinkles and off wrinkles. As summarized in Table 3.1, local elastic moduli of pericyte membranes off wrinkles were 45 % lower than those on wrinkles, which implied that the creation of wrinkles on PDMS substrata was mediated by stiff actin bundles and actin-related force exertion such as filament assembly/disassembly and actomyosin contraction. The pharmacological inhibitors, including latrunculin A, blebbistatin, and ML-7, triggered the loss of wrinkles as visualized through optical microscopy and AFM contact mode imaging. Mechanical measurements on pericyte microdomain showed a decrease in local elastic moduli after the addition of these inhibitors, implying that the actin cytoskeleton maintains the membrane stiffness of cells. These results were supported by fluorescent images that showed the resulting changes in cell morphology and the density of the actin cytoskeleton. In contrast, nocodazole and jasplakinolide, which indirectly and directly *activate* the actin cytoskeleton, respectively, increased or retained the membrane stiffness. This result was consistent with AFM and optical images showing that the number of wrinkles created on PDMS substrata were also maintained or increased for these pharmacological challenges. With mechanical tests, optical / fluorescence microscopy and AFM imaging, we demonstrated that the actin

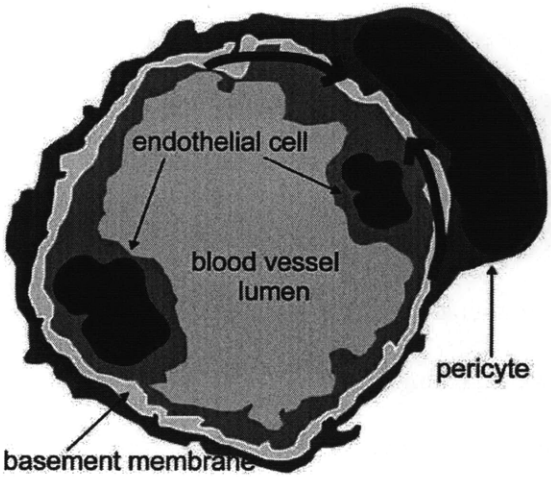

Figure 3.6 Schematic of pericyte force exertion to the basement membrane and endothelial cell. This figure represents a cross section of a capillary blood vessel. The cell surrounding the vessel is pericyte, and endothelial cell makes a lining of the capillary blood vessel. The basement membrane plays a role as a substratum between pericyte and endothelial cell. Pericytes generate contractile force (blue arrows) against the basement membrane and may modify the mechanical properties of the underlying basement membrane or substratum (e.g., silicone rubber in this paper), which affects the microenvironment of endothelial cells.

cytoskeleton plays a critical role in maintaining cell morphology, attachment to, and contraction of underlying substrata.

Note that nocodazole, which inhibits microbule polymerization, increased and maintained the membrane stiffness, indirectly activating and thickening the actin cytoskeleton (Fig. 3.3); blebbistatin and ML-7, which bind to myosin II, changed cell morphology dramatically (Fig. 3.4). This may be caused by the disturbed balance between the actin cytoskeleton and microtubules, a balance regulated by myosin II as reported by Even-Ram et al.[4], where one dominates over the other when either is inhibited.

Many researchers have suggested that pericytes play critical roles in (anti)angiogenesis[5,6,10,11]. Specifically, most research results have been focused on the communication between pericytes and endothelial cells via biochemical factors such as ligand-receptor interactions. However, we have shown that pericytes can also change the effective mechanical properties of an underlying substratum, here PDMS, by exerting actin-mediated forces (Fig. 3.5). It is known that the morphology, adhesion, and certain functions of vascular endothelial cells can be altered by the mechanical

stiffness of extracellular materials[28-30]. Thus, we suggest that the pericytes' potential modification of an underlying substrata's mechanical properties may influence morphological changes of endothelial cells and eventually angiogenesis: pericytes' contraction may change the effective stiffness of underlying substrata (*in vitro*) or basement membranes (*in vivo*) that both pericytes and endothelial cells contact, and this exposes endothelial cells to modified mechanical environment (see Fig. 3.6). Reinhart-King et al.[28] recently reported that endothelial cells can detect and respond to mechanical stimuli created by neighboring cells. Our observation, together with Reinhart-King et al.'s and Kutcher et al.'s results for endothelial cells[6,28] strongly suggest the mechanical and chemical coupling between pericytes and endothelial cells (Fig. 3.6). As Thompson et al.[30] have reported, mechanical properties of underlying substrata impact the adhesion of endothelial cells. Other researchers [29] observed the change in morphology of endothelial cells under different mechanical stimuli, potentially affecting angiogenesis. From our current results, pericytes can exert strains on PDMS substrata ranging from 1.3 – 38 %. If we assume a reasonable estimate of the elastic moduli of crosslinked silicone (E ~ 0.5 – 1 MPa), we can estimate the pericyte-generated stresses ($\sigma = E \cdot \varepsilon$) of 31 kPa – 1.22 MPa. This range of pericyte-exerted stresses is up to one order of magnitude larger than the stress generated by other cell types, such as fibroblasts [31] and endothelial cells[32]. Note that endothelial cells also generate stress against the underlying substrata[32] but that endothelial cell-exerted stress is smaller than that exhibited by pericytes. This may mean that, although these two cell types mechanically influence one another, the larger stresses exerted by pericytes may be sufficient to strain the basement membrane within the nonlinear elastic regime and thus significantly modify the endothelial cells' micromechanical environment. Even if

the pericyte contraction is insufficient to alter the effective extracellular matrix stiffness, the larger stresses exerted by the pericytes against the basement membrane may still indirectly strain the adjacent endothelial cells.

As reported previously[5,10], endothelium and capillary blood vessels that are not surrounded by pericytes or smooth muscle cells results in an increased degree of neovascularization and angiogenesis. The adhesion of endothelial cells to the basement membrane should be reduced for neovascularization or angiogenesis to occur. From the report by Thompson et al.[30], endothelial cells adhere more efficiently to stiffer substrata, and our results demonstrate the substrata stiffening by pericytes. Therefore, pericytes may alter the adhesion of endothelial cells to the basement membrane or underlying substrata, and thus inhibit neovascularization and angiogenesis that accompany morphological changes of endothelial cells on substrata. In this respect, we posit that pericyte-endothelial cell interaction and, furthermore, angiogenesis and neovascularization, would be affected not only by chemical factors such as ligand-receptor interactions but also through the pericytes' exertion of mechanical forces that are communicated to nearby endothelial cells and that potentially modify the effective stiffness of the underlying substrata.

3.4 MATERIALS AND METHODS

3.4.1 Cell culture

Pericytes were cultured from capillary fragments isolated from mammalian or human retinas as previously described[33-36]. Briefly, capillary fragments were isolated by collagenase digestion of minced retinas followed by sieving.The capillary fragments were plated into tissue culture flasks in Dulbecco's modified Eagle's medium (DMEM)

supplemented with 10% calf serum. The pericytes were identified and distinguished from endothelial cells by their larger size and irregular morphology, by their noncontact-inhibited growth patterns, by their staining with anti-3G5 IgG, anti-smooth muscle actin IgG and the lack of staining with di-I-acyl-LDL and antisera to bovine Factor VIII, criteria established by our laboratories and subsequently used by others to identify capillary pericytes[33-36].

3.4.2 Analysis of pericyte contractile phenotype: deformable silicone substrata

Deformable silicone substrata were essentially prepared as described previously[6,37]. In essence, 20-50 μL of poly(dimethyl siloxane) (PDMS, Sigma-Aldrich) was pipetted using a positive displacement pipettor onto 35-mm round glass coverslips. The PDMS substratum was permitted to spread at room temperature prior to cross-linking by passing the coverslip with PDMS attached through a Bunsen burner flame. The PDMS-coated coverslip was then placed within a glow discharge apparatus[6,38], which is comprised of an anode, a cathode for generating a glow discharge between the cathode and the anode upon application of a negative pulse, and a triggering electrode for starting the glow discharge. As this has been successful for creating hydrophilic surfaces, e.g., Formvar-coated electron microscope grids coated with carbon, the glow discharge apparatus places an electrically discharged plasma onto the surface of the silicone, which enhances its hydrophilic properties, permits coating with extracellular matrix proteins, e.g., collagen in Tris-HCl buffer, pH 7.4, and then attachment of pericytes.

3.4.3 Measurement of elastic moduli and AFM contact mode imaging

Atomic force microscopy (AFM, Agilent Technology) was incorporated within optical microscope (IX 81, Olympus) to enable facile positioning of AFM cantilevered probes above pericyte plasma membranes (See Figs. 3.1 – 3.3). Calibration of AFM cantilevers of nominal spring constant k = 0.01 nN/nm and probe radius R = 25 nm (Veeco) was conducted as described previously[30,39,40]. Briefly, inverse optical lever sensitivity [nm/V] (InvOLS) was measured from deflection-displacement curves recorded on rigid glass substrates. Spring constants [nN/nm] of AFM cantilevers were measured via thermal activation recording of deflection and the Fourier Transform (FFT) of cantilever amplitude as a function of oscillation frequency fitted with simple harmonic oscillation function. For each measurement of elastic moduli, at least 30 replicate indentations were acquired to maximum depths of 10 nm. Acquired probe deflection-displacement responses were converted offline (Scanning Probe Imaging Processor, Image Metrology), using measured spring constants and InvOLS, to force-depth responses. Elastic moduli E were calculated by applying a modified Hertzian model of spherical contact to the loading segment of the force-depth response, as detailed elsewhere[30,41] with the scientific computing software Igor Pro (Wavemetrics). Computed elastic moduli E are reported as average +/- standard deviation, and all statistical analyses were conducted with one-way ANOVA (Tukey analysis). Before AFM contact mode imaging and elastic moduli measurement, x- and y-axes hystereses in the closed loop scanner were calibrated to improve the positioning of AFM cantilevered probes on pericyte membranes and PDMS substrata. The force that AFM cantilevers exerted on pericyte membranes during contact mode imaging did not exceed 500 pN to minimize the effect of mechanical contact between pericytes and AFM cantilevers. Pericytes that changed morphology or attachment on PDMS substrata due to the AFM imaging and mechanical

tests were excluded for further experiments.

3.4.4 Measurement of PDMS strain

Length and height information on PDMS substrata was provided from topography images obtained in AFM contact mode. Because topography images provide length and height information simultaneously, nominal uniaxial engineering strain was calculated from the following formulae: ε = (final length – original length of PDMS span) / original length = $\Delta l / l_o$, with the assumption that the length of unwrinkled PDMS (l_o) is flat (see purple line in Fig. 3.6). More than thirty images comprising wrinkles were analyzed for this strain calculation (n = 30).

3.4.5 Fluorescence microscopy imaging – actin staining

For staining of F-actin, pericytes were fixed with 4% formaldehyde for 15 min at room temperature, followed by membrane permeation with 0.1% Triton-X solution in 1X PBS for three min. Pericytes were then incubated with Alexa Fluor 488 phalloidin (green, Invitrogen, 1/300 concentration) for one hour at room temperature. Pericytes were rinsed three times (5 min each) with 1X PBS, and actin-stained pericytes were ready for fluorescence microscopy imaging (IX-81, Olympus).

3. 5 CHAPTER SUMMARY AND CONCLUSION

Pericytes physically surround the capillary endothelium, contacting and communicating with associating endothelial cells via cell- and matrix-bound contacts. This intimate interaction among pericytes, endothelial cells and the extracelluar matrix microenvironment has stimulated great scientific interest, especially in studies focused

on the protein kinase-dependent signaling that modulate cell-cell and cell-matrix interactions during physiologic or pathologic angiogenesis. This study may significantly extend these findings by demonstrating that micromechanical signal transduction and mechanical coupling to the extracellular matrix control cell shape and contractility. By means of an atomic force microscope (AFM)-based mechanical test, we quantified the F-actin- and actomyosin-based dependence of microvascular pericyte membrane stiffness. Quantitative analysis of pericyte- and contractile protein-generated force transduction and substrata deformation was directly interrogated by the addition of cytoskeletal-specific pharmacological disrupting agents/inhibitors that were capable of reversibly regulating the generation of substrata attachment forces and plasma membrane stiffness. F-actin-mediated dependence was observable via changes in cell shape and membrane stiffness, which corresponded to F-actin (de)polymerization and/or inhibition of actomyosin ATPase-mediated contraction. Furthermore, the stress-strain response and topographical profile of underlying deformable substrata provided quantitative estimates of pericyte-exerted stresses and strains. Together, these data demonstrated that pericytes' actin-mediated forces can modify the effective mechanical properties (i.e., elastic moduli increases of 150%). It is possible that the modified mechanical properties of the substrata, through such pericyte-generated forces, are likely to affect cell-matrix and cell-cell associations in vivo. In this way, pericytes and endothelial cells could directly influence both physiologic and pathologic angiogenesis.

REFERENCES

1. Lee S, Kotecki, M., Zeiger, A., Van Vliet, K. J., and Herman, I. M. Actin-mediated force exertion: Microvascular pericyte-dependent substrate deformation. Submitted 2009.
2. Ayscough KR, Stryker, J., Pokala, N., Sanders, M., Crews, P., and Drubin, D. G. High Rates of Actin Filament Turnover in Budding Yeast and Roles for Actin in Establishment and Maintenance of Cell Polarity Revealed Using the Actin Inhibitor Latrunculin-A. Journal of Cell Biology 1997;137:399-416.
3. Bergers G, and Song, S. The role of pericytes in blood-vessel formation and maintenance. Neuro-Oncology 2005;7:452-464.
4. Even-Ram S, Doyle, A.D., Conti, M.A., Matsumoto, K., Adelstein, R.S., and Yamada, K.M. Myosin IIA regulates cell motility and actomyosin–microtubule crosstalk. Nat Cell Biol 2007;9:299-309.
5. Adams RH, and Alitalo, K. Molecular regulation of angiogenesis and lymphangiogenesis. Nature Review Molecular Cell Biology 2007;8:464-478.
6. Kutcher ME, Kolyada, A. Y., Surks, H. K., and Herman, I. M. Pericyte Rho GTPase Mediates Both Pericyte Contractile Phenotype and Capillary Endothelial Growth State. The American Journal of Pathology 2007;171:693-701.
7. Rosenthala R, Choritzb, L., Schlottb, S., Bechrakisa, N. E., Jaroszewskic, J., Wiederholtb, M., and Thieme, H. Effects of ML-7 and Y-27632 on carbachol- and endothelin-1-induced contraction of bovine trabecular meshwork. Experimental Eye Research 2005;80:837-845
8. Saitoh M, Ishikawa, T., Matsushima, S., Naka, M., and Hidaka, H. Selective

inhibition of catalytic activity of smooth muscle myosin light chain kinase. Journal of Biological Chemistry 1987;262:7796-7801.

9. Vasquez RJ, Howell, B., Yvon, A.M., Wadsworth, P., and Cassimeris, L. Nanomolar concentrations of nocodazole alter microtubule dynamic instability in vivo and in vitro. Mol Biol Cell 1997;8:973–985.

10. Armulik A, Abramsson, A., and Betsholtz, C. Endothelial/Pericyte Interactions. Circulation Research 2005;97:512-523.

11. Papetti M, and Herman, I. M. Mechanisms of normal and tumor-derived angiogenesis. Am J Physiol Cell Physiol 2002;282:C947–C970.

12. Bubb MR, Spector, I., Beyer, B. B., and Fosen, K. M. Effects of Jasplakinolide on the Kinetics of Actin Polymerization. The Journal of Biological Chemistry 2000;275:5163–5170.

13. Lázaro-Diéguez F, Aguado, C., Mato, E., Sánchez-Ruíz, Y., Esteban, I., Alberch, J., Knecht, E., and Egea, G. Dynamics of an F-actin aggresome generated by the actin-stabilizing toxin jasplakinolide. Journal of Cell Science 2008;121:1415-1425.

14. Bondjers C, Kalén, M., Hellström, M., Scheidl, S. J., Abramsson, A., Renner, O., Lindahl, P., Cho, H., Kehrl, J., Betsholtz, C. Transcription profiling of PDGF-B deficient embryos identifies RGS5 as a novel marker for pericytes and vascular smooth muscle cells. Am J Pathol 2003;162:721–729.

15. Gerhardt H, and Betsholtz, C. Endothelial-pericyte interactions in angiogenesis. Cell Tissue Res 2003;314:15-23.

16. Sun Z, Martinez-Lemus, L. A., Hill, M. A., and Meininger, G. A. Extracellular matrix-specific focal adhesions in vascular smooth muscle produce mechanically

active adhesion sites. Am J Physiol Cell Physiol 2008;295:268-278.

17. Davis MJ, and Hill, M. A. Signaling mechanisms underlying the vascular myogenic response. Physiol Rev 1999;79:387-423.

18. Davis MJ, Wu, X., Nurkiewicz, T. R., Kawasaki, J., Davis G. E., Hill, M. A., Meininger, G. A. Integrins and mechanotransduction of the vascular myogenic response. Am J Physiol Heart Circ Physiol 2001;280:H1427-H1433.

19. Falcone JC, Davis, M. J., Meininger, G. A. Endothelial independence of myogenic response in isolated skeletal muscle arterioles. Am J Physiol Heart Circ Physiol 1991;260:H130-H135.

20. Garmy-Susini B, Jin, H., Zhu, Y., Sung, R. J., Hwang, R., Varner, J. Integrin alpha4beta1-VCAM-1-mediated adhesion between endothelial and mural cells is required for blood vessel maturation. The Journal of clinical investigation 2005;115:1542-1551.

21. Graziolia A, Alvesb, C. S., Konstantopoulosb, K., and Yang, J. T. Defective blood vessel development and pericyte/pvSMC distribution in α4 integrin-deficient mouse embryos. Developmental Biology 2006;293:165-177

22. Galbraith CG, Yamada, K.M., and Sheetz, M.P. The relationship between force and focal complex development. The Journal of Cell Biology 2002;159:695–705.

23. Mogilner A, and Oster, G. Force Generation by Actin Polymerization II: The Elastic Ratchet and Tethered Filaments. Biophys J 2003;84:1591–1605.

24. Takagi Y, Homsher, E.E., Goldman, Y.E., and Shuman, H. Force Generation in Single Conventional Actomyosin Complexes under High Dynamic Load. Biophysical Journal 2006;90:1295–1307.

25. Zhua J, and Carlsson, A. E. Growth of attached actin Filaments. Eur Phys J E

2006;21:209-222.

26. Goldschmidt ME, McLeod, K. J., and Taylor, W. R. Integrin-mediated mechanotransduction in vascular smooth muscle cells: frequency and force response characteristics. Circ Res 2001;88:674-680.

27. Shlomovitz R, and Gov, N. S. Membrane Waves Driven by Actin and Myosin. Phys Rev Letts 2007;98:168103.

28. Reinhart-King CA, Dembo, M., and Hammer, D. A. Cell-cell mechanical communication through compliant substrates. Biophysical Journal 2008.

29. Shukla A, Dunn, A. R., Moses, M. A., and Van Vliet, K. J. Endothelial cells as mechanical transducers: Enzymatic activity and network formation under cyclic strain. Mechanics and Chemistry of Biosystems 2004;1:279-290.

30. Thompson MT, Berg, M. C., Tobias, I. S., Rubner, M. F., and Van Vliet, K. J. Tuning compliance of polyelectrolyte multilayers to modulate cell adhesion. Biomaterials 2005;26:6836-6845.

31. Sabass B, Gardel, M. L., Waterman, C. M., and Schwarz, U. S. High Resolution Traction Force Microscopy Based on Experimental and Computational Advances. biophysical Journal 2008;94:207–220.

32. Shiu Y-T, Li, S., Marganski, W. A., Usami, S., Schwartz, M. A., Wang, Y.-L., Dembo, M., and Chien, Shu. Rho Mediates the Shear-Enhancement of Endothelial Cell Migration and Traction Force Generation. Biophysical Journal 2004;86:2558–2565.

33. Helmbold P, Nayak, R. C., Marsch, W. C., Herman, I. M. Isolation and in vitro characterization of human dermal microvascular pericytes. Microvasc Res 2001;61:160-165.

34. Herman IM, D'Amore, P. A. Microvascular pericytes contain muscle and nonmuscle actins. Journal of Cell Biology 1985;101:43-52.

35. Nayak RC, and Herman, I. M. . Microvascular Pericytes: Isolation, Propagation and Identification. Totowa, New Jersey: The Humana Press Inc; 2001. 247-264 p.

36. Newcomb PM, Herman, I. M. Pericyte growth and contractile phenotype: modulation by endothelial-synthesized matrix and comparison with aortic smooth muscle. J Cell Physiol 1993;155:385-393.

37. Harris AK, Wild, P., Stopak, D. . Silicone rubber substrata: a new wrinkle in the study of cell locomotion. Science 1980;208:177–179.

38. Aebi U, and Pollard, T.D. . A glow discharge unit to render electron microscope grids and other surfaces hydrophilic. J. Electron Microscopic Technique 1987;7:29-33.

39. Butt HJ, and Jaschke, M. Calculation of thermal noise in atomic force microscopy. Nanotechnology 1995;6:1-7.

40. Hutter JL, and Bechhoefer, J. Calibration of atomic- force microscope tips. Rev Sci Instrum 1993;64:1868-1873.

41. Thompson MT, Berg, M. C., Tobias, I. S., Lichter, J. A., Rubner, M. F., Van Vliet, K. J. Biochemical functionalization of polymeric cell substrata can alter mechanical compliance. Biomacromolecules 2006;7:1990-1995.

Chapter 4

Direct measurement of pN-scale cytoskeletal force dynamics at individual focal complexes on intact cells

Parts of the following study were submitted for publication in 2009 with co-authors Dessislava Nikova and Ira M. Herman[1].

4.1 INTRODUCTION

Adherent cells exert force at macromolecular adhesion complexes, which comprise extracellular matrix (ECM) ligands, transmembrane integrin receptors, intracellular adaptor proteins, and actin cytoskeletal filaments. Reversible binding between integrin receptors and ligands in ECM proteins such as fibronectin (FN) contributes to the dynamic assembly of these adhesion complexes at the cell-material interface, defining and modulating the connection between the ECM and actin cytoskeleton[4]. This concentrated association among adhesion complex components facilitates transmission of cell-generated mechanical force to the ECM, which can reciprocally regulate cell-matrix interactions and enable processes such as cell adhesion to and migration through extracellular matrices[4,5].

Mechanical forces transmitted via μm-scale adhesion or adhesion complexes (ACs)[7] are attributed to cytoskeletal actin dynamics, including F-actin assembly processes and/or actomyosin-based contractile events[9,10]. The nanoNewton (nN)-scale forces generated at whole ACs have been observed through several methods including micromachined devices[11] and microarray-based mechanosensors[12]. Other researchers have reported picoNewton (pN)-scale force generated by individual myosin motor

proteins and actin monomer assembly[10,13]. However, these disparate force scales have not yet been bridged experimentally to relate the magnitude of cytoskeletal force transmitted through the integrin-ECM ligand pairs that comprise a adhesion complex. Time scales of actin-mediated force generation and associated membrane displacements have also been considered: Sheetz et al. reported cell force generated at ACs with minute-scale-resolution via specialized, micromachined devices[11], and later reported ms-scale membrane ruffling dynamics using differential interference contrast microscopy[14]. However, to our knowledge, existing methods have not enabled the real-time measurement of nN-scale, intracellularly generated force that is transmitted at ACs over several-minutes duration with ms-scale temporal resolution. Experimental approaches that elucidate the biophysical roles of these force dynamics, connecting the force- and time- scales relevant to macromolecular complexes and individual ligand-receptor pairs, will facilitate better understanding of complex processes that govern cell adhesion and migration.

Here, we demonstrate direct measurement of oscillatory, cytoskeletal forces generated by intact cells via atomic force microscope (AFM)-enabled cell force spectroscopy. This approach enables the measurement of cell-generated force dynamics with pN-scale force resolution and ms-scale temporal resolution. In addition, we use functionalized force imaging (FFI)[15] to visualize individual nanometer-scale molecules and link the nN-scale forces measured at adhesion complexes with the pN-scale forces required to rupture individual FN-integrin pairs. This connects forces measured at the level of ACs with those generated at the level of individual myosin motors (or actin monomer assembly). By separately inhibiting major sources of dynamic force generation (actin de/polymerization and actomyosin contraction), we demonstrate which

molecular mechanisms are involved in the measured intracellular force oscillations in fibroblasts. Finally, we pose a quantitative hypothesis for the rupturing of FN-integrin binding events during cell processes such as fibroblast migration. The demonstrated method for quantification of cell-generated force dynamics can be applied to the study of other ligand-receptor complexes or to further dissect the mechanisms of mechanotransduction for a range of cell types.

4.2 RESULTS

4.2.1 Real time measurement of intracellular force dynamics and localization of FN-conjugated probes on cell surfaces

Nanomechanical profiling of intracellular force spectra was conducted using AFM cantilevered probes that were covalently functionalized with FN, an ECM protein comprising integrin-binding ligands. This approach is related to AFM-enabled molecular force spectroscopy[15,16], but differs notably in that here the cantilever *passively* records force generated by the cell, rather than actively applying force to the cell via feedback-controlled piezoactuation of the AFM cantilever. (For example, Sun et al.[17] have illustrated the mechanical displacement of vascular smooth muscle cells in response to constant tensile forces applied via atomic force microscopy with ECM ligand-conjugated probes, maintaining active feedback against the cell surface.) An integrated optical microscope facilitated positioning of cantilevered probes on NIH 3T3 fibroblast surfaces (Figs. 4.1 and 4.3). The formation of force-generating ACs against FN-functionalized beads at dorsal cell surfaces has been verified previously by other biotechnological tools such as optical traps and magnetic bead twisting rheometry[4,18], and confirmed here via staining for the AC adaptor protein, vinculin (Supplementary

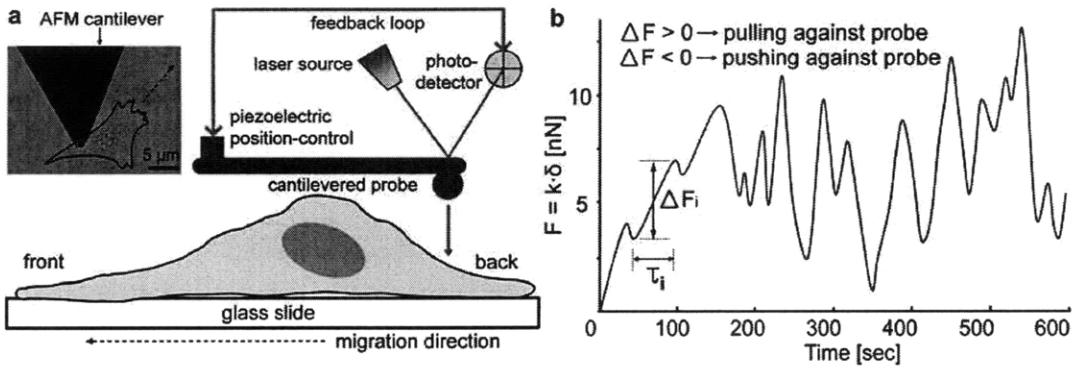

Figure 4.1 Fig. 1. Schematic of AFM-enabled measurement of intracellular force dynamics. (a) Integrated optical microscopy facilitates positioning of spherical probes on specific cell surface regions. FN is conjugated to cantilevered probes, and mechanical contact is achieved via feedback between cantilever deflection (photodiode) and cantilever position (piezoactuator). The feedback loop is then disengaged and subsequent deflection generated via the cell is recorded as in (b); this deflection is converted to force via the cantilever spring constant *k*. ΔF_i is defined as force amplitude between sequential force minima; τ_i, time period of force exertion.

Fig. 4.1). The cytoplasmic domains of transmembrane integrin receptors are physically associated with the actin cytoskeleton through adaptor proteins such as vinculin[19]. Therefore, forces generated by the actin cytoskeleton can be transmitted through integrins to ligands on the cantilevered probes, inducing cantilever deflection. Cantilever deflection, in units of photodiode output [V] in real time *t* was recorded as schematized in Fig. 4.1b, and converted to force *F* [N] (see Materials and Methods); the observed force profiles *F(t)* are considered representative of intracellular force dynamics at adhesion complexes.

The measured cell-induced deflection of FN-functionalized probes exhibited significant nanoNewton- and millisecond-scale oscillations over several minutes of observation (Fig. 4.1b). Through pharmacological alteration of actin polymerization and actomyosin contraction, we confirmed that this oscillating deflection was mediated via actin-dependent intracellularly generated force. As noted, there are two established

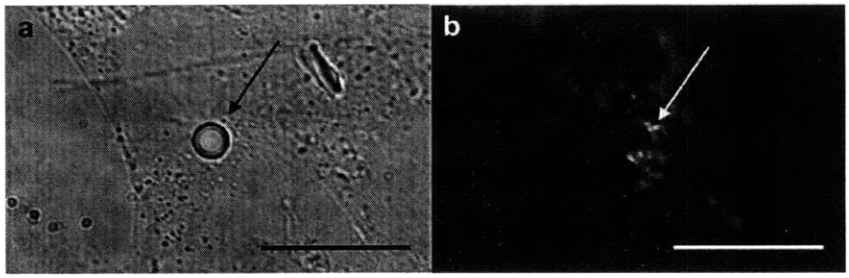

Figure 4.2 NIH 3T3 fibroblast (fixed) under fluorescence microscopy and optical microscopy with a fibronectin-conjugated bead. (a) fibronectin-conjugated bead (2.5 μm in diameter) placed on the fibroblast membrane. The black arrow indicate the fibronectin-conjugated bead. (b) vinculin-stained fluorescent image for same region as the optical image of (a), using anti-vinculin antibody. Vinculin was used as a marker of adhesion complex. (b) demonstrates the creation of vinculin around the fibronectin-conjugated bead and further the formation of adhesion complex. The white arrow shows vinculin near the bead. Scale bars = 10 μm.

sources of cytoskeletally mediated mechanical forces: actin de/polymerization and myosin contraction of actin filaments[2,14,20]. We used pharmacological inhibitors (blebbistatin, nocodazole, and cytochalasin D) to decouple the mechanical linkage, and to determine which molecular components played dominant roles in generating the observed force oscillations. Table 4.1 summarizes the targets and mechanisms of action of these agents.

Optical microscopy-aided AFM cellular force spectroscopy was conducted on specific areas of cell surfaces, before and after the addition of inhibitors as shown in Fig. 4.3 for blebbistatin. Dynamic cell-generated force spectra were acquired on the same cells before and after introduction of all pharmacological inhibitors. The recovery of cell morphology after the addition of fresh media and severe dilution of inhibitors demonstrates that cells were not irreversibly altered or killed by the inhibitors, and that results from real-time force measurement were not artifacts of cell death. Prior to acquisition of cell-generated force spectra, fluorescence microscopy images were obtained to observe changes in cell morphology and in filamentous actin (F-actin)

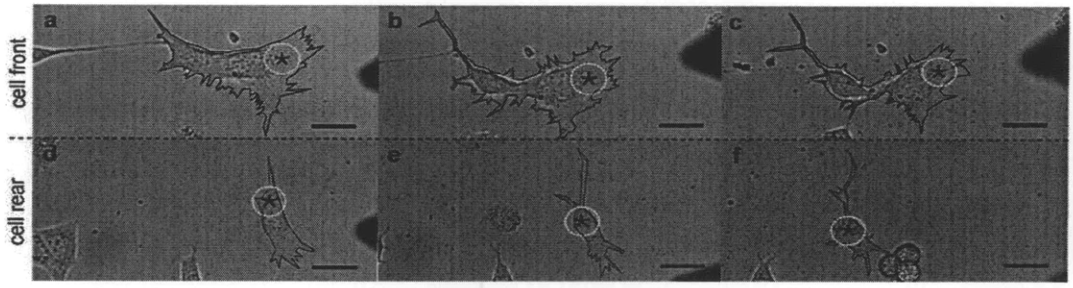

Figure 4.3 Changes in live 3T3 fibroblast morphology with addition of blebbistatin and fresh medium. (a–f) demonstrate changes in live 3T3 fibroblast morphology under optical microscopy during measurement of cytoskeletal dynamics with cantilevered spherical probes, where blue asterisks indicate location of dynamic force spectra collection and dark triangle at right is AFM cantilever withdrawn from contact after data acquisition. (a–c) correspond to experiments for which spectra were acquired at the cell front, whereas (d–f) correspond to spectra acquired at the cell rear before; 1 hr after blebbistatin (room temperature); and after washout with fresh media (1 hr, room temperature), respectively. Probes were intentionally not placed on lamellipodial regions because it was reported that force generated in lamellipodial regions was minimal. Instead, probes were placed on ectoplasmic/lamella regions as shown in (a–c). Scalebars = 20 μm. Recovery upon washout of cytochalasin D and nocodazole was also confirmed; data not shown. See Fig. 4.4 for actin staining with pharmacological inhibitors.

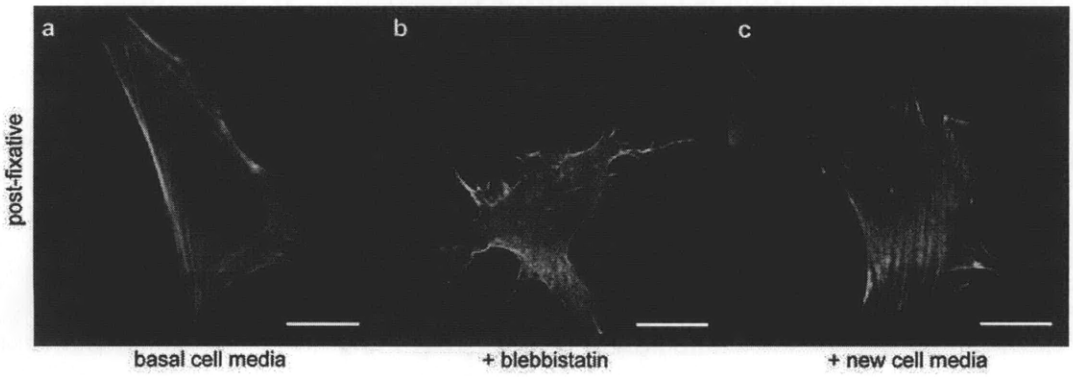

Figure 4.4 Fluorescence images of phalloidin-stained F-actin in 3T3 fibroblasts. (a–c) demonstrate changes in morphology of 3T3 fibroblast under fluorescence microscopy. (a) Fixed cells stained with phalloidin-FITC, before the addition of blebbistatin; (b), at 1 h after the addition of 25 μM of blebbistatin, which inhibits myosin II binding to the actin cytoskeleton (see Table 4.1); Since the balance between microtubules and F-actin was disrupted as the function of myosin II halted by blebbistatin, the cell morphology changed as shown in (b). (c) 3T3 fibroblast after 25 μM of blebbistatin, followed by wash-out of blebbistatin-containing medium and addition of fresh medium. Scale bars = 20 μm.

distribution, as a function of these inhibitors (Fig. 4.4).

4.2.2 Real time measurement of focal complex-level force and time periodicity

Figure 4.5 illustrates force dynamics measured on surfaces of NIH 3T3 fibroblasts with FN-functionalized probes. Fibronectin-conjugated spherical probes were placed at specific positions (see Fig. 4.1 schematic), and the sample stage was translated upward to initiate a contact force of ~550 pN; the piezoactuator force feedback loop was then disengaged, and the probe deflection over time was monitored and converted to force as detailed in Methods. Consistent with previous experiments, we observed that a finite amount of externally applied normal stress (here, 0.6 – 1.3 $nN/\mu m^2$) was required for cells to exert measurable mechanical force against the cantilevered probe. This normal stress applied to cell surfaces was comparable to previously reported traction or shear force (0.8 – 3 $nN/\mu m^2$)[4,21,22] using beads of approximately the same diameter and ligand-functionalization methods. As indicated by arrows in Fig. 4.5a, the cells exhibit a minute-scale periodic oscillations (0.7 – 4.2 min) in nN-scale force generation, which compares well with force magnitudes and periodicity ranges (1.6 – 4.8 min) observed previously for chicken embryo fibroblasts as measured via micromachined devices[11]. However, the temporal resolution of the cell-generated force spectra measured via AFM (200 ms, Fig. 4.5a) significantly exceeds that reported for micromachined devices (1 min)[11]. The high force- and time-resolution of such measurements enabled the detection of additional cyclic forces of second-scale periodicity. Before the addition of pharmacological inhibitors, fibroblasts generated distinct force spectra at the front and rear edges, with characteristic time periods τ_i and magnitudes of force generation ΔF_i summarized in Table 4.2 (see Fig. 4.1b). The magnitude of forces generated at these ACs (3.5 to 22.5 nN) is in good agreement with the force range measured with other

Table 4.1 Pharmacological inhibitors.

Inhibitors	Binding target	Mechanisms and Consequences
Blebbistatin	Myosin II ATPase	Binds to myosin II ATPase and thus blocks force exertion by actin-myosin contraction. Cellular consequence is that microtubules dominate over the actin cytoskeleton in maintentance of cell morphology and force generation in contrast to the effects from nocodazole [2,3].
Nocodazole	β-tubulin	Binds to β-tubulin and thus blocks microtubule assembly, disrupting microtubule dynamics during interphase and inhibits spindle formation during mitosis. Cellular consequences include inhibition of karyokinesis during M-phase while altering the actin-dependent contribution to cell morphology and force generation during interphase by disrupting cellular balance between actin and microtubule networks [2,6].
Cytochalasin D	Actin filament	Binds to the actin filament's fast growing end and thus inhibits assembly and elongation. Cellular rounding occurs as actin-filament dependent processes are disrupted [8].

methods for living cells adhered to FN-functionalized surfaces[11,12,20]. Likewise, the average temporal periods of force generation (6.0 sec and 12.7 sec) compare well with reported rates of mouse embryonic fibroblast leading edge protrusion and retraction (4.6 sec and 19.2 sec)[14]. Our measurements indicated no clear correlation between the temporal periods and force magnitudes (i.e., smaller force peaks ΔF_i were not associated with shorter or longer periods τ_i). To our knowledge, this real-time, dynamic force oscillation in the pN- to nN-scale has not been reported via other technological platforms.

To consider possible intracellular mechanisms underlying these additional

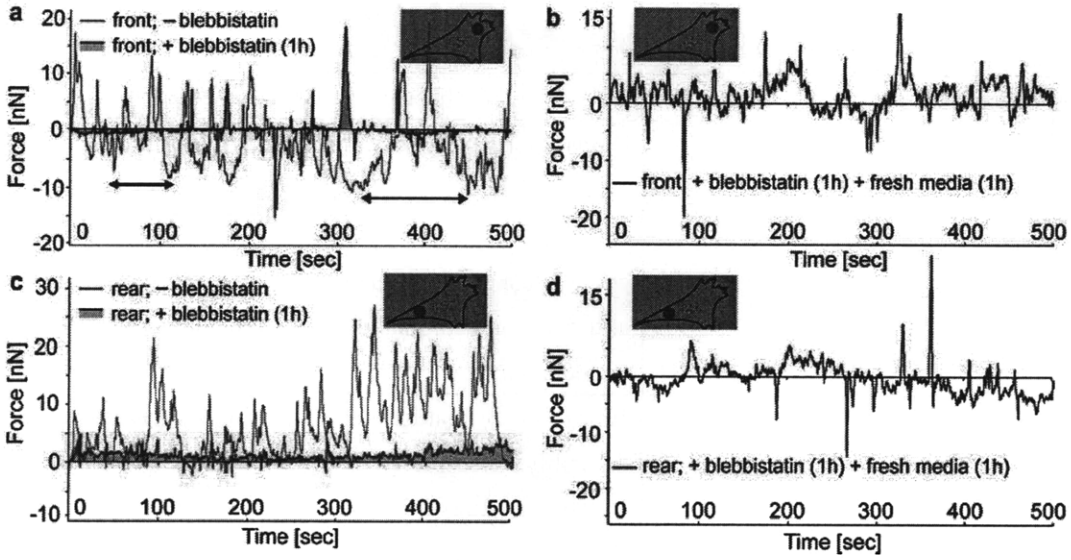

Figure 4.5 Measurement of cell dynamics transmitted through focal complexes. (**a–b**) demonstrate force spectra measured at the front of 3T3 fibroblast by actin cytoskeleton, as measured via AFM cantilevered FN-coated spherical probes. Green, purple, and blue curves represent dynamic force before, 1 hr after the addition of 25 μM blebbistatin, and 1 hr after addition of fresh medium, respectively. (**c**) and (**d**) demonstrate force spectra measured on rear regions of 3T3 fibroblasts. Green, red, and blue curves represent dynamic force before, 1 hr after the addition of 25 μM blebbistatin, and after addition of fresh medium. Arrows in (**a**) represent minute-scale oscillations as refer to a reported result by Galbraith et al. Red circles indicate regions of measurement on 3T3 fibroblast surfaces. As noted in Materials and Methods, force curves in (**a–d**) were shown, corrected for intrinsic drift (≈ 9 pN/sec, n = 30) due to thermal fluctuations.

cyclic forces, we acquired force spectra at the front and rear regions of cell surfaces, and in the presence of pharmacological inhibitors: blebbistatin, nocodazole, and cytochalasin D. Results in Fig. 4.5 are representative examples +/- blebbistatin (25 μM) and after addition of fresh media, and are associated with the optical microscopy images shown in Fig. 4.3. After addition of blebbistatin, an inhibitor of actomyosin contraction, both the minute-scale and second-scale force oscillations were not statistically different from oscillations observed with BSA-functionalized probes. However, intermittent nN-scale forces were still generated near the leading or front regions of cells, despite the presence of blebbistatin (Fig. 4.5). Force dynamics were recovered against FN-

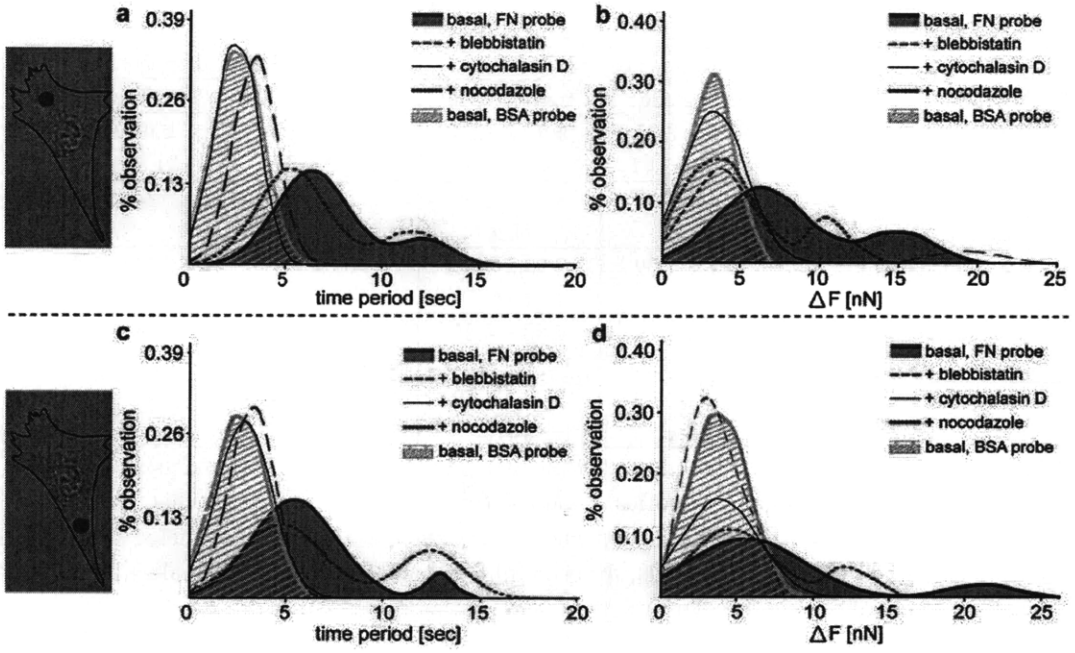

Figure 4.6 Summary of 3T3 fibroblast cell-generated force dynamics in response to pharmacological challenges. (a–b) each include five different spectra, where the blue spectrum consistently represents cell responses for fibronectin-functionalized spherical probes before the addition of pharmacological inhibitors. Cell responses were measured at 1 hr after the addition of blebbistatin (25 μM), cytochalsin D (900 nM), and nocodazole (660 nM) on the same cells, to observe any changes in cell responses. BSA-functionalized probes were used as a control for integrin binding-mediated interactions. (a) time periods of cell-generated forces at cell leading edge; (b) force oscillations at cell leading edges; (c) time periods of cell-generated forces at cell trailing edge; (d) force oscillations at cell trailing edges. Refer to Tables 4.1 and 4.2. Data analyses were conducted with five spectra acquired on each of five cells, for each inhibitor and/or probe functionalization.

functionalized probes, upon dilution of blebbistatin with fresh media, at both the front and rear of the cell. These observations indicate that actomyosin contraction contributed strongly to cell-generated force against the FN-functionalized probes, but that force generation was not wholly eliminated by blebbistatin over these timescales. We next considered cell responses in the presence of cytochalasin D and nocodazole (see Table 4.1). The addition of cytochalasin D, an inhibitor of actin polymerization[23], allowed us to consider the disruption of actin de/polymerization as opposed to actomyosin

Table 4.2 Measured second-scale periodicity of cell-generated forces.

Media (*Probe functionalization*)	Time period (sec)		Force peak (nN)	
	leading edge	trailing edge	leading edge	trailing edge
Basal media (*FN*)	**6.38 ± 2.25** **12.25 ± 2.61**	**5.45 ± 2.03** **13 ± 1.21**	**6.28 ± 1.98** **15.02 ± 2.54**	**6.00 ± 2.47** **21.33 ± 1.45**
+ Blebbistatin (*FN*)	3.26 ± 1.87 N/A	3.57 ± 1.94 N/A	3.92 ± 1.81 **20 ± 2.87**	3.61 ± 1.11 N/A
+ Cytochalasin D (FN)	2.40 ± 1.09 N/A	2.93 ± 1.50 N/A	3.59 ± 2.67 N/A	4.52 ± 2.86 N/A
+ Nocodazole (*FN*)	**5.30 ± 1.79** **11.58 ± 1.65**	**4.88 ± 2.21** **12.94 ± 1.70**	3.89 ± 2.22 **10.28 ± 1.28**	4.69 ± 2.64 **12.57 ± 1.27**
Basal media (*BSA*)	2.68 ± 1.62 N/A	2.33 ± 1.52 N/A	3.67 ± 1.77 N/A	4.42 ± 2.43 N/A

All statistical analyses were conducted with one-way ANOVA (Tukey analysis). Bolded values represent statistically significant values ($p < 0.05$) compared to that for BSA-functionalized probes (See Materials and Methods). Data analyses were conducted with five spectra acquired on each of five cells, for each inhibitor and/or probe functionalization. N/A indicates a lack of second force or time peak.

contraction. The addition of nocodazole, which interferes with microtubule polymerization[6] allowed us to increase the role of the actin cytoskeleton in intracellular force generation, relative to that of microtubules. Results from real-time measurements before and after addition of blebbistatin, nocodazole, and cytochalasin D are summarized in Fig. 4.6 and Table 4.2. As a control for all experiments, bovine serum albumin (BSA)-functionalized probes were also used. Since BSA does not induce the formation of adhesion complexes, the responses detected with BSA-functionalized probes were ostensibly generated by membrane displacement of these living cells or thermal drift of the cantilever deflection signal.

4.2.3 Estimation of pN-scale force transmitted through a single FN/integrin pair

To calculate the force exerted through a single FN-integrin pair, functionalized force imaging (FFI)[15], also known as recognition imaging[16], was performed to identify the spatial distribution of nm-scale FN molecules conjugated to spherical glass borosilicate

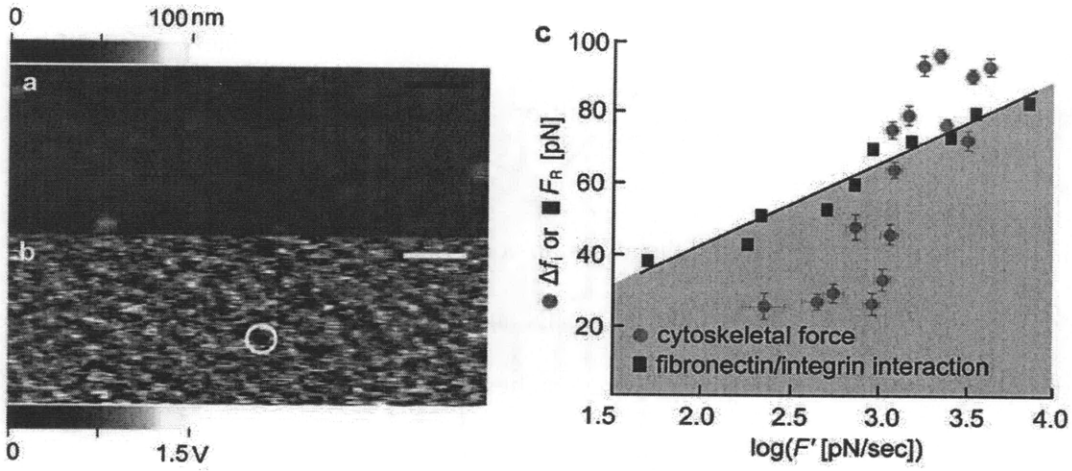

Figure 4.7 Biophysical role of intercellularly generated force through FN-integrin pairs. (**a–b**) are representative areas of FN-conjugated substrata including glass slides and spherical probe surfaces via mapping of FN conjugated on glass substratum with an anti-FN-functionalized cantilever through FFI. (**a**) is a topography image, which provides height information of substrata; (**b**) is a recognition image of the same area as (**a**), where specific interactions are recognized via perturbation of the oscillating cantilever. Dark spots in (**b**), such as within the white circle, represent specific binding events between FN and anti-FN to indicate the distribution of FN molecules on substrata. Image scalebars = 200 nm; gradient scales for (a) and (b) represent range of height and truncated cantilever oscillation reported as photodiode voltage, respectively. (**c**) demonstrates the range of unbinding forces vs. loading rates in FN-integrin complexes. Orange circles represent intracellularly generated cytoskeletal force normalized per complex (Δf_i); blue squares, molecular rupture force of ligand/receptor pairs (F_R) from Li et al. Vertical and horizontal error bars represent standard deviation of force and effective loading rate, respectively.

probes (Fig. 4.7a-b). As FFI and other methods to accurately determine the number and distribution of individual molecules on cantilevered probes are prohibitively challenging, we instead estimated the number of FN molecules on identically FN-functionalized, planar borosilicate glass substrata. FFI was employed using anti-FN antibody-functionalized AFM probes to image FN-functionalized glass. Quantification of FFI images (Fig. 4.7b) indicated average FN density of 383 molecules/μm^2 and an average spacing of 30 nm between FN molecules. This distribution is similar to that reported for other protein conjugation systems[15,24], and is sufficiently close spacing to enable integrin/FN interactions according to previous reports[25]. In our experiments, the contact

area between spherical probes and cell surfaces was approximately 0.6 μm^2, as determined by the size and contact depth of such a resting spherical probe on a cell surface[4]. Therefore, we calculated that a maximum of $n = 230$ FN-integrin pairs existed in the contact area representing the adhesion complex. Assuming that our two dominant force peaks (Table 4.2, $\Delta F_i = 6.00 \pm 2.47$ nN and 21.33 ± 1.45 nN) are representative of the two peak forces generated by a single adhesion complex and are distributed equally among all FN-integrin pairs comprising the complex, the dominant forces (average ± standard deviation) exerted through individual FN-integrin pairs, $\Delta f_i = \Delta F_i / n$, via actin polymerization and actomyosin contraction are $\Delta f_i = 26.1 \pm 10.5$ pN (for the lower force peak) and 92.7 ± 6.2 pN (for the higher force peak), respectively.

4.2.4 Estimation of intracellular cytoskeletal force rupturing ligand-receptor pairs and focal complexes

To consider the biophysical reason that cells generate this specific range of force ($\Delta f_i =$ 26.1 ± 10.5 pN and 92.7 ± 6.2 pN) through FN-integrin pairs, we integrated results from several distinct experiments. The macroscopic, nN-scale intracellular forces applied against a adhesion complex can be related to the pN-scale forces required to rupture individual ligand-receptor pairs via application of Bell's model[26]. This model and subsequent modifications[15,27] state that applied force biases an intermolecular pair toward the unbound state, and that the most frequently observed (characteristic) intermolecular rupture force, F_R, increases strongly with an increasing applied loading rate, $dF/dt = \dot{F}$[26,28]. In other words, F_R is an increasing function of $\dot{F}$, and forces approaching or exceeding F_R will significantly shorten the lifetime of the complex. For each force generation event ($\Delta f_i = \Delta F_i / n$) transmitted through the integrin-associated

ACs, we calculated the effective, intracellularly generated loading rates, F', from the slopes between peak events for $F(t)$ spectra such as Fig. 4.5.

We related these results to previously reported FN-integrin rupture forces F_R acquired via conventional (*active*) molecular force spectroscopy over a range of AFM-applied loading rates F', analyzed according to Bell's model[26,27]. These results are summarized in Fig. 4.7c. Note that 40% of intracellularly generated forces (Δf_i, orange circles) exceeded the most frequently observed or characteristic FN-integrin rupture forces (F_R, blue squares), indicating that these intracellularly generated forces are sufficient to significantly decrease the lifetime of FN-integrin complexes. In contrast, at the corresponding loading rates, actin-mediated forces falling below the FN-integrin characteristic rupture forces would not as strongly bias the FN-integrin pairs within a adhesion complex to rupture. The range of intracellularly generated forces (Fig. 4.7c, orange circles) traverse this threshold, which indicates that actin-mediated forces may or may not be sufficient to significantly decrease the lifetime of FN-integrin pairs, depending on the effective loading rate generated at that particular adhesion complex.

4.3 DISCUSSION

To identify the molecular mechanisms underlying the measured cell-generated force spectra, we considered a panel of cytoskeletal disrupting agents with known mechanisms of action. This approach allowed us to either incorporate or rule out specific cytoskeletal contributors, including actin (de)polymerization and actomyosin contraction, as responsible for actin-mediated force generation. When we treated living cells with pharmacological inhibitors and measured cellular dynamics using FN-conjugated AFM probes (Fig. 4.1), we found that intracellular actin-mediated processes

generated the observed periodic forces. These data indicate that the two force peaks ΔF_i (~ 6 nN and 12 nN) and three periodicities τ_i (~ 6 sec, 13 sec, and 2 min) of force oscillation are not all due to the same actin-mediated mechanisms. The cyclic force of 20 ± 2.87 nN at the cell front was not eliminated by addition of blebbistatin (25 μM). As blebbistatin inhibits myosin-II ATPase activity, and blocks actomyosin contraction / force exertion[3], we inferred that this force oscillation of ~20 nN was not wholly attributable to actomyosin-dependent contraction. These oscillations could be abrogated with nM concentrations of cytochalasin D that are believed to be incapable of severing actin filaments. Therefore, we concluded that actin (de)polymerization contributed to force generation in this front region of the cell. Interestingly, addition of cytochalasin D eliminated both the time and force peaks to levels that were not statistically different from those acquired with BSA-functionalized probes. The effects of cytochalasin D, therefore, demonstrate that actin filament dynamics contribute to both the periodicity and magnitude of force generation, and that disruption of cellular actin assembly processes also ceases transmission of actomyosin contraction via adhesion complexes. This result supports previous studies that claimed that the functions of actin de/polymerization and actomyosin contraction are strongly coupled[29].

These findings offer insights into the mechanical linkage between the cell surface and the internal cytoskeleton. As we disrupted particular components contained within the actin or microtubule-associated cellular networks, we observed notable perturbation in the balance of forces originating from and/or being transduced between these two networks. For example, nocodazole indirectly alters myosin II-maintained cellular contractility and tension by downregulating microtubule polymerization[2]. This mechanism could cause one to hypothesize that both the magnitudes and temporal

periods of myosin II-mediated and actin filament-dependent forces would increase upon addition of nocodazole. However, we observed the opposite: the actin-associated force magnitude and temporal periods both decreased after the addition of nocodazole, with the percentage decrease of force magnitude (up to 41.1%) larger than that of the temporal periods (up to 16.9%). Thus, increased dominance of the actin cytoskeleton does not necessarily correlate with increased contractile force transduced across integrin-associated ACs. We speculate that the reason for the decreased force oscillation upon addition of nocodazole may be due to an increase in actin (de)polymerization dynamics that result in lower magnitudes of maximum force developed at the adhesion complex.

The demonstration that actin (de)polymerization and actomyosin contraction together exert forces that may be sufficient to more rapidly induce rupture FN-integrin pairs (Fig. 4.7c) suggests that, even in a macroscopically stationary adhesion complex, the binding between FN and integrin dimers is in dynamic equilibrium. That is, intracellular forces that are mediated by and transduced through the actin cytoskeleton are capable of engaging and disrupting integrin-extracellular interactions during cell adhesion or motility. Such flexible capacity for the cell to more or less rapidly disassemble adhesion complexes, depending on rates of actin-mediated contractile force generation, suggests potential hypotheses for the observed range of magnitudes and rates of cell-generated forces. For example, cell migration may proceed by using adhesion complexes as temporary anchorage points at which the actin cytoskeleton pulls against FN-integrin pairs with forces/loading rates that are insufficient to significantly alter the binding lifetime of the pairs. It is plausible that rupture of FN-integrin pairs within the adhesion complex may occur rapidly when intracellular forces exceed the

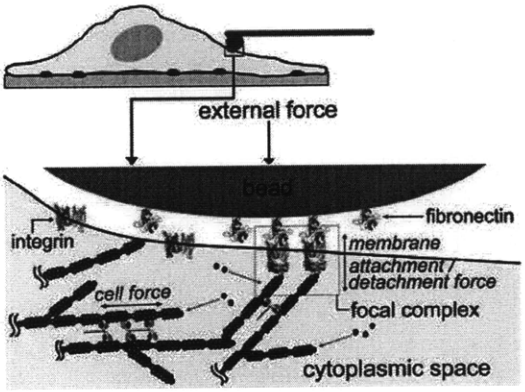

Figure 4.8 Schematic of force transmission by actin cytoskeleton against a ligand-presenting surface or probe. Force measurement via a cantilevered spherical probe, with region of interest expanded. Adhesion complexes are created between the plasma membrane and substrata. When finite compressive force is exerted on cells by spherical probes functionalized with FN, this triggers the formation of adhesion complexes and intracellularly generated force. This force generated by cells (green, solid arrow) and by actin polymerization (gray, dotted arrows) is detected via cantilevered probe deflection. Cytoskeletal force may transmit via membrane attachment/detachment force, or directly via physical linkage among integrins, adaptor proteins, and actin. Gray discs represent actin monomers that constitute actin filaments; green objects between actin fibers are myosin II motor proteins. Red-yellow complexes are integrin dimers, adjacent to intracellular adaptor proteins.

threshold in Fig. 4.7c, enabling adhesion complex dissolution and/or trailing edge retraction. That is, intracellular force mediated by the actin cytoskeleton, in addition to established mechanisms of proteolysis-mediated dissolution of adhesion complexes[30] and any attendant, force-induced conformational changes in other AC proteins[31], takes part in continuously creating and remodeling the engagement of fibronectin/integrin pairs during the formation, stabilization, and even dissolution of the multimolecular adhesion complexes required of many cell processes.

Figure 4.8 illustrates possible mechanisms by which such actin-mediated force may be generated and transmitted to ECM ligands, such as those presented from a cantilevered AFM probe. Fibronectin functionalized to the probe surface binds transmembrane integrins. Adaptor proteins such as talin and vinculin[7] are physically

associated with integrin dimers, and the cyclic cytoskeletal force generated through actomyosin contraction and/or actin polymerization is directly transmitted either at the engaged adhesion complexes or adjacent to those complexes via various intracellular membrane attachment/detachment forces[32].

In summary, we demonstrate that dynamic cell-generated force spectra can be reliably and reproducibly quantified using an AFM-enabled method of passive force spectroscopy. Such direct observations elucidated oscillatory forces of specific magnitudes and loading rates, correlating the previously reported nN-scale forces and minute- and second-scale oscillations of cell-material interfaces[4,11,14]. These force spectroscopy and imaging data indicated a subset of cell-generated forces that were sufficient to significantly shorten the lifetime of engaged FN-integrin pairs at cell-generated loading rates. Taken together, our results suggest that actin filaments associated with integrin-rich adhesion complexes are capable of transducing dynamic, intracellular forces that can actively regulate the lifetime of such ligand (FN)-receptor (integrin) pairs. More broadly, these findings demonstrate the potential for AFM-enabled mechanical analysis of cell/molecular dynamics, including the regulatory role of actin dynamics in mediating cell-ECM interactions.

4.4 MATERIALS AND METHODS

4.4.1 Cell culture and pharmacological challenges

NIH 3T3 fibroblasts were cultured in Dulbecco's Modified Eagle Medium, 10% calf serum, 1% penicillin-streptomycin, 1% glutamine (Invitrogen), on tissue culture treated coverslips (NalgeNunc). Pharmacological inhibitors were added at the following concentrations at room temperature, and cell force spectra were acquired 1 hr after

incubation: blebbistatin (25 μM), cytochalsin D (900 nM), and nocodazole (660 nM). Gross cell morphology was recovered upon washout with fresh media (1 hr) for all three reagents; Fig. 4.3 in the main text illustrates this for the case of blebbistatin.

4.4.2 AFM cantilever calibration

AFM cantilever calibration was conducted as described previously[33-35]. Briefly, photodiode inverse optical lever sensitivity (InvOLS) [nm/V] was measured from deflection-displacement curves recorded on rigid glass slides. Spring constants [nN/nm] of each AFM cantilever were measured via the power spectral density method of thermal oscillations[33,34]. For passive cell force spectra (e.g., Fig. 4.5), deflection reported by the photodiode in [V] was converted to force [nN] via multiplication by the InvOLS [nm/V] and these experimentally determined spring constants [nN/nm].

4.4.3 Functionalization of AFM cantilevers and recognition imaging

For fibronectin-functionalization on spherical probe cantilevers and beads (BioForce Nanosciences and Bangs Laboratory, nominal spring constant: 0.03 – 0.11 N/m, probe diameter: 2,500 nm), chemical vapor deposition of 1:3 N,N-diisopropylethylamine and 3-aminopropyltriethoxysilane (Sigma-Aldrich) was achieved in a vacuum dessicator for 2 hrs[15]. Cantilevers were treated with 1% glutaraldehyde (Sigma-Aldrich) for 2 hrs, followed by the immobilization of fibronectin. To functionalize anti-fibronectin antibody (Invitrogen) for FFI, Si_3N_4 cantilevers, backside-magnetically coated by the manufacturer (MAC-IV levers, Agilent/Molecular Imaging, nominal force constant = 0.04 N/m) were rinsed in dichloromethane for 10 min, followed by oxygen plasma cleaning for 10 min. Chemical vapor deposition of 1:3 N,N-diisopropylethylamine and

3-aminopropyltriethoxysilane (Sigma-Aldrich) was achieved in a vacuum dessicator for 2 hrs, followed by conjugation of pyridyl dithio-polyethylene glycolsuccinimidylpropionate (5 mg, PDP-PEG, Agilent/Molecular Imaging) in 0.5 mL of dichloromethane and 7 μL of triethylamine (Sigma-Aldrich). Monoclonal anti-fibronectin was conjugated with a 15-fold molar excess of N-Succinimidyl 3-(acetylthio)propionate (sATP, Pierce) in dimethylsulfoxide (Sigma-Aldrich). This conjugated antibody was bound to PDP-PEG-treated cantilevers for 2 hrs via deacetylation with 0.5 M hydroxylamine (Sigma-Aldrich), 25 mM ethylene diamine tetraacetic acid (EDTA, Pierce) in 150 mM phosphate buffered saline at pH = 7.36.

Recognition imaging of fibronectin was conducted in TopMAC mode (PicoPlus AFM, Agilent) as previously discussed[15,36]. Regions of 1 μm × 1 μm were scanned at a rate of 1 Hz, at a driving amplitude of ~0.5 V or ~5 nm (n = 10 images). Recognition image contrast is reported in units of [V] from the TREC signal, where dark spots indicate truncated cantilever oscillation amplitude upon strong probe-surface interactions over multiple adjacent pixels[15,16]. For additional protocols detailing this FFI, see Reference[15].

4.4.4 Real time measurement of cell dynamics

An AFM (PicoPlus, Agilent) was incorporated with an inverted microscope (IX81, Olympus) to facilitate positioning of AFM cantilevered probes on cell surfaces (Fig. 4.3). Probes were placed on cell surfaces and normal force was applied to cell surfaces through stage displacement in actuator feedback to a specified deflection set point (corresponding to a normal force of 350 – 800 pN); immediately upon this contact, the piezoactuator and associated feedback loop were turned off to measure the dynamic

cell-induced probe deflection in real time. The magnitude of normal forces [nN] applied to cell surfaces at the time of probe contact and forces generated by the actin cytoskeleton were calculated by multiplying real time deflection recorded as photodiode voltage [V] by InvOLS [nm/V] and spring constants [nN/nm] (See Supplementary Information). The normal stress applied by the cantilevered AFM probes was calculated from the normal force (350 – 800 pN) divided by the contact area between beads and cell surfaces (~0.6 μm^2)[4]. We observed in experiments that normal forces measured through AFM spectroscopy were independent of the orientation of cantilevered probes with respect to cell polarization direction.

4.4.5 Migration of fibroblasts

The movement of fibroblasts (0.2 – 0.7 μm/min at 37°C, and much slower at room temperature) [37,38] was negligible during the measurement of the intracellular dynamics over this duration and spatial resolution because the measurement of cell dynamics was conducted at room temperature.

4.4.6 Analysis of cell force spectra periodicity, peaks, and loading rates

Force peaks and associated temporal durations (e.g, Fig. 4.5) were measured from the left lowest point to the right highest point of each peak in the F vs. t spectra, where a peak was defined as a change in force exceeding the force resolution (~10 pN) over a duration exceeding the temporal resolution (~200 ms) of the measurements under these conditions. Based on this criterion, each value of force peak ΔF_i over a corresponding temporal duration τ_i was collected ($n > 600$ per experimental condition); bin increments of adhesion complex-level force and temporal durations used to construct distributions

was 200 pN and 0.4 sec, respectively. When adhesion complex-level force was converted to FN-integrin pair-level force, the bin increment was 2 pN. Loading rate (pN/sec) of intracellular force exerted to individual FN-integrin pairs was calculated from the slopes of real time force (nN) vs. time (sec) curves defined at each force peak as shown in Figs. 4.1b and 4.5. The resulting data were grouped into (loading rate, force) pairs as (F, F_R) or (F, Δf_i) to construct Fig. 4.7c, using the average of bin increments equal to 100 pN/sec and 2 pN, respectively. AFM cantilever deflection signal exhibited intrinsic (thermal) drift of average 9 pN/sec (4.5 nN / 500 sec, n = 30). This rate was measured with BSA-coated probes that do not activate integrin-mediated adhesion complex formation. Force spectra with FN-conjugated probes were corrected for this thermal drift.

4.4.7 Fluorescence microscopy imaging of 3T3 fibroblasts

For staining of the actin (F-actin) cytoskeleton, 3T3 fibroblasts were fixed with 2% formaldehyde for 15 min, followed by membrane permeation with Triton-X (0.1%) and bovine serum albumin (0.5%, Sigma Aldrich) in 1X PBS. Cells were incubated for 1 hr at room temperature in Alexa Fluor 488 phalloidin (6.6 mM, Invitrogen/Molecular Probes, Chicago, IL) prior to epifluorescence imaging (IX 81, Olympus).

4.4.8 Statistical analysis of cell generated force (Table 4.2)

All statistical analyses were conducted with one-way ANOVA (Tukey analysis).

1. Statistical analyses of temporal durations of force generation for the leading or front regions of cells were conducted: Time peaks τ_i of + blebbistatin, + cytochalasin D, and BSA-functionalized probe were not statistically different ($p > 0.05$). Differences in the

shorter time periods exhibited for FN-coated probes +/- nocodazole were not significantly different ($p > 0.05$). However, two groups (+ blebbistatin, + cytochalasin D, BSA-functionalized probe vs. FN-functionalized probe and + nocodazole) were significantly different ($p < 0.001$).

2. Statistical analyses of temporal durations of force generation on rear or trailing regions of cells were conducted: Time peaks τ_i of + blebbistatin, + cytochalasin D, and BSA-functionalized probe were not statistically different ($p > 0.05$). Shorter time periods of FN coated and + nocodazole were not significantly different ($p > 0.05$). Two groups (+ blebbistatin, + cytochalasin D, BSA-functionalized probe vs. FN-functionalized probe and + nocodazole) were significantly different ($p < 0.001$).

3. Statistical analyses of force peak magnitudes on leading or front regions: Differences in force peaks of + blebbistatin, + cytochalasin D, BSA-functionalized probe, and + nocodazole were not statistically significant ($p > 0.05$). However, two groups (+ blebbistatin, + cytochalasin D, BSA-functionalized probe, and + nocodazole vs. FN-functionalized probe) were statistically different ($p < 0.001$).

4. Statistical analyses of force peak magnitudes on rear or trailing regions of cells: Differences in force peaks of + blebbistatin, + cytochalasin D, BSA-functionalized probe, and + nocodazole were not statistically significant ($p > 0.05$). However, two groups (+ blebbistatin, + cytochalasin D, BSA-functionalized probe, and + nocodazole vs. FN-functionalized probe) were statistically different ($p < 0.001$).

4.5 CHAPTER SUMMARY AND CONCLUSION

The cytoskeletal actin dynamics at focal complexes is critical to intracellular force generation contributing to cell morphology and function. Several experimental techniques have been developed to study actin-mediated forces; however, these approaches have been insufficient to observe the complex temporal evolution of these forces. In this chapter, we presented AFM-enabled measurements of intracellular force dynamics at focal complexes, through which intracellularly generated forces were measured with picoNewton force resolution and millisecond temporal resolution. We found that the force at focal complexes is cyclic, with distinct force peaks. Through AFM-enabled recognition imaging, we estimated the number of fibronectin (FN)/integrin pairs within such complexes and the magnitude of force transmitted through individual FN/integrin complexes. Together with pharmacological challenges to actin-mediated force generation, these direct observations demonstrated that cytoskeletal force can be sufficient to rupture FN/integrin pairs, suggesting that ligand-receptor binding within focal complexes is in a dynamic equilibrium that can be modulated in part by intracellular force generation.

REFERENCES

1. Lee S, Nikova, D., Herman, I. M., and Van Vliet, K. J. Direct measurement of pN-scale cytoskeletal force dynamics at individual focal complexes on intact cells. Submitted 2009.
2. Even-Ram S, Doyle, A.D., Conti, M.A., Matsumoto, K., Adelstein, R.S., and Yamada, K.M. Myosin IIA regulates cell motility and actomyosin–microtubule crosstalk. Nat Cell Biol 2007;9:299-309.
3. Straight AF, Cheung, A., Limouze, J., Chen, I., Westwood, N. J., Sellers, J. R., Mitchison, T.J. Dissecting Temporal and Spatial Control of Cytokinesis with a Myosin II Inhibitor. Science 2003;299:1743 - 1747.
4. Galbraith CG, Yamada, K.M., and Sheetz, M.P. The relationship between force and focal complex development. J Cell Biol 2002;159:695–705.
5. Geiger B, Spatz, J. P., and Bershadsky, A. D. Environmental sensing through focal adhesions. Nat Rev Mol Cell Biol 2009;10:21-33.
6. Vasquez RJ, Howell, B., Yvon, A.M., Wadsworth, P., and Cassimeris, L. Nanomolar concentrations of nocodazole alter microtubule dynamic instability in vivo and in vitro. Mol Biol Cell 1997;8:973–985.
7. Zamir E, and Geiger, B. Molecular complexity and dynamics of cell-matrix adhesions. J Cell Sci 2001;114:3583-90.
8. Schliwa M. Action of cytochalasin D on cytoskeletal networks. The Journal of Cell Biology 1982;92:79-91.
9. Mogilner A, Oster, G. Force Generation by Actin Polymerization II: The Elastic Ratchet and Tethered Filaments. Biophys J 2003;84:1591–1605.
10. Zhua J, Carlsson, A. E. Growth of attached actin Filaments. Eur Phys J E

2006;21:209-222.

11. Galbraith CG, Sheetz, M. P. A micromachined device provides a new bend on fibroblast traction forces. Proc Natl Acad Sci USA 1997;94:9114–9118.

12. Tan JL, Tien, J., Pirone, D., Gray, D. S., Chen, C. S. Cells lying on a bed of microneedles: An approach to isolate mechanical force. Proc Natl Acad Sci USA 2003;100:1484-1489.

13. Molloy JE, Burns, J.E., Kendrick-Jones, J., Tregear, R.T., White, D.C. Movement and force produced by a single myosin head. Nature 1995;378:209–212.

14. Giannone G, Dubin-Thaler, B.J., Rossier, O., Cai, Y., Chaga, O., Jiang, G., Beaver, W., Dobereiner, H.-G., Freund, Y., Borisy, G., and Sheetz, M.P. Lamellipodial Actin Mechanically Links Myosin Activity with Adhesion-Site Formation. Cell 2007;128:561-675.

15. Lee S, Mandic, J, and Van Vliet, K.J. Chemomechanical mapping of ligand–receptor binding kinetics on cells. Proc Natl Acad Sci USA 2007;104:9609–9614.

16. Stroh C, Wang, H., Bash, R., Ashcroft, B., Nelson, J., Gruber, H., Lohr, D., Lindsay, S. M., Hinterdorfer, P. Single-molecule recognition imaging microscopy. Proc Natl Acad Sci USA 2004;101:12503-12507.

17. Sun Z, Martinez-Lemus, L. A., Hill, M. A., and Meininger, G. A. Extracellular matrix-specific focal adhesions in vascular smooth muscle produce mechanically active adhesion sites. Am J Physiol Cell Physiol 2008;295:268-278.

18. Van Vliet KJ, Bao, G., and Suresh, S. The biomechanics toolbox: experimental approaches for living cells and biomolecules. Acta Materialia 2003;51:5881–5905.

19. Wiesner S, Lange, A. and Fassler, R. Local call: from integrins to actin assembly. Trends Cell Biol 2006;16:327-329.

20. Zamir E, Katz, M., Posen, Y., Erez, N., Yamada, K. M., Katz, B. -Z., Lin, S., Lin, D. C., Bershadsky, A., Kam, Z., and Geiger, B. Dynamics and segregation of cell–matrix adhesions in cultured fibroblasts. Nat Cell Biol 2000;2:191-196.

21. Balaban NQ, Schwarz, U.S., Riveline, D., Goichberg, P., Tzur, G., Sabanay, I., Mahalu, D., Safran, S., Bershadsky, A., Addadi, L., and Geiger, B. Force and focal adhesion assembly: a close relationship studied using elastic micropatterned substrates. Nature Cell Biology 2001;3:466–472.

22. Beningo KA, Dembo, M., Kaverina, I., Small, J. V., and Wang, Y. L. Nascent focal adhesions are responsible for the generation of strong propulsive forces in migrating fibroblasts. Journal of Cell Biology 2001;153:881–888.

23. Schliwa M. Action of cytochalasin D on cytoskeletal networks. J Cell Biol 1982;92:79-91.

24. Hinterdorfer P, and Dufrêne, Y.F. Detection and localization of single molecular recognition events using atomic force microscopy. Nat Methods 2006;3:347 - 355.

25. Arnold M, Cavalcanti-Adam, E.A., Glass, R., Blummel, J., Eck, W., Kantlehner, M., Kessler, H., and Spatz, J.P. Activation of Integrin Function by NanopatternedAd hesive Interfaces. ChemPhysChem 2004;5:383 - 388.

26. Bell GI. Models for the specific adhesion of cells to cells. Science 1978;200(12):618-627.

27. Li F, Redick, S.D., Erickson, H.P., and Moy, V.T. Force Measurements of the a5b1 Integrin–Fibronectin Interaction. Biophys J 2003;84:1252–1262.

28. Merkel R, Nassoy, P., Leung, A., Ritchie, K., Evans, E. Using dynamic force spectroscopy to explore energy landscapes of receptor-ligand bonds. Nature 1999;397:50-53.

29. Shlomovitz R, and Gov, N. S. Membrane Waves Driven by Actin and Myosin. Phys Rev Letts 2007;98:168103.

30. Potter DA, Srirangam, A., Fiacco, K. A., Brocks, D., Hawes, J., Herndon, C., Maki, M., Acheson, D., Herman, I. M. Calpain Regulates Enterocyte Brush Border Actin Assembly and Pathogenic Escherichia. J Biol Chem 2003;278:30403-30412.

31. Vogel V, and Sheetz, M. Local force and geometry sensing regulate cell functions. Nat Rev Mol Cell Biol 2006;7:265-275.

32. Ma Z, Janmey, P.A., and Finkel, T.H. The receptor deformation model of TCR triggering. FASEB J 2007;22:1002-1008.

33. Butt HJ, and Jaschke, M. Calculation of thermal noise in atomic force microscopy. Nanotechnology 1995;6:1-7.

34. Hutter JL, and Bechhoefer, J. Calibration of atomic- force microscope tips. Rev Sci Instrum 1993;64:1868-1873.

35. Thompson MT, Berg, M. C., Tobias, I. S., Rubner, M. F., Van Vliet, K. J. Tuning compliance of polyelectrolyte multilayers to modulate cell adhesion. Biomaterials 2005;26:6836-6845.

36. Walton EB, Lee, S., Van Vliet, K.J. Extending Bell's model: how force transducer stiffness alters measured unbinding forces and kinetics of molecular complexes. Biophys J 2008;94:2621–2630.

37. Cornwell KG, Downing, B. R., Pins, G. D. Characterizing fibroblast migration

on discrete collagen threads for applications in tissue regeneration. Journal of Biomedical Materials Research Part A 2004;71A:55-62.

38. Sun S, Wise, J., and Cho, M. Human Fibroblast Migration in Three-Dimensional Collagen Gel in Response to Noninvasive Electrical Stimulus. Tissue Engineering 2004;10:1548-1557.

Chapter 5

PicoNewton-scale cytoskeletal actin force dynamics play a key role in cell rolling

Parts of the following study were submitted for publication in 2009 with co-authors SeungPyo Hong, Vanessa Lundin, Huanan Zhang, Jeffrey M. Karp, and Robert Langer[1]. All experiments were conducted by the thesis author, with the exception of the cell rolling experiments detailed in Fig. 5.1.

5.1 INTRODUCTION

The final chapter of this thesis considers cell-cell chemomechanical interactions generated by ligand-receptor binding and modulated by intracellularly generated force. The formation of transient ligand-receptor interactions occurs commonly between cells flowing in the blood and the vascular endothelium. This physiological process is known as cell rolling[2,3], and facilitates many biologically important processes such as recruitment of leukocytes to sites of inflammation, homing of hematopoietic progenitor cells after intravenous injection, tumor cell metastasis and other inflammatory processes[4,5]. Such behavior is typically mediated by dynamic interactions between selectins (P- and E-selectins) on the vascular endothelial cell surface and membrane proteins including P-selectin glycoprotein ligand-1 (PSGL-1) on the rolling cells[3,4,6]. The dynamic nature of cell rolling, which is the first stage of leukocyte extravasation, is understood to be primarily governed by: (i) shear force exerted on the vascular endothelial cells and the cells flowing in suspension via hematic pressure; and (ii) rapid binding and unbinding of selectin-mediated bonds with high dissociation rates[7-9]. The

fluid shear stress can be easily mimicked by artificial flow-based systems, and has enabled cell separation devices based on differential cell rolling[11]. However, the dynamic cellular mechanisms involved in the ligand-receptor dissociation process remain unclear and thus have been the subject of considerable study and debate. In particular, there are two distinct conceptualizations of cell rolling mechanisms which have not yet been integrated: (i) the effective stiffness of the cell and/or cell membrane is altered under fluid shear flow, which thus alters rolling speed[12-14]; and (ii) ligand-receptor binding kinetics are altered under fluid shear flow, which thus alters rolling speed[15-17]. However, to our knowledge these factors have not been related quantitatively, and additional contributions of actin dynamics to ligand-receptor kinetics and rolling of these cells have not been detailed. Here we show that cytoskeletal actin within the rolling cell plays an important role in connecting these two concepts. Our experiments indicate that the dynamic state of this intracellular network serves to both modulate cell deformability and to mediate application of an additional, internally generated force to ligand-receptor complexes.

The actin cytoskeleton is an important structural network involved in cell motion or migration, and maintenance of cell morphology[18,19]. Actin has been reported to generate dynamic force via actin polymerization/depolymerization and/or myosin motor protein contraction of actin filaments[20-22]. Although Snapp et al.[23] demonstrated that the physical engagement of transmembrane PSGL-1 to the actin cytoskeleton via adaptor protein moesin is required for human promyelocytic leukemia cells (HL-60) to roll on P-selectin immobilized substrata or endothelial cells that endogenously express P-selectin, the role of cytoskeletal actin's spatiotemporal dynamics has not been considered in modulation of cell rolling. This is largely due to a lack of effective tools

for real-time measurement of intracellular force generation[19,24]. In addition, existing models of cell rolling have focused on the effects of external shear force exerted by the bloodstream on molecular interactions and binding kinetics between P-selectin and PSGL-1[15,16,25]. Here we demonstrate that the dynamic force generated via the actin cytoskeleton against P-selectin/PSGL-1 complexes plays an important role in the rolling of HL-60 cells.

These direct measurements of cytoskeletal force dynamics are enabled by two atomic force microscopy (AFM)-based approaches: cellular force spectroscopy (CFS), which passively measures mechanical force exerted by the cell against a cantilevered probe over time, and functionalized force imaging (FFI)[26]. Traditional AFM force spectroscopy uses the AFM-cantilever to apply or maintain force against a molecule-functionalized surface or a cell[26-29]. In contrast, in CFS the force is instead generated by the cell against the ligand-functionalized probe in the absence of a feedback control loop between cantilever position and deflection, due ostensibly to intracellular force generation mediated by actin. Thus, interactions between these probes and contacted surfaces are recorded as temporal changes in probe deflection, which is directly proportional to the force generated by the cell. To our knowledge, this is the first time that passive CFS has been used to quantify cell-generated force spectra exhibited by leukocytes (or by other cell types). This approach enabled direct measurement of the nN-scale forces exerted by HL-60 cells against multiple, engaged P-selectin/PSGL-1 complexes. Functionalized force imaging, termed recognition imaging when initially applied to functionalized surfaces[28] and later to cells[26,30], quantifies the position of single molecules on sample surfaces via specific interactions between molecules on the probes and on the surfaces. This approach enables direct imaging of the spatial

distribution of nanoscale molecules, and thus an estimate of the pN-scale forces exerted by these cells on individual ligand-receptor complexes.

5.2 RESULTS

5.2.1 Cytoskeletal actin contributes to cell rolling

To demonstrate the active role of cytoskeletal actin and PSGL-1 engagement in initial rolling of HL-60 cells, rolling experiments under external fluid shear flow were conducted on surfaces to which P-selectin had been covalently conjugated[31], both before and after the addition of cytochalasin D (see Fig. 5.1). Cytochalasin D is a cell permeable inhibitor of actin polymerization, resulting in disruption of actin network organization[31]. Figure 5.1 shows video frames of HL-60 cells on P-selectin coated surfaces at t = 0 and 20 sec post-addition of cytochalasin D; see Supporting Information online for video. As shown in Fig. 5.1A and 5.1B, untreated HL-60 cells exhibited the typical rolling behavior that was specific to P-selectin-conjugated regions. (No cell adhesion was observed on the regions that were not functionalized with P-selectin.) The measured average cell velocity was 2.7 μm/sec, which is in the range of previously reported values[32]. In contrast, the majority of HL-60 cells treated with cytochalasin D did not roll on the surface, and instead remained adhered but stationary on the P-selectin regions as reported previously[33]. As HL-60 cells also express CD24, which also binds to P-selectin[34], HL-60 cells incubated with monoclonal anti-CD24 antibody were also analyzed in rolling experiments +/- cytochalasin D (data not shown). The absence of any discernible differences in rolling of cells with ostensibly blocked CD24 ligands, as compared with results in Fig. 5.1, confirms that HL-60 cell rolling was mediated by specific P-selectin/PSGL-1 interactions. Note that this rolling is distinct from the

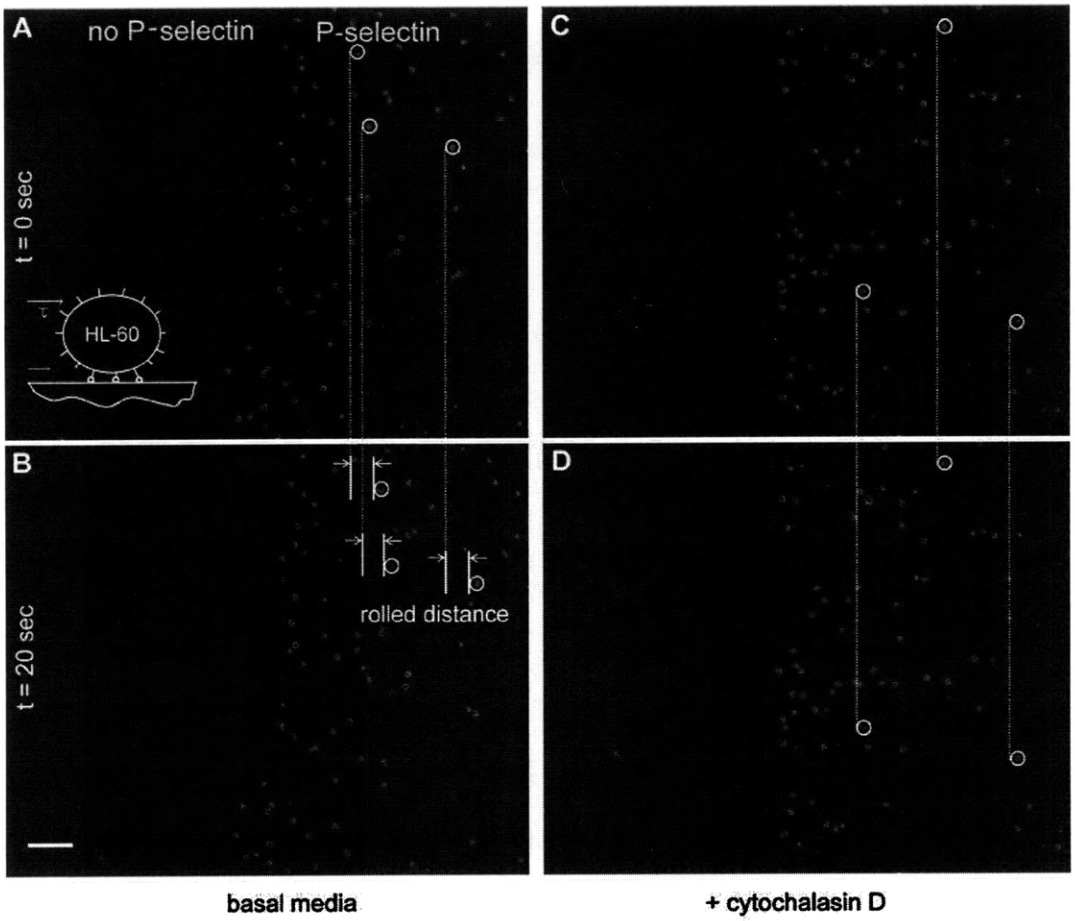

Figure 5.1 Time-course images of HL-60 cell rolling. Inset schematic in (A) shows HL-60 cells on P-selectin conjugated substrata under fluid shear stress. HL-60 cells exhibit the rolling behavior selectively on the P-selectin conjugated region in (A) and (B), whereas cells treated with cytochalasin D (1, 20, and 40 μM) do not roll, but instead bind and remain stationary on the P-selectin congugated region in (C) and (D). Scale bar = 50 μm

slow(er) rolling that is the second stage of leukocyte extravasation, in which integrin-ligand binding has been shown to reduce initial rolling velocity[35].

The observed stationary adhesion of HL-60 cells after cytochalasin D treatment indicates that the P-selectin/PSGL-1 binding under shear stress is not the only factor that induces and maintains the capacity of cells to roll. As shown in fluorescence microscopy images of HL-60 cells (Fig. 5.2), the actin cytoskeleton (demonstrated to be physically linked to PSGL-1 via moesin[23] in these cells) becomes nonuniformly

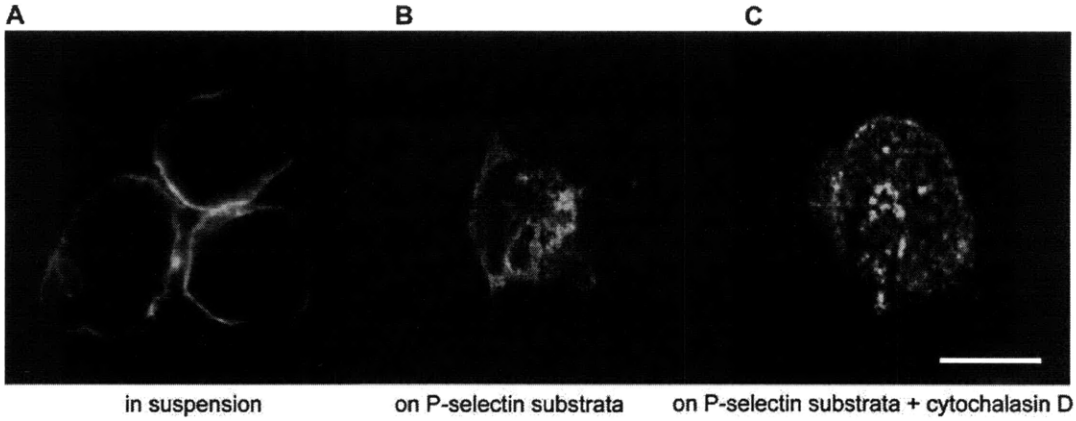

Figure 5.2 Fluorescence microscopy images of F-actin in HL-60. (A) F-actin of HL-60 cells that were not activated by P-selectin in suspension was stained with Alexa-phalloidin, with the image focal plane adjusted to approximately the midpoint of cell height. It is well established that actin is concentrated near the perimeter of the plasma membrane for suspended cells. For (B) and (C), the image focal plane was fixed at the interface between HL-60 cells and P-selectin-immobilized slides to visualize the area of contact under two conditions: before (B) and after (C) the addition of 1 M cytochalasin D. When HL-60 cells were activated by P-selectin (B), actin became non-uniformly distributed. After the addition of cytochalasin D, which disrupts actin cytoskeleton (C), the distribution of actin was further altered and formed aggregates. Scale bar = 10 μm.

distributed when PSGL-1 on HL-60 cells binds to P-selectin. The addition of cytochalasin D altered the extent of localization and distribution of filamentous actin (F-actin). This change in the density and distribution of F-actin ostensibly thwarted active involvement of the actin cytoskeleton in traction at HL-60 cell surfaces (e.g., via cell surface receptor associations that may be concentrated at microvilli). Figure 5.1 demonstrates that HL-60 cell adhesion under flow is maintained while cell rolling is terminated, indicating maintenance of adhesive P-selectin/PSGL-1 complexes upon cytoskeletal disruption. Further, Fig. 5.3 shows that HL-60 microvilli substructures are maintained after the addition of cytochalasin D concentrations equivalent to those used in our cell rolling and cellular force spectroscopy experiments, as has also been demonstrated previously for cytochalasin D-treated human acute lymphoblastic T-cell leukemia (CEM) cells[36].

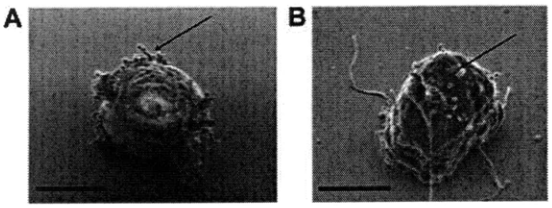

Figure 5.3 Scanning electron micrographs of HL-60 cells. HL-60 cells fixed (A) before and (B) after the addition of cytochalasin D. Note that there is no gross change in cell morphology or induction of uropoidal substructures upon addition of the inhibitor, and that microvilli substructures are maintained. Scale bar = 5 μm. Arrows in (A) and (B) indicate microvilli.

5.2.2 Real-time measurement indicates intracellular force generation

AFM-cantilevered probes were functionalized with P-selectin via covalent conjugation [32], and employed to measure HL-60 cell-generated forces at the cell-probe interface, termed cellular force spectroscopy (CFS). HL-60 cells were immobilized on rigid glass substrata that was physisorbed with P-selectin (Fig. 5.4A), as stable attachment of cells onto substrata is essential for AFM-based analysis. Note that this physisorption of these adhesive ligands to glass substrata was intended only to facilitate stable cell adhesion during probing of the apical cell surface. Optical microscopy-aided AFM enabled facile positioning of cantilevered probes with respect to HL-60 cells (Fig. 5.4C). Upon probe contact with the surface, the AFM feedback loop was disengaged and the probe deflection δ was measured through a calibrated photodiode (see Materials and Methods); δ was converted to force F through the intrinsic spring constant of the AFM cantilevers. Cell-generated force vs. time responses were thus acquired in real time, as schematized in Fig. 5.4B. Here, oscillations in force amplitude were quantified between sequential force minima and maxima as ΔF_i that were exerted over a corresponding time span τ_i; see Materials and Methods. The cytoplasmic domain of PSGL-1 is physically associated with the actin cytoskeleton[23], and PSGL-1 ostensibly binds to P-selectin-

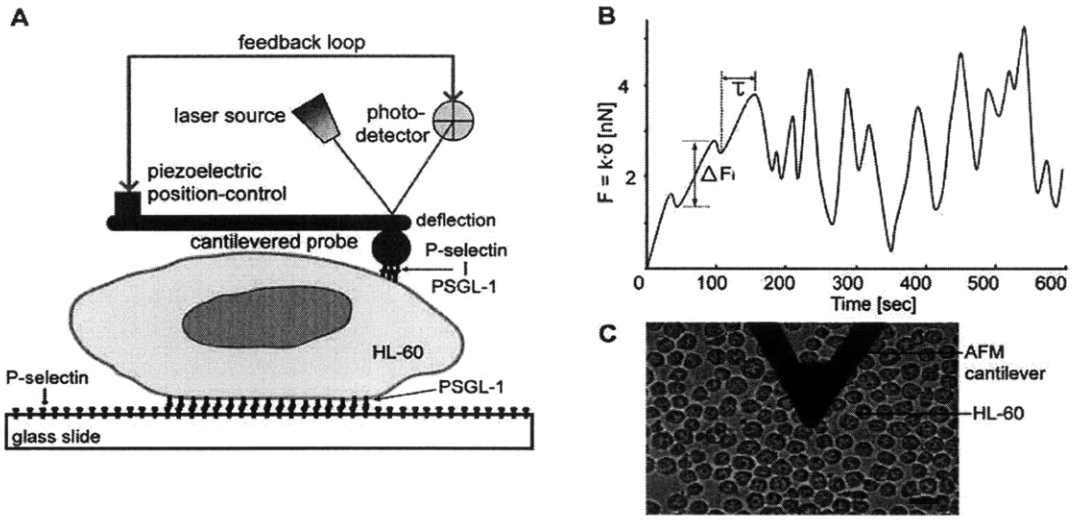

Figure 5.4 Schematic of AFM-enabled measurement of cell-generated force dynamics. (A) P-selectin is covalently conjugated to a cantilevered spherical probe (see Methods and Fig. 5.6 for density of conjugated P-selectin). HL-60 cells are adhered to glass substratum via specific binding of PSGL-1 to physisorbed P-selectin. AFM piezoactuator-photodiode feedback loop is disengaged upon contact with the cell surface, and cell-generated force dynamics are detected as deflection of the cantilevered probe. (B) Schematic of real-time force vs. time spectra, where force F is the product of cantilever spring constant k and . ΔF_i is defined as force amplitude between sequential force minima and maxima; here, $\Delta F_i > 0$ indicates cell pulling against probe; τ_i, time period of force exertion (See Materials and Methods). (C) Optical microscopy-mediated AFM enables the localization of spherical probes on HL-60 cell surfaces. Scale bar = 20 μm.

functionalized probes. Thus, the transmission of force shown in Fig. 5.4B could be generated serially via the actin cytoskeleton, PSGL-1 cytoplasmic domain, PSGL-1 extracellular domain, P-selectin covalently functionalized to probes, and AFM cantilevers. Therefore, intracellular force dynamics can be directly transmitted to cantilevered probes.

As shown in Fig. 5.5A, HL-60 cells generated oscillatory mechanical force upon specific binding between P-selectin-functionalized probes and PSGL-1 on the HL-60 cell surfaces (solid blue). When cytochalasin D was added to the basal imaging media (1 μM), this periodic force generation ceased (shaded red), confirming that the dynamic force spectra of HL-60 cells in basal media required polymerization and/or

connectivity of actin filaments. From comparison of force spectra in Fig. 5.5A, it is clear that cell-generated forces are considerably reduced – as compared to HL-60 force generation against P-selectin-conjugated probes in basal media – in two cases: in the absence of specific binding between P-selectin and PSGL-1 (with bovine serum albumin (BSA)-functionalized probes in Fig. 5.5A; green) or in the presence of P-selectin/PSGL-1 engagement after cytochalasin D treatment (Fig. 5.5A and 5.5C; shaded red). Average force amplitudes ΔF_i generated by the cell decreased from 2.2 ± 1.5 nN against the P-selectin probe in basal media (Fig. 5.5B), down to 0.54 ± 0.38 nN (BSA-probe) and 0.41 ± 0.41 nN (+cytochalasin D). In particular, the lack of periodic force measured upon contact with a BSA-functionalized probe indicates that this intracellular mediation of ~2 nN-scale force to the cell-probe interface includes specific P-selectin/PSGL-1 binding interactions, and that the forces inferred from deflection of a P-selectin-functionalized probe are not membrane undulations that would be observable independent of such specific ligand-receptor interactions.

The temporal periodicity of this force generation, τ, measured from spectra such as Fig. 5.5A, was τ = 3.2 ± 1.05 sec; this period corresponds with the reported periodicity of retraction and protrusion at the leading edges of adherent cells on stiff substrata [37]. This suggests that HL-60 cells could use a mechanism for rolling that is related to the actin-mediated cell migration/crawling mechanisms of adherent cell types such as fibroblasts. However, here we attribute force dynamics not to possible integrin/ligand interactions which are involved in the later stage of slow(er) leukocyte rolling or in adherent cell migration, but to specific P-selectin/PSGL-1 interactions mediating the initiation of cell rolling. Non-specific adsorption of proteins (which could possibly be integrin ligands) to the probe is unlikely: Karnik et al.[38] have demonstrated

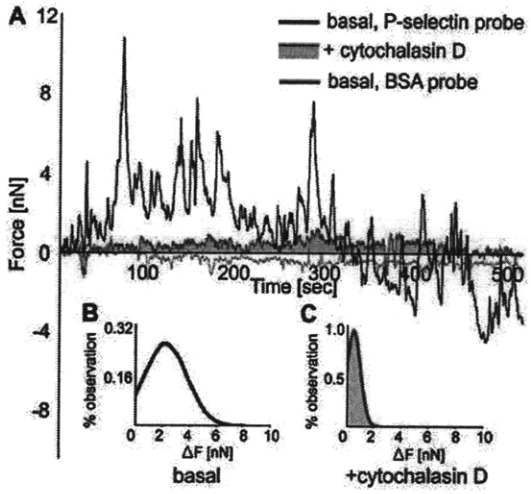

Figure 5.5 Cell-generated force measurement with P-selectin-conjugated spherical probes. As in Fig. 2, P-selectin cantilevered probes were placed on HL-60 surfaces and bound to PSGL-1 on HL-60 cells; probe deflection was converted to force. (A) Oscillating force is generated by HL-60 cells in basal media against the P-selectin probe (blue). The magnitude of these force spectra decreases significantly 1 hour after addition of 1 μM cytochalasin D (shaded red), and is comparable to that exerted by cells in basal media against BSA-conjugated probes (green). (B) Distribution of force maxima ΔF_i exhibited by cells against P-selectin probes under basal media characterized by an average $\langle \Delta F_i \rangle = 2.22 \pm 1.53$ nN. (C) $\langle \Delta F_i \rangle$ is reduced to 0.41 ± 0.41 nN after addition of cytochalasin D; and to 0.54 ± 0.38 nN against BSA probes on cells in basal media. Data reported as avg. ± std. dev.

that non-specific protein adsorption is prevented by P-selectin conjugation, and these cells do not adhere to glass in full media unless the glass is conjugated with P-selectin. Further, the time scales of cell-P-selectin interactions in both the rolling experiments and the CFS measurements (minutes) is insufficient for the cells to express significant ECM proteins.

One may initially posit that these ~2 nN-scale force oscillations ΔF_i could be due to reversible engagement of individual P-selectin/PSGL-1 complexes. However, these magnitudes significantly exceed unforced, reversible binding between molecular pairs. (Although unbinding of such ligand-receptor complexes can be caused by external tensile force of critical magnitude F_R that increases with applied loading rate [8,27], these forces are on the order of 10s to 100s of pN at applied velocities accessible via AFM.)

Further, in these CFS experiments no external tensile force was applied; probes were rested on the HL-60 cell surfaces. The force sensitivity and absolute compliance of typical (and our) AFM cantilever-photodiode system is insufficient to measure reversible ligand-receptor binding under near-zero applied force and loading rate (i.e., resting cantilevered probe). Therefore, the force fluctuations demonstrated in Fig. 5.5A cannot be attributed to reversible binding of P-selectin/PSGL-1 complexes at the probe-cell interface, but to the subsequent intracellular force generated via actin engagement. Further, Fig. 5.3 indicates that the mitigated force fluctuations of HL-60 cells upon addition of cytochalasin D cannot be attributed to gross changes in overall cell shape, or to an increase in the cell-substrata interfacial contact area (and the associated number of binding complexes) that could plausibly result from drug-induced disruption of the actin cytoskeletal network. Here, we note that these experiments were designed to probe whether these cells could generate force against engaged ligands. It is possible that the action of a cell against a μm-scale probe may differ than its response against glass substrata of larger (even infinite) radius. However, the microscale AFM probe radius was chosen to approximate the contact area between probes and cells (~0.1 μm^2) to that which occurs between cells and the planar, P-selectin-functionalized glass slides on which cells roll during *in vitro* experiments and between leukocytes and vascular endothelial cells *in vivo*.

5.2.3 Functionalized force imaging quantifies P-selectin density

To estimate the force and effective loading rate exerted by the cell through one P-selectin/PSGL-1 complex, it is necessary to obtain the number and the distribution of the complexes. AFM-enabled functionalized force imaging (originally termed

recognition imaging[28]) was thus employed to determine the density (number per area) of P-selectin on the spherical probe surface. To facilitate statistical analysis over many replicate experiments and images, borosilicate glass slides of identical composition to the AFM probes used above were covalently conjugated with P-selectin under identical conditions [32]; these P-selectin surfaces were then imaged with PSGL-1-functionalized, magnetically actuated cantilevers to determine the P-selectin density. Via conjugation protocols detailed previously [32], we manipulated the distribution of P-selectin molecules on borosilicate glass slides and probes, and the resulting regular distribution of P-selectin is shown in Fig. 5.6. In this imaging mode, retardation of cantilever oscillations indicated locations of strong binding forces (i.e., binding recognition sites[26,39,40] or P-selectin locations) as punctate, dark spots (Fig. 5.6B). The average density of these sites was 120 P-selectin/μm^2 (n >15, where n is the number of images). Although dark spots represent the position of P-selectin molecules, it is reasonable to assume that the position and maximum number of specific ligand-receptor pairs on the contacted cell surface will be less than or equivalent to this P-selectin ligand density. In addition, the fact that molecular weight and size of PSGL-1 (250 kDa) on the HL-60 cell surface is larger than that of P-selectin (140 kDa)[32,41] on the probe increases the validity of this assumption. As a lower bound on the area of contact A_c between the P-selectin-functionalized spherical probe of diameter $D = 1$ μm and the cell surfaces ($D \sim 15$ μm), we adopted the bead-cell contact area measured by Galbraith et al.[19], $A_c = 0.1$ μm^2. In a probe surface area of 0.1 μm^2, there are 12 ± 2 P-selectin/PSGL-1 complex regions (or 120 P-selectin/μm^2), each of which represents one or two P-selectin molecules due to statistical considerations of chemistry and of P-selectin size[26,39].

This estimate of the density of engaged ligand-receptor complexes facilitates calculation

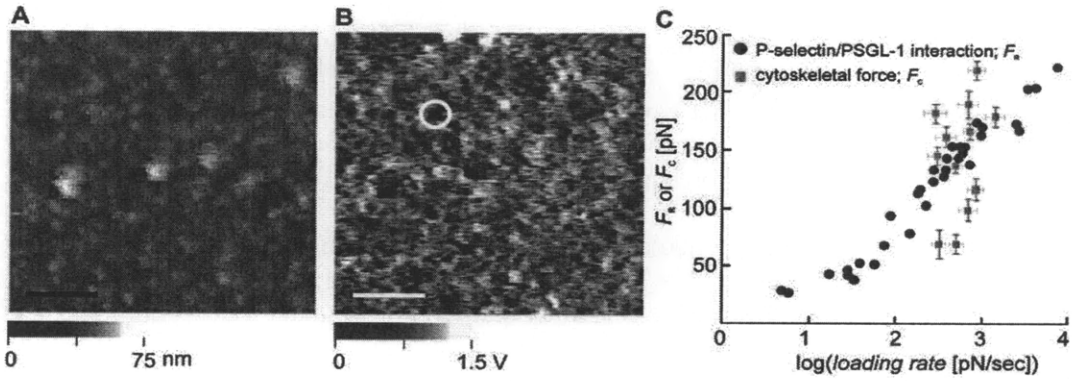

Figure 5.6 P-selectin distribution and comparison of cell-generated forces vs. characteristic rupture forces of single P-selectin/PSGL-1 complexes. (A) AFM topography image and (B) recognition image of glass substrata to which P-selectin is covalently conjugated (See Materials and Methods). Dark spots in (B) represent specific binding events (e.g., within circle) between P-selectin-conjugated glass and PSGL-1-functionalized silicon nitride cantilever, and are of average diameter 32 ± 4 nm. P-selectin density on glass probes is estimated from such images as 120 ± 20 P-selectin/μm^2 (avg. ± std. dev, n = 15 images). Scale bars = 250 nm. (C) Force vs. loading rate for P-selectin/PSGL-1 complexes. Blue circles, characteristic unbinding force (F_R) of single P-selectin/PSGL-1 complexes measured via molecular force spectroscopy [10]; orange squares, cytoskeletal force (F_C) as measured by our CFS and normalized by P-selectin density in the probe contact area. Cell-generated forces applied to the complex (orange squares) that exceed F_R of molecular pairs (blue circles) will significantly decrease lifetime of the ligand-receptor complex.

of the forces transmitted through one P-selectin/PSGL-1 complex due to internal cytoskeletal contraction. The average force transmitted from the bloodstream to individual P-selectin/PSGL-1 complexes during HL-60 cell rolling at a defined loading rate is the drag force normalized by the total number of engaged P-selectin/PSGL-1 complexes (see Materials and Methods). The actual force transmitted to each complex could be reduced further, due to elastic deformation (and concurrent energy dissipation) of the cell itself. Hanley et al.[10] reported the most frequently observed unbinding force F_R of a single P-selectin/PSGL-1 complex as a function of applied loading rate dF/dt in AFM molecular force spectroscopy experiments (Fig. 5.6C, blue circles). According to the established Bell-Evans model of forced molecular unbinding[8,26,42], the lifetime of P-selectin/PSGL-1 complexes will be decreased (i.e., unbinding will occur faster) under

applied tensile load, and the most frequently observed rupture force will increase with increasing loading rate. In other words, the strained complexes will rupture quite rapidly when the applied external force approaches and exceeds F_R, indicated by the blue circles in Fig. 5.6C, at any particular loading rate. However, external force generated by the bloodstream alone (as low as 1.4 pN per complex under our conditions; see Materials and Methods) at the associated, physiological shear flow-induced loading rates (~400 pN/s) can be at least one order of magnitude lower than the characteristic rupture force of these complexes. Our CFS experiments show that cytoskeletal actin mediates cyclic tensile (contractile) forces F_C as shown in Fig. 5.5A, and the associated loading rates for each peak contractile force can be calculated from the corresponding slope dF/dt of spectra such as in Fig. 5.5A. These cell-generated forces at specific loading rates are presented in Fig. 5.6C as orange squares, and are also normalized by the number of P-selectin/PSGL-1 complexes estimated in the contact area. This comparison of cell-generated forces and ligand-receptor rupture forces F_R indicates that rupture of P-selectin/PSGL-1 complexes, as required of cell rolling, will occur much more quickly when actin-mediated contractile forces are added to the external force generated by the bloodstream shear flow. This potential requirement for additional mechanical force to rupture the P-selectin/PSGL-1 complex is consistent with the observation that HL-60 cells remained bound to P-selectin-conjugated substrata after the function of the actin cytoskeleton was thwarted by cytochalasin D, even at physiological rates of external fluid shear flow (Fig. 5.1). Further, Fig. 5.6C indicates that cytoskeleton-mediated forces F_C can sometimes be sufficient to rapidly rupture the engaged complexes, even in the absence of fluid shear flow (i.e., when $F_C > F_R$ at a particular loading rate).

5. 3 DISCUSSION

This quantitative analysis through video microscopy (Fig. 5.1), cell-generated force spectra (Figs. 5.4 and 5), and functionalized force imaging (Fig. 5.6) demonstrate that the spatiotemporal dynamics of the actin cytoskeleton is critical to cell rolling in non-adherent cells such as HL-60 cells. Association of transmembrane PSGL-1 with the actin cytoskeleton may occur directly (Fig. 5.7A) or more plausibly via intracellular anchorage molecules (Fig. 5.7B), such as moesin reported by Snapp et al. to be critical in this initial stage of HL-60 cell rolling[23]. Dynamic mechanical forces (fluid shear flow or actin-mediated contraction) should induce rapid unbinding of the activated P-selectin/PSGL-1 complexes if these forces exceed the rupture force at the corresponding loading rate (Fig. 5.7C)[43]. A further possibility is that this intracellular dynamic force may act as a membrane detachment/attachment force that alters nearby ligand-receptor binding kinetics (Fig. 5.7D)[44]. As suggested by Bell and Merkel et al.[8,27], the dissociation rate constant k_{off} increases with increasing external tensile force, as has been demonstrated for this complex under fluid shear flow[45]. Dynamic force generated by the actin cytoskeleton can act as a source of external force that affects binding kinetics of adjacent P-selectin/PSGL-1 complexes. Therefore, this cytoskeletal force perturbs the system, and is thus capable of increasing the molecular dissociation rate and cell rolling efficiency.

PSGL-1 receptors are concentrated on microvilli, which contain parallel bundles of actin filaments that rapidly undergo continuous assembly and disassembly[46]. Given the high density of rolling receptors on the microvilli surface[47], microvilli retraction appears to be required to enable leukocyte polarization and transendothelial

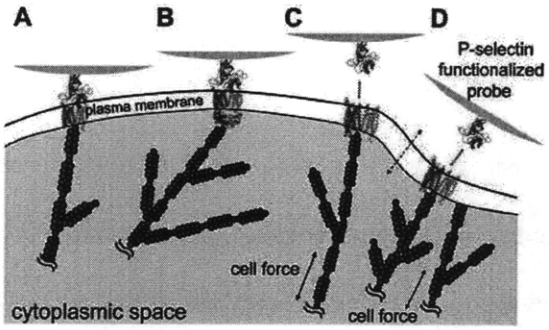

Figure 5.7 Schematic of potential cell-generated force transmission modes in HL-60 cells. P-selectin is conjugated to spherical probe surface; cytoskeletal actin, gray filaments; transmembrane PSGL-1, red; adaptor proteins linking actin cytoskeleton and PSGL-1, purple/green. (A) and (B) depict physical linkage between cytoskeleton and PSGL-1. (C) and (D) depict two mechanisms for cytoskeletal detachment required of HL-60 cell rolling on P-selectin-conjugated substrata (C) Conformational changes in PSGL-1 due to internal forces exerted via the actin cytoskeleton may trigger detachment/attachment of PSGL-1 from substrata. (D) Force transmitted through the actin cytoskeleton may act as membrane detachment/attachment force (blue arrow), rupturing P-selectin/PSGL-1 pairs. Microvilli omitted for clarity.

migration after mediating adhesion to the endothelium[48]. It is possible that the forces observed in our study represent the actin filament dynamics that mediate microvilli assembly and retraction against the ligand-functionalized probe surface. Such displacement and concurrent force generation is not inconsistent with our hypothesis that actin-mediated forces act on the ligand-receptor complex. However, we note that assembly and disassembly cycles of an entire, individual microvillus have been reported to proceed over ~12 min[49], approximately two orders of magnitude slower than the oscillating force periods observed in Fig 5.5A.

This capacity for real-time measurement of intracellularly generated force spectra and video capturing of HL-60 cells under flow, before and after actin-inhibitory challenges, demonstrated that actin-mediated dynamic force generation is a key factor in regulation of HL-60 cell rolling. Synthesis of glass substrata, onto which P-selectin was covalently conjugated at a uniform density confirmed via FFI [32], enabled the

quantification of force transmitted from the actin cytoskeleton to individual P-selectin/PSGL-1 complexes. Current models for rolling mechanisms of HL-60 cells have considered fluid-flow shear stress as the primary external force acting to drive ligand-receptor dissociation. However, these data indicate an additional contributor, namely the internal force transmitted via cytoskeletal actin, which can be sufficient to alter the binding lifetime of P-selectin with the HL-60 cell surface receptors, PSGL-1. These results suggest that cytoskeleton-mediated force, as well as external fluid shear stress, should be considered in evaluation of the dissociation rate constant k_{off} of P-selectin/PSGL-1 and associated cell rolling speeds. We note that Miner et al.[35] recently showed similar initial rolling velocities of cells, regardless of existence of actin-binding cytoplasmic domains of PSGL-1, for different cell types (primary leukocytes and modified CHO cells) than those considered here. This result is in contrast with the established findings of Snapp et al.[23] for the HL-60 cells considered here. Snapp et al. showed that cytoplasmic tail residue deletion significantly impaired leukocyte rolling and that PSGL-1 in HL-60 cells associated with the actin adaptor protein, moesin. They thus posited an anchorage role for actin, but did not directly probe or hypothesize any force generation of the cell via actin engagement of the PSGL-1/P-selectin complex. Our results are not in conflict with the findings of Miner et al., who used different cell types, and provide a new observation of cell-generated force for the HL-60 cells considered here and by Snapp et al.[23]. Thus, the novel approaches discussed herein should help to further elucidate the rolling mechanism of HL-60 and other leukocytes on endothelial cell surfaces by providing useful tools for studying the dynamics of both HL-60 and endothelial cells, as well as by defining the applied loading rates which modulate the rupture force and lifetimes of P-selectin/PSGL-1 complexes during

physiological and pathological cell rolling.

5. 4 MATERIALS AND METHODS

5.4.1 Surface immobilization of HL-60 cells

HL-60 cells (American Type Culture Collection, ATCC, Manassas, VA) were cultured in 75 cm^2 polystyrene tissue culture flasks (Invitrogen) in Iscove's Modified Dulbecco's Medium supplemented with 20% FBS (American Type Culture Collection, ATCC, Manassas, VA) at 37 °C under the 5% CO_2 atmosphere. Cell density was maintained between 10^5 and 10^6 cells/mL during the cell culture. P-selectin (Glycotech Inc., Gaithersburg, MD) was physically absorbed onto the SuperClean glass surfaces (Telechem International, Inc., Sunnyvale, CA). Briefly, the glass substrates were washed with 150 mM phosphate buffered saline three times (five minutes for each), followed by incubation with P-selectin at a 5 μg/mL concentration on a plate shaker at room temperature for 2 hrs. The surfaces were then washed again with 1X PBS three times for five minutes each. HL-60 cells at a 1×10^5/mL concentration were allowed to interact with P-selectin immobilized on the surface at 37 °C for 2 hrs, resulting in HL-60 immobilization on the surfaces through binding between P-selectin and PSGL-1 on the cells. For the functionalized force imaging (Fig. 5.6A and 5.6B), a set of surfaces with covalently immobilized P-selectin was also prepared using the epoxy-based chemistry as described earlier[32]. The density of P-selectin conjugated on substrata through physisorption was greater by a factor of five, compared to the density of covalently conjugated P-selectin, according to our AFM recognition images (data not shown).

5.4.2 Cell rolling experiments in a flow chamber

HL-60 cells were treated with cytochalasin D (CD, Sigma-Aldrich, St Louis, MO) at 37°C for 10 min. Untreated and CD treated cells were thereafter flowed over the P-selectin-immobilized glass surfaces in a rectangular parallel-plate flow chamber (Glytotech) with a gasket 6 cm long, 127 μm high, and 1 cm wide. HL-60 cells at densities of $3 - 5 \times 10^5$/mL in the cell culture medium were loaded in 5 mL syringes mounted on a syringe pump (New Era Pump Systems, Inc., Farmingdale, NY) for controlling the flow rate. A flow rate of 200 μL/min was used, which is correspondent to a shear stress of 1.39 dyn/cm^2, which is in the range of physiological shear stress (1 – 10 dyn/cm^2).. The rolling behavior of the cells was studied with an Axiovert 200 Zeiss inverted microscope (Carl Zeiss, Thornwood, NY) and images were obtained at the boundary between the P-selecin coated and uncoated region at 10 X magnification at a rate of 1 frame per second for two minutes. Flow was laminar (Re ~ 0.1-3) and shear stress (τ) was calculated using plane Poiseuille flow via the equation

$$\tau = \frac{6\mu Q}{wh^2}$$

where μ is kinematic viscosity, Q is volumetric flow rate, w is width of the flow chamber, and h is height of the flow chamber.

5.4.3 Calculation of loading rate and unbinding force generated by blood flow

Geometrical parameters of cells were obtained from AFM images of HL-60 cells and as reported by Dong et al.[13]: average radius of HL-60 cells is 6 μm, and area of contact between HL-60 cells and P-selectin-conjugated substrates is $\pi \cdot (1\ \mu m)^2 = 3.14\ \mu m^2$. Stokes' law describes the drag force $F_D = 6\pi\mu UR$, where μ is viscosity of the medium (assumed to be 1×10^{-3} Pa·sec), U is the average flow velocity, and R is the radius of HL-60 cells. Because the volumetric flow rate is 200 μL/min, and the cross-section area

of the flow chamber is 127 μm × 1 cm, U is 2.62×10^{-3} m/sec. Therefore, the drag force $F_D = 6\pi\mu UR \sim 296$ pN as Stokes' law is defined[50]. If torque contributions are included due to finite cell height, drag forces at specific loading rates increase by a factor of 1.4 – 2 (F_D = 420 – 592 pN) based on the analytical equations of Alon et al.[51], and Smith et al.[52]. Cell rolling velocity is 2.7 μm/sec, and the average time it takes for cells to roll 2 μm (diameter of contact area) is 0.74 sec. Therefore, the average loading rate is 296/0.74 = 400 pN/sec. As mentioned above, the area of contact between spherical probes and HL-60 cell surfaces is 0.1 μm^2, which contains 12 P-selectin/PSGL-1 complexes. Therefore, in the area of contact (3.14 μm^2), there are ~376 P-selectin/PSGL-1 complexes, and thus the average magnitude of force applying to individual P-selectin/PSGL-1 complexes is estimated to be 1.1 – 1.6 pN pN at a loading rate of 400 pN/sec. The drag force calculated based on energy dissipation is 6π times smaller than that calculated above[50], which then predicts an even smaller force (< 1.6 pN) on the complex due to shear flow.

5.4.4 AFM cantilever calibration

AFM cantilever calibration was conducted as described previously[53-55]. Briefly, inverse optical lever Sensitivity [nm/V] (InvOLS) was measured from deflection-displacement curves recorded on rigid substrates (here glass slides). Spring constant [nN/nm] of AFM cantilevers were measured via thermal activation recording of deflection and the Fourier Transform (FFT) of cantilever amplitude as a function of oscillation frequency fitted with simple harmonic oscillation function. Because intracellular forces are recorded as a form of deflection [V] in real time as shown in Fig. 5.5A, deflection was converted to force [nN] via multiplication of deflection [V] by the InvOLS [nm/V] and spring

constant [nN/nm].

5.4.5 Functionalization of AFM cantilevers and AFM imaging

For P-selectin functionalization of cantilevered, spherical borosilicate glass probes (BioForce Nanosciences, Ames, IA) were washed in phosphate buffered saline (PBS) and incubated with NHS-PEG-maleimide (NPm, 2mM, Pierce Biotechnology, Rockford, IL) for 1.5 hrs. NPm was removed and P-selectin (5 μg/mL) was added for immobilization on cantilevers. For PSGL-1 functionalization of PSGL-1 on cantilevers, amine derivitization and covalent attachment of bovine serum albumin-LC-BSA (Biotin-LC-BSA, Pierce Biotechnology) were done as published previously[26,56]. Biotin conjugated cantilevers were incubated with streptavidin (100 μg/mL, Pierce Biotechnology) for 20 minutes and rinsed five times with PBS, followed by incubation of biotinylated PSGL-1 (100 μg/mL, multivalent biotinylated sialyl Lewis(x)-poly(acrylamide), sLex-PAA-biotin, Glycotech, Gaithersburg, MD). After rinsing with PBS five times, cantilevers were ready for imaging. Immobilized HL-60 cells, P-selectin-immobilized glass slides and spherical probes were imaged with functionalized cantilevers in contact mode and TopMAC mode (PicoPlus AFM, Agilent/Molecular Imaging) as previously discussed[26,56].

5.4.6 Real time measurement of cell force spectra (CFS)

PicoPlus AFM (Agilent) was incorporated with optical/epifluorescence microscopy (IX 81, Olympus) to enhance the capability of placing AFM cantilevered probes on cell surfaces (Fig. 5.4C). Immediately after probes contacted cell surfaces, the piezo-actuator and associated feedback loop were turned off to measure the dynamic cell-

induced probe deflection in real time. The magnitude of normal forces [nN] applied to cell surfaces at the time of probe contact and forces generated by the actin cytoskeleton were calculated by multiplying real time deflection recorded as photodiode voltage [V] by InvOLS [nm/V] and spring constants [nN/nm].

5.4.7 Analysis of cell force spectra

From the oscillatory force vs. time spectra, the magnitude of force peaks F_i and time periods of force oscillation $\Delta\tau_i$ (Fig. 5.5A) were measured from the left lowest point to the right highest point of each peak. Based on this criterion, each value of time periodicity and force peak was collected ($n > 200$), and the bin size increments used to construct distributions of HL-60 cell-generated force and time periodicity was 100 pN and 0.4 sec, respectively. When cell generated force was normalized by the probe-cell contact area to calculate P-selectin/PSGL-1 pair-level force, the bin size was 2 pN. Loading rate (pN/sec) of intracellular force exerted to individual P-selectin/PSGL-1 pairs was calculated from the slope dF/dt of the force (nN) vs. time (sec) spectra between each peak as shown in Fig. 5.5A. The matrix of loading rate vs. F_R or F_C in Fig. 5.6C was based on the bin size increments of 100 pN/sec vs. 2 pN. Intrinsic thermal signal drift rate was measured with BSA-coated probes that did not activate P-selectin force generation, as 9 pN/sec ($n = 30$). Force vs. time spectra (e.g., Fig. 5A) were corrected for this thermal drift rate.

5.4.8 Fluorescence microscopy

For staining of the actin (F-actin) cytoskeleton, HL-60 cells immobilized on P-selectin immobilized glass slides or in suspension were fixed with 2 vol % formaldehyde for 15

min, followed by membrane permeation with Triton-X (0.1%) and bovine serum albumin (0.5%, Sigma Aldrich) in 1X PBS. Cells were incubated for 1 hr at room temperature in Alexa Fluor 488 phalloidin (6.6 mM, Invitrogen/Molecular Probes, Chicago, IL) prior to epifluorescence imaging (IX 81, Olympus)[26].

5.4.9 Scanning electron microscopy

For environmental scanning electron microscopy (ESEM, FEI-XL30) imaging, HL-60 cells were adhered to a P-selectin-conjugated silicon wafer. Cells were fixed with 2.5 vol % glutaraldehyde for 10 min, followed by 2 vol % osmium tetroxide (OsO_4) for 10 min all at room temperature. Fixed HL-60 cells were transferred to a series of graded ethanol/water solutions of increasing ethanol concentration: 25%, 50%, 75%, and 100%. HL-60 cells in 100 vol% ethanol solution were transferred to 1:1 ethanol/hexamethyldisilazane (HMDS) solution and finally to 100 vol% HMDS[57]. Cells were then air-dried before SEM imaging. Images were acquired in secondary electron mode under beam energy of 2.0 KeV.

5.5 CHAPTER SUMMARY AND CONCLUSION

Dynamics of P-selectin/PSGL-1 complexes with respect to shear flow are known to play a key role in rolling of cells including HL-60 leukemia cells. In this chapter, we suggested a new mechanism whereby cytoskeletal actin dynamics modulate dissociation of P-selectin/PSGL-1 complexes during cell rolling. Through atomic force microscope (AFM) cantilever-enabled cell force spectroscopy, we measured the picoNewton-scale, actin-mediated force generated by the cell at such complexes on HL-60 surfaces. Through oscillation of these ligand-conjugated AFM probes to image receptor distribution, termed functionalized force imaging or recognition imaging, we also estimated the intracellular force transmitted through a single ligand-receptor complex. These results indicated that intracellular force generated against this molecular complex is dependent upon cytoskeletal actin dynamics and contributes directly to unbinding of these complexes during shear flow rolling of HL-60 cells.

REFERENCES

1. Lee S, Hong, S., Lundin, V., Zhang, H., Karp, J. M., Langer, R., and Van Vliet, K. J. PicoNewton-scale cytoskeletal actin force dynamics play a key role in cell rolling. Submitted 2009.
2. Lasky LA. Selectin-Carbohydrate Interactions and the Initiation of the Inflammatory Response. Annu Rev Biochem 1995;64:113-139.
3. Tedder TF, Steeber, D. A., Chen, A., Engel, P. The Selectins - Vascular Adhesion Molecules. FASEB J 1995;9(10):866-873.
4. McEver RP. Selectins. Curr Opin Immunol 1994;6(1):75-84.
5. Simon SI, and Green, C. E. Molecular mechanics and dynamics of leukocyte recruitment during inflammation. Annu Rev Biomed Eng 2005;7:151-185.
6. Alon R, Hammer, D. A., Springer, T. A. Lifetime of the P-Selectin-Carbohydrate Bond and Its Response to Tensile Force in Hydrodynamic Flow. Nature 1995;374(6522):539-542.
7. Alon R, Kassner, P. D., Carr, M. W., Finger, E. B., Hemler, M. E., Springer, T. A. The Integrin Vla-4 Supports Tethering and Rolling in Flow on Vcam-1. J Cell Biol 1995;128(6):1243-1253.
8. Bell GI. Models for the specific adhesion of cells to cells. Science 1978;200(12):618-627.
9. Marshall BT, Long, M., Piper, J. W., Yago, T., McEver, R. P., Zhu, C. Direct observation of catch bonds involving cell-adhesion molecules. Nature 2003;423(6936):190-193.
10. Hanley W, McCarty, O., Jadhav, S., Tseng, Y., Wirtz, D., Konstantopoulos, K. Single Molecule Characterization of P-selectin/Ligand Binding. J Biol Chem

2003;278:10556–10561.

11. Chang WC, Lee, L. P., Liepmann, D. Biomimetic technique for adhesion-based collection and separation of cells in a microfluidic channel. Lab Chip 2005;5(1):64-73.

12. Caputo KE, Lee, D., King, M.R., Hammer, D.A. Adhesive Dynamics Simulations of the Shear Threshold Effect for Leukocytes. Biophys J 2007;92:787–797.

13. Dong C, Lei, X. X. Biomechanics of cell rolling: shear flow, cell-surface adhesion, and cell deformability. J Biomech 2000;33:35-43.

14. Jadhav S, Eggleton, C. D., Konstantopoulos, K. A 3-D computational model predicts that cell deformation affects selectin-mediated leukocyte rolling. Biophys J 2005;88:96-104.

15. Fritz J, Katopodis, A.G., Kolbinger, F., Anselmetti, D. Force-mediated kinetics of single P-selectinyligand complexes observed by atomic force microscopy. Proc Natl Acad Sci USA 1998;95:12283-12288.

16. King MR, Heinrich, V., Evans, E., Hammer, D.A. Nano-to-Micro Scale Dynamics of P-Selectin Detachment from Leukocyte Interfaces. III. Numerical Simulation of Tethering under Flow. Biophys J 2005;88:1676–1683.

17. Ramachandran V, Williams, M., Yago, T., Schmidtke, D. W., McEver, R. P. Dynamic alterations of membrane tethers stabilize leukocyte rolling on P-selectin. Proc Natl Acad Sci USA 2004;101:13519–13524.

18. Danuser G. Coupling the dynamics of two actin networks - new views on the mechanics of cell protrusion. Biochem Soc Trans 2005;33:1250-1253.

19. Galbraith CG, Yamada, K. M., Sheetz, M. P. The relationship between force and

focal complex development. J Cell Biol 2002;159:695–705.

20. Mogilner A, Oster, G. Force Generation by Actin Polymerization II: The Elastic Ratchet and Tethered Filaments. Biophys J 2003;84:1591–1605.

21. Takagi Y, Homsher, E. E., Goldman, Y. E., Shuman, H. Force Generation in Single Conventional Actomyosin Complexes under High Dynamic Load. Biophys J 2006;90:1295–1307.

22. Zhua J, Carlsson, A. E. Growth of attached actin Filaments. Eur Phys J E 2006;21:209-222.

23. Snapp KR, Heitzig, C.E., and Kansas, G.S. Attachment of the PSGL-1 cytoplasmic domain to the actin cytoskeleton is essential for leukocyte rolling on P-selectin. Blood 2002;99:4494-4502.

24. Galbraith C, Sheetz, M. P. A micromachined device provides a new bend on fibroblast traction forces. Proc Natl Acad Sci USA 1997;94:9114–9118.

25. Hammer DA, Apte, S. M. Simulation of cell rolling and adhesion on surfaces in shear flow: general results and analysis of selectin-mediated neutrophil adhesion. Biophys J 1992;63:35-57.

26. Lee S, Mandic, J., Van Vliet, K. J. Chemomechanical mapping of ligand–receptor binding kinetics on cells. Proc Natl Acad Sci USA 2007;104:9609–9614.

27. Merkel R, Nassoy, P., Leung, A., Ritchie, K., Evans, E. Using dynamic force spectroscopy to explore energy landscapes of receptor-ligand bonds. Nature 1999;397:50-53.

28. Stroh C, Wang, H., Bash, R., Ashcroft, B., Nelson, J., Gruber, H., Lohr, D., Lindsay, S. M., Hinterdorfer, P. Single-molecule recognition imaging microscopy. Proc Natl Acad Sci USA 2004;101:12503-12507.

29. Sun Z, Martinez-Lemus, L. A., Hill, M. A., and Meininger, G. A. Extracellular matrix-specific focal adhesions in vascular smooth muscle produce mechanically active adhesion sites. Am J Physiol Cell Physiol 2008;295:268-278.

30. Chtcheglova LA, Waschke, J., Wildling, L., Drenckhahn, D., Hinterdorfer, P. Nano-Scale Dynamic Recognition Imaging on Vascular Endothelial Cells. Biophys J 2007;93:L11 - L13.

31. Schliwa M. Action of cytochalasin D on cytoskeletal networks. J Cell Bio 1982;92:79-91.

32. Hong S, Lee, D., Zhang, H., Zhang, J. Q., Resvick, J. N., Khademhosseini, A., King, M. R., Langer, R., Karp, J. M. Covalent immobilization of p-selectin enhances cell rolling. Langmuir 2007;23(24):12261-8.

33. Sheikh S, Nash, G. B. Treatment of neutrophils with cytochalasins converts rolling to stationary adhesion on P-selectin. J Cell Physiol 1998;174(2):206-16.

34. Aigner S, Sthoeger, Z. M., Fogel, M., Weber, E., Zarn, J., Ruppert, M., Zeller, Y., Vestweber, D., Stahel, R., Sammar, M., Altevogt, P. CD24, a Mucin-Type Glycoprotein, Is a Ligand for P-Selectin on Human Tumor Cells. Blood 1997;89:3385-3395.

35. Miner JJ, Xia, L., Yago, T., Kappelmayer, J., Liu, Z., Klopocki, A. G., Shao, B., McDaniel, J. M., Setiadi, H., Schmidtke, D. W., McEver, R. P. Separable requirements for cytoplasmic domain of PSGL-1 in leukocyte rolling and signaling under flow. Blood 2008;112:2035-2045.

36. Parlato S, Giammarioli, A. M., Logozzi, M., Lozupone, F., Matarrese, P., Luciani, F., Falchi, M., Malorni, W., Fais, S. CD95 (APO-1/Fas) linkage to the actin cytoskeleton through ezrin in human T lympocytes: a novel regulatory

mechanism of the CD95 apoptotic pathway. EMBO J 2000;19:5123-5134.

37. Giannone G, Dubin-Thaler, B. J., Rossier, O., Cai, Y., Chaga, O., Jiang, G., Beaver, W., Dobereiner, H. -G., Freund, Y., Borisy, G., Sheetz, M. P. Lamellipodial Actin Mechanically Links Myosin Activity with Adhesion-Site Formation. Cell 2007;128:561-675.

38. Karnik R, Hong, S., Zhang, H., Mei, Y., Anderson, D. G., Karp, J. M., Langer, R. Nanomechanical Control of Cell Rolling in Two Dimensions through Surface Patterning of Receptors. Nano Lett 2008;8:1153–1158.

39. Hinterdorfer P, Dufrêne, Y. F. Detection and localization of single molecular recognition events using atomic force microscopy. Nat Methods 2006;3:347 - 355.

40. Van Vliet KJ, Hinterdorfer, P. Probing drug-cell interactions. Nano Today 2006;1:18-25.

41. Itoh S, Susuki, C., Takeshita, K., Nagata, K., and Tsuji, T. Redistribution of P-selectin glycoprotein ligand-1 (PSGL-1) in chemokine-treated neutrophils: a role of lipid microdomains. J Leukocyte Biol 2007;81:1414-1421.

42. Walton EB, Lee, S., Van Vliet, K.J. Extending Bell's model: how force transducer stiffness alters measured unbinding forces and kinetics of molecular complexes. Biophys J 2008;94:2621–2630.

43. Geiger B, Bershadsky, A. Assembly and mechanosensory function of focal contacts. Curr Opin Cell Biol 2001;13:584–592.

44. Ma Z, Janmey, P. A., Finkel, T.H. The receptor deformation model of TCR triggering. FASEB J 2008;22:1002-1008.

45. Alon R, Hammer DA, Springer TA. Lifetime of the P-Selectin-Carbohydrate

Bond and Its Response to Tensile Force in Hydrodynamic Flow. Nature 1995;374(6522):539-542.

46. Majstoravich S, Zhang, J., Nicholson-Dykstra, S., Linder, S., Friedrich, W., Siminovitch, K. A., Higgs, H. N. Lymphocyte microvilli are dynamic, actin-dependent structures that do not require Wiskott-Aldrich syndrome protein (WASp) for their morphology. Blood 2004;104:1396-1403.

47. Hasslen SR, von Andrian, U. H., Butcher, E. C., Nelson, R. D., Erlandsen, S. L. Spatial distribution of L-selectin (CD62L) on human lymphocytes and transfected murine L1-2 cells. Histochem J 1995;27:547-554.

48. Nijhara R, van Hennik, P. B., Gignac, M. L., Kruhlak, M. J., Hordijk, P. L., Delon, J., Shaw, S. Rac1 mediates collapse of microvilli on chemokine-activated T lymphocytes. J Immunol 2004;173:4985-4993.

49. Gorelik J, Shevchuk, A. I., Frolenkov, G. I., Diakonov, I. V., Lab, M. J., Kros, C. J., Richardson, G. P., Vodyanoy, I., Edwards, C. R. W., Klenerman, D., Korchev, Y, E. Dynamic assembly of surface structures in living cells. Proc Natl Acad Sci USA 2003;100:5819–5822.

50. Deen WM. Anal Transp Phenom: Oxford University Press; 1998.

51. Alon R, Chen, S., Puri, K. D., Finger, E. B., and Springer, T. A. The Kinetics of L-selectin Tethers and the Mechanics of Selectin-mediated Rolling. J Cell Biol 1997;138:1169–1180.

52. Smith MJ, Berg, E. L., and Lawrence, M. B. Å Direct Comparison of Selectin-Mediated Transient, Adhesive Events Using High Temporal Resolution. Biophysical Journal 1999;77:3371–3383.

53. Butt HJ, and Jaschke, M. Calculation of thermal noise in atomic force

microscopy. Nanotechnology 1995;6:1-7.

54. Hutter JL, and Bechhoefer, J. Calibration of atomic- force microscope tips. Rev Sci Instrum 1993;64:1868-1873.

55. Thompson MT, Berg, M. C., Tobias, I. S., Rubner, M. F., Van Vliet, K. J. Tuning compliance of polyelectrolyte multilayers to modulate cell adhesion. Biomaterials 2005;26:6836-6845.

56. Walton EB, Lee, S., and Van Vliet, K.J. Extending Bell's model: how force transducer stiffness alters measured unbinding forces and kinetics of molecular complexes. Biophysical Journal 2008;94:2621–2630.

57. Parlato S, Giammarioli, A.M., Logozzi, M., Lozupone, F., Matarrese, P., Luciani, F., Falchi, M., Malorni, W., and Fais, S. CD95 (APO-1/Fas) linkage to the actin cytoskeleton through ezrin in human T lympocytes: a novel regulatory mechanism of the CD95 apoptotic pathway. The EMBO Journal 2000;19:5123-5134.

Chapter 6 Conclusion

6. 1 THESIS SUMMARY

Throughout this thesis, AFM-based functionalized force imaging and force spectroscopy analysis were the main tools developed for visualization of nanometer-scale molecules on materials and cell membranes, for measuring elastic moduli of materials and cells, as well as for the measurement of picoNewton (pN)-scale cell-generated force dynamics. Immobilization of biological molecules on cantilevered probes was confirmed in each step of probe chemistry. Thus, the role of force dynamics in cell attachment, migration, and rolling relevant to chemomechanics of the microvasculature was studied (Fig. 6.1).

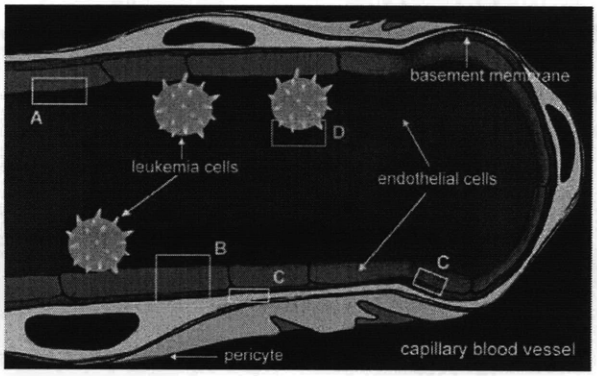

Figure 6.1 Overall structure of this thesis. (A) In chapter 2, endothelial cell membrane receptors were mechanically visualized through AFM-based functionalized force imaging. (B) In chapter 3, mechanical interaction between endothelial cells and pericytes that envelop capillary blood vessels was studied through AFM-based indentation and with pharmacological inhibitors. (C) In chapter 4, mechanical interaction between cells and underlying substrata, mediated by focal complexes, was studied through AFM-based real time force spectroscopy and with pharmacological reagents: in the schematic above, two rectangles (C) represent the interaction between pericytes and the basement membrane and interaction between endothelial cells and the basement membrane. (D) In chapter 5, mechanical interaction between endothelial cells and leukemia cells (HL-60 cells) in cell rolling was studied through AFM-based real time force spectroscopy and with pharmacological inhibitors. This thesis focuses on mechanical interactions in capillary blood vessels: relations among endothelial cells, pericytes, leukemia cells, and underlying substrata of cells.

Chapter 1 provided the motivation for this thesis: chemomechanical properties of materials and cells. This chapter explained the underlying principles of AFM imaging techniques which include contact mode and tapping mode. In particular, magnetic tapping mode is an advanced tapping mode for compliant biological materials such as cells and proteins. The important new use of force spectroscopy, which has been widely used by others for measuring molecular unbinding force, was to measure cell-generated forces in response to normal forces exerted by AFM probes. An important concept of mechanical communication in cell systems, mechanotransduction was summarized as a main cellular mechanism for which experimental approaches introduced above were all utilized.

Chapter 2 demonstrated that individual receptors can be mapped on cell surfaces, with whole cell binding kinetics determined by means of functionalized force imaging. This was achieved by atomic force microscopy and molecular force spectroscopy of intact cells with biomolecule-conjugated mechanical probes (see Fig. 6.1A). The number, distribution, and association / dissociation rate constants of vascular endothelial growth factor receptor-2 (VEGFR2) were quantified with respect to anti-VEGFR2 antibody on both living and fixed human umbilical vein endothelial cells. The direct receptor imaging via functionalized force imaging enabled the calculation of binding kinetics and the visualization of the non-uniform distribution of VEGFR2 with respect to the underlying cytoskeleton, providing spatiotemporal visualization of cell surface dynamics. The existence of a new, specific receptors for an oligopeptide, Loop 6, isolated from tissue inhibitor of metalloproteinase-2 (TIMP-2) was verified via functionalized force imaging using loop 6-functionalized AFM cantilevers, followed by the identification of Loop 6 receptors, insulin like growth factor receptor-1 (IGFR-1)

with blocking experiments with anti-IGFR-1 antibody. In addition, thermodynamic parameters of ligand-receptor pairs including biotin-streptavidin and VEGFR2-anti-VEGFR2 pairs were calculated using temperature-controlled AFM methods, together with functionalized force imaging.

In Chapter 3, it was demonstrated that mechanical interaction between endothelial cells and pericytes that physically surround the capillary endothelium, communicating with associated endothelial cells via cell- and matrix-bound contacts, may directly influence pathophysiological angiogenesis (see Fig. 6.1B). By means of an atomic force microscope (AFM)-enabled nanoindentation, the F-actin- and actomyosin-based dependence of microvascular pericyte microdomain stiffness was quantified as a function of PDMS substrata wrinkling: mechanisms of pericyte- and contractile protein-generated force transduction and substrata deformation were directly interrogated by the addition of cytoskeletal-specific pharmacological disrupting agents/inhibitors. F-actin-mediated dependence was observable via changes in cell shape and membrane stiffness, which corresponded to F-actin (de)polymerization and/or inhibition of actomyosin ATPase-mediated contraction. Together with the nonlinear elastic stress-strain response of the PDMS substrata materials, these experiments demonstrated that actin-mediated forces can modify effective elastic moduli of substrata by 150 %. This suggests that the modified mechanical properties of the substrata through such pericyte-generated forces may affect cell-matrix and cell-cell interactions *in vivo*.

Chapter 4 presented AFM-enabled measurements of intracellular force dynamics at focal complexes, through which intracellularly generated forces were measured with pN scale force resolution and millisecond temporal resolution (see Fig. 6.1C). It was found that the force at focal complexes is cyclic, with distinct force peaks.

Through AFM-enabled functionalized force imaging, the number of fibronectin (FN)/integrin pairs within such complexes and the magnitude of force transmitted through individual FN/integrin complexes were estimated. Together with pharmacological challenges to actin-mediated force generation, these direct observations demonstrated that cytoskeletal force can be sufficient to immediately rupture FN/integrin pairs, suggesting that ligand-receptor binding within focal complexes is in a dynamic equilibrium that can be modulated in part by intracellular force generation.

In Chapter 5, a new mechanism whereby cytoskeletal actin dynamics in leukemia cells (HL-60 cells) governs the dissociation of P-selectin/PSGL-1 complexes within cell rolling was suggested via AFM-based force spectroscopy analysis (see Fig. 6.1D). Specifically, the intracellular dynamics of HL-60 cells was measured via AFM-based real time force spectroscopy, and the number of P-selectin/PSGL-1 complexes involved was measured via functionalized force imaging of P-selectin-conjugated substrata. This enabled the calculation of intracellular force transmitted through single P-selectin/PSGL-1 complexes. Intracellular force generated by the actin cytoskeleton through single P-selectin/PSGL-1 complexes, combined with drag force through which the blood flow pushes rolling cells, exceeded force required to rupture P-selectin/PSGL-1 molecular complexes at particular loading rates. This suggested that, for HL-60 cells to roll, intracellular dynamic force should be considered in addition to the luid flow shear force.

In summary, this thesis has demonstrated that mechanical properties of biological materials and subcellular domains can be quantified and nanometer scale single molecules can be visualized to map the binding kinetics of ligand-receptor pairs.

In addition, it has been shown that intracellularly generated force dynamics are crucial for cell attachment and migration of adherent cells, and the rolling of leukemia cells. Throughout this thesis, various cellular systems have been explored for intracellular and extracellular mechanical interaction: endothelial cells, pericytes, leukemia cells, and fibroblasts. These results have provided and will provide new insights into open questions in cell mechanotransduction.

6.2 OUTLOOK AND SUGGESTIONS FOR FUTURE RESEARCH

The first part of this thesis (Chapter 2) demonstrated the way to visualize small molecules using AFM-based functionalized force imaging. Counting the number of molecules conjugated to surfaces has been conducted in different ways by other researchers, including radiolabeling methods (*1-3*) and fluorescence activated cell sorting (FACS)-based method (*4*), both of which are population-averaged methods. In contrast, the advantages of functionalized force imaging are the direct visualization of nanometer scale molecules in real-time without destroying compliant samples. This makes it possible to quantify the number and distribution of these molecules on surfaces. In addition to imaging VEGFR2 and biotin in Chapter 2, functionalized force imaging was useful for the quantification of the number of conjugated protein molecules on substrata: the visualization of fibronectin and PSGL-1 & P-selectin molecules on glass substrata in Chapters 4 and 5. Nevertheless, for functionalized force imaging to be a better imaging technique, the efficiency of imaging should be improved: imaging quality and efficiency depend on conjugation chemistry such as the orientation of conjugated molecules, the uniform layer conjugation, and the linker selection that can maximize the spatial room for conjugated molecules to bind to epitopes. One example is

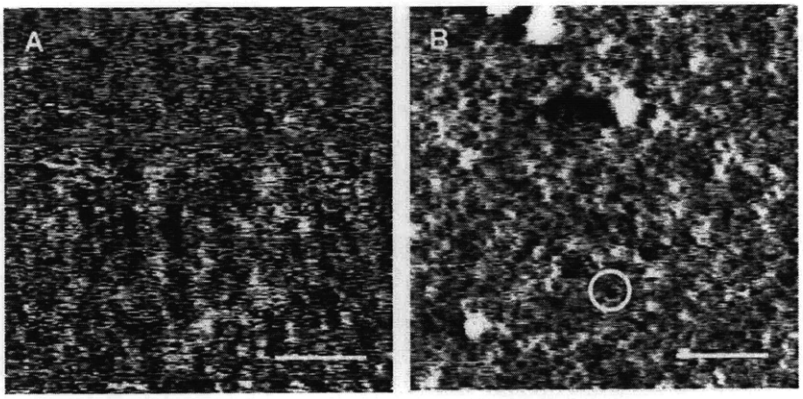

Figure 6.2 P-selectin conjugation on glass substrata without and with a specific linker. (A) P-selectin is conjugated to a glass substratum via physisorption. Binding sites are spread over the substratum, and P-selectin molecules are aggregated. (B) P-selectin was conjugated with a linker that has a maleimide group at one end. Dark spots (as represented with a white circle), which represent specific P-selectin-PSGL-1 interactions and therefore P-selectin molecules, are distributed with a regular spacing. P-selectin molecules do not aggregate. Scale bars = 300 nm.

the conjugation of P-selectin on the glass surface. It is known that P-selectin has only one cysteine amino acid on the opposite side of a PSGL-1 binding pocket (*5*). When a linker that has a maleimide group at one end of the linker was used and the binding pocket was directly exposed to outside the molecule, the imaging efficiency increased by three times as shown in Fig. 6.2. More research on conjugation chemistry should be conducted for improving the imaging quality and efficiency for AFM imaging and force spectroscopy analysis.

In Chapter 3, a new concept of mechanical effects of pericytes on angiogenesis was suggested. The factors that have been known to influence angiogenesis are various, including mechanical environment of blood vessels (*6-9*) and pericyte-endothelial cells communication (*10-12*). However, the mediators of pericytes in communication with endothelial cells have been limited to chemical factors such as growth factors or Rho-GTPase (*13*). However, the suggestion made in chapter 3 about pericyte-angiogenesis is different from the reports above. Pericytes, as a perivascular cell type that surrounds

capillary blood vessels, expresses smooth muscle actin and plays a similar role to that of smooth muscle cells (*14*). Therefore, pericytes can exert greater stresses than other cell types. As suggested in Chapter 3, pericytes can change the stiffness of underlying substrata, which may imply that pericytes are capable of changing the mechanical properties of the basement membrane on which both endothelial cells and pericytes grow *in vivo*. Therefore, pericytes may mechanically change the effective stiffness of the basement membrane, providing endothelial cells with modified mechanical environment, eventually affecting angiogenesis. To confirm this hypothesis, endothelial cell-pericyte co-culture study is needed. In addition, membranes such as matrigels that resemble the basement membrane *in vivo* would be useful to verify the hypothesis that endothelial cell phenotype is affected by mechanical stress of pericytes that modifies the mechanical environment during endothelial cells-pericytes communication.

Ongoing research topics on pericyte force exertion are about the effect of calpain on cell membrane stiffness. Calpain is a Ca^{2+} dependent protease involved in the physical attachment of talin to focal complexes (*15, 16*). Calpain affects the physical attachment of the actin cytoskeleton, adaptor proteins in focal complexes, and integrins. As demonstrated in Chapter 3, the mechanical stiffness of pericyte plasma membrane was influenced by actin-specific reagents such as blebbistatin and latrunculin A. Therefore, the current hypothesis is that calpain, which affects talin, may change the membrane stiffness by changing the physical connection between the actin cytoskeleton and integrin dimers. More experiments with calpain and calpastain, which is a calpain inhibitor, would demonstrate the effects of calpain on the plasma membrane stiffness.

In Chapters 3 and 4, pharmacological reagents that specifically bind to the actin cytoskeleton and microtubules were studied. As also mentioned in the chapters, the

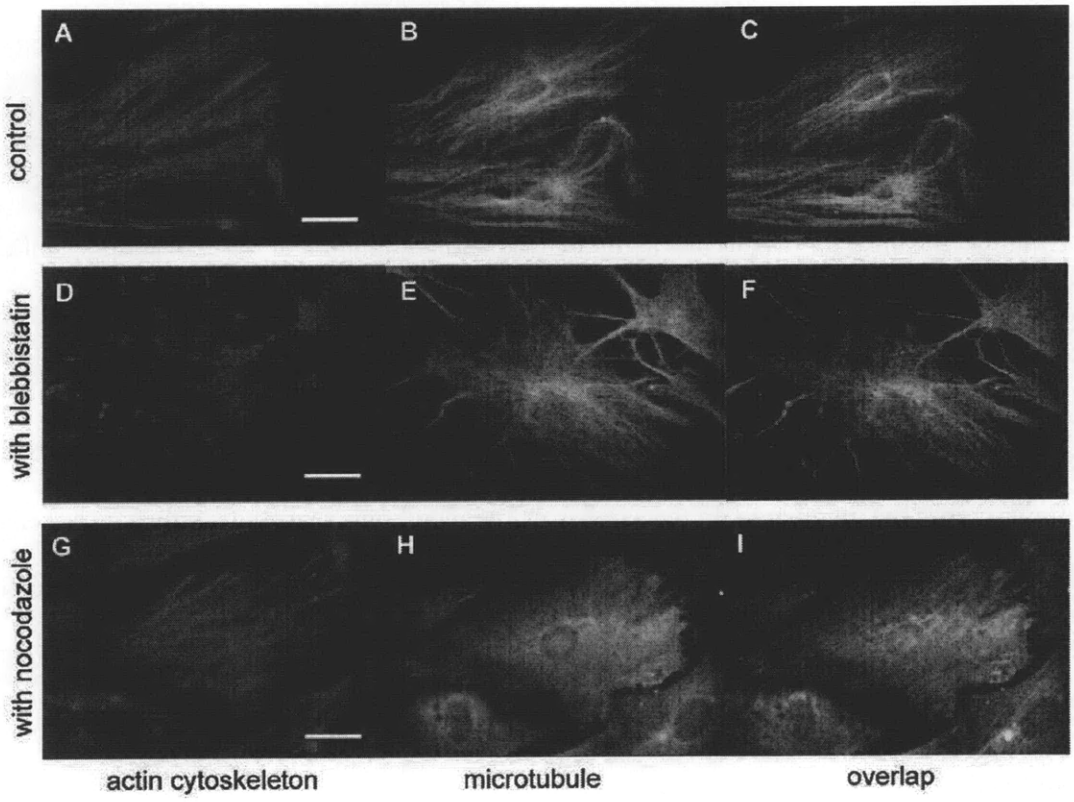

Figure 6.3 The actin cytoskeleton and microtubule of pericytes stained with rhodamine-phalloidin and alexa 488-secondary antibody 1 hour after incubation with blebbistatin (25 μM) and nocodazole (1 μM). (A), (D), and (G) represent the actin cytoskeleton stained in red; (B), (E), and (H), microtubule in green; (C), (F), and (I), actin and microtubule images overlapped. (A – C) represent control: pericytes with no pharmacological inhibitors; (D – F) after 1 hour incubation with blebbistatin; (G – I), actin and microtubule overlapped with nocodazole. Blue objects are nuclei stained with DAPI. Scale bars = 20 μm.

actin cytoskeleton and microtubules are in crosstalk, regulated by myosin IIA (*17*). My results also suggest that the addition of actin-specific reagents such as blebbistatin and latrunculin A activated microtubule, triggering dramatic change in cell morphology (Fig. 6. 3). In contrast, when a microtubule specific reagent, nocodazole, was added, microtubule fibers disappeared but actin stress fibers were thickened (Fig. 6.3). These images strongly support the idea of crosstalk between the actin cytoskeleton that reinforce cell attachment and microtubules that trigger cell migration. More research on the maintenance of cellular structure via the actin-microtubule crosstalk should be

conducted to establish whether there exists a mechanical balance between the actin cytoskeleton and microtubules.

In Chapter 5, it was demonstrated that leukemia cells cannot roll on P-selectin-conjugated substrata when the actin cytoskeleton is inhibited by an actin-specific pharmacological inhibitor. This provides the possibility of filtering cancer cells or leukemia cells. For example, a dialysis membrane as a replacement for the loss of kidney function is used to filter the blood for therapeutic hemodialysis, where blood flows across the membrane. In the same way, the membrane that filters only cancer cells or leukemia cells involved in cancer metastasis could be developed through the cell rolling mechanism presented in Chapter 5.

REFERENCES

1. L. R. Perk, Visser, G. W. M., Budde, M., Vosjan, M. J. W. D., Jurek, P., Kiefer, G. E., and van Dongen, G. A. M. S. , *Nature Protocols*, 10.1038/nprot.2008.22 (2008).
2. P. Scheidegger, Weiglhofer, W., Suarez, S., Console, S., Waltenberger, J., Pepper, M. S., Jaussi, R., and Ballmer-Hofer, K., *Biochemical Journal* **353**, 569 (2001).
3. J. Waltenberger, Claesson-Welsh, L., Siegbahnll, A., Shibuya, M. & Heldin, C.-H., *Journal of Biological Chemistry* **269**, 26988 (1994).
4. S. Serke, van Lessen, A., and Huhn, D., *Cytometry* **33**, 179 (1998).
5. S. Hong *et al.*, *Langmuir* **23**, 12261 (Nov 20, 2007).
6. A. B. Baker, and Sanders, J. E., *Microvascular Research* **60**, 177 (2000).
7. L. Krishnan, Underwood, C. J., Maas, S., Ellis, B. J., Kode, T. C., Hoying, J. B., and Weiss, J. A., *Cardiovascular Research* **78**, 324 (2008).
8. J.-S. Silvestre, Levy, B. I., and Tedgui, A., *Cardiovascular Research* **78**, 201 (2008).
9. A. M. van Rij, Jones, G. T., Hill, B. G., Amer, M., Thomson, I. A., Pettigrew, R. A., and Packer, S. G. K., *Circulation* **118**, 66 (2008).
10. C. Cursiefen, Hofmann-Rummelt, C., Küchle, M., Schlötzer-Schrehardt, U., *British Journal of Ophthalmology* **87**, 101 (2003).
11. V. Nehls, Denzer, K., and Drenckhahn, D., *Cell and Tissue Research* **270**, 469 (2004).
12. U. Ozerdem, and Stallcup, W. B., *Angiogenesis* **7**, 269–276 (2004).
13. M. E. Kutcher, Kolyada, A. Y., Surks, H. K., and Herman, I. M., *The American Journal of Pathology* **171**, 693 (2007).

14. R. H. Adams, and Alitalo, K., *Nature Review Molecular Cell Biology* **8**, 464 (2007).

15. S. J. Franco, Rodgers, M. A., Perrin, B. J., Han, J., Bennin, D. A., Critchley, D. R., and Huttenlocher, A., *Nature Cell Biology* **6**, 977 (2004).

16. S. J. Franco, and Huttenlocher, A., *J Cell Sci* **118**, 3829 (2005).

17. S. Even-Ram, Doyle, A.D., Conti, M.A., Matsumoto, K., Adelstein, R.S., and Yamada, K.M., *Nat Cell Biol* **9**, 299 (2007).

Appendix A

Modulation of hepatocyte phenotype in vitro via chemomechanical tuning of polyelectrolyte multilayers

This appendix contains parts of the following study published in 2008 with co-authors of Alice A. Chen, Salman Khetani, Sangeeta N. Bhatia (1). My contribution to this work is to measure the elastic moduli of polyelectrolyte multilayers to see the chemomechanical effects of underlying substrata on hepatocyte phenotype and attachment.

A. 1 INTRODUCTION

Tissue functions depend on the reciprocal and dynamic interactions of cells with their surrounding microenvironment or niche, which includes neighboring cells as well as biochemical, physical, and mechanical stimuli. Accordingly, it is becoming increasingly clear that the development of functional in vitro models of tissue patho/physiology depends on the ability to understand, predict, and harness the chemical and mechanical properties of extracellular substrata (*2, 3*). Several descriptive studies have highlighted the cooperative effects of ligand presentation and substrata stiffness on cellular functions ranging from adhesion and motility to morphogenesis and remodeling (*4, 5*); furthermore, these findings have led to the development of new synthetic substrata offering improved control over independent biochemical and mechanical cues (*6-13*). In particular, poly(acrylamide) (PA) hydrogels of approximate elastic modulus (E) of 10^1-10^5 Pa have been surface-functionalized with adhesion proteins or ligands, and used extensively to study

chemomechanical effects on a variety of cell fate processes including fibroblast migration and contractility (*6*), endothelial cell adhesion (*7, 8*), myotube formation (*9*), stem cell differentiation (*10*), and hepatocyte spreading (*11*). Polyethylene glycol (PEG)-based substrata exhibiting similar E comparable to those of PA hydrogels have also been used to evaluate the effects of mechanical compliance on cellular morphology and phenotype (*12*). However, because changes in composition or extent of crosslinking in natural and aforementioned synthetic systems may also affect surface ligand density, configurations, and distensibility (*13*), the interplay between biochemical and mechanical cues on cellular fates has not yet been fully decoupled. A system amenable to independent modulation of chemical composition, stiffness, and ligand presentation has the potential to help elucidate the mechanisms of cooperative chemomechanical feedback, as well as aid in the development of highly functional in vitro models of tissues.

Weak polyelectrolyte multilayers (PEMs) comprising poly(acrylic acid)/poly(allyl amine hydrochloride) are ionically crosslinked hydrogels that serve as a robust model system with unique advantages for decoupling the effects of chemical and mechanical stimuli on cellular processes. Distinct from PA or PEG synthetic systems, the elastic modulus of these weak PEM substrata is varied over several orders of magnitude ranging 10^4 – 10^8 Pa through control of layer-by-layer (LbL) assembly pH (*8*). LbL assembly is performed by alternately dipping substrates (e.g., glass or tissue culture polystyrene, TCPS) in solutions of polyanion and polycation chains with defined pH; for these weak PEMs, the degree of ionic crosslinking between the polyanion and polycation chains, and thus the mechanical stiffness defined by E, increases as pH increases from pH 2.0 to pH 6.5. Extensive characterization of these

PEM films, hydrated at near-neutral pH in water or buffered cell media, has confirmed that assembly pH reliably modulates mechanical stiffness over this range, without concurrent or statistically significant differences in surface roughness, surface charge, or hydrophobicity/philicity as determined by total interaction energy (*14*). We have previously employed these weak PEMs to show that increased stiffness can enhance the adherence of vascular endothelial cells (*8*) and fibroblasts (*14*), and that ligand functionalization can inadvertently also alter mechanical stiffness (*14*). Therefore, these PEMs are uniquely suited for the independent modulation of substrata mechanical compliance and ligand presentation for cell types less amenable to sustained in vitro manipulation and function.

Here, we leverage PEMs to systematically study the effects of mechanical and biochemical cues on primary rat hepatocytes towards the development of a functional in vitro model of liver tissue. Freshly isolated primary hepatocytes are widely considered to be ideal for construction of liver tissue models useful in fundamental biological studies (*1, 15*), bio-artificial liver devices (*16*), and drug screening (*17*); yet these cells rapidly (hours to a few days) lose viability and phenotypic functions upon isolation from the native in vivo microenvironment of the liver (*1, 18*). Several studies have enhanced the phenotypic functions of hepatocytes in vitro by modifying the chemomechanical microenvironment via gels formed from natural proteins (e.g., Matrigel® (*19-21*) and collagen gel sandwiches (*22*)). However, natural gel- and sandwich- culture systems are not ideal for systematic chemomechanical manipulation and testing due to variability among protein batches and challenges in decoupling or systematically varying the mechanical and biochemical properties. Synthetic polymeric systems do not generally suffer from such disadvantages but, to date, have

not sustained hepatocytes for longer than one week without stromal cells or chemically-conjugated ligands (*23-25*). Furthermore, compliance of PEMs used in previous reports was not quantified independently of added cellular or extracellular matrix cues. Thus, the systematic and reproducible investigation of biochemical and mechanical stimuli on pure hepatic phenotype has not been fully explored towards facile engineering of defined PEM microenvironments which influence broad classes of liver-specific functions over extended in vitro culture.

In this study, weak PEM substrata with elastic moduli ranging from 10^5 to 10^8 Pa were used to evaluate the independent and synergistic effects of multiple biochemical cues (type I collagen, proteoglycan decorin) and mechanical compliance on the adhesion, morphology and phenotypic functions of primary rat hepatocytes. Hepatocyte functions were evaluated on substrata that were chemomechanically optimized to promote the attachment and retention of hepatic spheroids, which have previously been shown to stabilize several liver-specific functions (*26-28*). More specifically, we demonstrated retention of broad classes of hepatic functions (albumin secretion, urea synthesis and CYP450 1A activity) for two weeks on optimized PEMs, as compared to the well-known loss of phenotype of primary hepatocytes on collagen-coated TCPS and to shorter retention durations achieved via other synthetic hydrogels. We also observed that substrata stiffness modulated the functional effects of substrata-bound decorin ligand on the duration and levels of hepatic functions. Decorin, previously shown to induce functions in primary rat hepatocytes when presented on collagen-coated TCPS (*1*), retained such behavior on stiff PEMS; however, this proteoglycan down-regulated hepatic functions when presented on highly compliant PEMs, a previously unreported finding. We thus conclude that liver-specific functions

are modulated strongly by the coupling between ligand presentation and mechanical compliance of the synthetic substrata, over a wide range of elastic moduli achievable in a scalable synthetic substrata platform.

A. 2 RESULTS

A.2.1 Effects of substrata compliance on hepatocyte adhesion and morphology

In order to evaluate the effect of mechanical compliance on the adhesion and morphology of primary rat hepatocytes, we assembled weak polyelectrolyte multilayer films (PEMs) of ~100 nm hydrated thickness, comprising ionically crosslinked polycationic poly(acrylic acid) (PAA) and polyanionic poly(allyamine hydrochloride) (PAH), onto tissue culture polystyrene (TCPS); see Fig. A.1A for general schematic. PEM substrata are typically described by the cation/anion pair and assembly pH for each polyelectrolyte, e.g., PAA/PAH 2.0/2.0 indicates a PEM assembled at pH 2.0 for both polyelectrolytes (*8*), but are denoted herein as PEM 2.0, etc. The assembly pH of the PEMs (e.g., PEM 2.0, 4.0, or 6.5) determines the extent of ionic crosslinking between the polycation and polyanion chains, and thus the extent of swelling and the mechanical stiffness (or, inversely, mechanical compliance) of the PEMs in solvents of pH ~ 7 (e.g., water and cell culture medium). Physical properties (*14*) and mechanical stiffness of these PEMs have been extensively characterized by our group, and indentation elastic modulus E was confirmed for the substrata assembled in this study via atomic force microscopy-enabled nanoindentation (see Materials and Methods) to range from 10^5 Pa (PEM 2.0) to 10^8 Pa (PEM 6.5). TCPS of $E \sim 10^9$ Pa (*8*) served as the rigid substratum control for our studies.

Primary rat hepatocytes were seeded onto substrata in serum-free culture

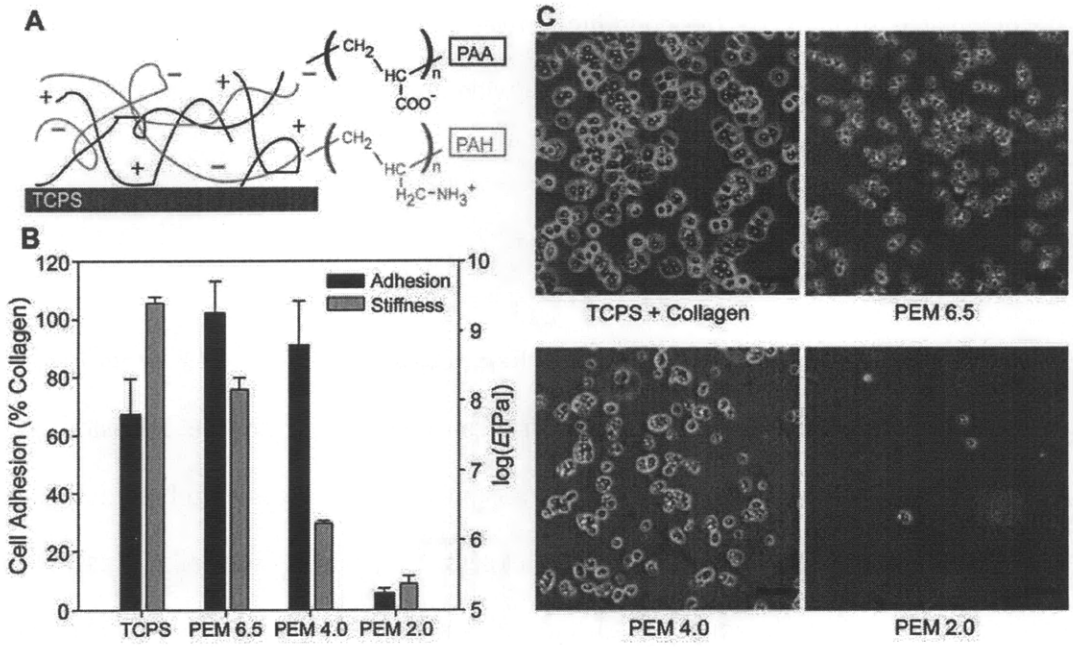

Figure A.1 Adhesion and morphology of primary rat hepatocytes on polyelectrolyte multilayers (PEMs). (A) Schematic depicting coating of tissue culture polystyrene (TCPS) with PEMs comprising interpenetrating poly(acrylic acid), PAA, and poly(allyamine hydrochloride) PAH. (B) Quantification of hepatocyte adhesion on rigid TCPS and PAA/PAH PEMs of varying compliance (assembly pH 6.5, 4.0 and 2.0). All data normalized to hepatocyte adhesion on collagen-coated TCPS. Indentation elastic modulus E for each substratum (measure of stiffness) also shown. Error bars represent SEM (n = 6-8). (C) Phase contrast micrographs showing hepatocyte morphology ~24 hours after seeding onto substrates of varying compliance. Scalebars =100 μm. Error bars represent SEM.

medium (to avoid cell attachment via serum proteins that adsorb onto the PEMs), and cell adhesion was quantified by counting cells in phase contrast micrographs acquired 6 to 8 hours after initial seeding. Attachment of hepatocytes on collagen-coated TCPS was used to normalize all subsequent adhesion values. Our results in Fig. A.1B indicate that, relative to collagen/TCPS controls, hepatocyte attachment was maximal (~100%) on PEM substrata of low compliance (PEM 6.5: E ~ 142 MPa), followed by substrata of intermediate compliance (PEM 4.0: E ~1.7 MPa and ~91% attachment relative to collagen/ TCPS). Negligible hepatocyte attachment (~5% of collagen/TCPS) was observed on the most compliant PEM substrata (PEM 2.0: E ~ 200 kPa) used in this

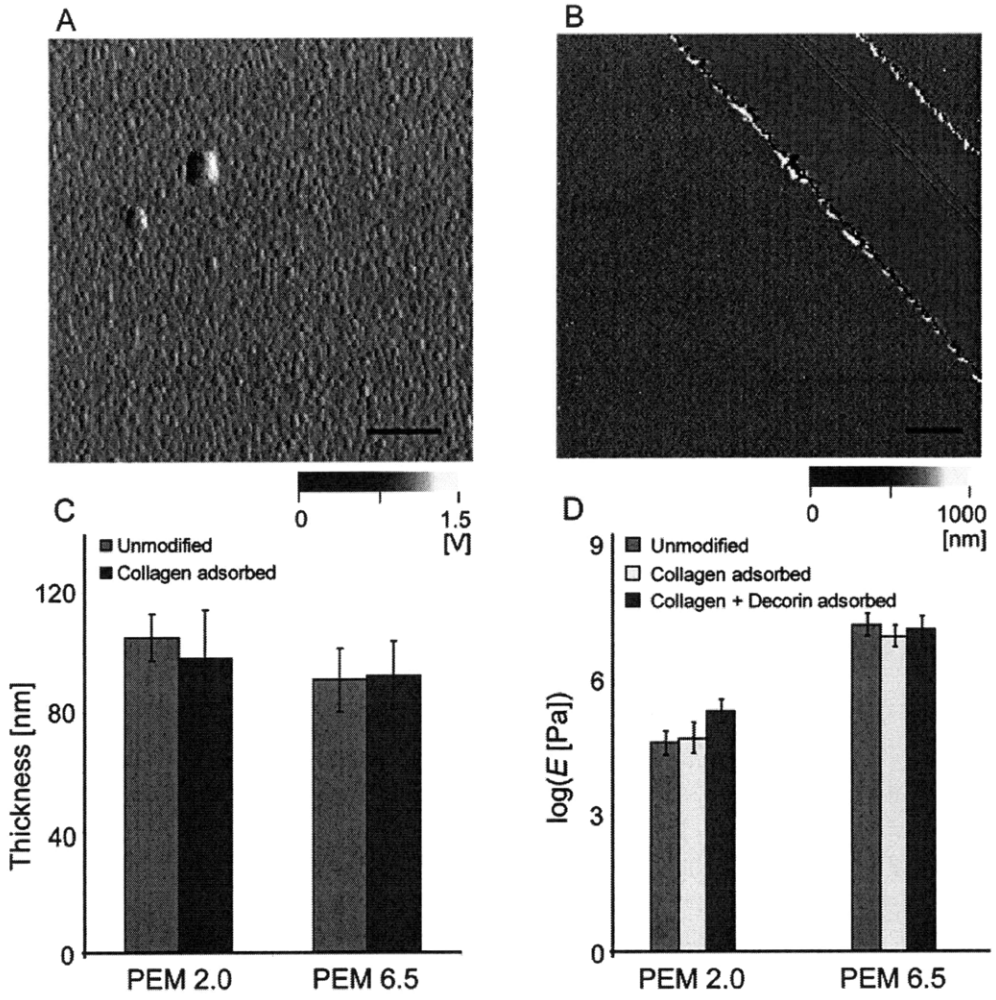

Figure A.2. PEM surface characterization. (*A*) Atomic force microscopy (deflection) image of PEM 2.0 surface hydrated in 150 mM NaCl phosphate buffered saline, pH 7.2. Scalebar = 1 μm. (*B*) Thickness of PEM with/without adsorption of collagen (+decorin) was measured from corresponding (height) image near a scratched region of the hydrated PEM surface. Scale bar = 10 μm. (*C*) Thickness of PEM substrata is unaltered by protein adsorption (100 μg/mL collagen), indicating that collagen is well-integrated at the PEM surfaces. (*D*) Effective elastic moduli E of PEM substrata differ significantly as a function of assembly pH (2.0 or 6.5), but not as a function of subsequent adsorption of collagen (+ decorin). E measured via AFM indentation of substrata hydrated in 150 mM NaCl phosphate buffered saline, pH 7.2. Error bars represent standard deviation from mean.

study. Hepatocyte attachment on rigid, unmodified TCPS (E ~ 2.5 GPa) was ~67% of that seen on collagen coated TCPS. Furthermore, hepatocytes formed spheroidal structures on PEMs 6.5 and 4.0, while cells spread upon attachment to collagen-

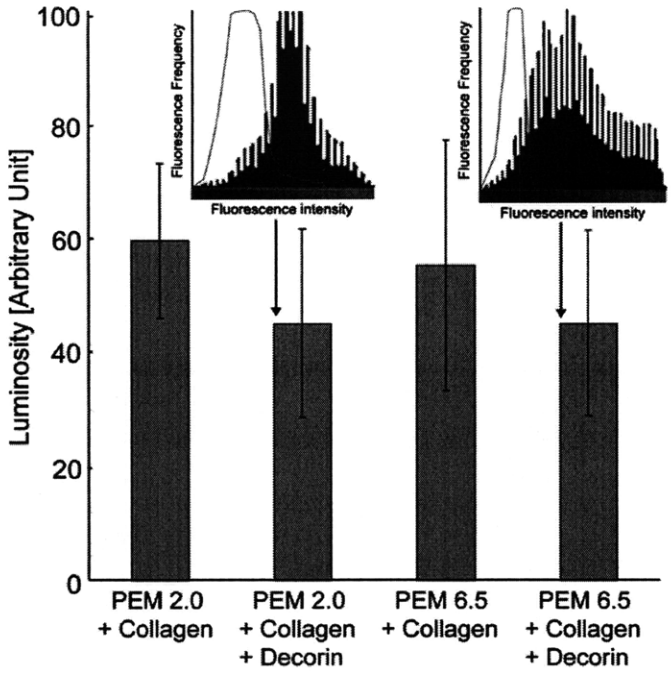

Figure A.3 Confirmation of antibody specificity and access to collagen and decorin. Collagen (100 μg/mL) ± decorin (25 μg/mL) was added to PEM 2.0 and PEM 6.5, and incubated for one hour at 37°C. Primary anti-collagen (for samples +collagen only) or anti-decorin (for samples +decorin) followed by FITC-conjugated secondary antibody (50 μg/mL) were added to each PEM to quantify the specificity and accessibility of antibody to collagen and decorin. With primary and secondary antibody, the fluorescence intensity of PEM 2.0 + collagen, PEM 2.0 + collagen + decorin, PEM 6.5 + collagen, and PEM 6.5 + collagen + decorin was 60.00 ± 13.70, 45.47 ± 16.51, 55.55 ± 22.04, and 45.50 ± 16.22 (arbitrary unit), respectively. These results were compared with control where primary and secondary antibodies were added to unmodified PEMs (-collagen and –decorin). Insets demonstrate the fluorescence signal specificity on PEM 2.0 and on PEM 6.5 (black bars), versus the fully synthetic PEM controls (gray solid line). Error bars represent SEM.

adsorbed TCPS (Fig. A.1C).

A.2.2 Chemomechanical modulation of hepatic adhesion, morphology and phenotypic functions

In order to evaluate the effect of chemomechanical stimuli on hepatocyte behavior, we modified the two PEM substrata of maximally disparate mechanical compliance (PEM 6.5 of $E \sim 142$ MPa and PEM 2.0 of $E \sim 200$ kPa) with type I, rat-tail collagen or with

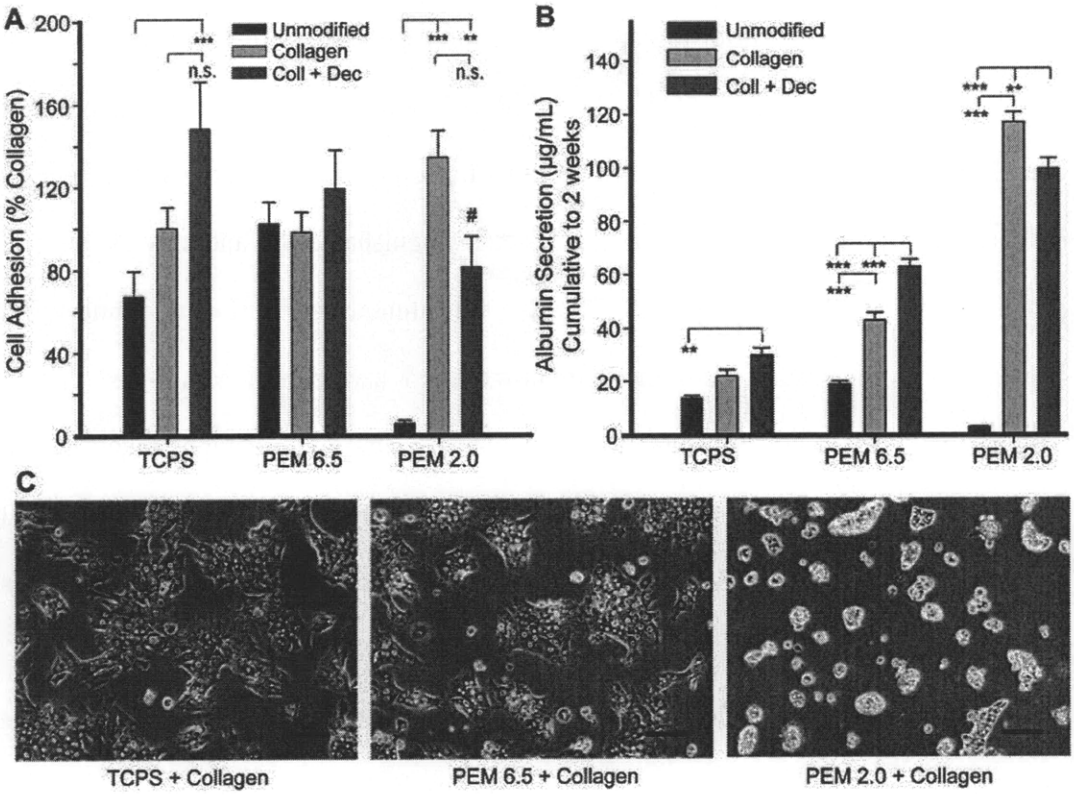

Figure A.4 Adhesion, morphology and phenotypic functions of primary rat hepatocytes on polyelectrolyte multi-layers (PEMs) modified with extracellular matrix proteins. (A) Quantification of hepatocyte adhesion on substrates modified with either type I collagen (100 µg/mL) or collagen mixed with the proteoglycan decorin (25 µg/mL). All data are normalized to hepatocyte adhesion on collagen-coated TCPS. Error bars are SEM (n = 6-8). Pairwise differences among collagen-modified substrates of varying compliance were not statistically significant (n.s.). # $p < 0.01$ vs. 'TCPS+Coll+Dec', ** $p < 0.01$, *** $p < 0.001$, for One-way ANOVA with Tukey's post-hoc test. (B) Quantification of hepatocyte functions on protein-modified substrates: cumulative albumin secretion over two weeks. Error bars are SEM (n=3). Pairwise differences among unmodified surfaces were not statistically significant (n.s.), among collagen-modified surfaces $p < 0.001$, and among collagen+decorin-modified surfaces $p < 0.001$. ** $p < 0.01$, *** $p < 0.001$ for One-way ANOVA with Tukey's post-hoc test. (C) Hepatocyte morphology on collagen-coated substrata of varying compliance, 2 days post-seeding. Hepatocyte morphology on substrata modified with collagen + decorin was similar. Scalebars = 100 µm. Error bars represent SEM.

collagen pre-mixed with the small proteoglycan decorin, previously demonstrated by our group to induce hepatic functions on collagen-modified TCPS (*1*). We have shown that decorin alone is insufficient to promote hepatocyte attachment; hence, mixing with

collagen was required. Prior to hepatocyte culture, we verified that this adsorption of proteins (collagen ± decorin) did not significantly alter the thickness, roughness, or compliance of the PEMs (Fig. A.2). Furthermore, collagen and decorin surface density on each PEM was shown to be statistically indistinguishable via antibody staining of protein-modified PEMs (Fig. A.3). As with unmodified surfaces, primary rat hepatocytes were seeded onto the protein-modified surfaces in serum-free culture medium and attachment was quantified via phase contrast micrographs taken 6 to 8 hours after initial seeding. Our results indicated that protein modification of the most compliant substratum (PEM 2.0) led to enhanced hepatocyte attachment which was statistically similar to the stiffer, unmodified and protein-modified substrata (Fig. A.4A). As Fig. A.2 shows, protein modification of PEMs did not alter mechanical compliance of each substrata type, suggesting that differences in hepatocyte attachment can be attributed to collagen I-modification of the compliant PEM 2.0 substratum. Similar cell attachment across the collagen I-modified surfaces of varying compliance thus enabled culture and compliant-dependent phenotypic evaluation of hepatocytes for two weeks in vitro.

Assessment of hepatic albumin secretion (a marker of liver-specific protein synthesis (*29*)) indicated increased hepatic function on protein-modified surfaces as compared to unmodified controls (Fig. A.4B). Furthermore, albumin secretion decreased with decreasing substrata mechanical compliance: secretion was highest on collagen I-modified PEM 2.0 substrata, lower on collagen I-modified PEM 6.5, and lowest on collagen I-modified TCPS. Consistent with our previous studies (*1*), we verified here that decorin pre-mixed with collagen induced hepatocyte functions on rigid TCPS (~150% of collagen/TCPS controls). We found that decorin induced

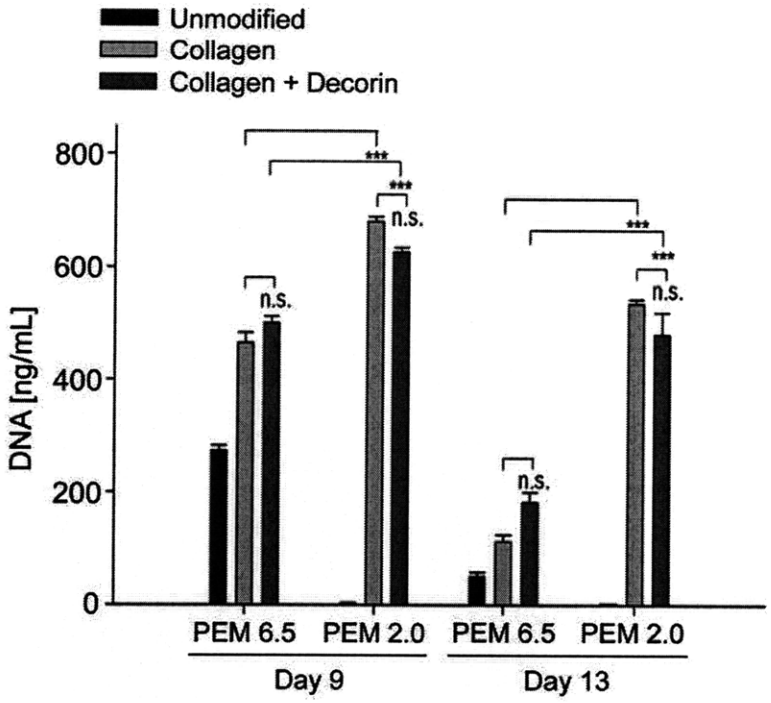

Figure A.5 Quantification of hepatocyte DNA on polyelectrolyte multi-layers (PEMs). PEMs of two compliances (stiff PEM 6.5 and compliant PEM 2.0) were used, unmodified or coated with protein (collagen at 100 μg/mL, decorin at 25 μg/mL) followed by seeding of primary rat hepatocytes. Cells were detached from substrates via trypsinization and DNA was quantified using PicoGreen (see Methods for details). Error bars represent SEM (n = 3). 'n.s.' indicates no statistical significance, *** $p < 0.001$ for one-way ANOVA with Tukey's post-hoc test.

hepatic functions on the stiffer PEM 6.5 to a similar extent as on rigid TCPS; however, functions were down-regulated on the more compliant PEM 2.0 (~80% of collagen/TCPS controls). Urea synthesis (data not shown), a surrogate marker of liver-specific nitrogen metabolism, showed trends similar to those seen for albumin secretion in Fig. A.4B. Quantification of hepatocyte DNA confirmed that protein-modified PEM 2.0 surfaces promoted hepatocyte attachment over at least two weeks, while hepatocytes were only weakly adhered to and released within one week from PEM 6.5 surfaces (Fig. A.5). Lastly, hepatocytes formed stable, spheroidal aggregates of approximately 50-100 m diameter on protein-modified PEM 2.0

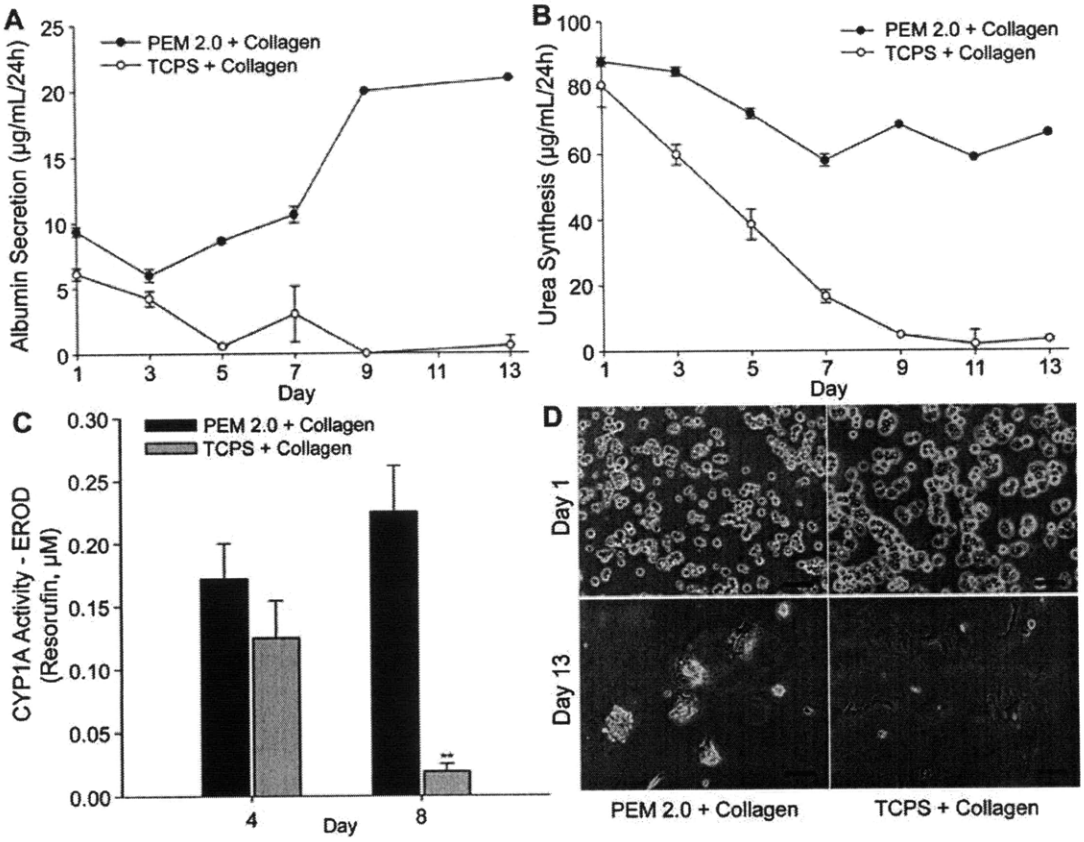

Figure A.6 Comparison of hepatocyte morphology and phenotypic functions on tissue culture polystyrene (TCPS) and compliant poly-electrolyte multi-layers (PEM 2.0) modified with type I collagen. (A) Rate of albumin secretion (marker of liver-specific protein synthesis) in hepatocytes on collagen-modified substrates over two weeks. (B) Rate of urea synthesis in hepatocytes on collagen-modified substrates over two weeks. (C) Activity of cytochrome P450 1A (CYP1A, marker of detoxification function) as measured via ethoxy-resorufin O-dealkylation (EROD) in hepatocytes, 4 and 8 days after seeding onto collagen-modified substrates. Error bars represent SEM (n=3). ** $p < 0.05$ vs. 'PEM 2.0 + Collagen (Day 8)' for One-way ANOVA with Tukey's post-hoc test. (D) Morphology of hepatocytes 1 and 13 days after seeding onto collagen-modified substrates. Scalebars = 100 µm. Error bars represent SEM.

surfaces, while the extent of cell spreading increased with reduction in substrata compliance (Fig. A.4C).

A.2.3 Retention of hepatic spheroids and functions on collagen-coated PEMs

We measured functional kinetics of hepatocytes on protein-modified PEM 2.0 surfaces

over two weeks in order to evaluate the longevity and phenotypic stability of hepatocytes interfaced with PEMs. Hepatocytes cultured on collagen-modified TCPS were considered as declining controls, as is conventional for in vitro hepatic studies (*1, 18*). Hepatic albumin secretion (Fig. A.6A), urea synthesis (Fig. A.6.B), and cytochrome P450 1A activity, a marker of liver-specific detoxification (Fig. A.6.C), were well retained on protein-modified PEM 2.0 substrata for 2 weeks, whereas a monotonic decline was confirmed on collagen-modified TCPS. Furthermore, over this extended culture, hepatocytes organized into stable spheroids maintained at approximately 50-100 m diameter on the compliant PEM 2.0 substrata, whereas cells spread on rigid TCPS to adopt a fibroblastic morphology, characteristic of unstable hepatocytes (Fig. A.6.D).

A.3 DISCUSSION

Cell fate processes are influenced not only by cell-autonomous programs, but also by the local microenvironment or "niche", which is composed of neighboring cells, biochemical stimuli and variable mechanical properties. Thus, development of functionally robust models of tissues for in vitro and therapeutic applications will require precise spatiotemporal control over such cues at multiple length and time scales. In this study, we have utilized synthetic, weak polyelectrolyte multilayer substrata (PEMs) to evaluate the independent and synergistic effects of biochemical and mechanical stimuli on the adhesion, morphology, and phenotypic functions of primary hepatocytes, which are considered highly important for liver tissue engineering yet are difficult to maintain in culture (15).

The compatibility of primary rat hepatocytes with purely synthetic hydrogels,

strong PEMs comprised of poly(diallyldimethylammonium chloride) (PDAC) and poly(sulfonated styrene) (PSS), was first demonstrated by Kidambi et. al. (*24*). The authors showed that PSS-terminated substrata promoted hepatocyte adhesion and spreading; yet liver-specific functions (albumin and urea production) on these synthetic substrates declined over one week in culture and were comparable to those seen on unmodified tissue culture polystyrene (*24*). Furthermore, the authors did not evaluate the dependence of hepatocyte morphology and functions on varying substrata mechanical compliances. In a follow-up study, the authors created co-cultures of hepatocytes and fibroblasts on protein-free surfaces by utilizing micropatterned domains of PEMs adhesive to either hepatocytes or fibroblasts (*25*). The authors verified the previously reported and well-known "co-culture effect" on their surfaces by showing that 3T3 murine embryonic fibroblasts were able to induce functions in primary rat hepatocytes via heterotypic signaling (*1, 15, 30*). It was unclear from this study, however, whether there were any synergistic effects of substrate mechanical compliance and heterotypic cell-cell interactions on liver-specific functions of hepatocytes. More recently, Janorkar et. al. functionalized polyacrylic acid (PAA) / polyethyleneimine (PEI) PEMs with extracellular matrix-like polypeptides to enhance liver-specific functions (*23*). Despite these experimental developments using PEMs, substrata compliance in the aforementioned reports could not be tuned via assembly pH and was not quantified independently of adjunct cells or ligands. Using PA hydrogels, Semler et. al. polymerized, cut, and adhered to tissue-culture plate surfaces a 9-condition array of substrates with varying elastic moduli and densities of immobilized fibronectin, identifying high compliance regimes (E = 1.9 kPa) in which hepatocyte cell-cell interactions dominated over hepatocyte-fibronectin interactions (*11*). While

highlighting the impact of mechanical and biochemical cooperative signaling on liver-specific functions and gene expression, the conditions of this study were limited to relatively small variations in mechanical stiffness (5.6 – 19 kPa) and a single protein (fibronectin). Furthermore, this study required multiple tedious steps for system assembly, which limits the facile, reproducible investigation of multiple stimuli towards engineering defined microenvironments for hepatocytes or other cells.

We probed hepatocyte attachment on fully synthetic PEM substrata that varied in compliance over several orders of magnitude (elastic moduli E ranging from 0.2 to 2500 MPa), using serum-free culture medium to avoid cell attachment due to serum proteins pre-adsorbing onto the substrate. We found that hepatocytes displayed maximal attachment (~100% of adhesion to TCPS/collagen control, $E \sim 2500$ MPa) on substrata of lower mechanical compliance (PEM 6.5, $E \sim 142$ MPa; and PEM 4.0, $E \sim 1.7$ MPa), while negligible attachment was observed on the most compliant substrata (PEM 2.0, $E \sim 0.2$ MPa). The inverse correlation between unfunctionalized substrata compliance and percentage of cell adhesion/spreading is consistent with previous observations for endothelial cells (*8*) and fibroblasts cultured on these PEMs (*31*), as well as for other adherent tissue cell types on polymer hydrogels (*32*). While the mechanism of this protein-free hepatocyte adhesion to unfunctionalized, weak PEM substrata is currently unknown, differential adhesion of hepatocytes on varying compliance cannot be attributed to surface charge, energy, or roughness of these PEMs, as we have shown that these physical properties are statistically indistinguishable for these substrata (*14*). Lack of hepatocyte attachment to PEM 2.0 was therefore most likely due to reduced cell-substratum adhesion via unstable focal contact or adhesion complexes, as observed with other adherent tissue cell types such as fibroblasts (*2*).

On the stiffer PEM substrata (PEM 6.5 and 4.0), however, the balance of cell-cell and cell-substrata interactions stabilized formation of hepatic aggregates for several days in culture. In comparison, as expected from our previous work (*1*), hepatocytes on collagen-modified, rigid TCPS rapidly spread to adopt a fibroblastic morphology. Thus, the results of our primary hepatocyte adhesion studies are consistent with others showing that a variety of adhesive cell types, including fibroblasts, cardiomyocytes and endothelial cells, adhere poorly to highly compliant hydrogels (*2, 8, 11*).

Unmodified PEM substrata of stiffness greater than E ~0.2 MPa promoted attachment and aggregation of hepatocytes; however, we found that cells detached from these stiffer substrata after only a few days of culture, due ostensibly to the dominance of cell-cell over cell-substrata interactions. We thus modified substrata with type I collagen, an extracellular matrix protein that has been shown to promote hepatocyte attachment for several weeks in culture (*1*). We found that protein modification affected neither the thickness nor the mechanical compliance of the stiffest and most compliant PEM substrata over distances and forces representative of cell-matrix adhesion interactions. The PEM system therefore enabled independent comparison of hepatocyte functions over several weeks in well-defined chemomechanical microenvironments. Following collagen-modification, hepatic spheroid formation was observed on PEMs exhibiting both low (PEM 6.5) and high (PEM 2.0) compliance. Spheroidal aggregates displayed higher levels of broad classes of liver-specific functions (albumin secretion, urea synthesis and CYP450 1A activity) as compared to well-spread hepatocytes on collagen-modified TCPS controls, a finding that is consistent with previously published reports (*26-28*). However, previous methods to create hepatic spheroids (e.g., tumor-derived Matrigel®, roller bottles, non-adhesive

dishes) are either confounded by coupled changes in ligand density (i.e. Matrigel), or limited by challenges in handling and processing spheroids as they form and coalesce to become large cellular masses with necrotic cores. In this study, the compliant, collagen-modified PEM 2.0 substrata promoted attachment and long-term (two weeks) retention of hepatic spheroids (approximately 50-100 m in diameter) over stiffer PEM 6.5 substrata, as evaluated by the quantification of adherent hepatocyte DNA over time. Tethered spheroids eliminated the need for sedimentation steps during culture medium changes for suspended spheroid cultures, and facilitated evaluation of hepatic morphology and functions with varying chemomechanical stimuli on a reproducible and synthetic PEM platform.

Type I collagen typically does not induce liver-specific functions in hepatocytes and is instead used with hepatocytes primarily as an adhesive cue on solid substrates. Although we used type I collagen to promote long-term retention of highly functional hepatic spheroids on PEM substrata, a primary objective of this study was to utilize the tunable PEM system to investigate the incorporation of hepatocyte-stabilizing biochemical cues on mechanically distinct substrata. Several such molecular cues have been previously implicated in induction of hepatic functions when presented alone on solid substrates or in combination with adhesive factors such as collagen (*1, 15*). Using a functional genomic screen on hepatocyte-fibroblast co-cultures, we have previously shown that decorin, a chondroitin suflate-dermatan sulfate proteoglycan that binds collagen and is present in the native liver (*33, 34*), can induce phenotypic functions in primary rat hepatocytes adhered to collagen-coated TCPS (*1*). In this study, we sought to evaluate the interplay of decorin and substrata mechanical compliance on the hepatic phenotype over extended in vitro culture. We observed that

the presence of decorin caused hepatic functions of cultured hepatocytes to be up-regulated similarly on rigid TCPS and PEM 6.5 substrates. However, on highly compliant PEM 2.0 substrata, the presence of decorin led to down-regulation of liver-specific functions in hepatic spheroids, and such down-regulation was not attributable to statistically significant differences in initial attachment of cells or to differential retention of hepatic spheroids on collagen-only controls (evaluated by DNA quantification over time). Furthermore, the inability of decorin to enhance hepatic functions on PEM 2.0 was not due to saturation of albumin secretion, as hepatocytes secrete much higher albumin levels (~2-3 fold) upon co-cultivation with supporting fibroblasts at the cell seeding densities used in this study [15, 39]. Such multifaceted effects of mechanical compliance and ligand type/density are not unexpected (*9, 19*), given the common components of mechanotransductive and other functional signaling pathways. Semler et al. have also reported a monotonic coupling for fibronectin-functionalized polyacrylamide hydrogels (*11*), noting increased albumin secretion for gels of lower compliance and constant fibronectin concentration; however, the authors considered shorter durations (one week) and a much narrower range of substrata stiffness (shear elastic storage modulus $G' \sim 2 - 9$ kPa) than considered in this study.

Although we demonstrated via antibody staining that the extent of collagen and decorin adsorption to PEMs was statistically indistinguishable, it remains possible that ligand orientation and/or altered collagen fibril structure (*33, 35*) may differ among these PEMs in a manner correlative with mechanical compliance. These correlative factors are very challenging to quantify on hydrogel surfaces and are beyond the scope of the present study, but remain important considerations in the distinction between causal and correlative effects of substrata stiffness on tissue cell function. We also note

that the mechanical stiffness of the most compliant hydrogels considered in this study (E ~ 200 kPa) is within the range of normal liver tissue measured via various methods (E ~ 1 kPa – 750 kPa (*36, 37*); however, it is difficult to draw a direct analogy between the tunable, synthetic PEM platform used in vitro here and microenvironments present in patho/physiological states in vivo. Future studies in our laboratories will further tune and improve hepatic functions in vitro via the use of combinatorial mixtures of polymer-tethered ligands and soluble factors (e.g., growth factors), on two- and three-dimensional materials that display spatial variations in compliance and ligand-tether flexibility.

A.4 MATERIALS AND METHODS

A.4.1 Preparation of PEM substrata

Poly(acrylic acid) (PAA, Polysciences; M_w ~70,000 g/mol) and poly(allylamine hydrochloride) (PAH, Sigma-Aldrich; M_w ~90,000 g/mol) were prepared as dilute solutions of polyelectrolytes (0.01 M by repeating unit molecular weight) in deionized water, and pH adjusted to 2.0, 4.0, or 6.5 using HCl or NaOH. Layer by layer (LbL) assembly was employed, using a programmable slide stainer (Zeiss) to coat multi-well tissue culture-treated polystyrene plates (TCPS, Becton Dickinson) and glass coverslips (VWR International) with alternating layers of PAA and PAH adjusted to the same pH, resulting in ionically crosslinked PEMs (*8*). Substrata are denoted by assembly pH, e.g., "PEM 2.0" indicates that the substrata was assembled for PAA and PAH solutions both adjusted to pH = 2.0, with PAA as the last dipping solution. The number of layers was varied to obtain a uniform hydrated thickness of ~100 nm: PEM 2.0, 4.0, and 6.5 samples contained 11, 15, and 42 bilayers, respectively (*8*). Prior to cell seeding, all

surfaces were sterilized in 70% EtOH for 1 hour, followed by 3X rinses with sterile ddH_20. Substrates were coated with 100 µg/mL collagen-I or 100 µg/mL collagen-I pre-mixed with 25 µg/mL decorin (Sigma) for 2 to 3 hours at 37° C.

A.4.2 Rat hepatocyte isolation and culture

Hepatocytes were isolated from 2-3 month old adult female Lewis rats (Charles River Laboratories) using a modified procedure of Seglen (*38*) and seeded at 0.3×10^6 cells per well (12-well plates modified with PEMs) in serum-free culture medium comprising high glucose DMEM, 0.5 U/mL insulin, 7 ng/mL glucagons, 7.5 µg/mL hydrocortisone, 10 U/mL penicillin, and 10 µg/mL streptomycin. Cells were cultured in serum-free medium at 37°C, 5% CO_2 for 6 to 8 hours to allow for attachment, followed by removal of unattached cells and replacement with serum-supplemented (10% FBS) medium. Culture medium was sampled and replaced daily.

A.4.3 Quantification of hepatocyte adhesion and functions

Quantification of cell adhesion was performed by counting cells in phase contrast micrographs (Nikon Ellipse TE200 and CoolSnap-HQ Digital CCD camera) taken 6 to 8 hours after cell seeding. Six 10X magnification fields of cells per condition were averaged for each condition and normalized to the average number adhered to positive control substratum (collagen modified TCPS). Albumin content in conditioned media was measured using an enzyme linked immunosorbent assay (ELISA) with horseradish peroxidase detection and peroxidase substrate 3,3',5,5'-tetramethylbenzidine as described previously (*1*). Urea concentration was quantified using a colorimetric endpoint assay based on acid- and heat- catalyzed condensation of urea with

diacetylmonoxime (Stanbio Labs). Cytochrome P450 (CYP1A1) enzymatic activity was measured by quantifying the amount of resorufin produced from the CYP-mediated cleavage of ethoxyresorufin O-deethylase (EROD). EROD (5 M) was incubated with cell cultures for 30 min, medium was collected, and resorufin fluorescence was quantified at 571/585 nm (excitation/emission wavelengths).

A.4.4 Statistical Analysis

Statistical significance was determined using two-tailed t-test or one-way ANOVA (analysis of variance) with Tukey's post-hoc test. Unless otherwise noted, error bars represent SEM (standard error of mean), with sample size (n) and p-value for each data set indicated in the corresponding figure captions.

A.4.5 PEM surface characterization

Hydrated thicknesses of PEMs in 150 mM phosphate buffered saline at pH = 7.2 were measured through atomic force microscopy (AFM; PicoPlus, Agilent Technologies). Scratches were made with razor blades on PEMs assembled on glass coverslips, and thicknesses of PEMs were measured near scratch regions from AFM height images acquired in tapping mode. Tapping mode imaging at randomly selected positions across the sample confirmed the uniform coverage of PEM across the sample surface area analyzed in cell culture, as has been established for this assembly protocol and is supported by uniform immunofluorescence staining of the protein-functionalized PEMs described below.

AFM cantilever spring constants were measured as discussed elsewhere (*8*) with the thermal noise method. The deflection sensitivity of each AFM cantilever (nm/V),

and cantilever spring constants, nominally k = 0.1 N/m, were measured for each experiment and used for analyses of elastic moduli of PEMs. Elastic moduli were calculated by applying a modified Hertzian model of spherical contact via AFM force spectroscopy as discussed in detail elsewhere (*8, 14*). Force-displacement responses collected from AFM force spectroscopy were converted offline to force-separation curves through the Scanning Probe Imaging Processor (Image Metrology), followed by customized analyses to calculate elastic moduli through the scientific computing software Igor (Wavemetrics). Note that, although hepatocyte experiments were conducted on PEMs assembled on TCPS and these thickness/stiffness experiments were conducted on PEMs assembled on glass to enable scratching, we have found the elastic moduli E of these PEMs to be independent of these substrate differences for the hydrogel thicknesses considered here, within the standard error of measurement among replicate samples (e.g., see Ref. 3 on TCPS and Ref. 11 on glass).

A.4.6 Immunostaining of proteins on PEM modified surfaces

Coverslips were pre-adsorbed with 100 μg/mL collagen, with or without 25 μg/mL decorin, and primary antibodies against collagen or against decorin (Chemicon/Millipore) incubated with coverslips at 50 g/mL. FITC-conjugated secondary antibody (abcam) was subsequently incubated at 50 g/mL, and antibody specificity was confirmed via controls including unmodified PEMs. Relative luminosity of each fluorescence image obtained from epifluorescence microscopy (IX 81, Olympus) was compared in Adobe Photoshop, version 7.0.

A.4.7 Quantification of cellular DNA

Cells were trypsinized (0.25% Trypsin/EDTA, Invitrogen), pelleted, resuspended in 1x TE buffer and lysed via 3 cycles of freeze-thaw followed by 5 minutes of sonication. Quanti-iT PicoGreen dsDNA reagent (Invitrogen) was used to quantify DNA against a standard curve according to manufacturer's instructions.

A. 5 CONCLUSION

In conclusion, we demonstrate that hepatocyte morphology and broad classes of phenotypic functions can be modulated via independent and synergistic tuning of biochemical and mechanical stimuli as presented on synthetic polymeric substrata. Facile assembly and synergistic effects of high substrata compliance and collagen presentation onto a standard 2D culture surface enabled creation of a robust, pure-hepatocyte tissue model which displayed enhanced liver-specific functions over collagen-modified TCPS controls for two weeks. We also discovered compliance-mediated effects of the proteoglycan decorin on hepatic functions, with hepatocyte functions down-regulated on highly compliant surfaces as compared to collagen-only controls but up-regulated on increasing PEM stiffness. Potential applications of our multi-well platform include medium- to high-throughput evaluation of interactions between exogenous compounds (e.g., drugs, environmental toxicants) and the various microenvironmental cues used to modulate fate processes of primary hepatocytes. Lastly, our approach of modulating chemomechanical cues towards improvement of cellular functions in vitro is amenable to multiple cell types (e.g., stem and precursor cells) for applications such as drug screening, cell-based therapies or the fundamental study of chemomechanical processes underlying tissue function and disease.

REFERENCES

1. Discher DE, Janmey P, Wang YL. Tissue cells feel and respond to the stiffness of their substrate. Science 2005 NOV 18;310(5751):1139-1143.

2. Lee S, Mandic J, Van Vliet KJ. Chemomechanical mapping of ligand-receptor binding kinetics on cells. Proc Natl Acad Sci U S A 2007 Jun 5;104(23):9609-9614.

3. Deroanne CF, Lapiere CM, Nusgens BV. In vitro tubulogenesis of endothelial cells by relaxation of the coupling extracellular matrix-cytoskeleton. Cardiovasc Res 2001 Feb 16;49(3):647-658.

4. Vailhe B, Lecomte M, Wiernsperger N, Tranqui L. The formation of tubular structures by endothelial cells is under the control of fibrinolysis and mechanical factors. Angiogenesis 1998;2(4):331-344.

5. Pelham RJ, Wang YL. Cell locomotion and focal adhesions are regulated by substrate flexibility. Proceedings of the National Academy of Sciences of the United States of America 1997 SEP 29;94(25):13661-13665.

6. Yeung T, Georges PC, Flanagan LA, Marg B, Ortiz M, Funaki M, et al. Effects of substrate stiffness on cell morphology, cytoskeletal structure, and adhesion. Cell Motil Cytoskeleton 2005 Jan;60(1):24-34.

7. Thompson MT, Berg MC, Tobias IS, Rubner MF, Van Vliet KJ. Tuning compliance of nanoscale polyelectrolyte multilayers to modulate cell adhesion. Biomaterials 2005 DEC;26(34):6836-6845.

8. Engler AJ, Griffin MA, Sen S, Bonnemann CG, Sweeney HL, Discher DE. Myotubes differentiate optimally on substrates with tissue-like stiffness: pathological implications for soft or stiff microenvironments. J Cell Biol 2004 Sep 13;166(6):877-887.

9. Engler AJ, Sen S, Sweeney HL, Discher DE. Matrix elasticity directs stem cell lineage specification. Cell 2006 AUG 25;126(4):677-689.

10. Semler EJ, Lancin PA, Dasgupta A, Moghe PV. Engineering hepatocellular morphogenesis and function via ligand-presenting hydrogels with graded mechanical compliance. Biotechnol Bioeng 2005 Feb 5;89(3):296-307.

11. Peyton SR, Raub CB, Keschrumrus VP, Putnam AJ. The use of poly(ethylene glycol) hydrogels to investigate the impact of ECM chemistry and mechanics on smooth muscle cells. Biomaterials 2006 Oct;27(28):4881-4893.

12. Walton EB, Oommen B, Van Vliet KJ. How stiff and thin can an engineered extracellular matrix be? Modeling molecular forces at the cell-matrix interface. Conf Proc IEEE Eng Med Biol Soc 2007;2007:6419-6421.

13. Lichter JA, Thompson MT, Delgadillo M, Nishikawa T, Rubner MF, Van Vliet KJ. Substrata mechanical stiffness can regulate adhesion of viable bacteria. Biomacromolecules 2008 Jun;9(6):1571-1578.

14. Thompson MT, Berg MC, Tobias IS, Lichter JA, Rubner MF, Van Vliet KJ. Biochemical functionalization of polymeric cell substrata can alter mechanical compliance. Biomacromolecules 2006 Jun;7(6):1990-1995.

15. Khetani SR, Szulgit G, Del Rio JA, Barlow C, Bhatia SN. Exploring interactions between rat hepatocytes and nonparenchymal cells using gene expression profiling. Hepatology 2004 Sep;40(3):545-554.

16. Bhatia SN, Balis UJ, Yarmush ML, Toner M. Effect of cell-cell interactions in preservation of cellular phenotype: cocultivation of hepatocytes and nonparenchymal cells. Faseb J 1999 Nov;13(14):1883-1900.

17. Allen JW, Hassanein T, Bhatia SN. Advances in bioartificial liver devices.

Hepatology 2001 Sep;34(3):447-455.

18. Hewitt NJ, Lechon MJ, Houston JB, Hallifax D, Brown HS, Maurel P, et al. Primary hepatocytes: current understanding of the regulation of metabolic enzymes and transporter proteins, and pharmaceutical practice for the use of hepatocytes in metabolism, enzyme induction, transporter, clearance, and hepatotoxicity studies. Drug Metab Rev 2007;39(1):159-234.

19. Guguen-Guillouzo C, Guillouzo A. Modulation of functional activities in cultured rat hepatocytes. Mol Cell Biochem 1983;53-54(1-2):35-56.

20. Semler EJ, Ranucci CS, Moghe PV. Mechanochemical manipulation of hepatocyte aggregation can selectively induce or repress liver-specific function. Biotechnol Bioeng 2000 Aug 20;69(4):359-369.

21. Gross-Steinmeyer K, Stapleton PL, Tracy JH, Bammler TK, Lehman T, Strom SC, et al. Influence of Matrigel-overlay on constitutive and inducible expression of nine genes encoding drug-metabolizing enzymes in primary human hepatocytes. Xenobiotica 2005 May;35(5):419-438.

22. Semler EJ, Moghe PV. Engineering hepatocyte functional fate through growth factor dynamics: the role of cell morphologic priming. Biotechnol Bioeng 2001 Dec 5;75(5):510-520.

23. Dunn JC, Tompkins RG, Yarmush ML. Hepatocytes in collagen sandwich: evidence for transcriptional and translational regulation. J Cell Biol 1992 Feb;116(4):1043-1053.

24. Janorkar AV, Rajagopalan P, Yarmush ML, Megeed Z. The use of elastin-like polypeptide-polyelectrolyte complexes to control hepatocyte morphology and function in vitro. Biomaterials 2008 Feb;29(6):625-632.

25. Kidambi S, Lee I, Chan C. Controlling primary hepatocyte adhesion and spreading on protein-free polyelectrolyte multilayer films. J Am Chem Soc 2004 Dec 22;126(50):16286-16287.

26. Kidambi S, Sheng L, Yarmush ML, Toner M, Lee I, Chan C. Patterned co-culture of primary hepatocytes and fibroblasts using polyelectrolyte multilayer templates. Macromol Biosci 2007 Mar 8;7(3):344-353.

27. Tong JZ, De Lagausie P, Furlan V, Cresteil T, Bernard O, Alvarez F. Long-term culture of adult rat hepatocyte spheroids. Exp Cell Res 1992 Jun;200(2):326-332.

28. Hamilton GA, Westmorel C, George AE. Effects of medium composition on the morphology and function of rat hepatocytes cultured as spheroids and monolayers. In Vitro Cell Dev Biol Anim 2001 Nov-Dec;37(10):656-667.

29. Dvir-Ginzberg M, Elkayam T, Aflalo ED, Agbaria R, Cohen S. Ultrastructural and functional investigations of adult hepatocyte spheroids during in vitro cultivation. Tissue Eng 2004 Nov-Dec;10(11-12):1806-1817.

30. Seglen PO. Preparation of isolated rat liver cells. Methods Cell Biol 1976;13:29-83.

31. Bhatia SN, Toner M, Tompkins RG, Yarmush ML. Selective adhesion of hepatocytes on patterned surfaces. Ann N Y Acad Sci 1994 Nov 30;745:187-209.

32. Corlu A, Ilyin G, Cariou S, Lamy I, Loyer P, Guguen-Guillouzo C. The coculture: a system for studying the regulation of liver differentiation/proliferation activity and its control. Cell Biol Toxicol 1997 Jul;13(4-5):235-242.

33. Khetani SR, Bhatia SN. Microscale culture of human liver cells for drug development. Nat Biotechnol 2008 Jan;26(1):120-126.

34. Berg MC, Yang SY, Hammond PT, Rubner MF. Controlling mammalian cell

interactions on patterned polyelectrolyte multilayer surfaces. Langmuir 2004 Feb 17;20(4):1362-1368.

35. Janmey PA, McCulloch CA. Cell mechanics: integrating cell responses to mechanical stimuli. Annu Rev Biomed Eng 2007;9:1-34.

36. Khetani SR, Chen AA, Ranscht B, Bhatia SN. T-cadherin modulates hepatocyte functions in vitro. Faseb J 2008 Jul 17.

37. Pogany G, Vogel KG. The interaction of decorin core protein fragments with type I collagen. Biochem Biophys Res Commun 1992 Nov 30;189(1):165-172.

38. Hogemann B, Edel G, Schwarz K, Krech R, Kresse H. Expression of biglycan, decorin and proteoglycan-100/CSF-1 in normal and fibrotic human liver. Pathol Res Pract 1997;193(11-12):747-751.

39. Bhatia SN, Balis UJ, Yarmush ML, Toner M. Probing heterotypic cell interactions: hepatocyte function in microfabricated co-cultures. J Biomater Sci Polym Ed 1998;9(11):1137-1160.

40. Pogany G, Hernandez DJ, Vogel KG. The in vitro interaction of proteoglycans with type I collagen is modulated by phosphate. Arch Biochem Biophys 1994 Aug 15;313(1):102-111.

41. Li Z, Dranoff JA, Chan EP, Uemura M, Sevigny J, Wells RG. Transforming growth factor-beta and substrate stiffness regulate portal fibroblast activation in culture. Hepatology 2007 Oct;46(4):1246-1256.

42. Constantinides G, Kalcioglu ZI, Van Vliet KJ. Probing mechanical properties of fully hydrated gels and biological tissues. Journal of Biomechanics, 2008, *In press.*

Appendix B

Stop-Flow Lithography for the Production of Shape-Evolving Degradable Microgel Particles

This appendix contains parts of the following study accepted for publication in 2009 with co-authors of Dae Kun Hwang, John Oakey, Mehmet Toner, Jeffrey A. Arthur, Kristi S. Anseth, Adam Zeiger, and Patrick S. Doyle (1).

B.1 CONTRIBUTION

The purpose of AFM-based indentation is to confirm whether elastic moduli of biodegradable hydrogels also decrease over a course of time as suggested in fluorescence intensity experiment. My contribution to this work is to measure the elastic moduli of biodegradable hydrogels over a period of time, confirming that the elastic moduli of biodegradable hydrogels decrease as they lose mass over time.

B. 2 MATERIALS AND METHODS

B.2.1 Atomic force microscopy-enabled nanoindentation

An atomic force microscope (AFM, Agilent Technology) was incorporated within an optical microscope (IX 81, Olympus) to enable facile positioning of AFM cantilevers above individual particles (See Fig. B.1C). Calibration of AFM Si_3N_4 cantilevers of nominal spring constant k = 0.1 N/m and probe radius R = 25 nm (Veeco) was conducted as described previously(*2-4*). Briefly, inverse optical lever sensitivity [nm/V] (InvOLS) was measured from deflection-displacement curves recorded on rigid glass substrates. Spring constants [nN/nm] of AFM cantilevers were measured via thermal

activation recording of deflection and the Fourier Transform (FFT) of cantilever amplitude as a function of oscillation frequency fitted with simple harmonic oscillation function. For each particle composition and degradation time point, at least 30 replicate indentations were acquired to maximum depths of 10 nm. Microhydrogel particles of ~30 μm thickness were indented in the fully immersed state in phosphate buffered saline (PBS), and stored at room temperature between observation intervals. Acquired probe deflection-displacement responses were converted offline (Scanning Probe Imaging Processor, Image Metrology), using measured spring constants and InvOLS, to force-depth responses. Elastic moduli E were calculated by applying a modified Hertzian model of spherical contact to the loading segment of the force-depth response, as detailed elsewhere(*3, 4*) with the scientific computing software Igor Pro (Wavemetrics). Computed elastic moduli E are reported as average +/- standard deviation, and all statistical analyses were conducted with one-way ANOVA (Tukey analysis).

B.3 RESULTS

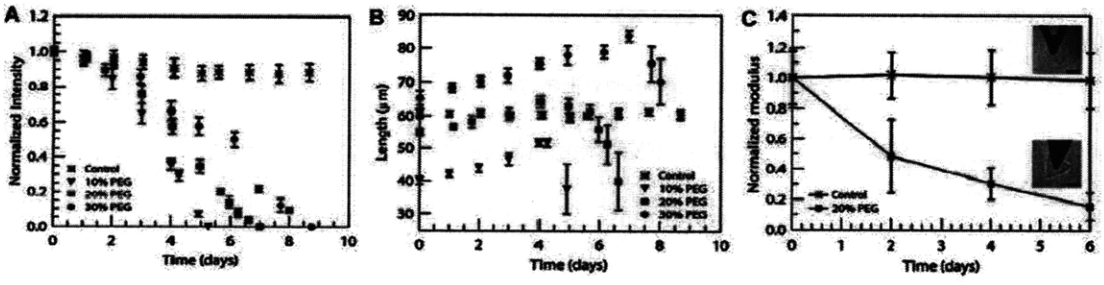

Figure B. 1 (A) Fluorescence intensity, normalized by intensity at Day 0 for each sample, and (B) growth of the side length of non-degradable (control, rectangles of PEGDA 30 wt %) and degradable (triangles, PEG-*b*-PLA 30 wt %, 20 wt %, and 10 wt %) hydrogel particles. (C) Elastic modulus E, normalized by E at Day 0 for each sample, for non- (control, rectangles, PEGDA 30 wt %) and degradable hydrogels (triangles, PEG-*b*-PLA 20 wt %) using AFM-enabled nanoindentation. PEG-b-PLA represents for poly(lactic acid)-poly(ethylene glycol)-poly(lactic acid)-poly(ethylene glycol); PEGDA, poly(ethylene glycol) diacrylate.

Distinct erosion profiles can be seen in Fig. B.1A and Fig. B.1.B. A decline of measured fluorescent intensity is observed for particles of all initial PEG-*b*-PLA concentrations (Fig. B.1A). Mass loss is markedly different from the behavior commonly reported for typical bulk degradable hydrogels, which normally exhibit a sharp decrease in the mass loss immediately prior to gel dissolution (i.e., the last 20 % of mass loss(*5*)). The swelling behavior of degradable microgel particles is also qualitatively different from macroscale hydrogels (Fig. B.1B). The increase in side length reaches a maximum and subsequently decreases, which is quite different from bulk hydrogels, which display exponential growth in their equilibrium swollen volume over time(*5*). We also measured the elastic moduli E of individual hydrogel particles via atomic force microscopy (AFM)-enabled indentation (Fig. B.3C). As expected of PEG-based hydrogels, E of control particles (PEGDA 30 wt %) was in the kPa-range (E = 11.0 $\pm$ 4 kPa) and did not decrease significantly with time ($P<0.05$) over 6 days immersed in PBS. In contrast, E of PEG-*b*-PLA 20 wt % particles decreased by 84 %, from E = 7.5 $\pm$ 1.5 kPa (Day 0) to E = 1.2 $\pm$ 0.7 kPa (Day 6). Beyond Day 6, the stiffness of these degrading hydrogel particles was statistically lower than that of the control particles ($P < 0.001$) throughout the degradation process (days 2, 4, and 6). This decreased stiffness of individual degrading particles quantifies the trends observed in reduced fluorescence intensity over time: Fig. B.1A indicates approximately 80% reduction in mean fluorescence of these particle at day 6. This decreased stiffness of individual hydrogel particles is consistent with decreased mass and/or degree of crosslinking within the hydrogel during bulk degradation of the hydrogel network. These data also demonstrate equivalent behavior with previous reports of mechanical behavior for eroding bulk

PEG-based hydrogels.

REFERENCES

1. D. K. Hwang, Oakey, J., Toner, M., Arthur, J. A., Anseth, K. S., Lee, S., Zeiger, A., Van Vliet, K. J., Doyle, P. S., *Journal of American Chemical Society* **Accepted** (2009).
2. H. J. Butt, and Jaschke, M., *Nanotechnology* **6**, 1 (1995).
3. M. T. Thompson, Berg, M. C., Tobias, I. S., Rubner, M. F., and Van Vliet, K. J., *Biomaterials* **26**, 6836 (2005).
4. M. T. Thompson, Berg, M. C., Tobias, I. S., Lichter, J. A., Rubner, M. F., Van Vliet, K. J., *Biomacromolecules* **7**, 1990 (2006).
5. A. T. Metters, Anseth, K. S., and Bowman, C. N. , *Polymer* **41**, 3993 (2000).

Appendix C

Chemical characterization of biological glues

This appendix contains parts of the following study conducted with Natalie Artzi and Elazer Edelman.

C.1 CONTRIBUTION

My contribution to this work is to measure unbinding force between biological glues and amine-functionalized probes to confirm that binding between biological glues and living tissues is mediated by amine-aldehyde binding.

C. 2 MATERIALS AND METHODS

C.2.1 Amine functionalization and AFM force spectroscopy analysis

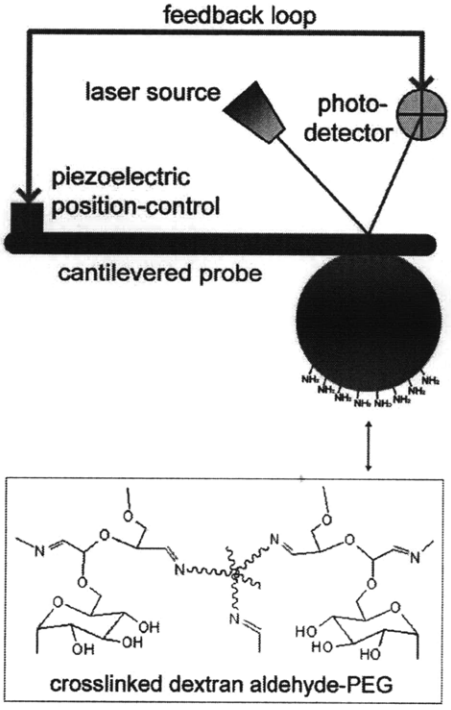

Figure C. 1 Schematic of interaction between dextran-based biological glue and an amine-functionalized AFM cantilevered probe. Aldehyde groups in the glue binds to amine groups on the spherical AFM probe.

Spherical cantilevers made of silicon (AppNano, spring constant = 0.1 nN/nm, radius of spheres = 1 μm) were rinsed in dichloromethane for 10 min, followed by oxygen plasma cleaning for 20 min. Chemical vapor deposition of 1:3 N,N-diisopropylethylamine and 3-aminopropyltriethoxysilane (Sigma-Aldrich Corporation) was achieved in a vacuum dessicator for two hours, which conjugates amine groups on spherical cantilevers. As shown in Fig. C.1, unbinding force is recorded as a form of cantilever deflection, controlled by the piezo-actuator-based feedback loop as shown in the schematic. Deflection [V] is converted to force [nN] using spring constant [nN/nm] and inverse optical lever sensitivity [nm/V] (InvOLS) of the cantilever. InvOLS was measured from deflection-displacement curves recorded on rigid glass substrates. Spring constants [nN/nm] of AFM cantilevers were measured via thermal activation recording of deflection and the Fourier Transform (FFT) of cantilever amplitude as a function of oscillation frequency fitted with simple harmonic oscillation function(*1, 2*). Four glue samples categorized by the crosslinking density, the number of aldehyde groups, and the degree of oxidation as summarized in Fig. C.2 were prepared by the Edelman lab of MIT-Harvard Division of Health Science and Technology.

C. 3 RESULTS

Four samples are being confirmed by *in vivo* experiments in the Edelman lab. The results of measured unbinding force for the samples are summarized in Fig. C.2.

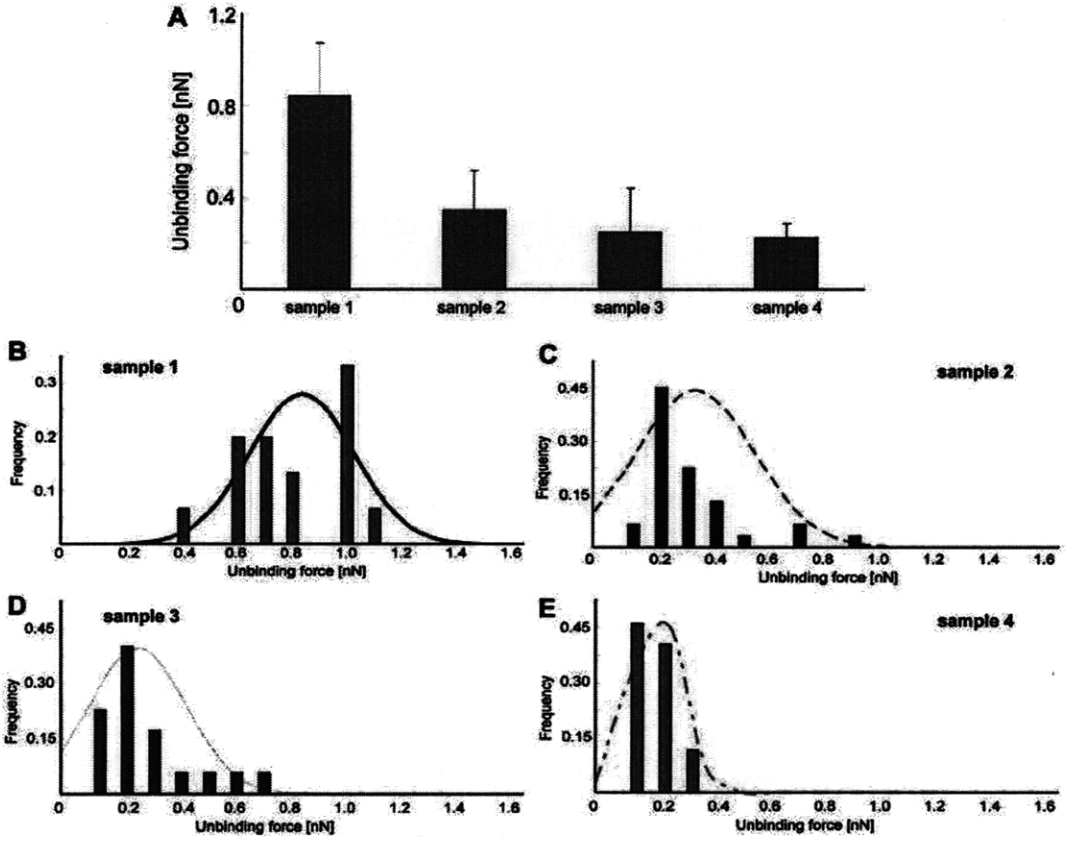

Figure C.2 Unbinding force between dextran-based glues and amine-functionalized probes. (A) shows unbinding forces of four different samples categorized by the density of aldehyde groups. Unbinding force of sample 1 was 0.842 ± 0.231 nN; sample 2, 0.349 ± 0.173 nN; sample 3, 0.252 ± 0.193 nN; and sample 4, 0.225 ± 0.063 nN. Unbinding forces of four samples are statistically different ($p < 0.05$). (B – E) represent frequency vs. unbinding force graphs associated with sample 1 – 4 whose unbinding forces were measured with amine-functionalized probes. Based on the frequency of unbinding forces, Gaussian curves was drawn , and average & standard deviation are calculated as shown in (A).

REFERENCES

1. S. Lee, Mandic, J., and Van Vliet, K. J., *Proceedings of the National Academy of Sciences of the United States of America* **104**, 9609–9614 (2007).
2. E. B. Walton, Lee, S., and Van Vliet, K.J., *Biophysical Journal* **94**, 2621–2630 (2008).

Appendix D

Extending Bell's Model: How Force Transducer Stiffness Alters Measured Unbinding Forces and Kinetics of Molecular Complexes

This appendix contains parts of the following study published in 2008 with co-authors of Emily B. Walton (1). My contribution to this work is to conduct experiments to prove that AFM cantilevers of different stiffness alters measured unbinding forces and binding kinetics of biotin-streptavidin pairs.

D. 1 INTRODUCTION

Ligand-receptor kinetics and energetics have been measured typically through experimental methods that quantify population-averaged responses (*5*), but a range of new experiments and simulations enables the probing of individual complexes to explore important variations in binding responses within and among ligand or cell populations (*11-13*). Biotin-streptavidin is among the strongest known ligand-receptor interactions and, as such, it has been widely studied as a model system (*16-25*) and utilized in biological experiments (*26-34*). Despite the ubiquitous application of the biotin-streptavidin complex in biotechnology and biophysics as a molecular glue capable of strong, specific interactions and long binding lifetime, there is considerable disagreement among experiments regarding the actual strength of this complex (*8, 35*). Many studies of the dynamic strength of biotin-streptavidin have been reported, using diverse experimental tools such as optical traps (*36*), laminar flow chambers (*37*), electric fields (*14*), magnetic fields (*15*), the biomembrane force probe (*7*), and the atomic force microscope (*2-4, 9, 10, 38-41*) to rupture the complex. Although these

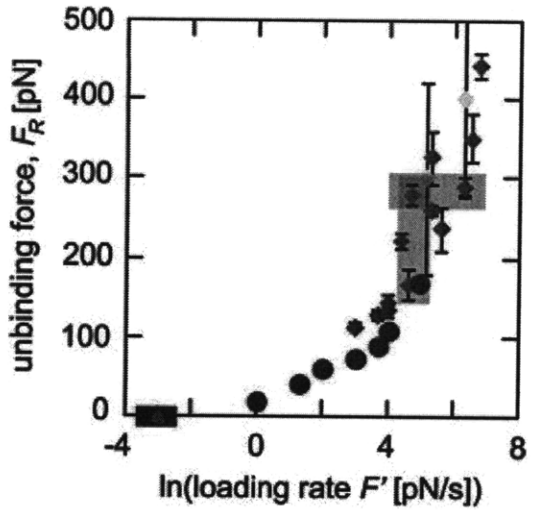

Figure D.1 Experiments to determine the unbinding force spectrum of biotin-streptavidin have not reached a consensus. Reported data on the unbinding force of biotin-streptavidin is shown as measured by AFM MFS (*diamonds* in *green(2-4)*, *orange(9)* and *yellow(10)*), electric fields (*blue triangles(14)*), magnetic fields (*purple squares(15)*, points overlap), and BFP (*red circles(7)*). Error bars indicating the standard deviation among experimental measurements are shown for all data points, but in some cases are smaller than the symbols. The shaded rectangles highlight measurements at similar loading rates where measured unbinding forces differ by a factor of two and measurements of similar unbinding forces where the loading rate differed by two orders of magnitude.

experimental methods differ from each other in many ways, they all aim to measure the unbinding force F_R of the same molecular system. However, even among experiments at comparable loading rates—a known controlling factor of F_R—the magnitude and rate dependence of F_R can vary widely (*8, 35*), as illustrated in Fig. D.1. The dynamic strength of this complex has also been studied through various computational and analytical methods, such as steered molecular dynamics (*42*) and Langevin dynamics (*6*).

Accurate measurements of F_R are necessary if experiments and simulations are to provide quantitative value to chemomechanical imaging of cell surfaces (*43, 44*), biophysical studies of unbinding trajectories (*12*), and prediction of binding kinetics (*44*). Bell's model of specific adhesion under applied force (*11, 45, 46*) is commonly

applied to such experiments to extract kinetic and energetic binding constants. For a monotonically increasing applied force, an adaptation of this model relates the unbinding force to experimental, kinetic, and energetic parameters as

$$F_R = \frac{k_B T}{x_b} \ln \frac{F' x_b}{k_B T k_{off}}, \tag{D.1}$$

where k_B is Boltzmann's constant, T is absolute temperature, x_b is the distance between the bound state, and the energetic maximum, $F' = kv$ is the loading rate (where k is the stiffness of the force transducer and v is the velocity), and k_{off} is the kinetic rate of binding dissociation at equilibrium. From forced dissociation of molecules far from equilibrium, the extrapolated value of $\ln(F')$ at $F_R = 0$ and the slope of F_R versus $\ln(F')$ are critical for estimating both the kinetic (k_{off}) and energetic (x_b) parameters of the complex at equilibrium. To obtain accurate estimates of k_{off} and x_b, it is necessary to understand both the bandwidth of such measurements and the extent to which experimental or computational parameters perturb F_R.

To the best of our knowledge, we have reviewed all reported studies of the forced unbinding of the biotin-streptavidin complex. Experiments in which the loading rate or the unbinding force could not be determined were excluded, and our focus was limited to studies utilizing methods that attempted to apply a monotonically increasing force to the ligand-receptor complex, including applied electric (*14*) and magnetic (*15*) fields, the biomembrane force probe (BFP) (*7*), the atomic force microscope (AFM) (*2-4, 9, 10, 38-41*), and optical traps (*36*), as reviewed by Van Vliet et al. (*47*). We also excluded studies of slightly different molecules such as immunobiotin or avidin, to eliminate as many extraneous factors as possible.

After applying these criteria, eight experimental studies remained: Breisch et al.'s use of electric fields to apply force (*14*), Panhorst et al.'s use of magnetic fields (*15*), Merkel et al.'s use of the BFP (*7*), and five separate studies using the AFM to conduct molecular force spectroscopy (MFS) (*2-4, 9, 10*). Fig. D.1 shows the unbinding or rupture forces F_R reported in these studies as a function of the logarithm of the reported loading rate $\dot{F}$. It appears clear that the reported unbinding force F_R is not a unique function of $\dot{F}$: experiments differing by more than an order of magnitude in $\dot{F}$ measured very similar unbinding force distributions, and unbinding forces measured at the same $\dot{F}$ differ by as much as 200 %. One possible explanation is that discrepancies in reported unbinding forces could arise from subtle differences in experimental technique, such as the type of molecular linker utilized. However, this would not account for results reported by a single research group utilizing the same experimental approach that do not agree within the reported range of error, such as those of Lo et al. (*2-4*). Another rationale is that F_R depends not just on loading rate, but also on the entire loading history of the complex; this is plausible yet difficult to quantify (*8, 35*).

In light of these well-established discrepancies among experimental results for a model ligand-receptor complex, we performed new steered molecular dynamics (SMD) simulations (*12*) of forced unbinding of the biotin-streptavidin complex. These simulations allowed exploration of the effects of molecular structure, loading direction, and experimentally accessible parameters including force transducer stiffness k and velocity v on the observed unbinding force F_R and inferred kinetic and energetic properties of the complex. The biotin-streptavidin pair was one of the first systems studied with SMD (*42*); while that report was groundbreaking in terms of technique, we performed new simulations because there were several aspects that would benefit from

advances in computational resources and protocols over the past decade, including the current capacity to simulate the entirety of the streptavidin tetramer over nanosecond timescales. In both the experimental and simulated loading rate regimes, we find that several experimentally accessible factors other than loading rate significantly affect both the observed F_R and the calculated binding parameters. Each of these factors can alter the ligand's exploration of the energy landscape presented by the receptor. In particular, an increase in the effective stiffness of the molecular force transducer k directly perturbs the energy landscape, leading to an increase in the observed F_R and to wide variation in extrapolated binding parameters. A new model, which corrects for the effects of k on unbinding force and kinetic dissociation rates, is introduced.

D.2 RESULTS AND DISCUSSION

D.2.1 Effects of initial macromolecular structure

We simulated identical, forced unbinding experiments on a range of ostensibly equilibrated biotin-streptavidin tetramer structures to consider how slight variation of the initial atomic positions and velocities in the ligand-receptor complex affects the observed unbinding force and inferred unbinding kinetics. Rather than choosing a single structure from the equilibration trajectory as a starting point for the SMD simulations (see Methods), we selected nine distinct sets of atomic coordinates from that trajectory, spaced at 10-ns intervals. We used each of these sets of atomic coordinates as initial structures for separate SMD simulations with the same set of initial atomic velocities (as described in Methods). Additionally, we considered one of these structures (i.e., one set of atomic coordinates) with three different sets of initial atomic velocities in separate SMD simulations. These simulations were designed to probe the stochastic nature of

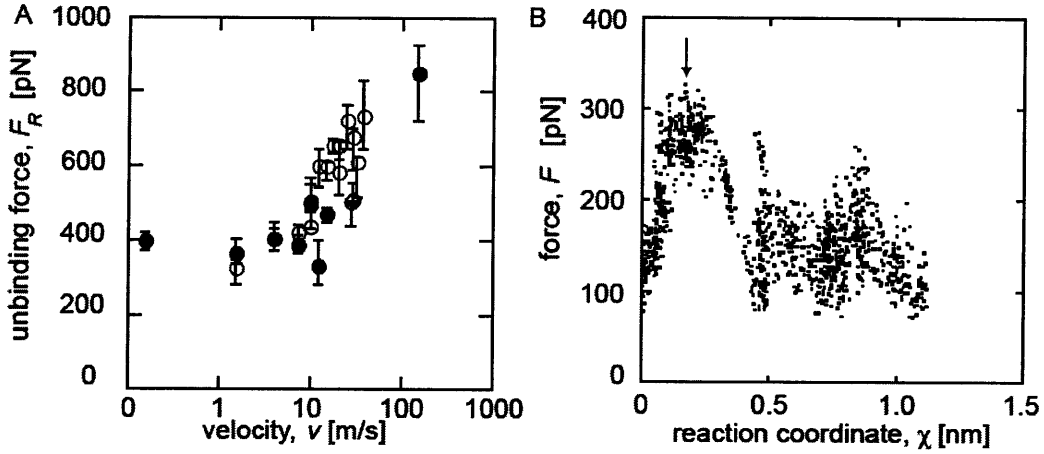

Figure D.2 (A) Steered Molecular Dynamics simulations were performed on the non-physiological biotin-streptavidin monomer in 1996 by Grubmüller et al. (40). As a starting point for our investigation of the tetramer, we replicated these early results on the monomer. Our results (solid black) agree reasonably well with those of Grubmüller et al. (open, adapted from (40)). Since the spring constant k is the same in all simulations shown, this is equivalent to unbinding force F_R as a function of loading rate F′ on a logarithmic scale. Rupture force at v = 150 m/s analyzed via tetramer method, as rupture occurred in less time (4 ps) than the smoothing width time of Ref. (40). (B) An example force-reaction coordinate response during simulated unbinding under conditions k = 2.8 N/m, v = 0.8 m/s. The unbinding force F_R in this particular trajectory is indicated by the arrow.

individual ligand-receptor unbinding events by varying initial configurations (atomic positions and velocities) independently from loading conditions.

We found marked variation in the force-distance responses (e.g., Fig. D.2B) among different equilibrated configurations (both initial atomic positions and initial atomic velocities) subjected to the same loading conditions. This distribution led to a range of ~20% in observed unbinding forces, as shown in Fig. D.3. We achieved this range whether we varied the initial atomic positions or the initial atomic velocities, indicating that either can be varied to enhance sampling in SMD simulations. Further, this range suggests the minimum variation in F_R that corresponding experiments can be expected to achieve, independent of instrument precision.

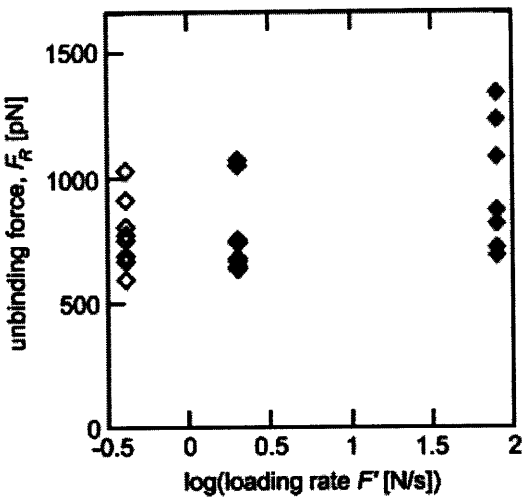

Figure D.3 Steered molecular dynamics simulations were performed on nine different biotin-streptavidin complex configurations (some symbols overlap), with three sets of simulated experiments, differing in loading rate F' (*open, solid, shaded*). Within each set of experiments the only difference among unbinding trajectories was the starting configuration of the atoms within the complex. Between each set of simulated experiments, the only difference is the velocity v, and therefore the loading rate $F' = kv$ (*open*, $v = 0.4$ m/s; *solid*, $v = 0.8$ m/s; and *shaded*, $v = 4$ m/s). The force transducer stiffness k was 2.8 N/m in all simulations. The large range in observed unbinding force (20%), based only on the initial configuration of the molecular complex, suggests a structural reason for the experimentally observed variation in unbinding force.

We also considered the effects of slight changes in the loading history of the ligand-receptor complex by changing loading vector orientation with respect to the binding pocket normal and also by varying the loading profile. Vector rotation by $\pm 5^\circ$ and $\pm 10^\circ$ around the x, y, and z axes led to variations in F_R of ~10%. We further found that changing the loading history of the complex by first pushing and then pulling along the loading vector (as would occur in AFM MFS experiments) had no effect on the measured unbinding force; the limited effect of loading history observed here was expected because the ligand was intentionally placed in the most energetically favorable bound state during the equilibration trajectory.

D.2.2 Effects of experimentally accessible parameters

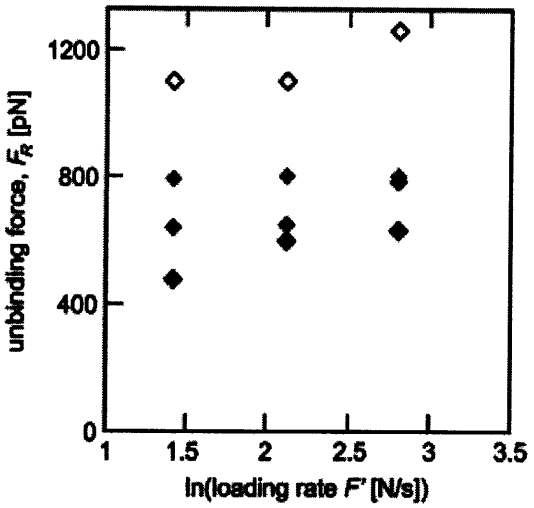

Figure D.4 Testing the assumption that loading rate is the controlling variable for unbinding force, we systematically varied force transducer stiffness k (*solid*, 0.83 N/m; *dark shaded*, 1.66 N/m; *light shaded*, 4.15 N/m; *open*, 8.3 N/m) and velocity v to produce three different loading rates (F' = 4.15 N/s, 8.3 N/s, and 16.6 N/s) in SMD simulations of biotin-streptavidin rupture. At the same loading rate, a stiffer force transducer correlated with a higher unbinding force (*open points* are the stiffest force transducers, shading to *black*, which are the most compliant).

We designed a set of simulated experiments to investigate the effect of experimentally accessible parameters on the measured value of F_R by systematically varying the force transducer spring constant k and the velocity v to produce three different effective loading rates F', while maintaining the initial structure (atomic positions and velocities) of the complex constant. As shown in Fig. D.4, we observe the expected loading rate dependence of F_R for a given transducer stiffness k. These results also show that the magnitude of k strongly affects observed F_R. At the same loading rate F', simulations using larger values of k consistently exhibited higher unbinding forces F_R. In contrast to these results, Bell's model implies that the loading rate is the controlling variable for the observed unbinding force (*45, 48*).

In our simulations, the force transducer stiffness k increased by more than an order of magnitude, and correlating with an increase of ~200% in observed unbinding

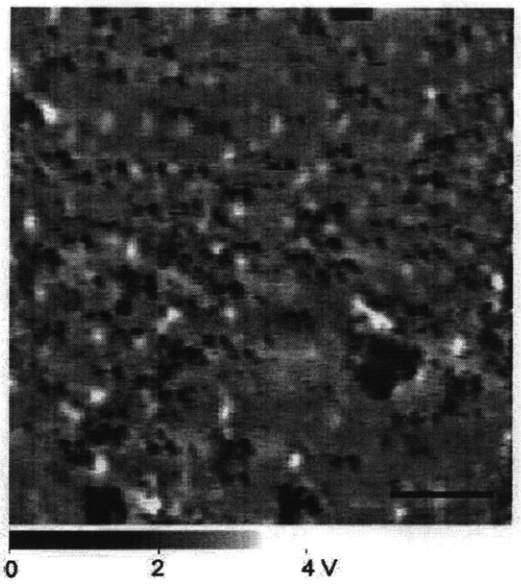

Figure D.5 Before performing AFM MFS experiments, the streptavidin-functionalized mica surface was imaged with biotin-functionalized cantilevers in TopMAC mode, allowing for precise placement of the cantilever tip before beginning forced unbinding experiments. The recognition image above (scale bar = 300 nm) demonstrates many streptavidin molecules, which are recognizable by their characteristic dark spots. The cantilever oscillator truncation is the feedback signal voltage and is scaled as 0 V corresponding to large truncation (adhesion). Since these dark spots represent strong binding events between the biotin-functionalized probe and the streptavidin-functionalized mica, positioning the tip near a dark spot significantly increased the probability that each approach-retract cycle would include a biotin-streptavidin binding event.

forces. Consequently, the calculated dissociation rate k_{off} of the biotin-streptavidin complex varied by more than an order of magnitude, from $1.32\times10^{-8}s^{-1}$ for the stiffest force transducer (k = 8.3 N/m) to $5.3\times10^{-9}s^{-1}$ for the most compliant force transducer (k = 0.83 N/m). In contrast, calculations of the location of the energetic barrier x_b, which depend only on the slope of the linear fit to F_R versus ln(F), resulted in a range of x_b between 0.05 and 0.06 nm. Estimates of x_b from a combination of dynamic force spectroscopy experiments, flow chamber studies, and molecular dynamics simulations indicate an energetic barrier distance of ~0.1 nm (*6-8*).

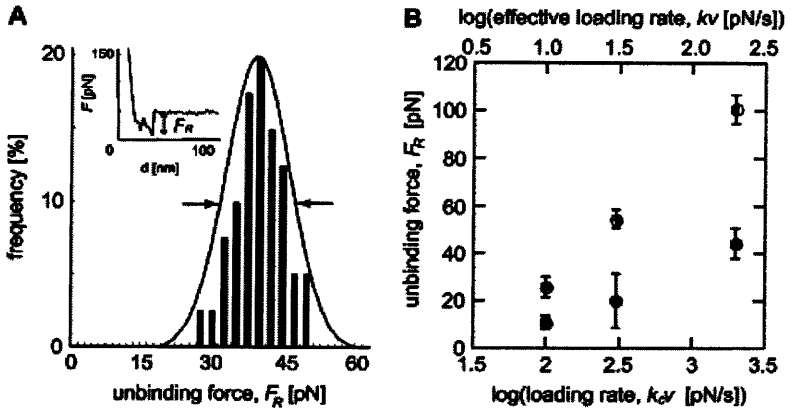

Figure D.6 (*A*) Experimental measurements of biotin-streptavidin unbinding force F_R were performed via atomic-force microscope-enabled molecular force spectroscopy, utilizing cantilevers of two different spring constants. For each set of loading conditions (effective force transducer stiffness k and retraction rate v) at least 50 force-displacement (F–Δ) responses for single rupture events were recorded, with F_R calculated as indicated. (*Inset*) A single rupture event of F_R = 46 pN, under effective k = 4.12 mN/m and v = 0.073 μm/s. A Gaussian distribution was fit to the histogram of unbinding forces for each set of conditions (here, k_c = 35 mN/m and v = 0.073 μm/s), and the distribution maximum was reported as F_R. Arrows indicate the FWHM. (*B*) Unbinding force F_R as a function of the logarithm of the loading rate F', as measured by AFM using two different cantilevers: k_c = 35 mN/m (*solid circles*) and k_c = 58mN/m (*open circles*); error bars represent one standard deviation in F_R and effective F', and may appear smaller than symbols. In all cases, the stiffer cantilevers measured higher unbinding forces than the more compliant cantilever, indicating that the dependence of measured F_R on the stiffness of the force transducer k is not limited to the extreme loading rates achieved in simulation.

D.2.3 Comparison with experimental measurements

We performed AFM MFS experiments on the biotin-streptavidin system to consider whether our simulation predictions — that higher unbinding forces are measured with stiffer force transducers for a fixed loading rate — held true in the experimental loading-rate regime. An initial investigation was carried out with two cantilevers of differing spring constants (k_c = 35 mN/m and 58 mN/m), and the cantilever retraction velocity v was varied to measure unbinding forces at the same effective loading rates. The effective force transducer stiffness k was approximately one order-of-magnitude lower than k_c for each biotin-functionalized cantilever, as expected (k = 3.9 mN/m and

6.9 mN/m, respectively); see Methods and the literature (*9, 49*). The unbinding force F_R, measured between a biotin-functionalized cantilever and a streptavidin-functionalized mica surface (Fig. D.5), was determined as the mean of a Gaussian fit to histograms constructed from at least 50 replicate single rupture events acquired under the same loading conditions (force transducer stiffness k and velocity v), as shown in Fig. D.6A. The resulting unbinding forces are presented in Fig. D.6B as a function of $\ln(F')$, showing that the apparent strength of the complex increases as k increases - even if the loading rate F' is maintained constant. That is, the correlation of stiffer cantilevers with higher measured unbinding forces continued in the experimental loading rate regime (on the order of nN/s). It is interesting to note that an equivalent effect was reported as an incidental observation for the biotin-streptavidin system, even before the appreciation that unbinding force depended on loading rate: for a fixed velocity (ranging from 1 to 50 μm/s) and unbinding force, a stiffer AFM cantilever yielded a shorter measured lifetime of the complex (*10*). In our experiments, the apparent strengthening effect of a stiffer cantilever had notable effects on calculated energetic and kinetic quantities, with an increase in effective k of 185 % resulting in an increase in the measured unbinding force F_R of ~150 %, a decrease in the calculated energetic unbinding length x_b of ~ 100 % (0.15 nm to 0.07 nm), and an increase in the calculated dissociation rate k_{off} of ~ 250 % ($8.3 \times 10^{-7} s^{-1}$ to $2.0 \times 10^{-6} s^{-1}$). Here, k_{off} and x_b were calculated from a linear regression to the full distribution of unbinding forces, rather than the mean unbinding forces F_R.

The unbinding force distribution can be expressed as full-width half maximum (FWHM) of the experimentally measured histograms of F_R observed in replicate AFM MFS experiments at a given loading rate (see, e.g., Fig. D.6A). This FWHM

corresponded well with the observed range in SMD-simulated unbinding forces among ostensibly equilibrated structures (~20 % of the mean F_R). However, due to the computational resources required for SMD simulations of solvated proteins, it is currently not feasible to execute the large number of forced unbinding simulations for a given parameter set (structure, k, and v) that would be required to construct the histograms and probability density functions of F_R attainable in experiments. Thus, simulations suggest but do not prove that the stochastic nature of forced unbinding of single ligand-receptor interactions is attributable in part to sampling small variations in atomic positions and velocities.

Due in part to the incomplete sampling of an ensemble response and the large difference in loading rates attainable in experiments (nN/s) and in simulations (N/s), it is not expected that the magnitude of F_R or the extrapolated kinetic and energetic parameters will agree quantitatively (*6*). However, SMD simulations remain valuable tools for studying forced unbinding because they can reveal atomic-level detail of mechanisms and pathways not accessible by experiment (*12*). Here, both simulations and experiments on the biotin-streptavidin complex show clear effects of force transducer stiffness k on measured unbinding forces. One important implication of this effect is that two experiments performed over the same loading rate range and with different, single values of k would not necessarily obtain the same magnitude or loading rate-dependence of the unbinding forces. This has been noted recently for SMD simulations (*50*) and optical trap experiments (*51*) on the mechanically forced unfolding of biopolymers. Thus, both simulations and experiments suggest that the accuracy of ligand-receptor binding parameters extracted from analyses of single complexes will be significantly enhanced by consideration of a range of both F and k.

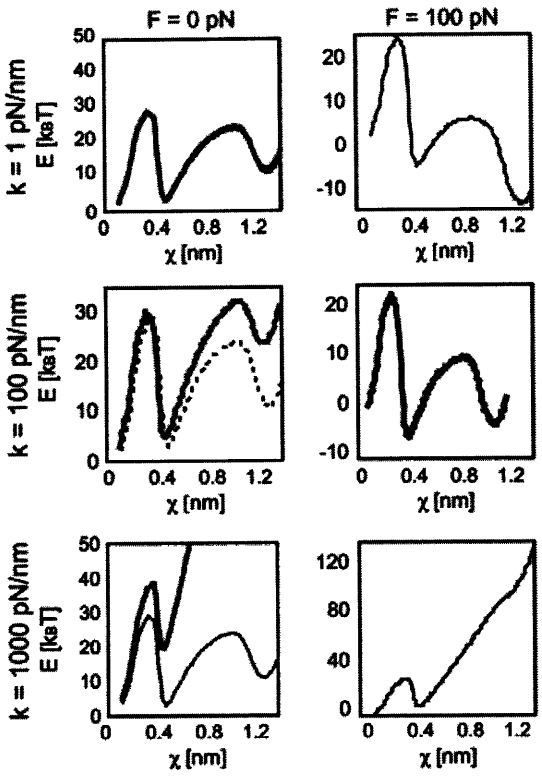

Figure D.7 The stiffness of the force transducer not only limits the exploration of the ligand in the energy landscape, but also changes the energy landscape the ligand traverses. Here, the effects of stiffness on the biotin-streptavidin energy landscape $E^{**}(F, x)$ (adapted from (*6-8*)) are shown, both before pulling begins ($F = 0$, *left column, gray solid line*) and at an applied load of 100 pN (*right column, black solid line*). Compliant cantilevers of $k < 1$ pN/nm are typical of BFP and optical trap experiments (*top row*). For such small k, the perturbed energy landscape ($E^{**}(F, x)$, *solid*) remains close to the equilibrium energy landscape ($E_0(x)$, *dashed*) in the absence of applied force. Stiff cantilevers of $k > 1000$ pN/nm are typical of SMD simulations (*bottom row*). Even in the absence of significant applied force of the ligand, the perturbed energy landscape ($E^{**}(F, x)$, *solid*) is far from the equilibrium landscape ($E_0(x)$, *dashed*). AFM cantilevers of $k \approx 10 - 100$ pN/nm are intermediate to these extremes (*middle row*). Since application of a nonzero force inherently implies a nonequilibrium state of the bound complex, no equilibrium landscape is depicted in the right column ($F = 100$ pN).

D.2.4 Effects of *k* on the energy landscape of the complex

Through SMD simulations and complementary AFM MFS experiments, we have shown that macromolecular structure, loading direction, and the loading conditions (k and v) can significantly affect the measured unbinding force F_R and inferred unbinding kinetics.

The commonality among these factors is that they all either perturb or alter exploration of the three-dimensional energy landscape $E(x, y, z)$ of the complex.

The kinetics of any given reaction depends on the energetic barrier crossed during the reaction. The effects of applied force on the energy landscape (and, therefore, on k_{off} and x_b) have been well documented: applied force tilts the simplified one-dimensional energy landscape such that $E_F(x) = E_0(x) - Fx$, where $E_0(x)$ is the unperturbed energy landscape, leading to a reduction in energetic barrier height (*11, 46, 52*). This reduction increases the kinetic off-rate as $k_{off}(F) = k_{off}^0 \exp(F_R/F_b)$, where k_{off}^0 is the equilibrium kinetic off-rate and F_b is x_b/k_BT. However, the effect of the force transducer stiffness k on the observed unbinding force and kinetics has been neglected. Evans has noted that a stiffer force transducer leads to a higher energetic barrier at a given applied force, but did not include this effect explicitly in analytical predictions of k_{off} under applied force (*52*). As we discuss below, this contribution can in fact be reasonably neglected for sufficiently compliant force transducers, such as the biomembrane force probe used in the experiments of Merkel et al. (*7*). Once the ligand is mechanically attached to the force transducer, the potential energy of the force transducer must be accounted for in the energy landscape as

$$E^*(x) = E_0(x) + \frac{1}{2}kx^2. \qquad \text{(D.2)}$$

Applying force to this perturbed energy landscape E^* then tilts the energy landscape such that

$$E^{**}(F, \chi) = E_0(\chi) - F\chi + \frac{1}{2}k\chi^2, \tag{D.3}$$

As shown in Fig. D.7, the barriers presented by the tilted landscape $E^{**}(F, \chi)$ at a particular value of applied force also depend on k. When force is applied by an ideal spring (*force* = $k\chi$), a stiffer force transducer leads to a higher energetic barrier to unbinding (and therefore a higher unbinding force) as shown by Eq. (D.3). The kinetic rate of dissociation is then

$$k_{off} = k_{off}^0 \exp((F_R - \frac{1}{2}kx_b)/F_b), \tag{D.4}$$

where F_b is x_b/k_BT and k_{off}^0 is the dissociation rate of the system at equilibrium (corresponding to $E_0(\chi)$). This implies that, rather than extracting the energetic and kinetic parameters of the complex from Eq. D.1, x_b and k_{off} should be extrapolated from

$$F_C = F_R - \frac{1}{2}kx_b = \frac{k_BT}{x_b}\ln\frac{F'x_b}{k_BTk_{off}}, \tag{D.5}$$

where F_C is the unbinding force at a particular loading rate F' that has been corrected for the barrier perturbation due to k.

For some experimental approaches such as BFP and optical traps, the force transducer stiffness is typically small enough ($k \approx 1$ pN/m) that the additional term $(1/2)kx_b$ may be negligible. In fact, this contribution to the observed unbinding force has been reasonably neglected in such experiments thus far. However, in both AFM MFS and SMD measurements of the unbinding force, the opposing force contribution

$(1/2)kx_b$ can be on the same order of magnitude as F_R. It is important to note that the effective stiffness of the force transducer k may depend on loading rate as well as the mechanical compliance of any molecular linkers (see MATERIALS AND METHODS). In Fig. D.7, we demonstrate the effect of force transducer stiffness on the biotin-streptavidin energy landscape (*6-8*) for three different values of k (1 pN/nm, which corresponds to optical trap and BFP experiments; 100 pN/nm, which corresponds to AFM MFS; and 1,000 pN/nm, which corresponds to SMD) and at two different instances of applied force ($F = 0$ pN, or before pulling begins, and $F = 100$ pN). Even before force is applied, the energy landscape is perturbed much more by the stiff force transducer than by more compliant force transducers. In the limit of an infinitely compliant force transducer ($k = 0$), the perturbed energy landscape $E^{**}(F, x)$ is equal to the equilibrium energy landscape E_0. In this case, $E^{*}(F, x)$ and $E^{**}(F, x)$ reduce to a single expression for the height of the energetic barrier at x_b. Very compliant force transducers, such as those used in biomembrane force probe experiments ($k \approx$ 1pN/nm for the strongly-bound biotin-streptavidin system (*7*)), may be considered to adhere to this compliant limit. However, as the force transducer stiffness increases, the perturbation of the energy landscape increases and the difference between $E^{*}(F, x)$ and $E^{**}(F, x)$ becomes significant. Next, we show that this correction of the observed unbinding force (Eq. D.5) eliminates the apparent dependence of k_{off} and x_b on force transducer stiffness k for both simulations (Fig. D.4) and experiments (Fig. D.6B).

To determine x_b from experiments using our corrected model, we fit the experimental unbinding forces F_R from two cantilevers ($k_c = 35$ and 58 mN/m) to Eq. (D.5), using least-mean-squares minimization of the residual defined as $\sum_n F_C(k_n) - F_C(k_0)$. Here, n is the number of different transducer stiffnesses considered

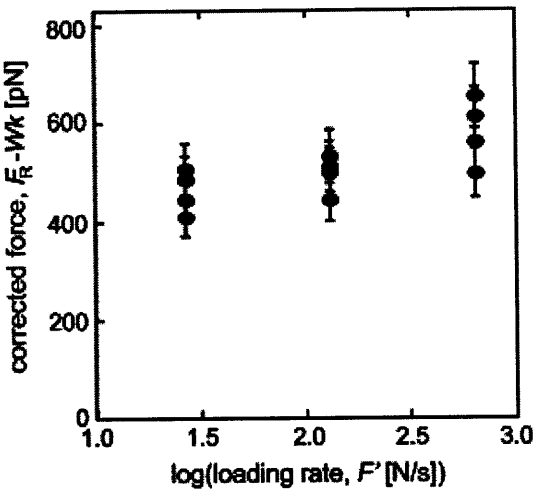

Figure D.8 After correcting biotin-streptavidin unbinding forces measured via SMD simulations according to Eq. (D.3), the corrected unbinding force F_C for all for all values of k agree within estimated error ranges (error estimated as ±10%, based on 20% FWHM of force distribution in both simulations and experiments). Uncorrected unbinding forces F_R are shown in Fig. D.3.

for a given loading rate (for our experiments, $n = 2$); and k_0 is the stiffness of the most compliant transducer (for our experiments, $k_0 = 3.9$ mN/m). To determine x_b from the simulations, the identical procedure was performed with the simulated stiffnesses k and unbinding forces F_R (for our simulations, $n = 4$ and $k_0 = 0.83$ N/m). As shown in Fig. D.8 for SMD simulations, correcting for the effects of k on the energy landscape as outlined above brings the corrected unbinding forces calculated with different force transducer stiffnesses k into agreement with each other, within the ±10% error attributable to the stochastic nature of ligand-receptor interactions. Corrections of the observed experimental unbinding forces F_R yielded similar results. Both x_b and k_{off} can be extracted from the corrected data, resulting in values of 0.05nm and $5.1 \times 10^{-9} s^{-1}$, respectively, for the simulations; and 0.11 nm and $2.1 \pm 0.5 \times 10^{-7} s^{-1}$, respectively, for the AFM experiments. To validate this correction of effective force transducer stiffness on the energy landscape and inferred unbinding kinetics, we also repeated the

calculation of k_{off} after including unbinding forces obtained with both stiffer cantilevers (k_c = 121 mN/m, F_R = 112.0 ± 4.9 pN) and more compliant cantilevers (k_c = 11 mN/m, F_R = 38.7 ± 5.4 pN) at a loading rate of 2,000 pN/s: k_{off} calculated over this wider range of force transducer stiffness ($2.7 \pm 0.6 \times 10^{7} s^{1}$ agreed within experimental error with that obtained over the narrower range of k_c = 35 and 58 mN/m. Our values of x_b from experiment and simulation agree well with previous experiments (*6-8*), which indicate that x_b is ~ 0.1 nm, the energetic distance of the innermost energy barrier accessible at these loading rates. The equilibrium dissociation rate of biotin-streptavidin as measured by competitive binding is $2.4 \times 10^{-6} s^{-1}$ (*53*), which is within an order of magnitude of our experimental k_{off}. Given our limited range of loading rates, we find this agreement to be reasonable. Although k_{off} inferred from SMD simulations does not extrapolate well to equilibrium dissociation rates, as anticipated for such large F (*12*), it is notable that this correction of simulated F_R by $(1/2)kx_b$ results in extracted energetic and kinetic parameters of the complex that agree much more closely with experimental estimates.

Another interpretation of the experimentally observed stiffness dependence of the unbinding force is that, at a given loading rate, a stiffer cantilever will lead to the AFM probe being in contact with the surface for a longer period of time (at a given F, a stiffer cantilever necessitates a slower v; total displacement remains constant). Although the contact times in the range of experimental loading rates we employed are well above the generally reported association time for biotin-streptavidin (~1 μs (*54*)), with more time to interact, one could conjecture that biotin may have sufficient time to sample a lower energy minimum in the streptavidin binding pocket. Note that while the probability of the complex rebinding is also dependent on stiffness (*52*), rebinding is

prohibited at the velocities employed in AFM MFS experiments and SMD simulations. As illustrated in Fig. D.7, the biotin-streptavidin energy landscape has three major energy minima (*6-8*); the timescale of our AFM experiments (≈ 0.2 - 2 s) is such that it is theoretically possible for both the deepest and the second-deepest minima to be populated (*8*). However, this would suggest that a multimodal distribution of unbinding forces would be observed for a given k and F. We did not observe such a distribution in our experiments, suggesting that our AFM MFS experiments consistently sampled a single energy minimum.

D.3 MATERIALS AND METHODS

D.3.1 Steered molecular dynamics

Grubmüller et al. (*42*) have reported SMD simulations of the forced unbinding of biotin from the streptavidin monomer, a choice due in large part to limited computational resources. As the residues of the biotin binding pocket are located on two streptavidin subunits, our physics-based procedure for equilibration of simulation proteins (*55*) confirmed that the biotin-streptavidin monomer was an inherently poor representation of this complex. For detailed information on the SMD simulations performed on the biotin-streptavidin monomer, see below. We subsequently conducted SMD simulations of the full streptavidin tetramer, with biotin bound in all four binding sites. The biotin-streptavidin tetramer (*24*) was simulated as described previously (*55*). Briefly, using the GROMACS molecular dynamics package, version 3.3 (*56, 57*), the protein was solvated in a cubic box of edge length 8.59 nm with 18,533 simple-point charge (SPC216) water molecules: 50 sodium ions and 42 chlorine ions were added to provide charge neutrality and to mimic physiological conditions. Steepest-descent minimization of the x-ray

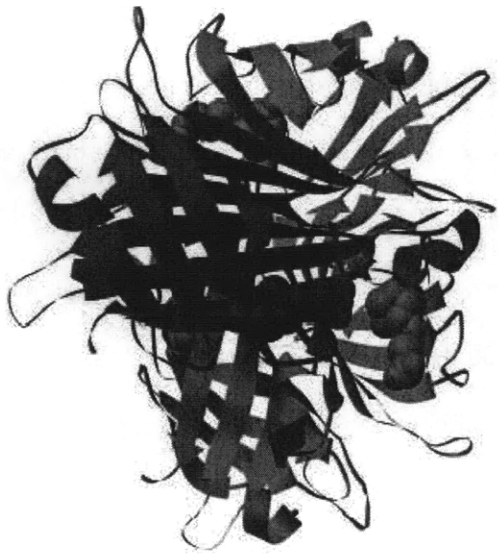

Figure D.9 The biotin-streptavidin complex is a tetrameric protein (ribbons) with four biotin molecules (spheres) bound. One subunit (monomer) is indicated in red. The binding pocket for each biotin consists of residues from two of the protein subunits. The blue sphere represents one of the oxygen atoms of the biotin, which is the atom believed to be linked to the force transducer in forced unbinding experiments.

diffraction structure was implemented to reduce the maximum force in the system to 2000 kJ $mol^{-1}nm^{-1}$. After minimization, unconstrained molecular dynamics simulation over 100 ns was performed to equilibrate the system. This required one week on 12 dual-processor Intel Xeon 3.0 GHz cluster nodes. The initial position of the force transducer (spring) in all SMD simulations coincided with one of the terminal oxygen atoms of the biotin (designated O2 in the PDB structure), the atom at which intermediate linkers ostensibly bond in the molecular force spectroscopy experiments. The position of this atom in the structure of biotin is shown in Fig. D.9.

Using the protocol developed in Walton and Van Vliet (*55*), we determined that the complex had entered a local energy minimum within 15 ns of beginning the equilibration trajectory. Structures were taken from this trajectory at intervals of 10 ns from time 15 ns to 95 ns. These were used as initial configurations for subsequent,

identical SMD simulations. One subunit of the tetramer was subjected to loading forces, although all four biotin binding sites were occupied. The tensile loading direction was defined as the vector between the initial center of mass of the streptavidin subunit and the O2 atom of the biotin bound to that subunit. The center of mass of the streptavidin tetramer was fixed, but the system was allowed to rotate about the center of mass. Transducer spring constants k ranged from 500 to 5000 kJ $mol^{-1}nm^{-2}$ (0.83 - 8.3 N/m) while velocities v ranged from 0.4 to 10 m/s. Effective loading rates $\dot{F}$ ranged from 0.4 to 11 N/s.

We performed three sets of simulations on the biotin-streptavidin tetramer. In the first set, the loading conditions (velocity v and spring constant k) were maintained while the initial equilibrated structure was varied as above. This set of simulations was designed to test the effects of initial complex structure on the measured unbinding force. In the second set, the loading direction was varied by vector rotation of $\pm 5^{\circ}$ and $\pm 10^{\circ}$ around the x, y, and z directions. In the third set, the initial structure was maintained while the loading conditions were varied. The structure taken from the equilibration trajectory at 20 ns was used. This set of simulations was designed to test the effects of experimentally accessible parameters on the unbinding force measurement — that is, parameters that are amenable to intentional variation in physical experiments.

The resulting trajectories were analyzed to extract the force exerted by the spring and the reaction coordinate of the ligand as functions of simulation time. Here, the reaction coordinate χ is defined as the distance of the biotin O2 atom from its initial position, $\chi = \sqrt{(x-x_0)^2 + (y-y_0)^2 + (z-z_0)^2}$. In analysis of the tetramer, we examined the forces at 200 fs intervals to investigate how the applied force varied with reaction coordinate χ. Other time intervals were also explored; 200 fs was selected

because this interval allowed for examination of the trajectory without significant changes in the maximum unbinding force selected by visual inspection of force F versus reaction coordinate x (ΔF_R ~1 %). When the unbinding force F_R is referenced, it is the maximum force recorded during a particular trajectory (e.g., see Fig. D.2B). The energetic unbinding distance x_b and kinetic dissociation rate k_{off} were determined via a least-squares linear regression of F_R versus $\ln F$ to obtain the slope (m) and x-intercept (b). From Bell's model, it is easily found that $x_b = (k_B T/m)$ and $k_{off} = b\, x_b/k_B T$.

D.3.2 Methods for SMD simulation of the biotin-streptavidin monomer

The biotin-streptavidin monomer (PDB ID 1STP (13)) was simulated using the protocol described by Walton et al. (47). Briefly, the GROMACS molecular dynamics package, version 3.3 (48, 49) was used, and the protein was solvated in a cubic box of edge length 6.18 nm with 7205 simple point charge (SPC216) water molecules: 19 sodium ions and 17 chlorine ions were added to provide charge neutrality and to mimic physiological conditions. Steepest descents minimization was used on the x-ray diffraction structure to reduce the maximum force in the system to 2,000 kJ $mol^{-1}nm^{-1}$. After minimization, 1 ns of unconstrained molecular dynamics simulation was performed to equilibrate the system, and the timestep was 2 fs. To establish a protocol for steered molecular dynamics (SMD) simulations of the forced unbinding of biotinstreptavidin, we first replicated the simulations of Grubmüller et al. (40), using the streptavidin monomer bound to a single molecule of biotin. Under our updated equilibration method (47), the biotin fell out of the binding pocket before it reached equilibration, indicating that a single molecule of biotin bound to the streptavidin monomer (which is not a physiologically stable structure) may be unstable in MD

simulations of appreciable duration (greater than 2 ns). Grubmüller et al. did not report this observation of instability, owing to the necessarily shorter simulation times accessible in 1996. To enable some direct comparison with Grubmüller et al., however, we adopted the simple root-mean-square-deviation based method, resulting in an equilibration time of 200 ps; all SMD simulations on the monomer used the structure from t = 200 ps in the equilibration trajectory as their initial structures. The initial position of the force transducer (spring) in all SMD simulations coincided with one of the terminal oxygen atoms of the biotin (designated O2 in the PDB structure), the atom at which intermediate linkers ostensibly bond in the AFM MFS experiments. The position of this atom in the structure of biotin is shown in Supplemental Figure 2. The tensile loading direction was chosen as the initial (normalized) vector between the center of mass of the streptavidin monomer and the displaced atom of the biotin. The monomer's center of mass was fixed in place, but the system was allowed to rotate around the center of mass. The transducer spring constant was k =1686 kJ $mol^{-1}nm^{-2}$ (units used by GROMACS package, or 2.8 N/m). This value represented the physical stiffness of a cantilevered linker, and was taken from Grubmüller et al., while the range of applied velocities was increased (v = 0.15–15 m/s) to include and extend that reported by Grubmüller et al.. The resulting trajectories were analyzed to extract the force exerted by the spring and the reaction coordinate of the ligand as functions of simulation time. Here, the reaction coordinate χ is defined as the distance of the biotin O2 atom from its initial position, $\dot{\chi} = \sqrt{(x-x_0)^2+(y-y_0)^2+(z-z_0)^2}$. In analysis of the monomer, we followed the approach of Ref. (40) and took F_R as the maximum of the force profile after smoothing with a Gaussian smoothing function of 4 ps width, and with Gaussian smoothing functions of 2 and 8 ps widths to determine a corresponding

error estimate.

D.3.3 Replication of previous SMD results

In our SMD analysis, we first replicated the simulations presented in Ref. (40) to test our procedure for calculating the force applied to the ligand-receptor complex as a function of both distance and time as the biotin is displaced from the streptavidin binding pocket. Our unbinding force F_R as a function of loading rate F' is shown in Supporting Information Figure 1A along with that of Grubmüller et al. (40). Although we used the same protocol (i.e., equilibration algorithm and loading parameters) as Ref. (40), our simulations differed in terms of molecular dynamics software, molecular force field, and explicit water type. With these differences in mind, we find the agreement in F_R between our simulations and those of Grubmüller et al. to be acceptable, in that many of the remaining discrepancies are within the smoothing width-determined error range of F_R in such SMD simulations. However, a single molecule of biotin bound to the streptavidin monomer, which is not a physiologically stable structure, is unstable in MD simulations of appreciable duration (> 1 ns). Thus, we focused on the tetrameric complex (Supporting Information Figure 2) in our simulations of forced unbinding via displacement of a virtual force transducer of spring constant k, moving at velocity v to result in loading rates on the order of N/s.

D.3.4 Experiments

AFM-enabled molecular force experiments on biotin-streptavidin were conducted to obtain F_R, k_{off}, and x_b as a function of experimentally accessible variables such as loading rate and force transducer stiffness. Silicon nitride AFM cantilevers of varying

nominal spring constant k_c (11, 35, 58, and 121 pN/nm or mN/m) were used as force transducers (MLCT-AUHW, Veeco Instruments, Woodbury, NY; MAC-IV levers, Agilent/Molecular Imaging, Palo Alto, CA). These cantilevers were cleaned in piranha solution (30% hydrogen peroxide: 70% sulfuric acid) for 30min, followed by rinsing in deionized water. Cantilevers were then dried in a stream of nitrogen. *N,N*-Di-isopropylethylamine (300 μL, Sigma-Aldrich, St. Louis, MO) and 3-aminopropyltriethoxysilane (900 μL, Sigma-Aldrich) were used for amine derivatization of cleaned cantilevers and freshly cleaved mica in a vacuum desiccator via chemical vapor deposition for 2h. Biotinylated BSA (B-BSA, Pierce Biotechnology, Rockford, IL) in sodium bicarbonate (pH = 8.9, 0.5 mg/mL) was added to cantilevers and mica, and the adsorption reaction proceeded overnight at 37°C (*58, 59*). Cantilevers and mica were rinsed with 150mM NaCl phosphate-buffered saline (PBS) twice, followed by covalent attachment of B-BSA to the cantilevers and mica with 52mM 1-Ethyl-3-[3-dimethylaminopropyl]carbodiimide hydrochloride (EDC, Pierce Biotechnology) for 2 h. After the covalent conjugation of B-BSA via EDC, cantilevers and mica were rinsed five times with PBS. B-BSA-conjugated mica was incubated with 100 μL of streptavidin (Pierce Biotechnology) in PBS (0.5 mg/mL) for 20 min, followed by rinsing 10 times with PBS.

Streptavidin-conjugated mica was imaged with biotin-functionalized cantilevers in contact mode and TopMAC mode within a fluid cell (PicoPlus AFM, Agilent/Molecular Imaging), using backside magnetically coated Si_3N_4 cantilevers. The tip was positioned for forced unbinding events based on this image (see Fig. D.5). The sensitivity of the photodetector (nm/V) was measured from the slope of force-displacement curves on bare mica. Cantilever spring constants (k_c, mN/m) were

measured via thermal fluctuations, as reported elsewhere (*60, 61*). At least 50 replicate force-piezoactuator displacement (F-Δ) responses were acquired for each (k_c, v) condition; retraction rate v of the piezoactuated cantilever was approximately constant for a given k_c, ranging from 0.015 to 0.254 μm/s across this F' range. Force-displacement responses were corrected for effects of hydrodynamic drag as described in the literature (*62, 63*). Effective loading rate F' (~100, 300, and 2,000 pN/s) was calculated as the product of v and the effective spring constant $k = dF/d\Delta$ just before unloading for each F-Δ curve (*9, 49*). The average effective spring constants for the two cantilever types were k = 3.9 mN/m and 6.9 mN/m, respectively, but the value derived from each force-displacement slope was used to analyze the corresponding unbinding force and loading rate. Note that there exist commercially available AFM cantilevers of lower nominal stiffness than those used here, including k_c = 11 pN/nm which we used to validate our predictions for these stiffer cantilevers. In this study, we primarily used these stiffer cantilevers for two reasons. First, we significantly increased the efficiency of acquiring force spectra by initially imaging the streptavidin-conjugated mica in TopMAC mode; this intermittent contact mode of imaging is not achievable in fluid for the most compliant cantilevers available. Second, in our experience with this AFM, more compliant cantilevers (k_c < 30 mN/m) provide an insufficiently stable signal for a wide range of loading rates; and stiffer cantilevers (k_c > 60 pN/nm) provide an insufficiently sensitive signal to detect pN-scale unbinding over these loading rates. These stabilities and sensitivities depend on the particular AFM laser-photodiode configuration. From these experimentally obtained spectra, x_b and k_{off} were determined as in Steered Molecular Dynamics, using the full distribution of unbinding forces in the linear regression. In short, more compliant cantilevers provide an insufficiently stable

signal for a wide range of loading rates; and stiffer cantilevers provide an insufficiently sensitive signal to detect pN-scale unbinding.

In our AFM MFS experiments, we did not observe any loading rate dependence in effective spring constant $k = dF/d\Delta$ over the range of loading rates explored (100 to 50,000 pN/s). However, we did not use distensible linkers, which may be several nanometers in length (e.g., polyethylene glycol 800); such linkers may have an effective stiffness that depends on loading rate. Since unbinding force depends on both effective stiffness and loading rate, careful analysis of this loading rate dependence of effective k would be required to calculate accurate kinetic and energetic constants.

We note that in AFM MFS experiments, there are two potential definitions of the force transducer stiffness: cantilever stiffness k_c, as measured by methods such as simple harmonic oscillator displacement at room temperature (*60, 61*); and the effective stiffness of the cantilever-linker system k, as calculated from $dF/d\Delta$ just before each unbinding event. For typical bifunctional molecular linkers, k is smaller than k_c by one order of magnitude (*41, 64*). Therefore, when comparing results among experiments, it is important to consider whether a particular study defined the effective loading rate as $k_c v$ or kv.

D.4 CONCLUSION

Our computational and experimental analyses of forced unbinding for the biotin-streptavidin complex demonstrate that loading rate is not the only controlling factor of the observed unbinding force F_R and inferred unbinding kinetics. The effective stiffness k, which represents the mechanical resistance of the total force transducer inclusive of any molecular linkers, can lead to manifold changes in the magnitude and rate dependence of the observed F_R. Further, our consideration of multiple structures of this complex demonstrates that a common assumption of SMD simulations - namely, that a single equilibrated structure will not explore enough of its phase space to impact simulation results - is not true for forced unbinding of ligand-receptor pairs. Even in consideration of an incomplete ensemble of ostensibly equilibrated initial configurations, we observed variations of > 20 % in F_R attributable only to minute differences in atomic positions or velocities.

We have demonstrated that the measured unbinding force of a ligand-receptor complex depends on several experimentally accessible factors that perturb or limit exploration of the energy landscape. These factors are especially important in interpretation of results utilizing effective force transducer stiffness of $k > 1$ pN/nm, as is common in AFM MFS experiments and SMD simulations. Beyond the established dependence on F', the magnitude of the force transducer k has the most dramatic effect on the inference of equilibrium behavior, as captured by the velocity of dissociation k_{off} and the energetic distance x_b. Consideration and quantification of these factors is necessary if forced unbinding experiments are used to infer the kinetics and energetics required for both predictive simulations and biomedical applications such as drug discovery. The demonstrated synergism between simulation and experiment elucidates

several key parameters that affect the nature and interpretation of forced ligand-receptor unbinding. In particular, although it has been known that the magnitude of k effectively limits the exploration of the energy landscape of a ligand-receptor complex, these results show that this controllable parameter also directly perturbs that landscape to effect wide variations in F_R, k_{off}, and x_b. We have demonstrated that this perturbation of the energy landscape via force transducer stiffness can be accounted for to obtain an effective unbinding force at each loading rate, and thus the equilibrium energetic and kinetic parameters of the complex. Beyond these model systems and experiments, our results suggest that the force required to dissociate molecular complexes can be altered by the mechanical compliance of the macromolecular structures to which the ligand (or receptor) is tethered, e.g., that of the extracellular matrix. Both experimental and computational analyses of biologically relevant ligand-receptor complexes under mechanical constraints or strain (*65*) will benefit from consideration of the sources and magnitude of variation in the observed unbinding forces and inferred kinetics.

REFERENCES

1. E. B. Walton, Lee, S., and Van Vliet, K.J., *Biophysical Journal* **94**, 2621–2630 (2008).
2. Y.-S. Lo, Huefner,N.D., Chan,W.S., Stevens,F., Harris,J.M., and Beebe,T.P., *Langmuir* **15**, 1373 (1999).
3. Y.-S. Lo, Zhu,Y.-J., and Beebe,T.P., *Langmuir* **17**, 3741 (2001).
4. Y.-S. Lo, Simons,J., and Beebe,T.P. , *J. Phys. Chem. B* **106**, 9847 (2002).
5. P. Scheidegger, Weiglhofer, W., Suarez, S., Console, S., Waltenberger, J., Pepper, M. S., Jaussi, R., and Ballmer-Hofer, K., *Biochemical Journal* **353**, 569 (2001).
6. S. Izrailev, Stepaniants,S., Balsera,M., Oona,Y., and Schulten,K., *Biophys J* **72**, 1568 (1997).
7. R. Merkel, Nassoy, P., Leung, A., Ritchie, K., and Evans, E., *Nature* **397**, 50 (1999).
8. F. Pincet, and Husson,J. , *Biophys J* **89**, 4374 (2005).
9. C. Yuan, Chen, A., Kolb, P., and Moy, V.T., *Biochemistry* **39**, 10219 (2000).
10. G. U. Lee, Kidwell,D.A., and Colton,R.J., *Langmuir* **3**, 354 (1994).
11. E. A. Evans, and Calderwood, D. A., *Science* **316**, 1148 (2007).
12. M. Sotomayor, and Schulten, K. , *Science* **316**, 1144 (2007).
13. K. Van Vliet, and Hinterdorfer, P., *Nano Today* **1**, 18 (2006).
14. S. Breisch, Gonska,J., Deissler,H., and Stelzle,M., *Biophysical Journal* **89**, L19 (2005).
15. M. Panhorst, Kamp,P.-B., Reiss,G., and Bruckl,H., *Biosens. Bioelectron* **20**, 1685 (2005).
16. A. Chilkoti, and Stayton, P.S., *Journal of American Chemical Society* **117**, 10622

(1995).

17. R. W. Dixon, and Kollman, P. , *Proteins* **36**, 471 (1999).

18. S. Freitag, Chu, V., Chu, V.. Penzotti, J.E., Klumb, L.A., To, R., Hyre, D., Trong, I.L., Lybrand, T.P., Stenkamp, R.E., and Stayton, P.S., *Proceedings of the National Academy of Sciences of the United States of America* **96**, 8384–8389 (1999).

19. W. A. Hendrickson, Pahler, A., Smith, J. L., Satow, Y., Merritt, E. A., and Phizackerley, R. P., *Proc Natl Acad Sci USA* **86**, 2190 (1989).

20. D. E. Hyre, Le Trong,I., Freitag,S., Stenkamp,R.E., and Stayton,P.S. , *Protein Science* **9** (2000).

21. D. E. Hyre, Amon,L.M., Penzotti,J.E., Trong,I.L., Stenkamp,R.E., Lybrand,T.P., and Stayton,P.S., *Nature Structural Biology* **9**, 582 (2002).

22. L. A. Klumb, Chu, V., and Stayton, P. S., *Biochemistry* **26**, 7657 (1998).

23. Y. Lindqvist, and Schneider,G. , *Curr. Opin. Struct. Biol.* **6**, 798 (1996).

24. P. C. Weber, Ohlendorf,D.H., Wendoloski,J.J., and Salemme,F.R., *Science* **243**, 85 (1989).

25. P. C. Weber, Wendoloski, J.J., Pantoliano, M.W., and Salemmet, F.R., *Journal of American Chemical Society* **114**, 3197 (1992).

26. K. L. Ewalt, Haigis,R.W., Rooney,R., Ackley,D., and Krihak,M., *Anal. Biochem.* **289**, 162 (2001).

27. A. Kurihara, Deguchi,Y., and Pardridge,W.M., *Bioconjug. Chem* **10**, 502 (1999).

28. A. Maraveyas, Rowlinson-Busza,G., Murray,S., and Epenetos,A.A., *Int. J. Cancer* **78**, 610 (1998).

29. V. R. Muzykantov, Atochina,E.N., Gavriljuk,V., Danilov,S.M., and Fisher,A.B.,

J. Nucl. Med. **35**, 1358 (1994).

30. S. F. Rosebrough, and Hashmi,M. , *J. Pharmacol. Exp. Ther.* **276**, 770 (1996).
31. B. Schechter, Chen,L.M., Arnon,R., and Wilchek,M., *J. Drug Target* **6**, 337 (1999).
32. M. Wilchek, and Bayer,E.A., *Anal. Biochem.* **171**, 1 (1988).
33. Z. S. Yao, Zhang,M.L., Kobayashi,H., Sakahara,H., Nakada,H., Yamashina,I., and Konishi,J. , *J. Nucl. Med.* **36**, 837 (1995).
34. M. L. Zhang, Yao,Z.S., Sakahara,H., Saga,T., Nakamoto,Y., Sato,N., Zhao,S.J., Nakada,H., Yamashina,I., and Konishi,J., *Nucl. Med. Biol.* **25**, 101 (1998).
35. B. T. Marshall, Sarangapani,K.K., Lou,J., McEver,R.P., and Zhu,C., *Biophys J* **88**, 1458 (2005).
36. T. Ota, Sugiura,T., and Kawata,S., *Appl. Phys. Lett.* **87**, 043901 (2005).
37. A. Pierres, Touchard,D., Benoliel,A.-M., and Bongrand,P., *Biophys J* **82**, 3214 (2002).
38. E.-L. Florin, Moy, V.T., Gaub, H.E., *Science* **264**, 415 (1994).
39. V. T. Moy, Florin, E.L., Gaub, H.E, *Science* **266**, 257 (1994).
40. J. Wong, Chilkoti,A., and Moy,V.T., *Biomol. Eng.* **16**, 45 (1999).
41. X. Zhang, and Moy,V.T., *Biophys. Chem.* **104**, 271 (2003).
42. H. Grubmüller, Heymann,B., and Tavan,P. , *Science* **271**, 954 (1996).
43. L. A. Chtcheglova, Waschke, J., Wildling, L., Drenckhahn, D., and Hinterdorfer, P., *Biophysical Journal* **93**, L11 (2007).
44. S. Lee, Mandic, J., and Van Vliet, K. J., *Proceedings of the National Academy of Sciences of the United States of America* **104**, 9609–9614 (2007).
45. G. I. Bell, *Science* **200**, 618 (1978).

46. E. Evans, and Ritchie,K, *Biophys J* **72**, 1541 (1997).

47. K. J. Van Vliet, Bao, G., Suresh, S., *Acta Materialia* **51**, 5881 (2003).

48. E. Evans, *Biophys. Chem.* **82**, 83 (1999).

49. T. Puntheeranurak, Wildling, L., Gruber, H. J., Kinne, R. K. H., and Hinterdorfer, P. , *Journal of Cell Science* **119**, 2960 (2006).

50. H. Karcher, Lee,S.E., Kaazempur-Mofrad,M.R., and Kamm,R.D. , *Biophys J* **90**, 2686 (2006).

51. J.-D. Wen, Manosas,M., Li,P.T.X., Smith,S.B., Bustamante,C., Ritort,F., and I.,T. , *Biophys J* **92**, 2996 (2007).

52. E. Evans, *Annu. Rev. Biophys. Biomol.* **30**, 105 (2001).

53. U. Piran, and Riordan,W. , *J. Immunol. Methods* **133**, 141 (1990).

54. M. H. Qureshi, Yeung,J.C., Wu,S.-C., and Wong,S.-L., *J Biol Chem* **276**, 46422 (2001).

55. E. B. Walton, and Van Vliet,K.J. , *Phys. Rev. E Stat. Nonlin. Soft Matter Phys.* **74**, 061901 (2006).

56. H. Berendsen, van der Spoel,D., and van Drunen,R. , *Comput. Phys. Commun.* **91**, 43 (1995).

57. E. Lindahl, Hess,B., and van der Spoel,D., *J. Mol. Model* **7**, 306 (2001).

58. A. Chen, and Moy, V.T., *Methods in Cell Biology* **68**, 301 (2000).

59. C. Stroh, Wang, H., Bash, R., Ashcroft, B., Nelson, J., Gruber, H., Lohr, D., Lindsay, S. M., and Hinterdorfer, P., *Proceedings of the National Academy of Sciences of the United States of America* **101**, 12503 (2004).

60. H. J. Butt, and Jaschke, M., *Nanotechnology* **6**, 1 (1995).

61. J. L. Hutter, and Bechhoefer, J., *Rev Sci Instrum* **64**, 1868 (1993).

62. J. Alcaraz, Buscemi,L., de Morales,M.P., Colchero,J., Baro,A., and Navajas,D., *Langmuir* **18**, 716 (2002).

63. H. Janovjak, Struckmeier,J., and Muller,D.J., *Eur. Biophys. J.* **34**, 91 (2005).

64. G. Neuert, Albrecht,C., Pamir,E., and Gaub,H.E. , *FEBS Lett.* **580**, 505 (2006).

65. V. B. Shenoy, and Freund,L.B., *Proc Natl Acad Sci USA* **102**, 3213 (2005).

Appendix E

Imaging of neurons in AFM contact mode

This appendix contains parts of the following unpublished study, conducted with Neville Sanjana and Prof. Sebastian Seung (Department of Brain and Cognitive Sciences at MIT).

E.1 CONTRIBUTION

The purpose of AFM imaging of these neurons is to trace every neurite back to its cell body in a culture that shows multiple neurons and crossing neuritis. My contribution to this work is to image neurons grown on glial cells to see the connection between axons and dentrites and count the number of axons and dentrites coming from a neuron.

E. 2 MATERIALS AND METHODS

E.2.1 AFM imaging of neurons

Neurons prefer to grow on glial cells seeded on glass cover slips. Neurons and glial cells were prepared for AFM imaging on glass cover slips. Neuron samples are fixed with the mixture of 1 % formaldehyde and 0.1 % glutaraldehyde, followed by 1 % Tris-buffer to quench excess aldehyde groups(*1*). If Tris buffer is not treated after fixation, cell surfaces become sticky, which generates AFM images of low quality due to abnormal interaction between cells and silicon nitride cantilevers. Cantilevers of nominal spring constant k = 0.01 nN/nm was used to prevent neurons from being scratched off from glass substrata, and imaging speed was maintained at 0.5 lines/sec. Fast imaging above 1 line/sec may move cells, which will change the position of

neurons or sever axons and dentrites. Optical microscopy-aided AFM was used for positioning of AFM cantilevers at specific locations of interest.

E. 3 RESULTS

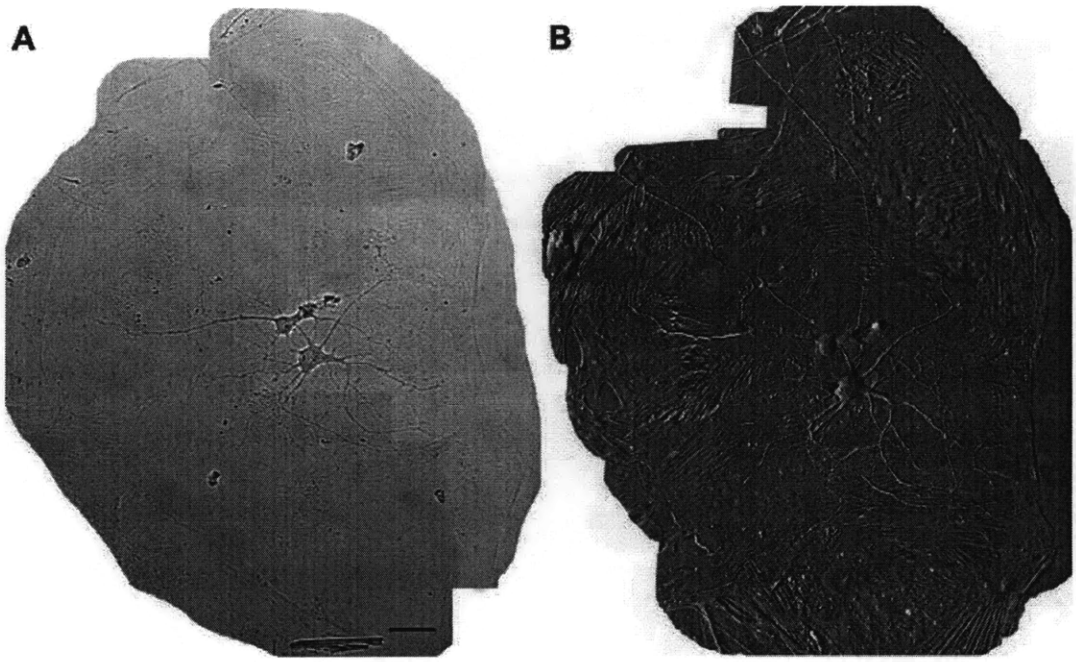

Figure E. 1 AFM contact mode image of neurons. (A) is an optical image that shows two neurons at the center of a glial cell. (B) two neurons and a glial cells underneath them are imaged in contact mode. (B) shows the same area as (A). Scale bar = 20 μm.

Neurons grown on glial cells were firmly attached and were better for AFM imaging. Although neuron images were clear and every neurite was visualized, it was not possible to tell axons and dendrites from crossing neurites. In addition, tracing neurites back to their neuron bodies was not possible from AFM contact mode imaging. Scanning electron microscopy (SEM) would be a better approach for this project. Two other approaches are suggested: taking time lapse imaging with optical microscopy over a period of time, which would clearly show the movement of each neurite; using antibody staining from the fact that unphosphorylated tau is only in axons and

microtubule-associated protein 2 (MAP2) is only in dendrites.

REFERENCES

1. S. Lee, Mandic, J., and Van Vliet, K. J., *Proceedings of the National Academy of Sciences of the United States of America* **104**, 9609–9614 (2007).